

University of Belgrade  
Faculty of Physics

Vladimir Veljić

**QUANTUM KINETIC THEORY FOR  
ULTRACOLD DIPOLAR  
FERMI GASES**

Doctoral Dissertation

Belgrade, 2019

Univerzitet u Beogradu  
Fizički fakultet

Vladimir Veljić

**KVANTNA KINETIČKA TEORIJA ZA  
ULTRAHLADNE DIPOLNE  
FERMI GASOVE**

Doktorska disertacija

Beograd, 2019.

---

# Thesis defense committee

---

Thesis advisor, Committee member:

**Dr. Antun Balaž**

Research Professor

Institute of Physics Belgrade

University of Belgrade

Committee member:

**Dr. Ivana Vasić**

Associate Research Professor

Institute of Physics Belgrade

University of Belgrade

Committee member:

**Dr. Milan Damnjanović**

Full Professor

Faculty of Physics

University of Belgrade

Committee member:

**Dr. Milan Knežević**

Full Professor

Faculty of Physics

University of Belgrade

---

*To my family*

$\overleftrightarrow{RAD}$

---

# Acknowledgments

---

This Thesis was completed at the Scientific Computing Laboratory, National Center of Excellence for the Study of Complex Systems of the Institute of Physics Belgrade. The presented research was supported by the Ministry of Education, Science, and Technological Development of the Republic of Serbia under the Project ON171017. Part of the work was also supported by the bilateral projects with Germany (QDDB, IBEC, BEC-L) and with Austria (DUDFG). I thank Dr. Antun Balaž, who was the PI for all of these projects, for giving me the opportunity to actively participate and scientifically contribute to these projects.

Dr. Antun Balaž supervised with great passion and immense help all aspects of my PhD studies. His enthusiasm and dedication accompanied me throughout this time and motivated me to continue, particularly at the most challenging times. I would also like to express my gratitude to Dr. Axel Pelster from the Technical University of Kaiserslautern, Germany, for all the generous help, productive discussions and countless teaching sessions. From both of them, I learnt good scientific practice, distinguished by meticulousness, thoroughness and attention to detail.

Belgrade, June 2019

Vladimir V.

---

# Abstract

---

Interactions between particles play an important role in quantum degenerate gases. In fact, the system's behavior is usually largely determined by the strength, range, and symmetry of the interactions, even if very weak. For more than two decades after the first experimental realization of a Bose-Einstein condensate (BEC) in 1995, investigations of ultracold atomic gases have mainly considered contact-type interactions, which model the short-range van der Waals interactions between the atoms in terms of a single parameter, the  $s$ -wave scattering length. However, some atomic or molecules species possess a magnetic or electric dipole moment and additionally interact among each other via the dipole-dipole interaction (DDI), which is long-ranged and anisotropic. Signatures of the DDI have been first observed in a BEC of chromium atoms in 2005. In the last several years, a new class of atoms from the lanthanide series, e.g., dysprosium and erbium, with stronger dipolar properties, have come into play. This permits a more full-fledged study of dipolar effects in BECs. Furthermore, ultracold molecules and highly excited Rydberg atoms are other promising examples for futures studies of systems where dipolar interaction will be even more dominant, but they still need experimental efforts to achieve the desired quantum regime. Whereas the weak DDI in a chromium BEC is well described with the Gross-Pitaevskii equation, stronger dipolar interactions certainly necessitate a beyond-mean-field description within a Bogoliubov theory.

In parallel to research on bosons, cold fermions also trigger great interest because they are actually often found in nature, e.g., within the electron gas of metals, as neutrons of heavy stars, or as quarks in plasmas as constituent elements of composite particles. Contrary to Bose systems, quantum degeneracy in experiments is much more difficult to achieve in Fermi systems, since  $s$ -wave scattering is absent between identical fermions, due to the Pauli exclusion principle. It was first achieved in 1999 for alkali atoms using a technique based on the sympathetic cooling with a second spin state, another species, or a different isotope. For highly magnetic atoms, quantum degeneracy was achieved for dysprosium in 2012 using the standard sympathetic cooling technique, while in 2014 erbium was cooled deep into the degenerate regime using a direct evaporative cooling mediated by dipolar collisions. This direct cooling scheme

---

allows producing very dense Fermi gas down to 10% of the Fermi temperature.

Furthermore, a novel kind of strongly dipolar quantum gases became available in the last several years. These are weakly bound polar molecules produced from atoms with large magnetic dipole moments, such as erbium. Only very recently a quantum degenerate dipolar Fermi gas of potassium-rubidium molecules has been experimentally realized. Unlike previously considered magnetic systems, heteronuclear molecules such as potassium-rubidium possess large electric dipole moments. The next natural step is to polarize this system in a preferential direction by an external electric field, such that the DDI dominates the behavior of the system, which would open up the realm for experimental investigation of strong dipolar Fermi gases.

The research whose results are presented in this Thesis aims to describe influence of many-body dipolar effects in Fermi gases, which are quite subtle as they energetically compete with the large kinetic energy at and below the Fermi surface (FS). Recently it was experimentally observed in a sample of erbium atoms that its FS is deformed from a sphere to an ellipsoid due to the presence of the DDI. Moreover, it was suggested that, when the dipoles' orientation is varied by means of an external field, the FS follows their orientation, thereby keeping the major axis of the momentum-space ellipsoid parallel to the dipoles. In order to explain this from the theoretical side, we have generalized a previous Hartree-Fock mean-field theory to systems confined in a triaxial trap with an arbitrary orientation of the dipoles relative to the trap. Using this newly developed approach, we have studied for the first time the effects of the dipoles' arbitrary orientation on the ground-state properties of the system. In particular, we have shown that the stability of trapped dipolar fermions is universal as it only depends on the trap aspect ratios and the dipoles' orientation.

Beside the ground-state properties of dipolar Fermi gases, we have also explored the dynamics during the time-of-flight expansion by using the quantum kinetic Boltzmann formalism in the relaxation-time approximation for the collision integral. We have studied the aspect ratios of the fermionic cloud in real and momentum space, including the deformation of the FS. In particular, we have extended the existing theoretical models such that we could describe all experimentally relevant regimes: collisionless, collisional, and hydrodynamic. Furthermore, taking into account the geometry of the system, we have shown how the ellipsoidal FS deformation can be reconstructed, assuming ballistic expansion, from the experimentally measurable real-space aspect ratio after a free expansion. We have compared our theoretical results with experimental data measured with erbium Fermi gas for various trap parameters

---

and dipole orientations. The observed remarkable agreement demonstrates the ability of our theory to capture the full angular dependence of the FS deformation. Moreover, for systems with even larger dipole moments, our theory predicts an additional unexpected effect: the FS does not simply follow rigidly the orientation of the dipoles, but softens showing a change in the aspect ratio depending on the dipoles' orientation relative to the trap geometry, as well as on the trap anisotropy itself.

**Keywords:** Fermi gas, dipole-dipole interaction, Fermi surface, Hartree-Fock theory

**Research field:** Physics

**Research subfield:** Condensed matter physics

**UDC number:** 538.9

---

# Abstract in Serbian

---

Interakcije između čestica igraju važnu ulogu u razumevanju ponašanja degenerisanih kvantnih gasova, koje je u velikoj meri određeno jačinom, dometom i simetrijama interakcija, čak i ako su veoma slabe. Tokom više od dve decenije nakon prve eksperimentalne realizacije Boze-Ajnštajn kondenzatacije 1995. godine, istraživanje ultrahladnih atomskih gasova je uglavnom bilo fokusirano na proučavanje kontaktnih interakcija između atoma, što je jednoparametarski model za kratkodometne van der Valsove interakcije, koji kao parametar uzima u obzir samo dužinu rasejanja u simetričnom ( $s$ ) kanalu. Međutim, neke vrste atoma ili molekula poseduju magnetni ili električni dipolni moment, pa moramo da uzmemo u obzir i dipol-dipol interakcije (DDI) između čestica. DDI su dugodometne i anizotropne, i njihov uticaj je prvi put eksperimentalno izmeren u kondenzovanom gasu atoma hroma 2005. godine. Nova klasa atoma iz grupe lantanoida, kao što su disprozijum i erbijum, sa jačim dipolnim osobinama, postala je dostupna u poslednjih nekoliko godina. Ovo omogućava potpunije istraživanje dipolnih efekata u Boze-Ajnštajn-kondenzovanim sistemima. Dalje, ultrahladni molekuli i visoko pobuđeni Ridbergovi atomi predstavljaju druge moguće pravce za proučavanje sistema u kojima će dipolna interakcija biti još značajnija, ali ovo zahteva dodatne eksperimentalne napore kako bi se dostigao željeni kvantni režim. Dok se slaba DDI između atoma hroma u kondenzovanim sistemima može dobro opisati Gros-Pitaevski jednačinom, prisustvo jake DDI zahteva uračunavanje efekata koji nisu prisutni u teoriji srednjeg polja u Bogoljubovljevoj teoriji.

Paralelno sa istraživanjima bozona, hladni fermioni su takođe izazvali veliko interesovanje jer se često sreću u prirodi, na primer u sistemima kao što je elektronski gas u metalu, u sistemima neutrona u masivnim zvezdama, ili kao kvarkovi koji čine kvark-gluonsku plazmu u kompozitnim česticama. Za razliku od bozonskih sistema, postizanje kvantne degeneracije u eksperimentima je mnogo teže za fermionske sisteme, jer zbog Paulijevog principa isključenja nema rasejanja u  $s$ -kanalu za identične fermione. Kvantna degeneracija hladnih fermiona je ostvarena prvi put 1999. godine za alkalne atome korišćenjem tehnike zasnovane na simpatetičnom hlađenju pomoću atoma u drugom spinskom stanju, druge vrste atoma, ili različitog izotopa. Kod atoma sa jakim magnetnim momentom, kvantna degeneracija je ostvarena tek 2012. godine

---

za disprozijum, korišćenjem standardne tehnike simpatetičnog hlađenja, a 2014. godine za erbijum, koji je ohlađen duboko u degenerisani režim korišćenjem direktnog evaporativnog hlađenja pomoću dipolnog rasejanja. Ova direktna tehnika hlađenja je omogućila stvaranje veoma gustog Fermi gasa na oko 10% Fermi temperature.

Pored toga, nova vrsta jako dipolnog kvantnog gasa je postala eksperimentalno dostupna u poslednjih nekoliko godina. U pitanju su slabo vezani polarni molekuli proizvedeni od atoma sa velikim magnetnim dipolnim momentima, kao što je erbijum. Tek prošle godine je eksperimentalno realizovan i kvantno-degenerisani dipolni Fermi gas molekula kalijum-rubidijuma. Za razliku od prethodno razmatranih magnetnih sistema, heteronuklearni molekuli kao što je kalijum-rubidijum poseduju jak električni dipolni moment. Sledeći prirodni korak je polarizacija takvog sistema u željenom pravcu pomoću spoljašnjeg električnog polja, tako da DDI dominira u ponašanju sistema. Ovo bi otvorilo novo polje za eksperimentalno istraživanje Fermi gasova sa jakim DDI.

Cilj istraživanja čiji su rezultati predstavljeni u ovoj doktorskoj disertaciji je opis uticaja mnogočestičnih dipolnih efekata na osobine hladnih Fermi gasova. Pošto ovi efekti mogu da budu maskirani velikom kinetičkom energijom na i ispod Fermijeve površine, njihov opis zahteva izuzetno pažljiv pristup. Nedavno je eksperimentalno opaženo da je Fermi površina (FP) u gasu atoma erbijuma deformisana, odnosno da umesto sfere ima oblik elipsoida usled prisustva DDI. Štaviše, kada se orijentacija dipola menja pomoću spoljašnjeg polja, eksperimentalni rezultati ukazuju da FP prati njihovu orijentaciju, zadržavajući tako glavnu osu elipsoida u momentnom prostoru paralelnu sa dipolima. U ovoj doktorskoj disertaciji je ovo opisano kroz uopštenje postojeće Hartri-Fok teorije srednjeg polja za sisteme u asimetričnim potencijalnim zamkama sa proizvoljnom orijentacijom dipola u odnosu na zamku. Razvoj ovog novog pristupa nam je omogućio da po prvi put proučavamo efekte proizvoljne orijentacije dipola na svojstva osnovnog stanja sistema. Od posebnog značaja je rezultat o univerzalnosti stabilnosti zarobljenih dipolnih fermiona, za koju smo pokazali da zavisi samo od odnosa frekvencija zamke i orijentacije dipola.

Pored svojstava osnovnog stanja dipolnog Fermi gasa, istraživali smo i dinamiku sistema tokom ekspanzije gasa nakon oslobađanja iz zamke, koristeći kvantni kinetički Bolcmanov formalizam u aproksimaciji relaksacionog vremena za kolizioni integral. Proučavali smo asimetričnost fermionskog oblaka u realnom i momentnom prostoru, uključujući i deformaciju FP usled prisustva DDI. Posebno, uopštili smo postojeće teorijske modele tako da mogu da opišu sve eksperimentalno relevantne režime: bez su-

---

dara, sa sudarima i hidrodinamički. Osim toga, uzimajući u obzir geometriju sistema, pokazali smo kako se elipsoidna deformacija FP može rekonstruisati iz eksperimentalno merljivog odnosa asimetričnosti oblaka gasa u realnom prostoru, uz pretpostavku balističke ekspanzije. Uporedili smo dobijene teorijske rezultate sa eksperimentalnim podacima koji su izmereni za različite parametre zamke i orijentacije dipola u atomskom gasu erbijuma. Dobijeno izvanredno slaganje ovih rezultata sa teorijom koja je razvijena u okviru ove doktorske disertacije potvrđuje da ona pruža potpuno razumevanje ponašanja FP i ugaone zavisnosti njene deformacije. Štaviše, za sisteme sa još jačim dipolnim momentom, teorija predviđa dodatni neočekivani efekat: FP ne samo da rigidno prati orijentaciju dipola, već menja i svoju zapreminu i dužine osa elipsoida u zavisnosti od orijentacije dipola u odnosu na geometriju zamke, kao i same anizotropije zamke.

**Ključne reči:** Fermi gas, dipol-dipol interakcija, Fermi površina, Hartri-Fok teorija

**Naučna oblast:** Fizika

**Uža naučna oblast:** Fizika kondenzovanog stanja

**UDK broj:** 538.9

---

# Contents

---

<b>Thesis defense committee</b> . . . . .	i
<b>Acknowledgments</b> . . . . .	iii
<b>Abstract</b> . . . . .	iv
<b>Abstract in Serbian</b> . . . . .	vii
<b>List of figures</b> . . . . .	xii
<b>List of tables</b> . . . . .	xvi
<b>1 Introduction</b> . . . . .	<b>1</b>
1.1 Quantum gases: fermions vs. bosons . . . . .	2
1.2 Free ideal Fermi gas . . . . .	5
1.3 Trapped ideal Fermi gas . . . . .	7
1.4 Trapped dipolar Fermi gas . . . . .	9
1.4.1 Dipole-dipole interaction . . . . .	9
1.4.2 Brief review of the field . . . . .	12
1.5 Motivation . . . . .	14
1.6 This Thesis . . . . .	16
<b>2 Ground state energy</b> . . . . .	<b>18</b>
2.1 Wigner function in equilibrium . . . . .	20
2.2 System energy in equilibrium . . . . .	26
2.2.1 Kinetic energy . . . . .	26
2.2.2 Trapping energy . . . . .	28
2.2.3 Hartree energy . . . . .	29
2.2.4 Fock energy . . . . .	33
2.2.5 Total energy for all scenarios . . . . .	37
2.3 Minimization of the total energy . . . . .	38
2.3.1 Variational parameters in momentum space . . . . .	39
2.3.2 Variational parameters in real space . . . . .	41
2.3.3 Comparing all scenarios . . . . .	43

---

<b>3</b>	<b>Ground state properties</b>	<b>46</b>
3.1	Dimensionless form of static equations . . . . .	48
3.2	Stability of the system . . . . .	52
3.3	Fermi surface deformation . . . . .	54
3.4	Gas cloud deformation . . . . .	65
3.5	Beyond Hartre-Fock mean-field theory . . . . .	70
<b>4</b>	<b>Dynamics of dipolar Fermi gases</b>	<b>74</b>
4.1	Boltzmann quantum kinetic equation . . . . .	75
4.2	Scaling ansatz . . . . .	79
4.2.1	Hartree and Fock kinetic integrals . . . . .	84
4.2.2	Special cases . . . . .	86
4.3	Time-of-flight dynamics . . . . .	89
4.3.1	Collisionless regime . . . . .	91
4.3.2	Hydrodynamic regime . . . . .	96
4.3.3	Collisional regime with constant relaxation time . . . . .	100
4.3.4	Collisional regime with self-consistent relaxation time . . . . .	102
<b>5</b>	<b>Comparison with experiment</b>	<b>108</b>
5.1	Aspect ratios and FS deformation . . . . .	109
5.2	Ballistic expansion . . . . .	110
5.3	Experimental and theoretical results . . . . .	111
5.4	Universal consequences of geometry . . . . .	115
<b>6</b>	<b>Conclusions</b>	<b>117</b>
<b>A</b>	<b>Fourier transform of dipolar interaction potential</b>	<b>120</b>
<b>B</b>	<b>Generalized anisotropy function</b>	<b>125</b>
B.1	Anisotropy function . . . . .	125
B.2	Anisotropy function for off-on-axis scenario . . . . .	126
B.3	Anisotropy function for off-off-axis scenario . . . . .	127
<b>C</b>	<b>Equations for variational parameters</b>	<b>129</b>
C.1	Spherical scenario . . . . .	129
C.2	On-on-axis scenario . . . . .	130
C.3	Off-on-axis scenario . . . . .	130
C.4	Off-off-axis scenario . . . . .	132

---

---

<b>D Averages and aspect ratios in real and in momentum space</b>	<b>133</b>
D.1 Phase-space averages $\langle \mathcal{K}_i^2 \rangle^0$ and $\langle \mathcal{R}_i^2 \rangle^0$ . . . . .	133
D.2 Aspect ratio in real space . . . . .	134
D.3 Aspect ratio in momentum space . . . . .	136
<b>Bibliography</b>	<b>138</b>
<b>Biography of the author</b>	<b>152</b>

---

# List of figures

---

1.1	(a) Maxwell-Boltzmann, Bose-Einstein and Fermi-Dirac distributions. (b) Fermi-Dirac distribution function for different temperatures . . . . .	4
1.2	Energy level occupations for noninteracting Fermi gas . . . . .	7
1.3	Dipole-dipole interaction . . . . .	11
2.1	Schematic illustration of: (a)-(c) FS in momentum space; (d)-(f) gas cloud in real space . . . . .	22
2.2	Schematic illustration of the most general arbitrary geometry of a dipolar Fermi gas, which corresponds to the one used in the Innsbruck ex- periment with erbium atoms . . . . .	43
2.3	Relative energy shift $\delta E$ for polarized Er atoms . . . . .	44
2.4	Relative total energy shift $\delta E$ for polarized KRb molecules . . . . .	45
3.1	Aspect ratios in real and momentum space as functions of relative dipole- dipole interaction strength $\varepsilon_{\text{dd}}$ for Fermi gases in global equilibrium for considered trap geometry with dipoles parallel to $z$ axis . . . . .	50
3.2	A universal stability diagram for harmonically trapped ultracold dipolar Fermi gases at quantum degeneracy: critical value of the relative dipole- dipole interaction strength $\varepsilon_{\text{dd}}^{\text{crit}}$ as a function of the trap aspect ratios $\omega_z/\omega_x$ and $\omega_z/\omega_y$ , for the dipoles parallel to $z$ axis . . . . .	53
3.3	Angular stability diagram for harmonically trapped ultracold dipolar Fermi gases at quantum degeneracy . . . . .	55
3.4	FS deformation $\Delta$ for $^{167}\text{Er}$ atoms with magnetic dipole moment $m =$ $7\mu_{\text{B}}$ . . . . .	56
3.5	FS deformation $\Delta$ for $^{40}\text{K}^{87}\text{Rb}$ molecules with electric dipole moment $m = 0.25 \text{ D}$ . . . . .	58

---

3.6	Illustration of the angular dependence of the FS deformation in momentum space for system in an anisotropic trap elongated along the horizontal $y$ axis . . . . .	59
3.7	The FS deformation $\Delta$ as a function of the trap frequencies $\omega_x$ and $\omega_y$ .	60
3.8	Angular dependence of FS deformation $\Delta$ for ultracold Fermi gas of $^{40}\text{K}^{87}\text{Rb}$ molecules . . . . .	61
3.9	FS deformation $\Delta$ as a function of $\omega_x$ and $\omega_y$ for a $^{40}\text{K}^{87}\text{Rb}$ gas . . . .	62
3.10	Angular dependence of FS deformation $\Delta$ for the target trap parameters of $^{40}\text{K}^{87}\text{Rb}$ gas . . . . .	63
3.11	Angular dependence of $\Delta$ for a fixed value of $d$ and trap parameters $(\omega_x, \omega_y, \omega_z) = 2\pi \times (100, 36, 2000)$ Hz, with $N = 3 \times 10^4$ molecules of $^{40}\text{K}^{87}\text{Rb}$ . . . . .	64
3.12	TF radii as functions of relative dipolar interaction strength $\varepsilon_{\text{dd}}$ for Fermi gases in global equilibrium for considered trap geometry with dipoles parallel to $z$ axis . . . . .	68
3.13	Angular dependence of relative cloud deformations for $^{167}\text{Er}$ , with parameters as in Figure 3.4(a) . . . . .	69
3.14	Angular dependence of relative cloud deformations for $^{40}\text{K}^{87}\text{Rb}$ for parameters as in Figure 3.8(a) . . . . .	70
3.15	Beyond-mean-field corrections to the FS deformation . . . . .	72
3.16	Beyond-mean-field corrections to the system's inverse compressibility .	73
4.1	Aspect ratios in real and momentum space in the collisionless regime during TOF expansion of ultracold gas of $^{167}\text{Er}$ . . . . .	93
4.2	Aspect ratios in real and momentum space in the collisionless regime converge to the same asymptotic values during TOF expansion of ultracold gas of $^{167}\text{Er}$ . . . . .	96
4.3	Aspect ratios in real and momentum space in the hydrodynamic regime during TOF expansion of ultracold gas of $^{167}\text{Er}$ . . . . .	98

---

---

4.4	Aspect ratios in real and momentum space in the hydrodynamic regime converge to the same asymptotic values during TOF expansion of ultracold gas of $^{167}\text{Er}$ . . . . .	99
4.5	Aspect ratios in real and momentum space in the collisional regime during TOF expansion of ultracold gas of $^{167}\text{Er}$ . . . . .	101
4.6	Aspect ratios in real space after $t = 10$ ms TOF as function of fixed relaxation time $\tau$ for different ultracold Fermi gases . . . . .	102
4.7	Aspect ratios in real and momentum space in the collisional regime during TOF expansion for $\theta = 0^\circ$ : (a) $^{167}\text{Er}$ , (b) $^{40}\text{K}^{87}\text{Rb}$ . . . . .	104
4.8	Self-consistently determined relaxation time as function of TOF $t$ for ultracold Fermi gas of $^{167}\text{Er}$ and $^{40}\text{K}^{87}\text{Rb}$ for $\theta = 0^\circ$ . . . . .	105
4.9	Aspect ratios in real space during TOF expansion in the collisional regime with self-consistently determined relaxation time for different ultracold Fermi gases for $\theta = 0^\circ$ . . . . .	106
4.10	(a) Real-space aspect ratio $A_R$ of the $^{40}\text{K}^{87}\text{Rb}$ molecular cloud as a function of time $t$ during the TOF expansion from the ground state, after the trap is switched off. $A_R(30$ ms) after the TOF expansion for $t = 30$ ms as a function of $d$ . . . . .	107
5.1	Comparison of our results for $\theta$ dependence of: (a) theoretical value of aspect ratio $A_K$ and its experimental estimate $A_R^{\text{exp}}(t = 12$ ms); (b) theoretical value of the FS deformation $\Delta$ and its experimental estimate	113
5.2	Aspect ratio in momentum space $A_K$ as a function of $\theta$ for Fermi gas of $^{167}\text{Er}$ . . . . .	115
5.3	Relation between intersection angles $\theta^*$ and $\varphi^*$ for $\alpha = 28^\circ$ , determined by Equation (5.9) . . . . .	116
A.1	(a) Schematic illustration of the dipoles' orientation and angles $\alpha, \beta, \gamma$ . (b) Spherical coordinates $r, \vartheta$ , and $\phi$ . . . . .	120

---

# List of tables

---

1.1	Maximal values of dipole moments of currently available dipolar quantum gases . . . . .	14
3.1	Dipole moments and relative interaction strengths of fermionic atoms and molecules to be used throughout the Thesis . . . . .	49
3.2	Trap configurations for confined ultracold Fermi gas with dipoles oriented along $z$ axis . . . . .	67
5.1	Number of atoms $N$ , trap frequency $\omega_i$ , mean frequency $\bar{\omega}$ and anisotropy $\lambda$ for three sets of experimental parameters . . . . .	112
5.2	Comparison of theoretical values of aspect ratios in momentum space $A_K$ in global equilibrium and TOF aspect ratios in real space . . . . .	113
5.3	Comparison of theoretical and experimental values for the FS deformation $\Delta$ averaged over $\theta$ . . . . .	114
5.4	Beyond-mean-field corrections to the FS deformation $\delta\Delta_h^2(\%)$ for $\theta = 0^\circ$ for all three considered cases from Table 5.1 . . . . .	115

# Introduction

---

Studies of atomic and molecular gases have greatly stimulated the development of statistical mechanics and later on quantum statistical physics, by revealing that a quantum mechanical treatment is necessary for a proper description of such systems, even at moderate temperatures. Early theoretical studies have furthermore suggested that exotic ultra-quantum behavior, dominated purely by quantum effects such as Bose-Einstein condensation (BEC), can be expected in the regime of very low temperatures. This has fueled the development of sophisticated cooling techniques and eventually the Nobel-winning experimental discovery of Bose-Einstein condensation in 1995. Interactions between particles play an important role in quantum degenerate gases. In fact, the system's behavior is usually largely determined by the strength, range, and symmetry of the interactions, even if very weak. These results have also instigated research related to optical lattices, studies of fermionic ultracold systems, as well as Fermi-Bose mixtures. By this constant exchange, progresses in both theoretical and experimental studies of quantum physics have been permanently triggering and enriching each other for almost a century. So it is not surprising that this field attracts many generations of physicists, including some of the greatest world minds ever.

The world of low-temperature physics offers many advantages for studying quantum phenomena, which leads to the novel states of matter with striking properties – superconductors, superfluids, supersolids. All these phenomena can now be observed in ultracold quantum gases with unprecedented control of system's parameters. Furthermore, they can be combined and used as elements in a toolbox for quantum simulators in solid state physics, or even in general relativity and other fields, following Richard Feynman's visionary idea [1].

## 1.1 Quantum gases: fermions vs. bosons

It is breathtaking how different the world looks at different scales. One of great examples that illustrate this are gases at different temperatures. Let us consider the air around us at the room temperature. The air is composed of specks of dust, molecules, and atoms, all moving around randomly and colliding frequently. The behavior of such high-temperature gases are very well described by the Boltzmann's kinetic theory. In contrast to that, the behavior of the gas which is cooled down close to quantum degeneracy changes dramatically, so that the Boltzmann's classical approach fails, and must be replaced with an appropriate quantum description.

The main difference between classical and quantum gases is that the properties of quantum gases strongly depend on the constituent atoms and their electronic structure. Namely, all classical gases exhibit the same behavior, which is reflected in the Boltzmann approach, where quantum statistics of the atoms is irrelevant. However, for quantum gases the statistics has a crucial role, since it is different for bosons and fermions. This can be illustrated, e.g., by considering the collisions, which occur more frequently in Bose quantum gases made of identical particles, than they do in a classical gas. On the other hand, the situation is just the other way around for Fermi quantum gases made of identical particles, where collisions are suppressed in comparison to a classical gas.

As mentioned, all these differences emerge purely from the different statistics for a classical, Bose, and Fermi gas. Namely, an ideal classical gas obeys the Maxwell-Boltzmann distribution, which gives the probability that the system is in a state with the given energy  $E$ , and reads

$$\nu_{\text{MB}}(E) = \frac{1}{e^{\beta(E-\mu)}}. \quad (1.1)$$

Here  $\mu$  represents the grand-canonical chemical potential, and  $\beta$  is the standard abbreviation

$$\beta^{-1} = k_{\text{B}}T, \quad (1.2)$$

where  $k_{\text{B}}$  is Boltzmann's constant and  $T$  is the temperature.

In classical mechanics, particles are always distinguishable and, in principle, their trajectories through phase space can be traced. In quantum mechanics, identical particles are indistinguishable, such as electrons in an atom, or atoms in a sample of a quantum gas. The indistinguishability of quantum particles, and the different

occupancy rules for bosons and fermions, affect their statistical behavior. The Bose-Einstein distribution function,

$$\nu_{\text{BE}}(E) = \frac{1}{e^{\beta(E-\mu)} - 1}, \quad (1.3)$$

gives the probability that the system of ideal bosons is in a state with the energy  $E$  at the temperature  $T$ . Bosons possess integer spin and many bosons can occupy a single-particle quantum state, which allows them to behave coherently. As a consequence, we have phenomena such as BEC, superfluids, superconductors, and lasers. Due to this, bosons are usually termed as "social" particles, while quantum statistics causes fermions to be "anti-social", i.e., to avoid each other [2]. Namely, fermions have half-integer spin, and include electrons, protons and neutrons. They obey the Pauli exclusion principle, which states that two identical fermions cannot occupy the same single-particle quantum state, and is the origin of their "anti-social" behavior. For ideal fermions, the energy distribution is given by the Fermi-Dirac distribution function,

$$\nu_{\text{FD}}(E) = \frac{1}{e^{\beta(E-\mu)} + 1}. \quad (1.4)$$

Since bosons possess integer spin and spin is additive, composite bosons may be formed from an even number of fermions. Therefore, when studying systems comprised of fermions, it is essential to understand if they behave as fermions, or perhaps composite bosons appear, such as the Cooper pairs in the Bardeen-Cooper-Schrieffer (BCS) theory.

If we compare the statistical distributions given by Equations (1.1), (1.3), and (1.4), the difference is in the denominators, where additional terms  $+1$  and  $-1$  appear for bosons and fermions, respectively. However, exactly this is the origin of profound and enormous consequences for the behavior of quantum gases. Having in mind that any probability distribution function must be non-negative, this implies that  $\mu \leq 0$  for the Bose-Einstein distribution, while for the Fermi-Dirac and Maxwell-Boltzmann distribution  $\mu$  can take any value and sign. For  $\beta(E - \mu) \gg 1$ , the Bose-Einstein and Fermi-Dirac distributions approach the Boltzmann distribution, as illustrated in Figure 1.1(a). In this regime, the average state occupancy is much smaller than 1, and therefore the effects of particle indistinguishability become negligible. Note that  $\mu$  itself has a non-trivial temperature dependence and tends to the ground state energy as  $T \rightarrow 0$ , and that is why one cannot conclude that the low temperatures favor classical behavior, as it would naively seem from the classical limit condition  $\beta(E - \mu) \gg 1$ . For

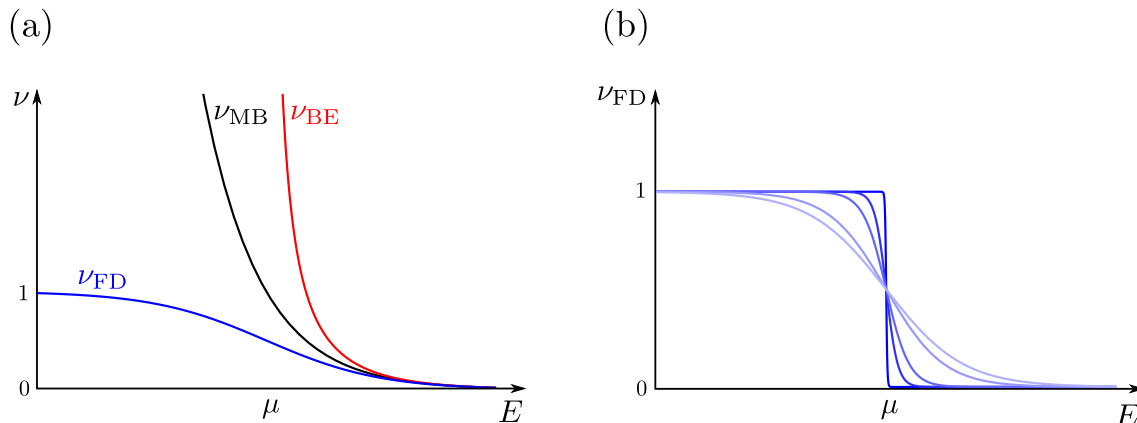


**Figure 1.1:** (a) Maxwell-Boltzmann (black), Bose-Einstein (red) and Fermi-Dirac (blue) distributions as functions of energy  $E$ , for fixed value of chemical potential  $\mu$ . (b) Fermi-Dirac distribution for different temperatures as a function of energy  $E$ . Lighter colors correspond to higher temperatures.

$E \ll \mu$ , the Fermi-Dirac distribution saturates to one particle per state, as required by the Pauli exclusion principle. For decreasingly lower temperatures, the distributions develop a sharper transition around  $E = \mu$ , approaching the Heaviside step function for  $T = 0$  K, as depicted in Figure 1.1(b).

Different quantum statistics for bosons and fermions plays a major role at low temperatures, making the study of the bosonic and fermionic systems complementary in many respects. Namely, in the Bose case quantum statistical effects are associated with the occurrence of a phase transition to the Bose-Einstein-condensed phase. On the other hand, in a noninteracting Fermi gas the quantum degeneracy temperature only corresponds to a smooth crossover between a classical and a quantum behavior. In contrast to the Bose case, the occurrence of a superfluid phase in a Fermi gas can only be due to the presence of interactions, which make possible the emergence of Cooper pairs. From the many-body standpoint, the study of the Fermi superfluidity opens up a different and richer class of questions [3].

A further important difference between Bose and Fermi gases concerns the collisional processes. For example, in Bose gases the  $s$ -wave scattering represents the main interaction channel, while in single-component Fermi gases it is inhibited due to the Pauli exclusion principle. This effect has important consequences for the experimental cooling mechanisms based on evaporation, where the thermalization plays a crucial role. The availability of Feshbach resonances, with the possibility of changing the value and even the sign of the scattering length by simply tuning an external magnetic field, has enabled the investigation of strongly interacting regimes of fermionic atoms when working close to resonances, where the scattering length can take very large values.

In contrast to Bose gases, in the case of fermions the three-body losses are inhibited by the Pauli exclusion principle, leading to a greater stability of the system and to the possibility of realizing the unitary regime of infinite scattering length. In this regime the system exhibits a universal behavior, independent of the details of the interatomic potential, such that the gas is at the same time dilute and strongly interacting [4].

## 1.2 Free ideal Fermi gas

Over the past few decades, an impressive amount of experimental and theoretical developments in the realm of ultracold gases was achieved, resulting in a number of physics Nobel prizes. These developments make possible to probe diverse quantum phenomena, especially in the domain of many-body physics, both for interacting and noninteracting systems. In ultracold systems the inter-atomic interactions can be experimentally tuned to unprecedentedly high degree, and even effectively removed. Therefore, we focus in this Section just on the free ideal Fermi gas model.

We consider a uniform system of ultracold quantum-degenerate Fermi gas at zero temperature consisting of  $N$  identical fermions of mass  $M$ , occupying a box of volume  $V = L^3$ . The single-particle states are plane waves,

$$\psi_{\mathbf{k}}(\mathbf{r}) = \frac{1}{V} e^{i\mathbf{k}\cdot\mathbf{r}}, \quad (1.5)$$

with the energy of the eigenstates

$$E_{\mathbf{k}} = \frac{\hbar^2 k^2}{2M}. \quad (1.6)$$

Here momentum  $\mathbf{k}$  enumerates the eigenstates and is determined by the usual periodic boundary conditions,  $\mathbf{k} = 2\pi\mathbf{n}/L$ , where  $\mathbf{n} \in \mathbb{N}^3$ . In this case the Fermi-Dirac distribution given by Equation (1.4) reduces to

$$\nu(E) = \text{H}(E - \mu), \quad (1.7)$$

where  $\text{H}$  denotes the Heaviside step function. Here, the chemical potential  $\mu$  defines the value of the Fermi energy  $\mu = E_{\text{F}}$ , so that all states below that threshold are occupied, and all others are empty. The total number of particles is given by

$$N = \int_0^{\infty} dE g(E) \nu(E), \quad (1.8)$$

where  $g(E)$  stands for the single-particle density of states, which reads [2–5]

$$g(E) = \frac{VM^{\frac{3}{2}}}{\sqrt{2}\hbar^3\pi^2}E^{\frac{1}{2}}. \quad (1.9)$$

With this, it is straightforward to integrate Equation (1.8), which sets the Fermi energy in terms of the particle density  $n = N/V$  as follows

$$E_F = \frac{\hbar^2}{2M}(6\pi^2n)^{\frac{2}{3}}. \quad (1.10)$$

From this we define the Fermi wavenumber  $k_F$ , which is given by

$$k_F = (6\pi^2n)^{\frac{1}{3}}, \quad (1.11)$$

as well as the Fermi momentum  $p_F = \hbar k_F$ .

The surface in momentum space that separates the occupied from the unoccupied fermionic states is called the Fermi surface (FS). For free noninteracting Fermi gas at zero temperature, all states in momentum space that satisfy  $|\mathbf{k}| \leq k_F$  are occupied, which follows from the condition  $E < E_F$ . This corresponds to the FS defined by

$$k_x^2 + k_y^2 + k_z^2 = k_F^2, \quad (1.12)$$

from which we see that it is a sphere with the radius  $k_F$ .

The total energy of the gas at zero temperature reads

$$U = \int dE E g(E) \nu(E) = \frac{3}{5} N E_F, \quad (1.13)$$

which, together with the pressure relation for an ideal gas,  $PV = 2U/3$ , leads to

$$p = \frac{2}{5} n E_F. \quad (1.14)$$

This represents the expression for the Pauli quantum pressure of the ideal Fermi gas. In contrast to Bose and classical gases, this pressure is finite even at zero temperature, meaning that it does not arise from thermal fluctuations. Instead, it is due to the stacking up of particles at energy levels starting from the ground state, as constrained by the quantum rules for fermions. Surprisingly, this effect can have important consequences even in astrophysics, where the degeneracy pressure prevents very dense stars, such as neutron stars, from collapsing under their own gravitational fields [2].

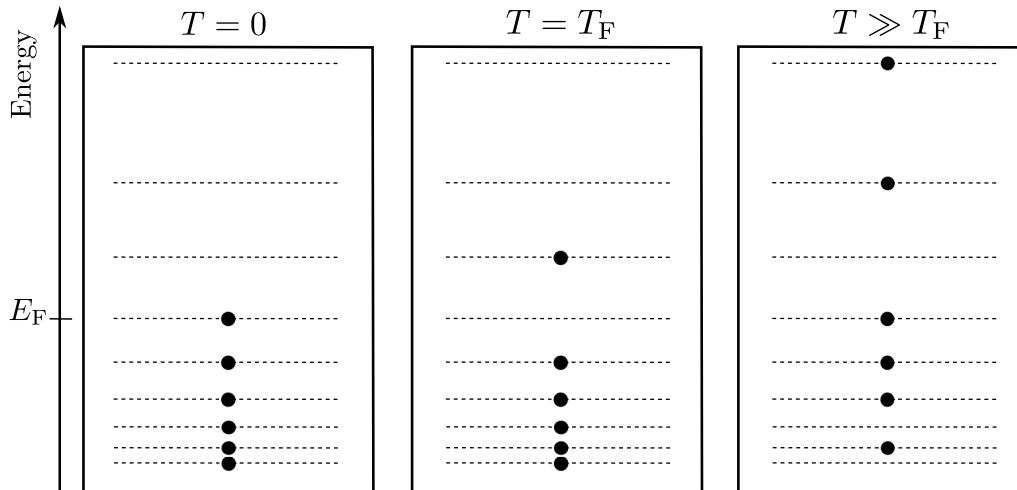


**Figure 1.2:** Energy level occupations for noninteracting Fermi gas. At  $T = 0$ , all states are occupied up to the Fermi energy  $E_F$ . At  $T = T_F$ , some particles with energies close to  $E_F$  are excited, while for  $T \gg T_F$  the system approaches the classical limit, with particles occupying many high-energy states.

It is also useful to express the Fermi energy in terms of the Fermi temperature,

$$T_F = \frac{E_F}{k_B}, \quad (1.15)$$

which is associated with the onset of degeneracy, i.e., when quantum effects start to dominate the behavior of the system. As the temperature is increased from zero, the step-like Fermi-Dirac distribution becomes broadened around  $E = E_F$ , as illustrated in Figure 1.1(b). This happens because at finite, but still low temperatures,  $T \sim T_F$ , the particles that are close to the FS can use their thermal energy and get excited into higher energy levels. However, in order for this to be possible, the difference between the particle energy and  $E_F$  has to be at most of the order of  $k_B T$ . On the other hand, in the high-temperature regime,  $T \gg T_F$ , a significant number of particles is excited and thermal effects dominate, so the system approaches the classical Maxwell-Boltzmann distribution [2]. These regimes are schematically presented in Figure 1.2.

### 1.3 Trapped ideal Fermi gas

Although free quantum gases are much easier to study theoretically, from the experimental point of view they have to be trapped, since otherwise the particles would just disperse. This is accomplished by using a sophisticated setups with the specially tailored magnetic fields and/or counter-propagating laser beams, which can confine the particles and keep them thermally isolated. In such a way quantum-degenerate

bosonic and fermionic quantum gases are trapped in magnetic, optical, or magneto-optical traps at temperatures in the nanokelvin regime. In this Section we give a brief summary of key properties of ideal Fermi gases confined in triaxial anisotropic harmonic traps. Such systems represent an excellent model, which is relevant not only for ultracold gases, but also for many diverse fields of physics, ranging from nuclear physics to the more recent studies of quantum dots [3, 5].

We again consider an ultracold quantum-degenerate Fermi gas at zero temperature consisting of  $N$  identical fermions of mass  $M$ , this time trapped by a triaxial anisotropic harmonic potential defined by

$$V_{\text{trap}}(\mathbf{r}) = \frac{M}{2} \left( \omega_x^2 r_x^2 + \omega_y^2 r_y^2 + \omega_z^2 r_z^2 \right), \quad (1.16)$$

where  $\omega_i$  denote the trap frequencies, which characterize the strength of the trap in each direction  $i \in \{x, y, z\}$ . Assuming that  $N$  is large, such that many single-particle states are occupied and the semiclassical approach can safely be used, the simplest semiclassical description of the Fermi-Dirac distribution function has the following form [3, 5, 6]

$$\nu_{\text{FD}}(\mathbf{r}, \mathbf{k}) = \frac{1}{e^{\beta[\epsilon(\mathbf{r}, \mathbf{k}) - \mu]} + 1}, \quad (1.17)$$

where  $\epsilon(\mathbf{r}, \mathbf{k}) = \frac{\hbar^2 \mathbf{k}^2}{2M} + V_{\text{trap}}(\mathbf{r})$  and  $\mu$  is fixed by the normalization condition,

$$N = \int d^3r \int \frac{d^3k}{(2\pi)^3} \nu_{\text{FD}}(\mathbf{r}, \mathbf{k}) = \int_0^\infty \frac{g(\epsilon) d\epsilon}{e^{\beta(\epsilon - \mu)} + 1}. \quad (1.18)$$

Here  $g(\epsilon)$  stands for the single-particle density of states, which is now given by

$$g(\epsilon) = \frac{\epsilon^2}{2\hbar^3 \bar{\omega}^3}, \quad (1.19)$$

with  $\bar{\omega} = (\omega_x \omega_y \omega_z)^{\frac{1}{3}}$  being the geometric average<sup>1</sup> of the trapping frequencies. Note that the density of states (1.19) differs from the corresponding density for a uniform system (1.9). Physical origin of this is the suppression of states in phase space due to the spatial confinement by the trapping potential [5].

At zero temperature the chemical potential  $\mu$  equate with the Fermi energy, thus a straightforward integration of Equation (1.18) yields

$$\mu = E_{\text{F}} = k_{\text{B}} T_{\text{F}} = \hbar \bar{\omega} (6N)^{\frac{1}{3}}. \quad (1.20)$$

---

<sup>1</sup>In this Thesis the bar sign denotes the geometric average, i.e.,  $\bar{O} = (O_x O_y O_z)^{\frac{1}{3}}$ .

This expression is important for future calculations, because it fixes the characteristic energy and temperature of the gas cloud. Furthermore, the Fermi energy (1.20) can be also used to define typical length and momentum scales, characterizing the Fermi distribution. The characteristic size of the gas cloud  $R_i^0$  in the direction  $i$  is defined in analogy to a classical particle with the total energy  $E_F$  in the trap potential with the frequency  $\omega_i$ ,

$$R_i^0 = \sqrt{\frac{2E_F}{M\omega_i^2}}. \quad (1.21)$$

Similarly, the characteristic size of the Fermi sphere is defined as the momentum of a free particle with the energy  $E_F$ ,

$$K_F^0 = \sqrt{\frac{2ME_F}{\hbar^2}}. \quad (1.22)$$

The quantities  $R_i^0$  and  $K_F^0$  represent the Thomas-Fermi (TF) radii and momenta, respectively, and can be rewritten in the following form

$$R_i^0 = a_{ho}(48N)^{\frac{1}{6}} \frac{\bar{\omega}}{\omega_i}, \quad K_F^0 = \frac{1}{a_{ho}}(48N)^{\frac{1}{6}}, \quad (1.23)$$

where  $a_{ho} = \sqrt{\frac{\hbar}{M\bar{\omega}}}$  denotes the harmonic oscillator length. The last two expressions for  $R_i^0$  and  $K_F^0$  represent the widths of the density distributions at zero temperature, which can be calculated by integrating the distribution function in momentum and real space, respectively [4]

$$n(\mathbf{r}) = \int \frac{d^3k}{(2\pi)^3} \nu_{\text{FD}}(\mathbf{r}, \mathbf{k}) = \frac{8}{\pi^2} \frac{N}{R^0{}^3} \left(1 - \sum_i \frac{r_i^2}{R_i^0{}^2}\right)^{\frac{3}{2}}, \quad (1.24)$$

$$n(\mathbf{k}) = \int d^3r \nu_{\text{FD}}(\mathbf{r}, \mathbf{k}) = \frac{8}{\pi^2} \frac{N}{K_F^0{}^3} \left(1 - \frac{k^2}{K_F^0{}^2}\right)^{\frac{3}{2}}. \quad (1.25)$$

## 1.4 Trapped dipolar Fermi gas

### 1.4.1 Dipole-dipole interaction

The dipole-dipole interaction (DDI) can be often found in nature, and determines the behavior of a broad range of systems. Furthermore, it is not important just from the physical point of view, since the DDI accounts also for many biologically significant phenomena. For instance, the biggest impact the DDI has on living organisms is its crucial role in the protein folding.

In this Thesis we consider the DDI between the fermions in ultracold polarized Fermi gases. This is based on the assumption that the van der Waals forces between the atoms can be approximated at low temperatures by an effective contact interaction [7–10]. This approximation considers only the  $s$ -wave scattering of the particles, which are suppressed due to the Pauli exclusion principle, and therefore the long-range DDI between the polarized fermionic point dipoles is dominant.

In general case, the DDI potential of two interacting particles with the dipoles oriented along directions determined by unit vectors  $\mathbf{e}_1$  and  $\mathbf{e}_2$ , and with the relative position  $\mathbf{r}$ , as depicted in Figure 1.3(a), has the following form

$$V_{\text{dd}}(\mathbf{r}) = \frac{C_{\text{dd}}}{4\pi} \frac{(\mathbf{e}_1 \cdot \mathbf{e}_2)\mathbf{r}^2 - 3(\mathbf{e}_1 \cdot \mathbf{r})(\mathbf{e}_2 \cdot \mathbf{r})}{|\mathbf{r}|^5}. \quad (1.26)$$

Here  $C_{\text{dd}}$  represents the dipolar interaction strength, which depends on the nature of the dipoles. Namely, for particles with electric dipoles  $\mathbf{d}$  it is defined as  $C_{\text{dd}}^e = d^2/\varepsilon_0$ , where  $\varepsilon_0$  is the vacuum permittivity, while for particles with magnetic dipole  $\mathbf{m}$  one has  $C_{\text{dd}}^m = \mu_0 m^2$ , where  $\mu_0$  is the vacuum permeability. Magnetic dipolar moments are usually measured in units of Bohr magneton ( $\mu_B = 9.27401 \times 10^{-24} \text{ JT}^{-1}$ ), and electric dipolar moments in units of Debye ( $\text{D} = 3.33564 \times 10^{-30} \text{ Cm}$ ). The DDI of polar molecules is much stronger than that of dipolar atoms, and the order of magnitude of this difference can be easily estimated. Since the magnetic dipole moment for atoms ranges from roughly  $1 \mu_B$  for alkali atoms to  $10 \mu_B$  for the lanthanoids, we can take that the typical dipolar interaction strength is of the order

$$C_{\text{dd}}^m = \mu_0 \mu_B^2 = \frac{\mu_0 e^2 \hbar^2}{4M_e^2}, \quad (1.27)$$

where  $e$  and  $M_e$  are the electron charge and mass, respectively. Similarly, the typical electric dipole moment for molecules can be estimated by assuming a net electron charge separated by a distance of the Bohr radius,  $a_0$ , which yields

$$C_{\text{dd}}^e = \frac{e^2 a_0^2}{4\varepsilon_0} = \frac{e^2 \hbar^2}{4\varepsilon_0 M_e^2 c^2 \alpha_S^2}, \quad (1.28)$$

where  $c$  is the speed of light in vacuum and  $\alpha_S = 7.297 \cdot 10^{-3}$  is the Sommerfeld fine-structure constant. Comparing the respective typical dipolar interaction strengths for magnetic and electric systems yields a ratio of

$$\frac{C_{\text{dd}}^e}{C_{\text{dd}}^m} = \alpha_S^{-2} \sim 10^4. \quad (1.29)$$

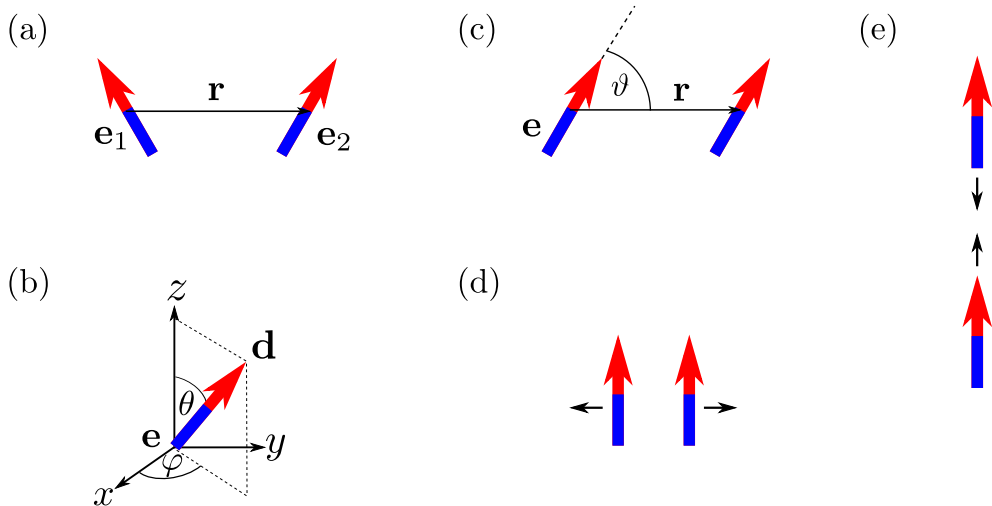


**Figure 1.3:** Dipole-dipole interaction. (a) Non-polarized case: two particles with the dipole moments oriented along the unit vectors  $\mathbf{e}_1$  and  $\mathbf{e}_2$  and with relative position  $\mathbf{r}$ . (b) Polarized dipole  $\mathbf{d}$  oriented along unit vector  $\mathbf{e}$  determined by spherical angles  $(\theta, \varphi)$ . (c) Polarized case: two particles with the dipole moments oriented along the unit vectors  $\mathbf{e}$  and with relative position  $\mathbf{r}$ . (d) Two polarized dipoles in the side-by-side configuration ( $\vartheta = 90^\circ$ ) repel each other, as indicated by black arrows. (e) Two polarized dipoles in the head-to-tail configuration ( $\vartheta = 0^\circ$ ) attract each other, as indicated by black arrows.

We assume that all dipole moments are parallel in the polarized Fermi gas, and their common orientation will be referred to as the polarization direction, determined by the unit vector  $\mathbf{e}$ , as illustrated in Figure 1.3(b). The DDI potential of two interacting fermions with the dipoles oriented along the same direction, as shown in Figure 1.3(c), is given by the reduced form of Equation (1.26), which reads

$$V_{\text{dd}}(\mathbf{r}) = \frac{C_{\text{dd}}}{4\pi} \frac{\mathbf{r}^2 - 3(\mathbf{e} \cdot \mathbf{r})^2}{|\mathbf{r}|^5}. \quad (1.30)$$

In this context, an important role is played by the Fourier transform of the DDI potential, whose original and detailed derivation is given in Appendix A. It has the following form

$$\tilde{V}_{\text{dd}}(\mathbf{k}) = \frac{C_{\text{dd}}}{3} \left[ 3 \frac{(\mathbf{e} \cdot \mathbf{k})^2}{k^2} - 1 \right]. \quad (1.31)$$

In order to explain the two defining characteristics of the DDI, its long range and anisotropy, we consider an even more simple case, when the dipoles are oriented along the  $z$  axis. The DDI potential now simplifies to

$$V_{\text{dd}}(\mathbf{r}) = \frac{C_{\text{dd}}}{4\pi |\mathbf{r}|^3} (1 - 3 \cos^2 \vartheta). \quad (1.32)$$

The fact that the DDI falls off with inter-particle distance according to the power law, i.e.,  $V_{\text{dd}}(\mathbf{r}) \sim 1/r^3$ , indicates a long-range type of the interaction, while its natural anisotropy can be understood through the  $\vartheta$ -dependence. Namely, depending on the angle  $\vartheta$ , the DDI potential can be positive or negative, meaning that the dipolar fermions can repel or attract each other. For example, for  $\vartheta = 90^\circ$  the dipoles are located side by side and repel each other, as illustrated in Figure 1.3(d). On the other hand, for  $\vartheta = 0^\circ$  the dipoles are in the head-to-tail configuration and attract each other, as shown in Figure 1.3(e). Note that the DDI vanishes for the special value of the angle  $\vartheta = \arccos(1/\sqrt{3}) = 54.7^\circ$ , which is called the magic angle.

These key features of the DDI make dipolar quantum gases extremely interesting, in particular from a quantum simulation point of view, as a number of fascinating interaction-driven effects emerge, which are not present in systems with purely short-range contact interaction [11].

## 1.4.2 Brief review of the field

Ultracold gases at quantum degeneracy offer a wide playground for studying quantum phenomena, especially within the realm of many-body physics, with important applications for the quantum simulation of a diverse range of systems and models, as well as for quantum information and quantum computing [3, 4, 12–40]. While usually the  $s$ -wave scattering is the main type of interaction in such systems, the presence of the anisotropic and long-range DDI in gases consisting of atoms or molecules with a permanent or induced magnetic or electric dipole moment leads to an even richer phenomena landscape. In particular, this is enabled by competing interaction effects and a high degree of their tunability. Furthermore, this remains true even for dipolar Fermi gases where, although the  $s$ -wave scattering is absent due to the Pauli exclusion principle, the anisotropic DDI competes with the large kinetic energy close to the FS, yielding a complex-enough energy landscape. This leads to novel many-body phenomena, including the deformation of the FS and a predicted fermionic pairing of one- and two-component systems [41–51].

Since the first experimental realization of a dipolar BEC of chromium atoms [52] and the subsequent demonstration of the presence of the anisotropic and long-range DDI in the laboratory [53], dipolar quantum gases have developed into a vast and fast-growing research field. Indeed, the interplay of the DDI and the isotropic and short-range contact interaction between the particles in these systems makes them particularly intriguing from both the experimental and the theoretical point of view

[14, 15, 54]. More recently, BECs of even more magnetic species, i.e., dysprosium [55] and erbium [56] have been created. Such species exhibit fascinating phenomena, such as the Rosensweig instability [57], the emergence of quantum-stabilized droplets [58–60] and roton quasiparticles [61]. Correspondingly, all these developments triggered much theoretical work, including, but not limited to, the numerical effort to simulate dipolar quantum gases in fully anisotropic traps, the roton instability in pancake-shaped condensates, the investigation of beyond-mean-field effects in one-component and two-component gases, the formation of the previously observed droplets, their ground-state properties and elementary excitations, the role of three-body interactions, and the self-bounded nature of the droplets [62–79]. Furthermore, the very recent experiments [80–82] demonstrate an amazing phenomenon, namely that dipolar gases of magnetic atoms can exhibit the supersolidity, a novel kind of behavior when the system is crystallized, but can still flow without friction. One of the next natural steps would be the exploration of the transition between the supersolids and the droplet crystals.

In parallel, the first experimental realization of a quantum degenerate dipolar Fermi gas of dysprosium  $^{161}\text{Dy}$  was in 2012 [83], and afterwards several more fermionic species, such as erbium  $^{167}\text{Er}$  [84] and chromium  $^{53}\text{Cr}$  [85], were successfully cooled down to quantum degeneracy. This enabled studies of the effects of weak to medium-range DDI strength. Remarkably, identical fermions of dipolar character do interact even in the low-energy limit because of the peculiar form of the dipolar scattering [86]. Few-body scattering experiments have indeed confirmed universal scaling in dipolar scattering among fermions [84, 87, 88]. Furthermore, in the recent theoretical and experimental research [89] a novel kind of strongly dipolar quantum gases was introduced. These are weakly bound polar molecules produced from atoms with large magnetic dipole moments, such as erbium and other lanthanides. These molecules can have a very large magnetic moment, which amounts to twice that of its individual atoms [11]. Many-body dipolar effects in Fermi gases are much more subtle to observe because of the competition with the large kinetic energy stored within the FS, which leads to the Fermi pressure. Recently, the key observation of the FS deformation was made [48], confirming previous theoretical predictions [90–96].

Although experimental realization of magnetic dipolar gases at quantum degeneracy has enabled studies of the effects of weak to medium-range DDI strength, the study of the strongly dipolar regime is still in its infancy, and awaits experimental availability of ultracold heteronuclear polar molecules with large dipole moments. In

**Table 1.1:** Maximal values of dipole moments ( $m$  for species with a magnetic dipole and  $d$  for species with an electric dipole) of currently available dipolar quantum gases.

species	$^{87}\text{Rb}$	$^{23}\text{Na}^6\text{Li}$	$^{53}\text{Cr}$	$^{167}\text{Er}$	$^{161}\text{Dy}$	$^{167}\text{Er}^{168}\text{Er}$
$m$	$0.5 \mu_{\text{B}}$	$2.0 \mu_{\text{B}}$	$6.0 \mu_{\text{B}}$	$7.0 \mu_{\text{B}}$	$9.9 \mu_{\text{B}}$	$14.0 \mu_{\text{B}}$
species	$^{23}\text{Na}^6\text{Li}$	$^{40}\text{K}^{87}\text{Rb}$	$^{87}\text{Rb}^{133}\text{Cs}$	$^{23}\text{Na}^{40}\text{K}$	$^{23}\text{Na}^{87}\text{Rb}$	$^7\text{Li}^{133}\text{Cs}$
$d$	0.20 D	0.57 D	1.2 D	2.7 D	3.3 D	5.5 D

the last decade, significant efforts to produce chemically stable cold polar molecules [11, 31] were based on photoassociation or the stimulated Raman adiabatic passage (STIRAP) [97]. As a result, samples of fermionic  $^{40}\text{K}^{87}\text{Rb}$  [98],  $^{23}\text{Na}^{40}\text{K}$  [99–102],  $^{23}\text{Na}^6\text{Li}$  [103] and bosonic  $^7\text{Li}^{133}\text{Cs}$  [104, 105],  $^{87}\text{Rb}^{133}\text{Cs}$  [106, 107] and  $^{23}\text{Na}^{87}\text{Rb}$  [108] were obtained in deeply bound molecular states. However, the quantum degeneracy was still not reached. Only very recently a quantum degenerate dipolar Fermi gas of  $^{40}\text{K}^{87}\text{Rb}$  has been realized at JILA [109]. This experimental protocol enabled to produce tens of thousands of unpolarized molecules at a temperature as low as 50 nK, which are well described by the Fermi-Dirac distribution. However, the molecules' dipoles can be straightforwardly polarized in a preferential direction by an external electric field [109], such that the DDI dominates the behavior of the system. This would be a long-awaited significant step forward, which would open up the realm for experimentally investigating strong dipolar Fermi gases.

The available dipolar Fermi gases in current ultracold experiments are listed in Table 1.1, with their maximal possible values of dipole moments. Note that the electric dipole moments  $d$  of molecular species can be tuned to smaller values by using an external electric field.

## 1.5 Motivation

The Fermi surface is one of the fundamental pillars of modern condensed matter physics [110]. It represents the surface in reciprocal space, which separates occupied from unoccupied fermionic states at zero temperature, and is a direct consequence of the Pauli exclusion principle. For instance, interacting electrons in a normal metal can be described within the Landau Fermi-liquid theory [111] as noninteracting fermionic quasi-particles with an effective mass, whose ground state forms such a FS. Due to the

isotropy of the Coulomb repulsion between electrons in a uniform space, the FS turns out to be a sphere, whose radius is given by the Fermi momentum. The concept of the FS is crucial for understanding transport processes in metals [112] and the Cooper pairing in superconductors [113, 114]. However, in case of complex interactions the FS can get modified. For example, in strongly-correlated electron systems the Fermi-liquid picture breaks down, giving rise to a spontaneous breaking of rotational invariance, which manifests itself in a deformation of the FS [115].

Studying Fermi surfaces has now also become accessible within the realm of ultracold quantum gases [3, 13, 15–17] due to their high degree of tunability. In Fermi gases consisting of atoms or molecules with a permanent or induced magnetic or electric dipole moment the anisotropic and long-range DDI competes with the large kinetic energy close to the FS [14]. As a consequence, many theoretical papers predicted an anisotropic version of the Landau Fermi-liquid theory [54, 116, 117], which involves a deformation of the Fermi sphere [91–94, 118, 119]. Furthermore, permanent dipole moments follow the orientation of external fields, which has been explored recently in both types of ultracold dipolar quantum gases, fermionic in the Innsbruck experiment [48] and bosonic in the Stuttgart experiment [120]. However, a general theory for fermions presented here, which takes the arbitrary orientation of the dipoles into account, including the deformation of the Fermi surface at that moment was still lacking. This has motivated us to aim our research in this direction, since this is expected to lead to novel many-body phenomena, in particular in connection with fermionic superfluidity [43–47, 51]. In a polarized one-component Fermi gas an intriguing interplay between an anisotropic order parameter with odd partial waves and the FS deformation enhances superfluid pairing via modifying the density of states [46]. In contrast to that the more conventional type of Cooper pairing is predicted in a two-component dipolar Fermi gas, where the usual Bardeen-Cooper-Schrieffer (BCS) theory together with the deformed FS leads to both spin-singlet even partial wave or spin-triplet odd partial wave Cooper pairs [45]. And it is suggested to obtain and observe a topological  $p$ -wave superfluid of microwave-dressed polar fermionic molecules in 2D lattices at temperatures of the order of tens of nanokelvins [121].

Time-of-flight (TOF) expansion measurements are to this day the most significant experimental technique to study properties of ultracold atoms, both fermionic and bosonic. Detailed analytical and numerical understanding of the TOF dynamics is necessary for the interpretation of the corresponding experimental data, and thus a precise modeling of the expansion dynamics of ultracold dipolar Fermi gases signifi-

cantly contributes to our ability to study their dynamical behavior, as well as their equilibrium properties, such as the ground state density profile, the aspect ratios in real and momentum space, and the Fermi surface deformation. The latter provides direct means to experimentally tackle effects purely due to the DDI, and are therefore of interest to a broader physics community. This has motivated us to include the theoretical modeling of the TOF dynamics in this Thesis.

Recent experiments [48, 49] measured that for a fermionic gas of magnetic dipolar erbium atoms an ellipsoidal deformation of the Fermi sphere occurs, which is of the order of 2%. Very recently, a quantum degenerate dipolar Fermi gas of fermionic  $^{40}\text{K}^{87}\text{Rb}$  polar molecules has been realized at JILA experiment [109]. Since these molecules possess the permanent electric dipole moment as large as 0.57 D, the future focus will be on the polarized systems, where the dipoles will be oriented along a preferential direction using an external electric field, in order to achieve the strong dipolar regime. This would be a long-awaited significant step forward, which would open up the realm for experimentally investigating strong dipolar Fermi gases. Thus, effects of the DDI in experiments will become more pronounced, and their accurate theoretical modeling will be required. Furthermore, a strong dipolar nature of such Fermi gases necessitates that they are treated in the collisional regime, i.e., one could not assume anymore that they are in the collisionless regime. So, we aim to develop here an approach precisely tailored to address this challenge, allowing us to take into account effects of collisions and of the DDI, in both the global equilibrium and during the TOF expansion.

This Thesis addresses an important open question of the full theoretical description of strongly dipolar Fermi gases with tilted dipoles at quantum degeneracy in a triaxial harmonic trap geometry. We believe that our theoretical research presented here provides a very timely theoretical complement to recent breakthrough experiments described above.

## 1.6 This Thesis

The present Thesis explores the physical properties of quantum-degenerate Fermi gases at zero temperature interacting via the anisotropic and long-range dipole-dipole interaction. Chapter 1 gives a brief introduction to the field, describing basic concepts related to free and trapped ideal Fermi gases. It then discussed quantum-degenerate dipolar Fermi gases and gives a brief overview and state-of-the-art in the field.

---

In Chapter 2 we develop and derive a general Hartree-Fock mean-field theory for trapped polarized Fermi gases with tilted dipoles. In particular, we introduce several physically motivated ansätze for the form of the system’s Wigner function. Considering the Hartree-Fock total energy of the system, we identify the optimal ansatz that yields the minimal energy for the ground state.

Chapter 3 presents our main results for the stability of dipolar Fermi systems, the FS deformation, as well as the gas cloud deformation. We also explore in detail how the ground-state properties depend on parameters of the system, such as orientation of the dipoles, the trap frequencies, the number of particles, and the DDI strength.

In Chapter 4 we introduce the quantum kinetic formalism based on the Wigner distribution function and perform a systematic study of the TOF dynamics for trapped dipolar Fermi gases from the collisionless to the hydrodynamic regime at zero temperature. To this end we solve the underlying quantum kinetic Boltzmann equation within the relaxation-time approximation in the vicinity of local equilibrium by using a suitable rescaling of the Wigner function. We consider experimentally realistic parameters and relaxation times that correspond to the collisionless, collisional, and hydrodynamic regime. The equations for the collisional regime are first solved in the approximation of a fixed relaxation time, and then this approach is extended to include a self-consistent determination of the relaxation time.

In Chapter 5 we directly compare our theoretical predictions with the novel experimental data obtained for a quantum-degenerate gas of erbium. The excellent agreement between the model and the measurements demonstrates the predictive power of our theory and establishes a general theoretical framework, which can be equally applied to ultracold polar molecules and highly magnetic atomic species.

Finally, Chapter 6 gathers our concluding remarks, emphasizing the role of the obtained results presented in this Thesis for the ultracold gases community. The main text of the Thesis is supplemented by four Appendices, which contain important and detailed derivation steps.

---

## Ground state energy

---

The isotropic and short-range contact interaction is suppressed by the Pauli exclusion principle in the case of a single-component Fermi gas. Also, as a consequence of the symmetry of the Pauli pressure, the Fermi surface (FS) is a sphere. In contrast to that, theoretical predictions that take the DDI into account have shown that this anisotropic and long-ranged interaction leads to the deformation of the FS into an ellipsoid [90]. Namely, the FS stretches from a sphere to an ellipsoid along the dipoles' orientation direction, which represents the direction of the maximum attraction of the DDI. The ground state [122, 123] and the dynamic properties of such systems have been systematically investigated using theoretical and numerical approaches in the collisionless regime [93, 95, 124], in the hydrodynamic regime [91, 92], as well as in the collisional range, between these two limiting cases [125, 126]. The FS deformation was also recently theoretically studied in mixtures of dipolar and non-dipolar fermions, as well as in the presence of a weak lattice confinement [127].

Within the Hartree-Fock mean-field theory for a many-body system, first-order contributions of the DDI to the total energy of the system include both the Hartree direct interaction and the Fock exchange interaction term. In the case of a Fermi gas with isotropic interaction, the Hartree and the Fock term cancel out [90], thus leading to a spherically symmetric FS. But in the case of a Fermi gas with the anisotropic DDI the Hartree term gives rise to a distortion in real space [118, 128], whereas the Fock term gives rise to a distortion in momentum space, i.e., to an ellipsoidal deformation of the Fermi sphere. Note in this context that the Fock exchange term in dipolar Fermi gases is the consequence of a combined effect of the DDI and the Pauli exclusion principle. The Hartree-Fock mean-field approximation, which includes

energy terms up to first-order in the DDI, is sufficiently accurate to qualitatively explain and quantitatively describe results of ongoing experiments [48]. In the current experimentally relevant range of dipolar interactions strengths the theory beyond the Hartree-Fock, where the total energy is determined up to second-order in the DDI, yields only small differences, which cannot be yet resolved experimentally. Thus, the Hartree-Fock mean-field approach yields already gives results which are quantitatively accurate enough for present-day experiments [129–131]. However, until now, existing theories were limited to a fixed orientation of the dipoles, which has to coincide with one of the trap axes [90, 118, 125, 126]. Such a restriction greatly simplified theoretical considerations, but, on the other hand, limited their scope since the anisotropy of the DDI is best controlled by the dipoles' orientation with respect to the trap axes.

Motivated by this, we develop here a general theory to describe the ground state of a dipolar Fermi gas for an arbitrary orientation of the dipoles and a triaxial trap geometry. Our full theoretical description provides a substantial advance in understanding of dipolar phenomena and in describing experimental observations in a very broad parameter range, see for example References [48–50]. In particular, our theory is capable to accurately describe both the cloud shape in real space and the FS in momentum space.

In this Chapter we present the derivation of our general theory, which is structured as follows. In Section 2.1 we introduce the Wigner function, the phase-space distribution function that we use to describe the properties of dipolar Fermi systems. Next, we present our theoretical model and several suitable ansätze for the form of the system's Wigner function, aiming to account for the effect of the DDI on both the shape of the atomic or molecular cloud in real space and the shape of the corresponding Fermi surface in momentum space. In Section 2.2 we give a detailed derivation of the total ground state energy of the system, considering the Hartree-Fock mean-field approach, which is precisely tailored to describe the polarized dipolar Fermi gas at zero temperature. Having obtained the total energy for all suitable ansätze, in Section 2.3 we first derive a set of equations that determines all considered variational parameters. Later on, this enables us to determine that configuration minimizes the system's total energy for a fixed particle number. Such a configuration can be considered as the most physically suitable ansatz for the description of the ground state of trapped dipolar fermions with tilted dipoles. We use the ansatz selected here for all further calculations in this Thesis.

## 2.1 Wigner function in equilibrium

A classical many-body system can be fully defined in terms of the coordinate and momentum space variables and phase-space distribution functions are often used to describe the properties of such systems. Similarly, a quantum many-body system can be described in terms of a quasidistribution function, the Wigner function, given by

$$\nu^0(\mathbf{r}, \mathbf{k}) = \int d^3r' e^{-i\mathbf{k}\cdot\mathbf{r}'} \rho\left(\mathbf{r} + \frac{1}{2}\mathbf{r}', \mathbf{r} - \frac{1}{2}\mathbf{r}'\right), \quad (2.1)$$

where

$$\rho(\mathbf{r}, \mathbf{r}') = \langle \hat{\Psi}^\dagger(\mathbf{r}) \hat{\Psi}(\mathbf{r}') \rangle, \quad (2.2)$$

represents the one-body density matrix. Namely, the Wigner function represents the Wigner-Weyl transform of the density matrix and is equivalent to a quantum-mechanical wave function [132, 133]. Despite being a distribution function, it can be negative within small areas of the phase space, which are shielded by the Heisenberg uncertainty relation. Therefore, the Wigner function is a quasiprobability distribution function, and integrating it over the space or the momentum variables leads to the respective probability distribution functions

$$n(\mathbf{r}) = \int \frac{d^3k}{(2\pi)^3} \nu^0(\mathbf{r}, \mathbf{k}), \quad (2.3)$$

$$n(\mathbf{k}) = \int d^3r \nu^0(\mathbf{r}, \mathbf{k}). \quad (2.4)$$

The quantum-mechanical expectation values of the system's observables, which are required for the calculation of the properties of nonrelativistic quantum systems, can be obtained as their phase-space averages, weighted by the Wigner function [134–138].

For instance

$$\langle O \rangle = \frac{\iint d^3r d^3k O(\mathbf{r}, \mathbf{k}) \nu^0(\mathbf{r}, \mathbf{k})}{\iint d^3r d^3k \nu^0(\mathbf{r}, \mathbf{k})}, \quad (2.5)$$

represents the expectation values of the observable  $O(\mathbf{r}, \mathbf{k})$ .

Considering a trapped ultracold dipolar Fermi gas, the equilibrium distribution function in phase space will rapidly decrease to zero outside a certain closed surface, due to a combined effect of the Pauli exclusion principle, which is responsible for the existence of the FS in momentum space, and the trapping in real space. Therefore, in order to model the global equilibrium distribution of the dipolar Fermi gas we use an

ansatz for the semiclassical Wigner function, which resembles the form of the Wigner-transformed Fermi-Dirac distribution of a noninteracting Fermi gas. Note that the temperature of the dipolar Fermi gas in the experiment of Reference [48] is very low, such that thermal fluctuations are expected to be of the order of  $(T/T_F)^2 \approx 3\%$  due to the Sommerfeld expansion. This justifies to use here the Wigner-transformed Fermi-Dirac distribution of a noninteracting Fermi gas at zero temperature approximation. Therefore, if the dipoles' orientation axis lies along one of the trapping axes (usually denoted as  $z$  axis), an accurate ansatz for the Wigner function takes the simple form [90–93, 95, 96, 122–126],

$$\nu_z^0(\mathbf{r}, \mathbf{k}) = \text{H} \left( 1 - \sum_i \frac{r_i^2}{R_i^2} - \sum_i \frac{k_i^2}{K_i^2} \right), (i = x, y, z). \quad (2.6)$$

Here H represents the Heaviside step function, while the variational parameters  $R_i$  and  $K_i$  stand for the Thomas-Fermi radii and the Fermi momenta for a trapped noninteracting Fermi gas at zero temperature. The FS is a sphere with the radius  $K_F^0$  given by Equation (1.22), as depicted in Figure 2.1(a), while the ellipsoidal shape of the gas cloud is determined by the trap potential and has semi-axes  $R_i^0$  given by Equation (1.21), as depicted in Figure 2.1(d).

A theory based on the above ansatz [90, 126] was successfully used to describe trapped polarized dipolar Fermi gases, while its extension [125] enabled a detailed analysis of the ground state and modeling of the time-of-flight (TOF) expansion dynamics of the system for different collisional regimes. Furthermore, numerical comparisons [124, 139] have confirmed that, even in the case of polar molecules with masses of the order of 100 atomic units and an electric dipole moment as large as 1 D, the above variational ansatz yields highly accurate results, within a fraction of per mille. This indicates that the ansatz (2.6), first introduced in a slightly different manner in Reference [90], is indeed very well suited to describe polarized dipolar Fermi gases. One of the main results of those previous findings were that both the FS and shape of the gas cloud stretch along the polarization direction ( $z$  axis), as depicted in Figures 2.1(b) and 2.1(e), respectively. However, the experiment of Reference [48] was performed for an arbitrary angle  $\theta$ , see Figure 1.3(b), and therefore the comparison with the theory [125, 126] was only possible for the special case of dipoles oriented along the  $z$  axis, i.e., for  $\theta = 0^\circ$ . In order to model the global equilibrium distribution of the dipolar Fermi gas for arbitrarily oriented dipoles and to provide an accurate description of the experiment, it is necessary to generalize the ansatz (2.6). Therefore, we apply here an

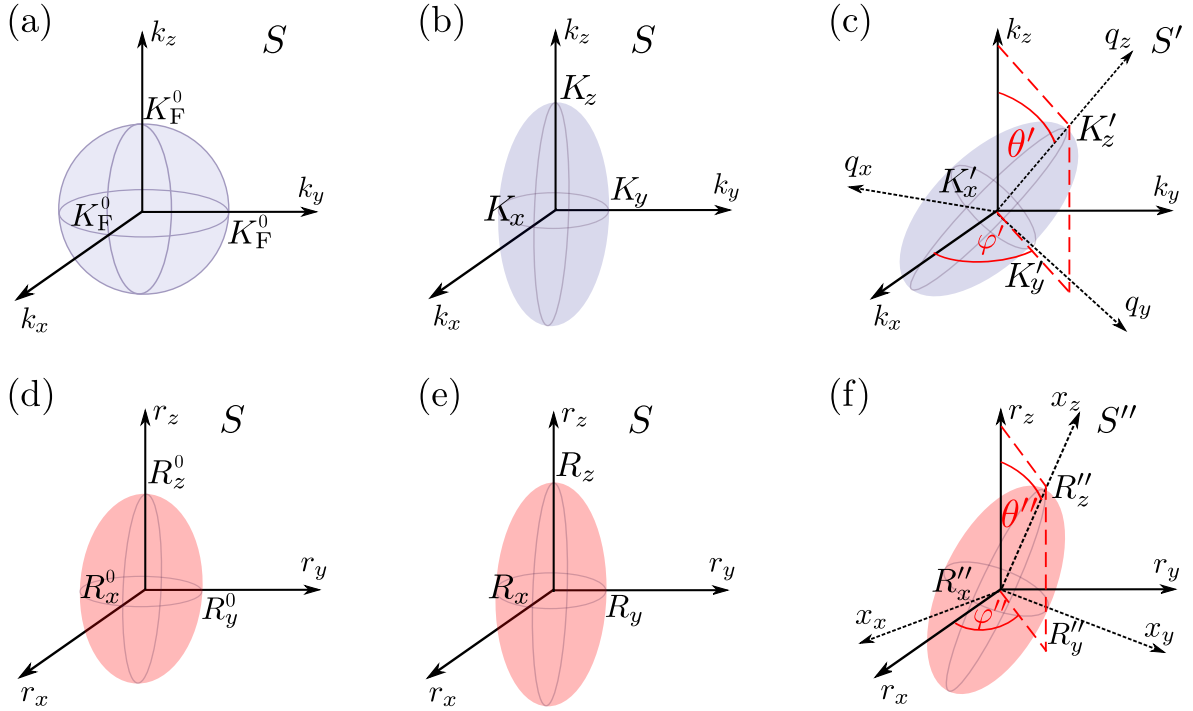


**Figure 2.1:** Schematic illustration of: (a)-(c) FS in momentum space; (d)-(f) gas cloud in real space. Illustrations (a) and (d) correspond to noninteracting Fermi gas, while (b) and (e) correspond to dipolar Fermi gas with FS and gas cloud stretched into ellipsoids whose axes coincide with the trap axes. Illustrations (c) and (f) depict the ellipsoidal FS and gas cloud of dipolar Fermi gas stretched in the direction determined by spherical angles  $(\theta', \varphi')$  and  $(\theta'', \varphi'')$ , respectively.

analogous reasoning and introduce the following ansatz for the Wigner distribution

$$\nu^0(\mathbf{r}, \mathbf{k}) = \text{H} \left( 1 - \sum_{i,j} r_i \mathbb{A}_{ij} r_j - \sum_{i,j} k_i \mathbb{B}_{ij} k_j \right), (i = x, y, z). \quad (2.7)$$

Here  $\mathbb{A}_{ij}$  and  $\mathbb{B}_{ij}$  are matrix elements that account for the generalized geometry of the system and determine the shape of the cloud in real space and of the FS in momentum space, respectively. The particle density distribution in real space is determined by both the trapping potential and the Hartree direct energy. On the other side, the momentum distribution is dominated by the interplay between the Pauli pressure, which is isotropic, and the Fock exchange energy, which is responsible for the deformation of the FS [90]. The experiment of Reference [48] suggest that the FS follows the orientation of the dipoles, which are parallel to the external field, keeping the major axis of the FS always parallel to the direction of the maximum attraction of the DDI. Motivated by this, we consider four possible scenarios for a detailed theoretical description of the system, in order to verify the above hypothesis.

### 1. Spherical scenario

For the sake of completeness, we start with a simple spherical scenario, in which the FS remains a sphere. This is depicted in Figures 1.3(b) and 1.3(e), where we additionally assume that all Fermi momenta are equal ( $K_i = K_F \neq K_F^0$ ) and the matrix  $\mathbb{B}$  is given by

$$\mathbb{B}_1 = \begin{pmatrix} 1/K_F^2 & 0 & 0 \\ 0 & 1/K_F^2 & 0 \\ 0 & 0 & 1/K_F^2 \end{pmatrix} = \mathbb{I}/K_F^2, \quad (2.8)$$

where  $\mathbb{I}$  is the  $3 \times 3$  identity matrix. Similarly, matrix  $\mathbb{A}_1$  is a diagonal matrix in the coordinate system  $S$ , which is defined by the harmonic trap axes, and it reads

$$\mathbb{A}_1 = \begin{pmatrix} 1/R_x^2 & 0 & 0 \\ 0 & 1/R_y^2 & 0 \\ 0 & 0 & 1/R_z^2 \end{pmatrix}. \quad (2.9)$$

In this way, we neglect the off-diagonal elements, which may arise due to the dipoles' arbitrary orientation, which is certainly justified for a weak DDI and elongated traps.

The normalization of the Wigner distribution (2.7) for this case is given by

$$N = \iint \frac{d^3r d^3k}{(2\pi)^3} \nu^0(\mathbf{r}, \mathbf{k}) = \iint \frac{d^3r dk k^2}{2\pi^2} \text{H} \left( 1 - \sum_i \frac{r_i^2}{R_i^2} - \frac{k^2}{K_F^2} \right) = \frac{\bar{R}^3 K_F}{48} \equiv N^{(1)}, \quad (2.10)$$

and there are four variational parameters: Fermi momenta  $K_F$  and three radii  $R_i$ .

### 2. On-on-axis scenario

We also consider a second, on-on-axis scenario, depicted in Figures 1.3(b) and 1.3(e) which now includes the FS deformation. Here the FS is an ellipsoid with fixed major axes coinciding with the trap axes, as shown in Figure 2.1(b). Therefore, the matrix  $\mathbb{B}$  is again diagonal in the coordinate system  $S$

$$\mathbb{B}_2 = \begin{pmatrix} 1/K_x^2 & 0 & 0 \\ 0 & 1/K_y^2 & 0 \\ 0 & 0 & 1/K_z^2 \end{pmatrix}, \quad (2.11)$$

but is not proportional to the identity matrix anymore. The matrix  $\mathbb{A}$  remains the same as in previous case ( $\mathbb{A}_2 = \mathbb{A}_1$ ), which recovers the old ansatz given by Equation (2.6).

The normalization of the Wigner distribution (2.7) in this case yields

$$N = \iint \frac{d^3r d^3k}{(2\pi)^3} \nu^0(\mathbf{r}, \mathbf{k}) = \iint \frac{d^3r d^3k}{(2\pi)^3} \text{H} \left( 1 - \sum_i \frac{r_i^2}{R_i^2} - \sum_i \frac{k_i^2}{K_i^2} \right) = \frac{\bar{R}^3 \bar{K}^3}{48} \equiv N^{(2)}, \quad (2.12)$$

and here we have six variational parameters: three momenta  $K_i$  and three radii  $R_i$ . We note that the first, spherical scenario is a special case of the second one, obtained by restricting the Fermi momenta to be equal, i.e. by neglecting the FS deformation.

### 3. Off-on-axis scenario

As a third and more general possibility, we consider the off-on-axis hypothesis motivated by experimental results of Reference [48]. Namely, we assume that the matrix  $\mathbb{B}$  has a diagonal form  $\mathbb{B}'_3$  in a rotated coordinate system  $S'$ , which is defined by the axes  $q_x$ ,  $q_y$  and  $q_z$ , as depicted in Figure 2.1(c)

$$\mathbb{B}'_3 = \begin{pmatrix} 1/K_x'^2 & 0 & 0 \\ 0 & 1/K_y'^2 & 0 \\ 0 & 0 & 1/K_z'^2 \end{pmatrix}. \quad (2.13)$$

Here the parameters  $K'_i$  represent the Fermi momenta in the rotated coordinate system  $S'$ . Strictly speaking, from the underlying physical point of view it is expected here that the  $q_z$  axis remains parallel to the orientation of the dipole moments. However, we will not assume this, because this can be derived within the theory and used later on as an additional test of our ansatz.

In order to describe the rotation from  $S$  to  $S'$ , we express the quantities  $\mathbb{B}_3$  and  $\mathbf{k}$  from  $S$  as  $\mathbb{B}'_3 = \mathbb{R}^T \mathbb{B}_3 \mathbb{R}'$  and  $\mathbf{q} = \mathbb{R}^T \mathbf{k}$ , with  $\mathbb{R}' = \mathbb{R}(\theta', \varphi')$ , where  $\mathbb{R}$  stands for the rotation matrix

$$\mathbb{R}(\theta, \varphi) = \begin{pmatrix} \cos \theta \cos \varphi & -\sin \varphi & \sin \theta \cos \varphi \\ \cos \theta \sin \varphi & \cos \varphi & \sin \theta \sin \varphi \\ -\sin \theta & 0 & \cos \theta \end{pmatrix}. \quad (2.14)$$

In this scenario the cloud shape is considered to be on-axis, i.e.  $\theta'' = \varphi'' = 0^\circ$  in Figure 1.3(f). Therefore, the matrix  $\mathbb{A}$  again has a diagonal form in the coordinate system  $S$ , such that  $\mathbb{A}_3 = \mathbb{A}_2 = \mathbb{A}_1$ .

The normalization of the Wigner distribution (2.7) now reads

$$N = \iint \frac{d^3r d^3k}{(2\pi)^3} \nu^0(\mathbf{r}, \mathbf{k}) = \iint \frac{d^3r d^3q}{(2\pi)^3} \text{H} \left( 1 - \sum_i \frac{r_i^2}{R_i^2} - \sum_i \frac{q_i^2}{K_i'^2} \right) = \frac{\bar{R}^3 \bar{K}'^3}{48} \equiv N^{(3)}. \quad (2.15)$$

In this case, we have eight variational parameters: three momenta  $K'_i$ , three radii  $R_i$ , and two angles  $\theta'$  and  $\varphi'$ .

We note that the on-on-axis scenario is a special case of the off-on-axis one when we restrict the angles  $\theta' = \varphi' = 0^\circ$ , which is justified when the dipoles are parallel to one of the trap axes. In that case the matrix  $\mathbb{B}_3$  is already diagonal and coincides with  $\mathbb{B}_2$ , i.e.,  $K'_i = K_i$ .

#### 4. Off-off-axis scenario

Finally, as a fourth and the most general possibility, we consider off-axis hypothesis for both the FS and the gas cloud ellipsoids, as depicted in Figures 2.1(c) and 2.1(f). Therefore, the matrix  $\mathbb{B}$  has the same form as in the off-on-axis scenario,  $\mathbb{B}_4 = \mathbb{B}_3$ , while the matrix  $\mathbb{A}$  is a diagonal only in the rotated coordinate system  $S''$ , which is defined by the axes  $x_x$ ,  $x_y$  and  $x_z$

$$\mathbb{A}_4 = \begin{pmatrix} 1/R_x''^2 & 0 & 0 \\ 0 & 1/R_y''^2 & 0 \\ 0 & 0 & 1/R_z''^2 \end{pmatrix}. \quad (2.16)$$

Here the parameters  $R_i''$  represent the TF radii in the rotated coordinate system  $S''$ . In order to describe the rotation from  $S$  to  $S''$ , we have  $\mathbb{A}_4'' = \mathbb{R}''^T \mathbb{A}_4 \mathbb{R}''$  and  $\mathbf{x} = \mathbb{R}''^T \mathbf{r}$ , where  $\mathbb{R}'' = \mathbb{R}(\theta'', \varphi'')$ .

The normalization of the Wigner distribution (2.7) in this case is

$$N = \iint \frac{d^3r d^3k}{(2\pi)^3} \nu^0(\mathbf{r}, \mathbf{k}) = \iint \frac{d^3x d^3q}{(2\pi)^3} \mathrm{H} \left( 1 - \sum_i \frac{x_i^2}{R_i''^2} - \sum_i \frac{q_i^2}{K_i''^2} \right) = \frac{\bar{R}''^3 \bar{K}''^3}{48} \equiv N^{(4)}, \quad (2.17)$$

and the total number of variational parameters here is ten: three momenta  $K'_i$ , three radii  $R_i''$ , and four angles  $\theta', \varphi', \theta'', \varphi''$ . We again note that the off-off-axis scenario can reproduce as a special case the off-on-axis, and all other scenarios as well. For example, for  $\theta'' = \varphi'' = 0^\circ$  the matrix  $\mathbb{A}_4$  is diagonal and coincides with  $\mathbb{A}_3$ , such that  $R_i'' = R_i$ .

In order to determine the values of the variational parameters for each scenario, as usual, we require that they minimize the total Hartree-Fock energy of the system. This leads, together with the corresponding particle number conservation, to algebraic set of equations that determine the TF radii, momenta, as well as the angles that determine the orientation of the FS and the gas cloud ellipsoids. Although algebraic, these equations are nonlinear and contain special functions described in Appendix B.

## 2.2 System energy in equilibrium

Now that we have identified several relevant ansätze for modeling the Wigner function of a dipolar Fermi gas of tilted dipoles, we proceed to determine the optimal values of the corresponding variational parameters. In order to do so, we have to minimize the total energy of the many-body Fermi system  $E_{\text{tot}}$ , which is in the Hartree-Fock mean-field theory given by the sum of the kinetic energy  $E_{\text{kin}}$ , the trapping energy  $E_{\text{trap}}$ , the Hartree direct energy  $E_{\text{dd}}^{\text{D}}$ , and the Fock exchange energy  $E_{\text{dd}}^{\text{E}}$ . Within a semiclassical theory, they can be written in terms of the Wigner function [118] as

$$E_{\text{kin}} = \iint \frac{d^3r d^3k \hbar^2 k^2}{(2\pi)^3 2M} \nu^0(\mathbf{r}, \mathbf{k}), \quad (2.18)$$

$$E_{\text{trap}} = \iint \frac{d^3r d^3k}{(2\pi)^3} V_{\text{trap}}(\mathbf{r}) \nu^0(\mathbf{r}, \mathbf{k}), \quad (2.19)$$

$$E_{\text{dd}}^{\text{D}} = \frac{1}{2} \iiint \frac{d^3r d^3r' d^3k d^3k'}{(2\pi)^6} V_{\text{dd}}(\mathbf{r} - \mathbf{r}') \nu^0(\mathbf{r}, \mathbf{k}) \nu^0(\mathbf{r}', \mathbf{k}'), \quad (2.20)$$

$$E_{\text{dd}}^{\text{E}} = -\frac{1}{2} \iiint \frac{d^3r d^3r' d^3k d^3k'}{(2\pi)^6} V_{\text{dd}}(\mathbf{r}') e^{i(\mathbf{k}-\mathbf{k}') \cdot \mathbf{r}'} \nu^0(\mathbf{r}, \mathbf{k}) \nu^0(\mathbf{r}, \mathbf{k}'). \quad (2.21)$$

The total energy of the system was calculated previously with the ansatz (2.6) for the case when the dipoles are parallel to one of the trap axes [90–92, 125, 126], our on-on axis scenario 2. Also, Reference [49] presents a derivation of the total energy for the system with tilted dipoles using ansatz described in the off-on-axis scenario 3. Therefore, we present here only the detailed derivation of all energy terms for the most general ansatz considered in the off-off-axis scenario 4, from which one can easily deduce the total energy of the system for any of the scenarios defined above [50].

### 2.2.1 Kinetic energy

We use the most general ansatz, which corresponds to the off-off-axis scenario, to calculate all four energy terms. Inserting this ansatz into the expression for the kinetic energy given by Equation (2.18) we get

$$E_{\text{kin}} = \iint \frac{d^3r d^3k \hbar^2 k^2}{(2\pi)^3 2M} \nu^0(\mathbf{r}, \mathbf{k}) = \iint \frac{d^3x d^3q \hbar^2 q^2}{(2\pi)^3 2M} \text{H} \left( 1 - \sum_j \frac{x_j^2}{R_j'^2} - \sum_j \frac{q_j^2}{K_j'^2} \right). \quad (2.22)$$

We first calculate the real space integral, where we can use spherical symmetry and switch to spherical coordinates. After rescaling the space variables according to  $x_i =$

$u_i R_i''$ , we obtain

$$E_{\text{kin}} = \int \frac{d^3 q}{(2\pi)^3} \frac{\hbar^2 q^2}{2M} \bar{R}''^3 \int_0^\infty du 4\pi u^2 \text{H} \left( 1 - \sum_j \frac{q_j^2}{K_j'^2} - u^2 \right). \quad (2.23)$$

Since the Heaviside step function has a value of 1 in the range  $|u| \leq u_{\text{max}} = \sqrt{1 - \sum_j q_j^2 / K_j'^2}$ , and vanishes otherwise, the boundary of the  $u$ -integral reduces to

$$E_{\text{kin}} = \int \frac{d^3 q}{4\pi^2} \frac{\hbar^2 q^2}{M} \bar{R}''^3 \text{H} \left( 1 - \sum_j \frac{q_j^2}{K_j'^2} \right) \int_0^{u_{\text{max}}} du u^2. \quad (2.24)$$

After solving the  $u$ -integral, we use rescaling  $k_i = K_i' v_i$ , which leads to

$$E_{\text{kin}} = \int \frac{d^3 v}{12\pi^2} \bar{R}''^3 \bar{K}'^3 \frac{\hbar^2 \sum_j K_j'^2 v_j^2}{M} (1 - v_x^2 - v_y^2 - v_z^2)^{\frac{3}{2}} \text{H} \left( 1 - \sum_j v_j^2 \right). \quad (2.25)$$

The three remaining integrals are computed one by one. We start with the  $v_z$ -integral

$$E_{\text{kin}} = \frac{1}{6\pi^2} \frac{\hbar^2 \bar{R}''^3 \bar{K}'^3}{M} \int dv_x dv_y \times \int_0^{\sqrt{1-v_x^2-v_y^2}} dv_z \left( \sum_j K_j'^2 v_j^2 \right) \left( 1 - \sum_j v_j^2 \right)^{\frac{3}{2}} \text{H}(1 - v_x^2 - v_y^2), \quad (2.26)$$

which, after another rescaling  $v_z = \sqrt{1 - v_x^2 - v_y^2} \cos \vartheta$ , simplifies to

$$E_{\text{kin}} = \frac{1}{6\pi^2} \bar{R}''^3 \bar{K}'^3 \frac{\hbar^2}{M} \int dv_x dv_y (1 - v_x^2 - v_y^2)^2 \text{H}(1 - v_x^2 - v_y^2) \times \int_0^{\frac{\pi}{2}} d\vartheta \sin^4 \vartheta \left[ K_x'^2 v_x^2 + K_y'^2 v_y^2 + K_z'^2 (1 - v_x^2 - v_y^2) \cos^2 \vartheta \right]. \quad (2.27)$$

The  $\vartheta$ -integral can be performed using the standard integrals

$$\int_0^{\frac{\pi}{2}} d\vartheta \sin^4 \vartheta = \frac{3\pi}{16}, \quad (2.28)$$

$$\int_0^{\frac{\pi}{2}} d\vartheta \sin^4 \vartheta \cos^2 \vartheta = \frac{\pi}{32}. \quad (2.29)$$

The other integrals over  $v_x$  and  $v_y$  can be solved in the same way, yielding the final expression for the kinetic energy

$$E_{\text{kin}} = \frac{N}{8} \sum_j \frac{\hbar^2 K_j'^2}{2M}. \quad (2.30)$$

### 2.2.2 Trapping energy

The trapping energy term can be calculated in a similar way as the kinetic energy term, nevertheless we present here all steps. The expression for the trapping energy given by Equation (2.19), together with the harmonic potential given by Equation (1.16), and the most general ansatz gives

$$\begin{aligned}
E_{\text{trap}} &= \iint \frac{d^3 r d^3 k}{(2\pi)^3} \frac{M}{2} \left( \sum_j \omega_j^2 r_j^2 \right) \nu^0(\mathbf{r}, \mathbf{k}) \\
&= \iint \frac{d^3 x d^3 q}{(2\pi)^3} \frac{M}{2} \left[ \sum_j \omega_j^2 \left( \sum_i \mathbb{R}_{ji}'' x_i \right)^2 \right] \text{H} \left( 1 - \sum_j \frac{x_j^2}{R_j''^2} - \sum_j \frac{q_j^2}{K_j'^2} \right) \\
&= \iint \frac{d^3 x d^3 q}{(2\pi)^3} \frac{M}{2} \left( \sum_{j,i} \omega_j^2 \mathbb{R}_{ji}''^2 x_i^2 \right) \text{H} \left( 1 - \sum_j \frac{x_j^2}{R_j''^2} - \sum_j \frac{q_j^2}{K_j'^2} \right). \quad (2.31)
\end{aligned}$$

The  $q$ -integral can be calculated by switching to spherical coordinates and by rescaling the momentum space variables according to  $q_i = u_i K_i'$ , which yields

$$E_{\text{trap}} = \int \frac{d^3 x}{(2\pi)^3} \frac{M}{2} \left( \sum_{j,i} \omega_j^2 \mathbb{R}_{ji}''^2 x_i^2 \right) \bar{K}''^3 \int_0^\infty du 4\pi u^2 \text{H} \left( 1 - \sum_j \frac{x_j^2}{R_j''^2} - u^2 \right). \quad (2.32)$$

The Heaviside step function is non-zero in the range  $|u| \leq u_{\text{max}} = \sqrt{1 - \sum_j x_j^2 / R_j''^2}$ , so

$$\begin{aligned}
E_{\text{trap}} &= \int \frac{d^3 x}{4\pi^2} M \left( \sum_{j,i} \omega_j^2 \mathbb{R}_{ji}''^2 x_i^2 \right) \bar{K}''^3 \text{H} \left( 1 - \sum_j \frac{x_j^2}{R_j''^2} \right) \int_0^{u_{\text{max}}} du u^2 \\
&= \int \frac{d^3 v}{12\pi^2} \bar{R}''^3 \bar{K}''^3 M \left( \sum_{j,i} \omega_j^2 \mathbb{R}_{ji}''^2 R_i''^2 v_i^2 \right) \left( 1 - \sum_j v_j^2 \right)^{\frac{3}{2}} \text{H} \left( 1 - \sum_j v_j^2 \right), \quad (2.33)
\end{aligned}$$

where we have used the rescaling  $x_i = R_i'' v_i$  in the last step. The three remaining integrals are computed similarly as before, and we start with  $v_z$ -integral,

$$\begin{aligned}
E_{\text{trap}} &= \frac{1}{6\pi^2} \bar{R}''^3 \bar{K}''^3 M \int dv_x dv_y \\
&\quad \times \int_0^{\sqrt{1-v_x^2-v_y^2}} dv_z \left( \sum_{j,i} \omega_j^2 \mathbb{R}_{ji}''^2 R_i''^2 v_i^2 \right) \left( 1 - \sum_j v_j^2 \right)^{\frac{3}{2}} \text{H}(1 - v_x^2 - v_y^2) \\
&= \frac{1}{6\pi^2} \bar{R}''^3 \bar{K}''^3 M \int dv_x dv_y (1 - v_x^2 - v_y^2)^2 \text{H}(1 - v_x^2 - v_y^2) \\
&\quad \times \int_0^{\frac{\pi}{2}} d\vartheta \sin^4 \vartheta \left[ \sum_j \omega_j^2 \left( \mathbb{R}_{jx}''^2 R_x''^2 v_x^2 + \mathbb{R}_{jy}''^2 R_y''^2 v_y^2 + \mathbb{R}_{jz}''^2 R_z''^2 (1 - v_x^2 - v_y^2) \cos^2 \vartheta \right) \right], \quad (2.34)
\end{aligned}$$

where we have used another rescaling  $v_z = \sqrt{1 - v_x^2 - v_y^2} \cos \vartheta$ . The  $\vartheta$ -integral is the same as for the kinetic energy term and can be solved using Equations (2.28) and (2.29). The other two integrals can be calculated analogously, which leads to the trapping energy expression

$$E_{\text{tr}} = \frac{N}{8} \frac{M}{2} \sum_{j,i} \omega_j^2 \mathbb{R}_{ji}''^2 R_i''^2. \quad (2.35)$$

### 2.2.3 Hartree energy

In order to reduce the number of integrals in the expression for the Hartree energy term given by Equation (2.20), we first rewrite it by means of the Fourier transform of the DDI potential according to

$$\begin{aligned} E_{\text{dd}}^{\text{D}} &= \frac{1}{2} \iiint \frac{d^3 r d^3 r' d^3 k d^3 k' d^3 k''}{(2\pi)^9} e^{i\mathbf{k}'' \cdot (\mathbf{r} - \mathbf{r}')} \tilde{V}_{\text{dd}}(\mathbf{k}'') \nu^0(\mathbf{r}, \mathbf{k}) \nu^0(\mathbf{r}', \mathbf{k}') \\ &= \frac{1}{2} \int \frac{d^3 k''}{(2\pi)^3} \tilde{V}_{\text{dd}}(\mathbf{k}'') \int \frac{d^3 k}{(2\pi)^3} \tilde{\nu}^0(-\mathbf{k}'', \mathbf{k}) \int \frac{d^3 k'}{(2\pi)^3} \tilde{\nu}^0(\mathbf{k}'', \mathbf{k}'). \end{aligned} \quad (2.36)$$

This results in decoupling of the integrals of the Fourier transform of distribution functions  $\tilde{\nu}^0$  and eliminates integrals over space variables. Next, we compute the Fourier transform of the corresponding Wigner function, with respect to the first argument

$$\begin{aligned} \tilde{\nu}^0(-\mathbf{k}'', \mathbf{k}) &= \int d^3 r e^{i\mathbf{k}'' \cdot \mathbf{r}} \text{H} \left( 1 - \sum_{i,j} r_i \mathbb{A}_{4ij} r_j - \sum_{i,j} k_i \mathbb{B}_{4ij} k_j \right) \\ &= \int d^3 x e^{i\mathbf{k}'' \cdot \mathbb{R}'' \mathbf{x}} \text{H} \left[ h(\mathbf{k}) - \sum_j \frac{x_j^2}{R_j''^2} \right], \end{aligned} \quad (2.37)$$

where  $h(\mathbf{k}) = 1 - \sum_{ij} k_i \mathbb{B}_{4ij} k_j$  is a suitable abbreviation for the momentum part of the argument of the Wigner function. The last equation can be rewritten straightforwardly

$$\begin{aligned} \tilde{\nu}^0(-\mathbf{k}'', \mathbf{k}) &= \int dx_x dx_y e^{i(c_x'' x_x + c_y'' x_y)} \\ &\quad \times \int_{-\infty}^{\infty} dx_z \text{H} \left( h(\mathbf{k}) - \sum_j \frac{x_j^2}{R_j''^2} \right) (\cos c_z'' x_z + i \sin c_z'' x_z), \end{aligned} \quad (2.38)$$

where  $\mathbf{c}'' = \mathbb{R}''^T \mathbf{k}''$ . The second term containing  $\sin c_z'' x_z$  vanishes due to symmetry reasons. The first term can be simplified since the Heaviside step function is non-zero only in the range  $|x_z| \leq x_z^{\text{max}} = R_z'' \sqrt{h(\mathbf{k}) - x_x^2/R_x''^2 - x_y^2/R_y''^2}$ , which, together with

the rescaling  $x_z = x_z^{\max} \cos \vartheta$ , yields

$$\begin{aligned} \tilde{\nu}^0(-\mathbf{k}'', \mathbf{k}) &= 2R_z'' \int dx_x dx_y e^{i(c_x'' x_x + c_y'' x_y)} \left( h(\mathbf{k}) - \frac{x_x^2}{R_x''^2} - \frac{x_y^2}{R_y''^2} \right)^{\frac{1}{2}} \mathrm{H} \left( h(\mathbf{k}) - \frac{x_x^2}{R_x''^2} - \frac{x_y^2}{R_y''^2} \right) \\ &\quad \times \int_0^{\frac{\pi}{2}} d\vartheta \sin \vartheta \cos \left[ c_z'' R_z'' \left( h(\mathbf{k}) - \frac{x_x^2}{R_x''^2} - \frac{x_y^2}{R_y''^2} \right)^{\frac{1}{2}} \cos \vartheta \right]. \end{aligned} \quad (2.39)$$

The last  $\vartheta$ -integral can be evaluated using the following formula [140, (3.715.20)]

$$\int_0^{\frac{\pi}{2}} dx \cos(z \cos x) \sin^{2\nu} x = \frac{\sqrt{\pi}}{2} \left( \frac{2}{z} \right)^\nu \Gamma \left( \nu + \frac{1}{2} \right) J_\nu(z), \quad \text{for } \operatorname{Re} \nu > -\frac{1}{2}, \quad (2.40)$$

where  $J_\nu(z)$  is a Bessel function of first kind. This leads to

$$\begin{aligned} \tilde{\nu}^0(-\mathbf{k}'', \mathbf{k}) &= \sqrt{\frac{2\pi R_z''}{c_z''}} \int dx_x e^{ic_x'' x_x} \int_{-\infty}^{\infty} dx_y \left( \cos c_y'' x_y + i \sin c_y'' x_y \right) \left( h(\mathbf{k}) - \frac{x_x^2}{R_x''^2} - \frac{x_y^2}{R_y''^2} \right)^{\frac{1}{4}} \\ &\quad \times J_{\frac{1}{2}} \left[ c_z'' R_z'' \left( h(\mathbf{k}) - \frac{x_x^2}{R_x''^2} - \frac{x_y^2}{R_y''^2} \right)^{\frac{1}{2}} \right] \mathrm{H} \left( h(\mathbf{k}) - \frac{x_x^2}{R_x''^2} - \frac{x_y^2}{R_y''^2} \right). \end{aligned} \quad (2.41)$$

This can be further simplified using similar steps as before to calculate the  $x_z$ -integral by limiting the  $x_y$ -integral due to the Heaviside function, and applying a similar substitution for the  $x_y$ -variable, yielding

$$\begin{aligned} \tilde{\nu}^0(-\mathbf{k}'', \mathbf{k}) &= \sqrt{\frac{8\pi R_z''}{c_z''}} R_y'' \int dx_x e^{ic_x'' x_x} \int_0^{\frac{\pi}{2}} du \sin^{\frac{3}{2}} u \left( h(\mathbf{k}) - \frac{x_x^2}{R_x''^2} \right)^{\frac{3}{4}} \mathrm{H} \left( h(\mathbf{k}) - \frac{x_x^2}{R_x''^2} \right) \\ &\quad \times J_{\frac{1}{2}} \left[ c_z'' R_z'' \left( h(\mathbf{k}) - \frac{x_x^2}{R_x''^2} \right)^{\frac{1}{2}} \sin u \right] \cos \left[ c_y'' R_y'' \left( h(\mathbf{k}) - \frac{x_x^2}{R_x''^2} \right)^{\frac{1}{2}} \cos u \right]. \end{aligned} \quad (2.42)$$

The  $u$ -integral can now be evaluated using [140, (6.688.2)],

$$\begin{aligned} &\int_0^{\frac{\pi}{2}} dx \sin^{\nu+1} x \cos(\beta \cos x) J_\nu(\alpha \sin x) \\ &= \sqrt{\frac{\pi}{2}} \alpha^\nu (\alpha^2 + \beta^2)^{-\frac{1}{2}\nu - \frac{1}{4}} J_{\nu+\frac{1}{2}} \left[ (\alpha^2 + \beta^2)^{\frac{1}{2}} \right], \quad \text{for } \operatorname{Re} \nu > -1. \end{aligned} \quad (2.43)$$

After computing the  $u$ -integral, the  $x_x$ -integral can be treated in a similar way. Hence, the Fourier-transformed Wigner distribution function reads

$$\tilde{\nu}^0(-\mathbf{k}'', \mathbf{k}) = \frac{(2\pi)^{\frac{3}{2}} \bar{R}''^3 h(\mathbf{k})^{\frac{3}{4}} \mathrm{H}[h(\mathbf{k})] J_{\frac{3}{2}} \left[ h(\mathbf{k})^{\frac{1}{2}} \left( c_x''^2 R_x''^2 + c_y''^2 R_y''^2 + c_z''^2 R_z''^2 \right)^{\frac{1}{2}} \right]}{\left( c_x''^2 R_x''^2 + c_y''^2 R_y''^2 + c_z''^2 R_z''^2 \right)^{\frac{3}{4}}}. \quad (2.44)$$

We note here that  $\tilde{\nu}^0(\mathbf{k}'', \mathbf{k})$  is an even function with respect to  $\mathbf{k}''$ . This simplifies next steps of the calculation, because the  $k$ - and  $k'$ -integrals over the Fourier-transformed Wigner function in Equation (2.36) turn out to be the same. Hence, it is only necessary to compute one of them, e.g.,

$$\begin{aligned} \int \frac{d^3 k}{(2\pi)^3} \tilde{\nu}^0(\mathbf{k}'', \mathbf{k}) &= \int \frac{d^3 q}{(2\pi)^3} \tilde{\nu}^0(\mathbf{k}'', \mathbb{R}' \mathbf{q}) \\ &= \frac{\bar{R}''^3}{(2\pi)^{\frac{3}{2}} \left( c_x''^2 R_x''^2 + c_y''^2 R_y''^2 + c_z''^2 R_z''^2 \right)^{\frac{3}{4}}} \int d^3 q \left( 1 - \sum_j \frac{q_j^2}{K_j''^2} \right)^{\frac{3}{4}} \\ &\times J_{\frac{3}{2}} \left[ \left( 1 - \sum_j \frac{q_j^2}{K_j''^2} \right)^{\frac{1}{2}} \left( c_x''^2 R_x''^2 + c_y''^2 R_y''^2 + c_z''^2 R_z''^2 \right)^{\frac{1}{2}} \right] \text{H} \left( 1 - \sum_j \frac{q_j^2}{K_j''^2} \right). \end{aligned} \quad (2.45)$$

In order to evaluate this integral, we perform the substitution  $q_i = K_i' u_i$  and use the spherical symmetry of the integrand, which yields

$$\begin{aligned} \int \frac{d^3 q}{(2\pi)^3} \tilde{\nu}^0(\mathbf{k}'', \mathbb{R}' \mathbf{q}) &= \frac{4\pi \bar{R}''^3 \bar{K}''^3}{(2\pi)^{\frac{3}{2}} \left( c_x''^2 R_x''^2 + c_y''^2 R_y''^2 + c_z''^2 R_z''^2 \right)^{\frac{3}{4}}} \int_0^1 du u^2 (1 - u^2)^{\frac{3}{4}} \\ &\times J_{\frac{3}{2}} \left[ (1 - u^2)^{\frac{1}{2}} \left( c_x''^2 R_x''^2 + c_y''^2 R_y''^2 + c_z''^2 R_z''^2 \right)^{\frac{1}{2}} \right]. \end{aligned} \quad (2.46)$$

This integral can be computed after a substitution  $u = \cos \vartheta$  and using [140, (6.683)],

$$\begin{aligned} &\int_0^{\frac{\pi}{2}} d\vartheta J_{\mu}(a \sin \vartheta) \sin^{\mu+1} \vartheta \cos^{2\rho+1} \vartheta \\ &= 2^{\rho} \Gamma(\rho + 1) a^{-\rho-1} J_{\rho+\mu+1}(a), \quad \text{for } \text{Re } \rho, \text{Re } \mu > -1. \end{aligned} \quad (2.47)$$

Thus, the integral of the Fourier-transformed Wigner function reads

$$\int \frac{d^3 q}{(2\pi)^3} \tilde{\nu}^0(\mathbf{k}'', \mathbb{R}' \mathbf{q}) = \tilde{n}(\mathbf{k}'') = \frac{\bar{R}''^3 \bar{K}''^3 J_3 \left[ \left( c_x''^2 R_x''^2 + c_y''^2 R_y''^2 + c_z''^2 R_z''^2 \right)^{\frac{1}{2}} \right]}{\left( c_x''^2 R_x''^2 + c_y''^2 R_y''^2 + c_z''^2 R_z''^2 \right)^{\frac{3}{2}}}. \quad (2.48)$$

We are now able to solve the last integral in the Hartree energy term. With the Fourier-transformed DDI potential given by Equation (1.31), we get

$$\begin{aligned} E_{\text{dd}}^{\text{D}} &= \frac{C_{\text{dd}}}{6} \int \frac{d^3 k''}{(2\pi)^3} \left( \frac{3(\sum_i \mathbb{R}_{zi}^T k_i'')^2}{k''^2} - 1 \right) \tilde{n}^2(\mathbf{k}'') = \frac{C_{\text{dd}}}{6} \int \frac{d^3 c''}{(2\pi)^3} \left( \frac{3(\sum_{i,j} \mathbb{R}_{zi}^T \mathbb{R}_{ij}'' c_j'')^2}{c''^2} - 1 \right) \\ &\times \frac{\bar{R}''^6 \bar{K}''^6}{\left( c_x''^2 R_x''^2 + c_y''^2 R_y''^2 + c_z''^2 R_z''^2 \right)^3} J_3^2 \left[ \left( c_x''^2 R_x''^2 + c_y''^2 R_y''^2 + c_z''^2 R_z''^2 \right)^{\frac{1}{2}} \right]. \end{aligned} \quad (2.49)$$

Due to the symmetry, all terms which are linear in  $c_j''$  vanish, yielding

$$E_{\text{dd}}^{\text{D}} = \frac{C_{\text{dd}}}{6} \int \frac{d^3 c''}{(2\pi)^3} \left( \frac{3 \sum_j \left( \sum_i \mathbb{R}_{zi}^T \mathbb{R}_{ij}'' \right)^2 c_j''^2}{c''^2} - 1 \right) \times \frac{\bar{R}''^6 \bar{K}''^6}{\left( c_x'' R_x''^2 + c_y'' R_y''^2 + c_z'' R_z''^2 \right)^3} J_3^2 \left[ \left( c_x'' R_x''^2 + c_y'' R_y''^2 + c_z'' R_z''^2 \right)^{\frac{1}{2}} \right]. \quad (2.50)$$

After a substitution  $c_i'' R_i'' = u_i$  and a switch into spherical coordinates, the integral leads to

$$E_{\text{dd}}^{\text{D}} = \frac{C_{\text{dd}} \bar{R}''^3 \bar{K}''^6}{6(2\pi)^3} \int_0^\pi d\vartheta \int_0^{2\pi} d\phi \sin \vartheta \int_0^\infty du \frac{J_3^2(u)}{u^4} \times \left[ 3 \left( \sum_i \mathbb{R}_{zi}^T \mathbb{R}_{ix}'' \right)^2 \frac{\sin^2 \vartheta \cos^2 \phi}{\cos^2 \phi \sin^2 \vartheta + (R_x''/R_y'')^2 \sin^2 \phi \sin^2 \vartheta + (R_x''/R_z'')^2 \cos^2 \vartheta} + 3 \left( \sum_i \mathbb{R}_{zi}^T \mathbb{R}_{iy}'' \right)^2 \frac{\sin^2 \vartheta \sin^2 \phi}{(R_y''/R_x'')^2 \cos^2 \phi \sin^2 \vartheta + \sin^2 \phi \sin^2 \vartheta + (R_y''/R_z'')^2 \cos^2 \vartheta} + 3 \left( \sum_i \mathbb{R}_{zi}^T \mathbb{R}_{iz}'' \right)^2 \frac{\cos^2 \vartheta}{(R_z''/R_x'')^2 \cos^2 \phi \sin^2 \vartheta + (R_z''/R_y'')^2 \sin^2 \phi \sin^2 \vartheta + \cos^2 \vartheta} - 1 \right]. \quad (2.51)$$

Subsequently, for the radial integral we apply the identity [140, (6.574.2)]

$$\int_0^\infty dt J_\nu(\alpha t) J_\mu(\alpha t) t^{-\lambda} = \frac{\alpha^{\lambda-1} \Gamma(\lambda) \Gamma\left(\frac{\nu+\mu-\lambda+1}{2}\right)}{2\lambda \Gamma\left(\frac{-\nu+\mu+\lambda+1}{2}\right) \Gamma\left(\frac{\nu+\mu+\lambda+1}{2}\right) \Gamma\left(\frac{\nu-\mu+\lambda+1}{2}\right)}, \quad \text{for } \text{Re}(\nu + \mu + 1) > \text{Re}(\lambda) > 0, \alpha > 0. \quad (2.52)$$

Together with Equation (2.17) for the conserved number of particles and using auxiliary functions and the generalized anisotropy function  $F_A$ , defined in Appendix B by Equations (B.6)-(B.8) and (B.15), respectively, we obtain

$$E_{\text{dd}}^{\text{D}} = -\frac{6N^2 c_0}{\bar{R}''^3} \left[ \left( \sum_i \mathbb{R}_{iz} \mathbb{R}_{ix}'' \right)^2 f\left(\frac{R_y''}{R_x''}, \frac{R_z''}{R_x''}\right) + \left( \sum_i \mathbb{R}_{iz} \mathbb{R}_{iy}'' \right)^2 f\left(\frac{R_x''}{R_y''}, \frac{R_z''}{R_y''}\right) + \left( \sum_i \mathbb{R}_{iz} \mathbb{R}_{iz}'' \right)^2 f\left(\frac{R_x''}{R_z''}, \frac{R_y''}{R_z''}\right) \right] = -\frac{6N^2 c_0}{\bar{R}''^3} F_A\left(\frac{R_x''}{R_z''}, \frac{R_y''}{R_z''}, \theta, \varphi, \theta'', \varphi''\right). \quad (2.53)$$

Here  $c_0$  is a constant related to the DDI strength, defined as

$$c_0 = \frac{2^{10} C_{\text{dd}}}{3^4 \cdot 5 \cdot 7 \cdot \pi^3}. \quad (2.54)$$

## 2.2.4 Fock energy

The Fock energy term is the most complex of the four energy terms, but it is still possible to analytically evaluate it by using the Fourier transformation. The idea is to switch the space and momentum variables of the Wigner functions via the two Fourier transformations, such that the Fock term can be rewritten in the following form

$$\begin{aligned} E_{\text{ex}} &= -\frac{1}{2} \int d^3r \int d^3r' \int \frac{d^3k}{(2\pi)^3} \int \frac{d^3k'}{(2\pi)^3} V_{\text{dd}}(\mathbf{r}') e^{i(\mathbf{k}-\mathbf{k}')\cdot\mathbf{r}'} \nu^0(\mathbf{r}, \mathbf{k}) \nu^0(\mathbf{r}, \mathbf{k}') \\ &= -\frac{1}{2} \int d^3r' \int \frac{d^3k'}{(2\pi)^3} \int \frac{d^3k''}{(2\pi)^3} \bar{\nu}^0(\mathbf{k}'', \mathbf{r}') \bar{\nu}^0(-\mathbf{k}'', -\mathbf{r}') \tilde{V}_{\text{dd}}(\mathbf{k}') e^{i\mathbf{r}'\cdot\mathbf{k}'}, \end{aligned} \quad (2.55)$$

where  $\tilde{\nu}^0(\mathbf{k}', \mathbf{k})$  denotes the Fourier transform of  $\nu^0(\mathbf{r}, \mathbf{k})$  with respect to the first variable and  $\bar{\nu}^0(\mathbf{r}, \mathbf{r}')$  the Fourier transformation with respect to the second variable. The order of the calculation of the integrals is determined by the interaction potential. Therefore, the first step is to calculate these two Fourier transforms of the Wigner function. We calculated  $\tilde{\nu}^0$  during calculation of the Hartree energy term, and result is given by Equation (2.44). Using this, we have

$$\begin{aligned} \bar{\nu}^0(-\mathbf{k}'', \mathbf{r}) &= \int \frac{d^3k}{(2\pi)^3} e^{i\mathbf{k}\cdot\mathbf{r}} \tilde{\nu}^0(-\mathbf{k}'', \mathbf{k}) = \int \frac{d^3q}{(2\pi)^3} e^{i\mathbf{q}\cdot\mathbb{R}'^T\mathbf{r}} \tilde{\nu}^0(-\mathbf{k}'', \mathbb{R}'\mathbf{q}) \\ &= \int \frac{d^3q}{(2\pi)^{\frac{3}{2}}} e^{i\mathbf{q}\cdot\mathbf{c}'} \frac{\bar{R}''^3 \left(1 - \sum_l \frac{q_l^2}{K_l'^2}\right)^{\frac{3}{4}} \text{H}\left(1 - \sum_j \frac{q_j^2}{K_j'^2}\right)}{g(\mathbf{k}'')^{\frac{3}{4}}} J_{\frac{3}{2}} \left[ \left(1 - \sum_m \frac{q_m^2}{K_m'^2}\right)^{\frac{1}{2}} g(\mathbf{k}'')^{\frac{1}{2}} \right], \end{aligned} \quad (2.56)$$

where  $g(\mathbf{k}'') = c_x''^2 R_x''^2 + c_y''^2 R_y''^2 + c_z''^2 R_z''^2$ ,  $\mathbf{c}'' = \mathbb{R}''^T \mathbf{k}''$  and  $\mathbf{c}' = \mathbb{R}'^T \mathbf{r}$ . The three  $q$ -integrals can be treated in the same way, so we compute here just the  $q_z$ -integral, to illustrate the procedure. This integral can be simplified, as before, since the Heaviside step function is non-zero only in the range  $|q_z| \leq q_z^{\text{max}} = K_z' \sqrt{1 - \frac{q_x^2}{K_x'^2} - \frac{q_y^2}{K_y'^2}}$ , which, together with rescaling  $q_z = q_z^{\text{max}} \cos \vartheta$ , yields

$$\begin{aligned} \bar{\nu}^0(-\mathbf{k}'', \mathbf{r}) &= \frac{\bar{R}''^3}{(2\pi)^{\frac{3}{2}}} \frac{1}{g(\mathbf{k}'')^{\frac{3}{4}}} \int dq_x dq_y e^{ic'_x q_x + ic'_y q_y} \text{H}\left(1 - \frac{q_x^2}{K_x'^2} - \frac{q_y^2}{K_y'^2}\right) \left(1 - \frac{q_x^2}{K_x'^2} - \frac{q_y^2}{K_y'^2}\right)^{\frac{5}{4}} \\ &\quad \times 2 \int_0^{\frac{\pi}{2}} d\vartheta \sin^{\frac{5}{2}} \vartheta K_z' \cos(c'_z q_z^{\text{max}} \cos \vartheta) J_{\frac{3}{2}} \left[ \frac{g(\mathbf{k}'')^{\frac{1}{2}} q_z^{\text{max}}}{K_z'} \sin \vartheta \right]. \end{aligned} \quad (2.57)$$

After this substitution, the  $\vartheta$ -integral can be calculated using Equation (2.43).

As already mentioned,  $q_x$ - and  $q_y$ -integral can be solved in the same way, so that

the Fourier transform  $\bar{\nu}^0$  reads

$$\bar{\nu}^0(-\mathbf{k}'', \mathbf{r}) = \frac{\bar{R}''^3 \bar{K}''^3 J_3 \left[ \left( g(\mathbf{k}'') + c_z'^2 K_z'^2 + c_y'^2 K_y'^2 + c_x'^2 K_x'^2 \right)^{\frac{1}{2}} \right]}{\left( g(\mathbf{k}'') + c_z'^2 K_z'^2 + c_y'^2 K_y'^2 + c_x'^2 K_x'^2 \right)^{\frac{3}{2}}}. \quad (2.58)$$

It is clear that  $\bar{\nu}^0(\mathbf{k}'', \mathbf{r})$  is an even function in both arguments, which simplifies further calculations. The next step is to calculate the  $\mathbf{r}'$ -integral in Equation (2.55). To avoid the appearance of a quadratic Bessel function, we use its integral representation [140, (6.519.2.2)]

$$\int_0^{\frac{\pi}{2}} dt J_{2\nu}(2z \sin t) = \frac{\pi}{2} J_\nu^2(z), \quad \text{for } \text{Re } \nu > -\frac{1}{2}, \quad (2.59)$$

which leads to an integral of a Bessel function

$$\begin{aligned} & J_3^2 \left[ \left( c_x'^2 K_x'^2 + c_y'^2 K_y'^2 + c_z'^2 K_z'^2 + g(\mathbf{k}'') \right)^{\frac{1}{2}} \right] \\ &= \frac{2}{\pi} \int_0^{\frac{\pi}{2}} dt J_6 \left[ 2 \sin t \left( c_x'^2 K_x'^2 + c_y'^2 K_y'^2 + c_z'^2 K_z'^2 + g(\mathbf{k}'') \right)^{\frac{1}{2}} \right]. \end{aligned} \quad (2.60)$$

Using this and a substitution  $\kappa' = \mathbb{R}'^T k'$ , the  $\mathbf{r}'$ -integral becomes

$$\begin{aligned} & \int d^3 r' \bar{\nu}^{02}(\mathbf{k}'', \mathbf{r}') e^{i\mathbf{k}' \cdot \mathbf{r}'} = \int d^3 r'' \bar{\nu}^0(\mathbf{k}'', \mathbb{R}' \mathbf{r}'')^2 e^{i\mathbf{k}' \cdot (\mathbb{R}' \mathbf{r}'')} = \int d^3 r'' \bar{\nu}^0(\mathbf{k}'', \mathbb{R}' \mathbf{r}'')^2 e^{i(\mathbb{R}'^T \mathbf{k}')^T \cdot \mathbf{r}''} \\ &= \int d^3 r' \frac{\bar{R}''^6 \bar{K}''^6 e^{i\kappa'_x r'_x + i\kappa'_y r'_y + i\kappa'_z r'_z}}{\left( r_x''^2 K_x'^2 + r_y''^2 K_y'^2 + r_z''^2 K_z'^2 + g(\mathbf{k}'') \right)^3} J_3^2 \left[ \left( r_x''^2 K_x'^2 + r_y''^2 K_y'^2 + r_z''^2 K_z'^2 + g(\mathbf{k}'') \right)^{\frac{1}{2}} \right] \\ &= \int dr_x'' dr_y'' dr_z'' \frac{\bar{R}''^6 \bar{K}''^6 e^{i\kappa'_x r'_x + i\kappa'_y r'_y + i\kappa'_z r'_z}}{\left( r_x''^2 K_x'^2 + r_y''^2 K_y'^2 + r_z''^2 K_z'^2 + g(\mathbf{k}'') \right)^3} \\ & \quad \times \frac{2}{\pi} \int_0^{\frac{\pi}{2}} dt J_6 \left[ 2 \sin t \left( r_x''^2 K_x'^2 + r_y''^2 K_y'^2 + r_z''^2 K_z'^2 + g(\mathbf{k}'') \right)^{\frac{1}{2}} \right], \end{aligned} \quad (2.61)$$

We again separately solve all three integrals, starting with the  $z''$ -integral. In order to evaluate it, we use the substitution  $u_z = r_z'' K_z'$ , as well as identities [140, (6.726.2)]

$$\begin{aligned} & \int_0^\infty dx (x^2 + b^2)^{-\frac{1}{2}\nu} J_\nu \left( a\sqrt{x^2 + b^2} \right) \cos(cx) = \sqrt{\frac{\pi}{2}} \frac{(a^2 - c^2)^{\frac{1}{2}\nu - \frac{1}{4}}}{a^\nu b^{\nu - \frac{1}{2}}} J_{\nu - \frac{1}{2}} \left( b\sqrt{a^2 - c^2} \right), \\ & \quad \text{for } 0 < c < a, b > 0, \text{Re } \nu > -\frac{1}{2}, \\ & \int_0^\infty dx (x^2 + b^2)^{-\frac{1}{2}\nu} J_\nu \left( a\sqrt{x^2 + b^2} \right) \cos(cx) = 0, \\ & \quad \text{for } 0 < a < c, b > 0, \text{Re } \nu > -\frac{1}{2}. \end{aligned} \quad (2.62)$$

After the integration over  $r_z''$  Equation (2.61) reads

$$\begin{aligned} \bar{R}''^6 \bar{K}''^6 \int dr''_x dr''_y e^{i\kappa'_x r''_x + i\kappa'_y r''_y} \frac{4}{\pi K'_z} \int_0^{\frac{\pi}{2}} dt \frac{\left(4 \sin^2 t - \frac{\kappa_z'^2}{K_z'^2}\right)^{\frac{11}{4}} \text{H}\left(2 \sin t - \sqrt{\frac{\kappa_z'^2}{K_z'^2}}\right)}{(2 \sin t)^6 \left(r_x''^2 K_x'^2 + r_y''^2 K_y'^2 + g(\mathbf{k}'')\right)^{\frac{11}{4}}} \\ \times \sqrt{\frac{\pi}{2}} J_{\frac{11}{2}} \left[ \left(4 \sin^2 t - \frac{\kappa_z'^2}{K_z'^2}\right)^{\frac{1}{2}} \left(r_x''^2 K_x'^2 + r_y''^2 K_y'^2 + g(\mathbf{k}'')\right)^{\frac{1}{2}} \right]. \end{aligned} \quad (2.63)$$

The Heaviside function in the last equation ensures that both possible solutions of Equation (2.62) are included when needed. The other two integrals are calculated in the same way, and therefore the solution of the  $\mathbf{r}'$ -integral is

$$\begin{aligned} \int d^3 r' \bar{V}^{02}(\mathbf{k}'', \mathbf{r}') e^{i\mathbf{k}'' \cdot \mathbf{r}'} = \left(\frac{\pi}{2^7}\right)^{\frac{1}{2}} \bar{R}''^6 \bar{K}''^3 \int_0^{\frac{\pi}{2}} \frac{dt}{\sin^6 t} \frac{\left(4 \sin^2 t - \sum_j \frac{\kappa_j'^2}{K_j'^2}\right)^{\frac{9}{4}}}{g(\mathbf{k}'')^{\frac{9}{4}}} \\ \times J_{\frac{9}{2}} \left[ g(\mathbf{k}'')^{\frac{1}{2}} \left(4 \sin^2 t - \sum_j \frac{\kappa_j'^2}{K_j'^2}\right)^{\frac{1}{2}} \right] \text{H}\left(2 \sin t - \sqrt{\sum_j \frac{\kappa_j'^2}{K_j'^2}}\right). \end{aligned} \quad (2.64)$$

The next step is to compute the  $\mathbf{k}''$ -integral. Using substitution  $u_i = \kappa'_i/K'_i$  and then transforming these new integration variables into spherical coordinates, one can use the identity [140, (6.561.17)]

$$\int_0^\infty \frac{J_\nu(ax)}{x^{\nu-q}} dx = \frac{\Gamma\left(\frac{1}{2}q + \frac{1}{2}\right)}{2^{\nu-q} a^{\nu-q+1} \Gamma\left(\nu - \frac{1}{2}q + \frac{1}{2}\right)}, \quad \text{for } -1 < \text{Re } q < \text{Re } \nu - \frac{1}{2}, \quad (2.65)$$

which leads to

$$\begin{aligned} I(\mathbf{k}') = \int d^3 k'' \int d^3 r' \bar{V}^{02}(\mathbf{k}'', \mathbf{r}') e^{i\mathbf{k}' \cdot \mathbf{r}'} \\ = \frac{\pi^2 \bar{R}''^3 \bar{K}''^3}{192} \int_0^{\frac{\pi}{2}} \frac{dt}{\sin^6 t} \left(4 \sin^2 t - \sum_j \frac{\kappa_j'^2}{K_j'^2}\right)^3 \text{H}\left(2 \sin t - \sqrt{\sum_j \frac{\kappa_j'^2}{K_j'^2}}\right). \end{aligned} \quad (2.66)$$

The last step of the Fock energy term calculation is to solve the  $\mathbf{k}'$ -integral, and therefore we again switch to another coordinate system by  $\mathbf{k}' = \mathbb{R}' \mathbf{q}$ , such that

$$\begin{aligned} E_{\text{dd}}^E = -\frac{1}{2(2\pi)^6} \int d^3 k' I(\mathbf{k}') \tilde{V}_{\text{dd}}(\mathbf{k}') = -\frac{1}{2(2\pi)^6} \int d^3 q I(\mathbb{R}' \mathbf{q}) \tilde{V}_{\text{dd}}(\mathbb{R}' \mathbf{q}) \\ = \frac{C_{\text{dd}} \bar{R}''^3 \bar{K}''^3}{73728\pi^4} \int d^3 q \int_0^{\frac{\pi}{2}} \frac{dt}{\sin^6 t} \left(4 \sin^2 t - \frac{q_x^2}{K_x'^2} - \frac{q_y^2}{K_y'^2} - \frac{q_z^2}{K_z'^2}\right)^3 \\ \times \text{H}\left(2 \sin t - \sqrt{\frac{q_x^2}{K_x'^2} + \frac{q_y^2}{K_y'^2} + \frac{q_z^2}{K_z'^2}}\right) \left[\frac{3(\sum_{i,j} \mathbb{R}_{zi}^T \mathbb{R}'_{ij} q_j)^2}{q^2} - 1\right], \end{aligned} \quad (2.67)$$

where we also use the Fourier transform of the DDI potential given by Equation (1.31). Due to the symmetry, such that all terms linear in  $q_j$  vanish, the above expression becomes

$$E_{\text{dd}}^E = -\frac{C_{\text{dd}}\bar{R}''^3\bar{K}'^3}{73728\pi^4} \int d^3q \int_0^{\frac{\pi}{2}} \frac{dt}{\sin^6 t} \left( 4\sin^2 t - \frac{q_x^2}{K_x'^2} - \frac{q_y^2}{K_y'^2} - \frac{q_z^2}{K_z'^2} \right)^3 \\ \times \text{H} \left( 2\sin t - \sqrt{\frac{q_x^2}{K_x'^2} + \frac{q_y^2}{K_y'^2} + \frac{q_z^2}{K_z'^2}} \right) \left[ \frac{3\sum_j(\sum_i \mathbb{R}_{zi}^T \mathbb{R}'_{ij})q_j^2}{q^2} - 1 \right]. \quad (2.68)$$

Using a substitution  $u_i = q_i/K'_i$  and afterwards switching to spherical coordinates, we get

$$E_{\text{dd}}^E = -\frac{C_{\text{dd}}\bar{R}''^3\bar{K}'^3}{73728\pi^4} \int_0^{2\pi} d\phi \int_0^\pi d\vartheta \sin\vartheta \int_0^{\frac{\pi}{2}} \frac{dt}{\sin^6 t} \int_0^{2\sin t} du u^2 \left( 4\sin^2 t - u^2 \right)^3 \\ \times \left[ 3 \left( \sum_i \mathbb{R}_{zi}^T \mathbb{R}'_{ix} \right)^2 \frac{\sin^2\vartheta \cos^2\phi}{\cos^2\phi \sin^2\vartheta + (K'_y/K'_x)^2 \sin^2\phi \sin^2\vartheta + (K'_z/K'_x)^2 \cos^2\vartheta} \right. \\ + 3 \left( \sum_i \mathbb{R}_{zi}^T \mathbb{R}'_{iy} \right)^2 \frac{\sin^2\vartheta \sin^2\phi}{(K'_x/K'_y)^2 \cos^2\phi \sin^2\vartheta + \sin^2\phi \sin^2\vartheta + (K'_z/K'_y)^2 \cos^2\vartheta} \\ \left. + 3 \left( \sum_i \mathbb{R}_{zi}^T \mathbb{R}'_{iz} \right)^2 \frac{\cos^2\vartheta}{(K'_x/K'_z)^2 \cos^2\phi \sin^2\vartheta + (K'_y/K'_z)^2 \sin^2\phi \sin^2\vartheta + \cos^2\vartheta} - 1 \right]. \quad (2.69)$$

The  $\vartheta$ - and  $\phi$ -integrals lead to the auxiliary functions, which are defined by Equations (B.6)-(B.8) in Appendix B, and the  $u$ - and  $t$ -integral can be solved straightforward. By having in mind Equation (2.17) for the conserved number of particles, the expression for the Fock energy term finally reads

$$E_{\text{dd}}^E = \frac{6N^2c_0}{\bar{R}''^3} \left[ \left( \sum_i \mathbb{R}_{iz} \mathbb{R}'_{ix} \right)^2 f \left( \frac{K'_x}{K'_y}, \frac{K'_x}{K'_y} \right) + \left( \sum_i \mathbb{R}_{iz} \mathbb{R}'_{iy} \right)^2 f \left( \frac{K'_y}{K'_x}, \frac{K'_y}{K'_x} \right) \right. \\ \left. + \left( \sum_i \mathbb{R}_{iz} \mathbb{R}'_{iz} \right)^2 f \left( \frac{K'_z}{K'_x}, \frac{K'_z}{K'_y} \right) \right] = \frac{6N^2c_0}{\bar{R}''^3} F_A \left( \frac{K'_z}{K'_x}, \frac{K'_z}{K'_y}, \theta, \varphi, \theta', \varphi' \right), \quad (2.70)$$

where  $c_0$  is constant given by Equation (2.54), and  $F_A(x, y, \theta, \varphi, \theta', \varphi')$  generalized anisotropy function given by Equation (B.15).

In both Hartree and Fock energy terms the features of the DDI are embodied into the generalized anisotropy function  $F_A(x, y, \theta, \varphi, \theta'', \varphi'')$  that includes explicitly the angular dependence of the DDI.

### 2.2.5 Total energy for all scenarios

The total energy of the many-body dipolar Fermi system has the following form

$$E_{\text{tot}} = E_{\text{kin}} + E_{\text{trap}} + E_{\text{dd}}^{\text{D}} + E_{\text{dd}}^{\text{E}}, \quad (2.71)$$

which, together with Equations (2.30), (2.35), (2.53), and (2.70), gives the total energy of the system in the most general off-off-axis scenario we consider,

$$E_{\text{tot}}^{(4)} = \frac{N}{8} \left( \sum_i \frac{\hbar^2 K_i'^2}{2M} + \sum_{i,j} \frac{M\omega_i^2 \mathbb{R}_{ij}''^2 R_j''^2}{2} \right) - \frac{6N^2 c_0}{R_x'' R_y'' R_z''} \\ \times \left[ F_A \left( \frac{R_x''}{R_z''}, \frac{R_y''}{R_z''}, \theta, \varphi, \theta'', \varphi'' \right) - F_A \left( \frac{K'_z}{K'_x}, \frac{K'_z}{K'_y}, \theta, \varphi, \theta', \varphi' \right) \right]. \quad (2.72)$$

Now, knowing the total energy for the most general ansatz, we are able to reconstruct expressions for the total energy of the system for any of the earlier mentioned scenarios.

In the case of the off-on-axis scenario 3, we allow for both the FS deformation and its rotation, as depicted in Figure 2.1(c), while the axes of the gas cloud ellipsoid remain parallel to the trap axes, as illustrated in Figure 2.1(e). In this case, the total energy of the system reads as

$$E_{\text{tot}}^{(3)} = \frac{N}{8} \sum_j \left( \frac{\hbar^2 K_j'^2}{2M} + \frac{M\omega_j^2 R_j^2}{2} \right) - \frac{6N^2 c_0}{R_x'' R_y'' R_z''} \\ \times \left[ f_A \left( \frac{R_x''}{R_z''}, \frac{R_y''}{R_z''}, \theta, \varphi \right) - F_A \left( \frac{K'_z}{K'_x}, \frac{K'_z}{K'_y}, \theta, \varphi, \theta'', \varphi'' \right) \right]. \quad (2.73)$$

Here  $f_A(x, y, \theta, \varphi) = F_A(x, y, \theta, \varphi, 0^\circ, 0^\circ)$  which can be expressed as

$$f_A(x, y, \theta, \varphi) = \mathbb{R}_{xz}^2 f\left(\frac{y}{x}, \frac{1}{x}\right) + \mathbb{R}_{yz}^2 f\left(\frac{x}{y}, \frac{1}{y}\right) + \mathbb{R}_{zz}^2 f(x, y), \quad (2.74)$$

where  $f(x, y)$  stands for the well-known anisotropy function derived, at first, for dipolar bosons[141]. Note that  $f(x, y) = f_A(x, y, 0^\circ, 0^\circ) = F_A(x, y, 0^\circ, 0^\circ, 0^\circ, 0^\circ)$ . This function is encountered also in previous studies of fermionic dipolar systems [92] in the hydrodynamic collisional regime, as well as in the transition from the collisionless to the hydrodynamic regime in both the TOF expansion dynamics [125] and in collective excitations [126]. More details on the anisotropy function  $f$  and its generalizations  $f_A$  and  $F_A$  are given in Appendix B.

In the on-on-axis scenario 2, the FS is deformed to an ellipsoid whose axes are

taken to be parallel to the trap axes, as depicted in Figure 2.1(b). This ansatz leads to the total energy of the system given by

$$E_{\text{tot}}^{(2)} = \frac{N}{8} \sum_j \left( \frac{\hbar^2 K_j^2}{2M} + \frac{M\omega_j^2 R_j^2}{2} \right) - \frac{6N^2 c_0}{R_x R_y R_z} \times \left[ f_A \left( \frac{R_x}{R_z}, \frac{R_y}{R_z}, \theta, \varphi \right) - f_A \left( \frac{K_z}{K_x}, \frac{K_z}{K_y}, \theta, \varphi \right) \right]. \quad (2.75)$$

Note that the energy (2.73) of the scenario 3 reduces, indeed, to expression (2.75) for the special case  $\theta' = \varphi' = 0$ .

In the spherical scenario, the total energy of the system can be calculated by setting  $K_i = K_F$  in the ansatz (2.7), where the Fock exchange energy term turns out to give no contribution, yielding

$$E_{\text{tot}}^{(1)} = \frac{N}{8} \left( \frac{3\hbar^2 K_F^2}{2M} + \sum_j \frac{M\omega_j^2 R_j^2}{2} \right) - \frac{6N^2 c_0}{R^3} f_A \left( \frac{R_x}{R_z}, \frac{R_y}{R_z}, \theta, \varphi \right). \quad (2.76)$$

Note that the energy (2.75) of the scenario 2 reduces, indeed, to energy (2.76) of the spherical scenario for the special case  $K_x = K_y = K_z = K_F$ , since  $f_A(1, 1, \theta, \varphi) = 0$ , as a consequence of  $f(1, 1) = 0$ .

## 2.3 Minimization of the total energy

Having obtained the total energy for all four scenarios, we now determine which configuration minimizes best the system's total energy for a fixed particle number and, hence, can be considered as the most physically suitable ansatz for the ground state of the system of dipolar fermions. Afterwards, we use it in Chapter 3 to numerically calculate the FS and the gas cloud deformation due to the DDI.

We proceed by considering expressions (2.76), (2.75), (2.73), and (2.72), and by minimizing the energy of the system for each scenario under the constraint that the particle number  $N$  is fixed to a given value. Therefore, the corresponding equations are obtained by extremizing the grand-canonical potential  $\Omega^{(k)} = E_{\text{tot}}^{(k)} - \mu N^{(k)}$  for  $k = 1, 2, 3, 4$  with respect to the variational parameters, where  $\mu$  is the chemical potential of the system, and the particle number  $N^{(k)}$  in the last term is replaced by one of the corresponding expressions (2.10), (2.12), (2.15) or (2.17) when  $\Omega^{(k)}$  is evaluated. In this way, the chemical potential acts as a Lagrange multiplier and fixes the particle number through the condition  $N^{(k)} = -\partial\Omega^{(k)}/\partial\mu$ . Therefore,  $\mu$  represents

an additional variational parameter in this approach.

In the spherical scenario, there are five variational parameters,  $(K_F, R_i, \mu)$ , where  $i = x, y, z$ . The corresponding five equations are obtained by setting the first derivatives of  $\Omega^{(1)}$  with respect to  $K_F$  and  $R_i$  to zero, plus the particle-number fixing equation, i.e.,  $N^{(1)} = -\partial\Omega^{(1)}/\partial\mu$ . The sets of equations for other scenarios are obtained similarly as in the previous case, just the number of equations differ. Namely, in the on-on-axis scenario we have seven variational parameters,  $(K_i, R_i, \mu)$ , in the off-on-axis scenario nine  $(K'_i, R_i, \theta', \varphi', \mu)$ , while in the off-off-axis scenario there are eleven parameters,  $(K'_i, R''_i, \theta', \varphi', \theta'', \varphi'', \mu)$ . The complete sets of equations for the respective variational parameters for all cases are given in Appendix C, while in the following section we give the detailed derivation of these equations for the most general ansatz considered in the off-off-axis scenario.

### 2.3.1 Variational parameters in momentum space

A minimization of the grand-canonical potential  $\Omega^{(4)} = E_{\text{tot}}^{(4)} - \mu N^{(4)}$  with respect to the Fermi momenta  $K'_i$  leads to following three equations,

$$\frac{N\hbar^2 K'_x}{8M} - \frac{6N^2 c_0}{\bar{R}''^3} \frac{K'_z}{K'_x} F_{A,1} \left( \frac{K'_z}{K'_x}, \frac{K'_z}{K'_y}, \theta, \varphi, \theta', \varphi' \right) - \frac{\mu}{48} \bar{R}''^3 K'_y K'_z = 0, \quad (2.77)$$

$$\frac{N\hbar^2 K'_y}{8M} - \frac{6N^2 c_0}{\bar{R}''^3} \frac{K'_z}{K'_y} F_{A,2} \left( \frac{K'_z}{K'_x}, \frac{K'_z}{K'_y}, \theta, \varphi, \theta', \varphi' \right) - \frac{\mu}{48} \bar{R}''^3 K'_x K'_z = 0, \quad (2.78)$$

$$\begin{aligned} \frac{N\hbar^2 K'_z}{8M} + \frac{6N^2 c_0}{\bar{R}''^3} \frac{1}{K'_x} F_{A,1} \left( \frac{K'_z}{K'_x}, \frac{K'_z}{K'_y}, \theta, \varphi, \theta', \varphi' \right) \\ + \frac{6N^2 c_0}{\bar{R}''^3} \frac{1}{K'_y} F_{A,2} \left( \frac{K'_z}{K'_x}, \frac{K'_z}{K'_y}, \theta, \varphi, \theta', \varphi' \right) - \frac{\mu}{48} \bar{R}''^3 K'_x K'_z = 0, \end{aligned} \quad (2.79)$$

while additional two equations are obtained by minimizing  $\Omega^{(4)}$  with respect to the momentum space angles  $\theta'$  and  $\varphi'$ , which yields to

$$F_{A,5} \left( \frac{K'_z}{K'_x}, \frac{K'_z}{K'_y}, \theta, \varphi, \theta', \varphi' \right) = 0, \quad (2.80)$$

$$F_{A,6} \left( \frac{K'_z}{K'_x}, \frac{K'_z}{K'_y}, \theta, \varphi, \theta', \varphi' \right) = 0, \quad (2.81)$$

where abbreviations  $F_{A,a}$  denote the derivatives of  $F_A$  with respect to its  $a$ -th argument, where  $1 \leq a \leq 6$ . Equations (2.77)–(2.79) depend explicitly on the Lagrange multiplier  $\mu$ . In order to determine it, we sum up those three equations, so that all terms containing the anisotropy function cancel each other, which leads to the following

expression for chemical potential,

$$\mu = \frac{1}{12} \sum_j \frac{\hbar^2 K_j'^2}{2M}. \quad (2.82)$$

Inserting this into Equations (2.77)–(2.79) leads to the following equations for the parameters  $K_j'$  in the global equilibrium, which do not include  $\mu$ ,

$$\frac{\hbar^2 K_x'^2}{2M} = \frac{1}{3} \sum_j \frac{\hbar^2 K_j'^2}{2M} + \frac{24N^2 c_0}{\bar{R}''^3} \frac{K_z'}{K_x'} F_{A,1} \left( \frac{K_z'}{K_x'}, \frac{K_z'}{K_y'}, \theta, \varphi, \theta', \varphi' \right), \quad (2.83)$$

$$\frac{\hbar^2 K_y'^2}{2M} = \frac{1}{3} \sum_j \frac{\hbar^2 K_j'^2}{2M} + \frac{24N^2 c_0}{\bar{R}''^3} \frac{K_z'}{K_y'} F_{A,2} \left( \frac{K_z'}{K_x'}, \frac{K_z'}{K_y'}, \theta, \varphi, \theta', \varphi' \right), \quad (2.84)$$

$$\begin{aligned} \frac{\hbar^2 K_z'^2}{2M} &= \frac{1}{3} \sum_j \frac{\hbar^2 K_j'^2}{2M} - \frac{24N^2 c_0}{\bar{R}''^3} \frac{K_z'}{K_x'} F_{A,1} \left( \frac{K_z'}{K_x'}, \frac{K_z'}{K_y'}, \theta, \varphi, \theta', \varphi' \right) \\ &\quad - \frac{24N^2 c_0}{\bar{R}''^3} \frac{K_z'}{K_y'} F_{A,2} \left( \frac{K_z'}{K_x'}, \frac{K_z'}{K_y'}, \theta, \varphi, \theta', \varphi' \right). \end{aligned} \quad (2.85)$$

Equations (2.80) and (2.81) can be solved analytically, independently of other equations, yielding the physically expected result,

$$\theta' = \theta \quad \text{and} \quad \varphi' = \varphi. \quad (2.86)$$

This means that the FS stretches along the dipoles' orientation, as it was observed experimentally and verified theoretically for the atomic erbium gas [49]. Here we obtain this result self-consistently within our approach [50], which demonstrates that ansatz (2.7) properly captures the ground-state properties of dipolar Fermi gases.

Note that Equations (2.83)–(2.85) are linearly dependent, but clearly show the influence of the DDI on the momentum distribution in phase space. By considering the symmetries of the total energy (2.72), one can obtain a simple relation between the variational parameters  $K_x'$  and  $K_y'$ . As a consequence of Equation (2.86), the generalized anisotropy function satisfies  $F_A(x, y, \theta, \varphi, \theta, \varphi) = f(x, y)$ , and due to the symmetry of the anisotropy function  $f(x, y) = f(y, x)$ , the total energy possesses the same symmetry between the  $q_x$  and  $q_y$  direction in momentum space in the system  $S'$ . This implies that the momentum distribution of a dipolar Fermi gas in global equilibrium remains cylindrically symmetric even in the case of a triaxial trap and an arbitrary orientation of the dipoles,

$$K_x' = K_y'. \quad (2.87)$$

This represent the generalization of the same conclusion obtained for the case when the dipoles are oriented along one of the trap axes [91, 92, 126]. Furthermore, Equation (2.87) enables us not only to estimate  $K'_y$ , but also simplify the equation for  $K'_z$  by taking into account that

$$\lim_{y \rightarrow x} x f_1(x, y) = \lim_{y \rightarrow x} y f_2(x, y) = -1 + \frac{(2 + x^2)f_s(x)}{2(1 - x^2)}, \quad (2.88)$$

where  $f_s(x) = f(x, x)$  denotes the cylindrically-symmetric anisotropy function, given by Equation (B.3). Subtracting Equation (2.83) from (2.85) and using the identity (2.88) we obtain

$$\frac{\hbar^2 K_z'^2}{2m} - \frac{\hbar^2 K_x'^2}{2m} = \frac{36N^2 c_0}{\bar{R}''^3} \left[ 1 + \frac{(2K_x'^2 + K_z'^2) f_s\left(\frac{K'_z}{K'_x}\right)}{2(K_z'^2 - K_x'^2)} \right]. \quad (2.89)$$

This equation directly gives the stretching of the FS due to the DDI.

### 2.3.2 Variational parameters in real space

The derivation of the equations which determine the real-space variational parameters that minimize the total energy is analogous to the calculation of the momentum-space parameters. Namely, minimization of  $\Omega^{(4)} = E_{\text{tot}}^{(4)} - \mu N^{(4)}$  with respect to the TF radii  $R_i''$  leads to

$$\begin{aligned} \frac{N}{8} M \sum_j \omega_j^2 \mathbb{R}_{jx}''^2 R_x'' + \frac{6N^2 c_0}{\bar{R}''^3} \frac{1}{R_x''} \left[ F_A \left( \frac{R_x''}{R_z''}, \frac{R_y''}{R_z''}, \theta, \varphi, \theta'', \varphi'' \right) - f_s \left( \frac{K'_z}{K'_x} \right) \right] \\ - \frac{6N^2 c_0}{\bar{R}''^3} \frac{1}{R_z''} F_{A,1} \left( \frac{R_x''}{R_z''}, \frac{R_y''}{R_z''}, \theta, \varphi, \theta'', \varphi'' \right) - \frac{\mu}{48} R_y'' R_z'' \bar{K}'^3 = 0, \end{aligned} \quad (2.90)$$

$$\begin{aligned} \frac{N}{8} M \sum_j \omega_j^2 \mathbb{R}_{jy}''^2 R_y'' + \frac{6N^2 c_0}{\bar{R}''^3} \frac{1}{R_y''} \left[ F_A \left( \frac{R_x''}{R_z''}, \frac{R_y''}{R_z''}, \theta, \varphi, \theta'', \varphi'' \right) - f_s \left( \frac{K'_z}{K'_x} \right) \right] \\ - \frac{6N^2 c_0}{\bar{R}''^3} \frac{1}{R_z''} F_{A,2} \left( \frac{R_x''}{R_z''}, \frac{R_y''}{R_z''}, \theta, \varphi, \theta'', \varphi'' \right) - \frac{\mu}{48} R_x'' R_z'' \bar{K}'^3 = 0, \end{aligned} \quad (2.91)$$

$$\begin{aligned} \frac{N}{8} M \sum_j \omega_j^2 \mathbb{R}_{jz}''^2 R_z'' + \frac{6N^2 c_0}{\bar{R}''^3} \frac{1}{R_z''} \left[ F_A \left( \frac{R_x''}{R_z''}, \frac{R_y''}{R_z''}, \theta, \varphi, \theta'', \varphi'' \right) - f_s \left( \frac{K'_z}{K'_x} \right) \right] \\ + \frac{6N^2 c_0}{\bar{R}''^3} \frac{R_x''}{R_z''^2} F_{A,1} \left( \frac{R_x''}{R_z''}, \frac{R_y''}{R_z''}, \theta, \varphi, \theta'', \varphi'' \right) \\ + \frac{6N^2 c_0}{\bar{R}''^3} \frac{R_x''}{R_z''^2} F_{A,2} \left( \frac{R_x''}{R_z''}, \frac{R_y''}{R_z''}, \theta, \varphi, \theta'', \varphi'' \right) - \frac{\mu}{48} R_x'' R_z'' \bar{K}'^3 = 0. \end{aligned} \quad (2.92)$$

As before, the additional two equations are obtained by minimizing  $\Omega^{(4)}$  with respect to the real-space angles  $\theta''$  and  $\varphi''$ , which yields

$$\begin{aligned} \frac{N}{8}M \left[ (\omega_x^2 - \omega_z^2) \cos^2 \varphi'' + (\omega_y^2 - \omega_z^2) \sin^2 \varphi'' \right] (R_z''^2 - R_x''^2) \sin \theta'' \cos \theta'' \\ - \frac{6Nc_0}{\bar{R}''^3} F_{A,5} \left( \frac{R_x''}{R_z''}, \frac{R_y''}{R_z''}, \theta, \varphi, \theta'', \varphi'' \right) = 0, \end{aligned} \quad (2.93)$$

$$\begin{aligned} \frac{N}{8}M(\omega_y^2 - \omega_x^2) \left[ (R_x''^2 - R_y''^2) \cos^2 \theta'' + (R_z''^2 - R_y''^2) \sin^2 \theta'' \right] \sin \varphi'' \cos \varphi'' \\ - \frac{6Nc_0}{\bar{R}''^3} F_{A,6} \left( \frac{R_x''}{R_z''}, \frac{R_y''}{R_z''}, \theta, \varphi, \theta'', \varphi'' \right) = 0. \end{aligned} \quad (2.94)$$

If we sum up Equations (2.90)–(2.92) in order to determine the Lagrange multiplier  $\mu$ , we get

$$\mu = \frac{1}{12} \sum_{i,j} \frac{M}{2} \omega_j^2 \mathbb{R}_{ji}''^2 R_i''^2 + \frac{6Nc_0}{\bar{R}''^3} \left[ F_A \left( \frac{R_x''}{R_z''}, \frac{R_y''}{R_z''}, \theta, \varphi, \theta'', \varphi'' \right) - f_s \left( \frac{K'_z}{K'_x} \right) \right]. \quad (2.95)$$

This formally differs from Equation (2.82) but represents a mathematically equivalent expression for  $\mu$  [118]. Inserting Equation (2.82) into Equations (2.90)–(2.92) yields

$$\begin{aligned} \sum_j \omega_j^2 \mathbb{R}_{jx}''^2 R_x'' + \frac{48N^2c_0}{M\bar{R}''^3} \frac{1}{R_x''} \left[ F_A \left( \frac{R_x''}{R_z''}, \frac{R_y''}{R_z''}, \theta, \varphi, \theta'', \varphi'' \right) - f_s \left( \frac{K'_z}{K'_x} \right) \right] \\ - \frac{48N^2c_0}{M\bar{R}''^3} \frac{1}{R_z''} F_{A,1} \left( \frac{R_x''}{R_z''}, \frac{R_y''}{R_z''}, \theta, \varphi, \theta'', \varphi'' \right) - \frac{1}{3} \sum_j \frac{\hbar^2 K_j'^2}{M^2} = 0, \end{aligned} \quad (2.96)$$

$$\begin{aligned} \sum_j \omega_j^2 \mathbb{R}_{jy}''^2 R_y'' + \frac{48N^2c_0}{M\bar{R}''^3} \frac{1}{R_y''} \left[ F_A \left( \frac{R_x''}{R_z''}, \frac{R_y''}{R_z''}, \theta, \varphi, \theta'', \varphi'' \right) - f_s \left( \frac{K'_z}{K'_x} \right) \right] \\ - \frac{48N^2c_0}{M\bar{R}''^3} \frac{1}{R_z''} F_{A,2} \left( \frac{R_x''}{R_z''}, \frac{R_y''}{R_z''}, \theta, \varphi, \theta'', \varphi'' \right) - \frac{1}{3} \sum_j \frac{\hbar^2 K_j'^2}{M^2} = 0, \end{aligned} \quad (2.97)$$

$$\begin{aligned} \sum_j \omega_j^2 \mathbb{R}_{jz}''^2 R_z'' + \frac{48N^2c_0}{M\bar{R}''^3} \frac{1}{R_z''} \left[ F_A \left( \frac{R_x''}{R_z''}, \frac{R_y''}{R_z''}, \theta, \varphi, \theta'', \varphi'' \right) - f_s \left( \frac{K'_z}{K'_x} \right) \right] \\ + \frac{48N^2c_0}{M\bar{R}''^3} \frac{R_x''}{R_z''^2} F_{A,1} \left( \frac{R_x''}{R_z''}, \frac{R_y''}{R_z''}, \theta, \varphi, \theta'', \varphi'' \right) \\ + \frac{48N^2c_0}{M\bar{R}''^3} \frac{R_y''}{R_z''^2} F_{A,2} \left( \frac{R_x''}{R_z''}, \frac{R_y''}{R_z''}, \theta, \varphi, \theta'', \varphi'' \right) - \frac{1}{3} \sum_j \frac{\hbar^2 K_j'^2}{M^2} = 0, \end{aligned} \quad (2.98)$$

Note that in the case of a spherically symmetric trap, Equations (2.93) and (2.94) can be solved analytically, independently of other equations, yielding  $\theta'' = \theta$  and  $\varphi'' = \varphi$ .

### 2.3.3 Comparing all scenarios

In order to compare the four ansätze, we solve the corresponding sets of equations and calculate the total energy of the system in each case. As a model system, we first consider the case of a dipolar Fermi gas of atomic  $^{167}\text{Er}$  using typical values from the Innsbruck experiments (see below and also Reference [48]),  $N = 6.6 \times 10^4$  atoms,  $(\omega_x, \omega_y, \omega_z) = (579, 91, 611) \times 2\pi$  Hz. The underlying geometry of the experimental setup is depicted in Figure 2.2.

In Figure 2.3 we compare the total energy of the system as a function of angles  $\theta$  and  $\varphi$  for all four different scenarios. The comparison is done in terms of the relative energy shift

$$\delta E = \frac{E_{\text{tot}}}{E_0} - 1, \quad (2.99)$$

where  $E_0 = \frac{3}{4}NE_F$  stands for the total energy of the ideal Fermi gas confined into a harmonic trap (1.16), and  $E_F$  denotes its Fermi energy given by Equation (1.20). Figure 2.3(a) presents the relative energy shifts as functions of the angle  $\theta$  for a fixed value of the angle  $\varphi = 14^\circ$ , corresponding to the typical experimental configuration (see Section 5.3). The three curves, from top to bottom, correspond to  $\delta E^{(1)}$ ,  $\delta E^{(2)}$ , and  $\delta E^{(3)}$ , respectively. As a cross-check, we note that the total energies  $E_{\text{tot}}^{(2)}$  and  $E_{\text{tot}}^{(3)}$  coincide for  $\theta = 0^\circ$ . This is expected, since the on-on-axis scenario is a special case

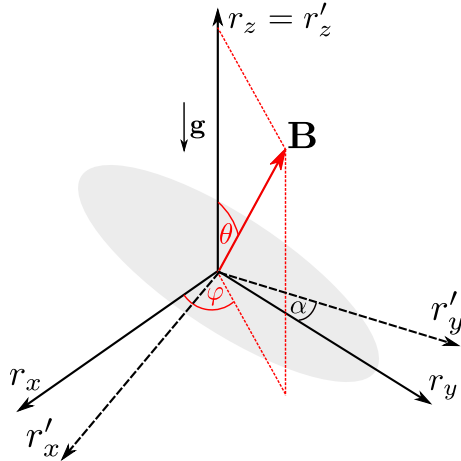


**Figure 2.2:** Schematic illustration of the most general arbitrary geometry of a dipolar Fermi gas, which corresponds to the one used in the Innsbruck experiment with erbium atoms, see later and also Reference [48]. Axes  $r_x, r_y, r_z$  indicate the harmonic trap axes. The external magnetic field  $\mathbf{B}$  defines the orientation of the atomic dipoles, which is given by the spherical coordinates  $\theta$  and  $\varphi$ . Earth’s gravitational field is parallel to the  $z$  axis. The imaging axis, denoted by  $r'_y$ , lies in the  $r_x r_y$  plane, and forms an angle  $\alpha$  with the  $r_y$  axis.

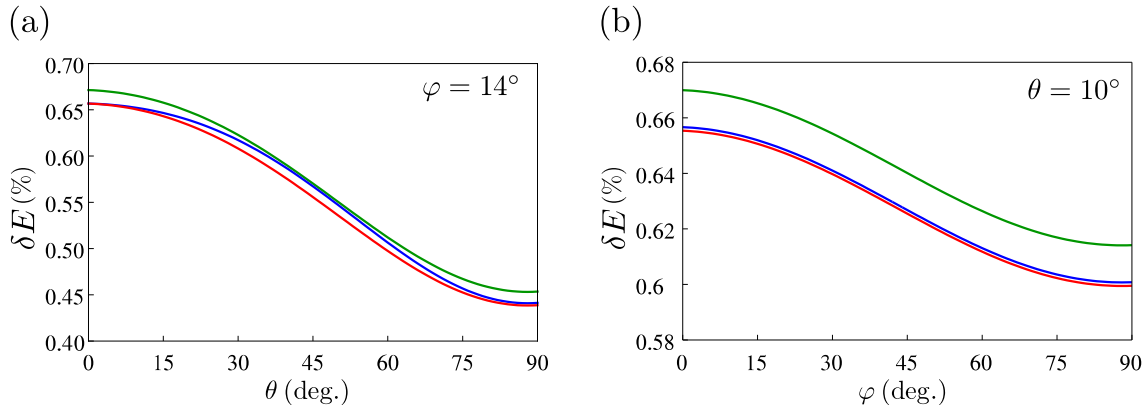


**Figure 2.3:** Relative energy shift  $\delta E$  given by Equation (2.99) for Er atoms for experimental parameters of Reference [48] as a function of: (a) angle  $\theta$ , for fixed  $\varphi = 14^\circ$ ; (b) angle  $\varphi$  for fixed  $\theta = 10^\circ$ . The three curves correspond to  $\delta E^{(1)}$  (green line, spherical scenario),  $\delta E^{(2)}$  (blue line, on-on-axis scenario), and  $\delta E^{(3)}$  (red line, off-on-axis scenario).

of the off-on-axis one for  $\theta = 0^\circ$ . From this Figure we immediately see that there are no intersections between the curves, and that it always holds  $E_{\text{tot}}^{(1)} \geq E_{\text{tot}}^{(2)} \geq E_{\text{tot}}^{(3)}$ . As a consequence, we conclude that the off-on-axis scenario, in which the FS is deformed into an ellipsoid that follows the orientation of the dipoles, is favoured among the considered cases as it has the minimal energy. The same conclusion is obtained if we consider the  $\varphi$ -dependence of the relative total energy shifts, depicted in Figure 2.3(b) for a fixed value of the angle  $\theta = 10^\circ$ .

Comparing Figures 2.3(a) and 2.3(b) we see that the relative energy shift always remains small, of the order of 0.4 – 0.7%, due to a relatively weak DDI between the erbium atoms compared to the energy scale set by the Fermi energy. We also see that the  $\theta$ -dependence of the total energy is much stronger than the corresponding  $\varphi$ -dependence. Furthermore, numerical calculations show that for these parameters  $E_{\text{tot}}^{(4)} \approx E_{\text{tot}}^{(3)}$ , and there is no significant difference between the off-on-axis and off-off-axis scenarios. Actually, it turns out that off-on-axis scenario is certainly justified for elongated traps and a weak-enough DDI, for which the cloud shape in the ground state is well determined by the trap. More exhaustive numerical calculations show that this remains to be true even for arbitrary values of the angles  $\theta$  and  $\varphi$ , trap frequencies, as well as number of fermions.

In order to emphasize the difference between the off-on-axis and off-off-axis scenarios, we now consider molecular  $^{40}\text{K}^{87}\text{Rb}$  gas with  $N = 7 \times 10^4$  fermions with the electric dipoles of  $d = 0.25$  D in the spherically symmetric trap with  $\omega_i = 500 \times 2\pi$  Hz. In this case the relative energy shifts as functions of the angle  $\theta$  for a fixed value of the angle

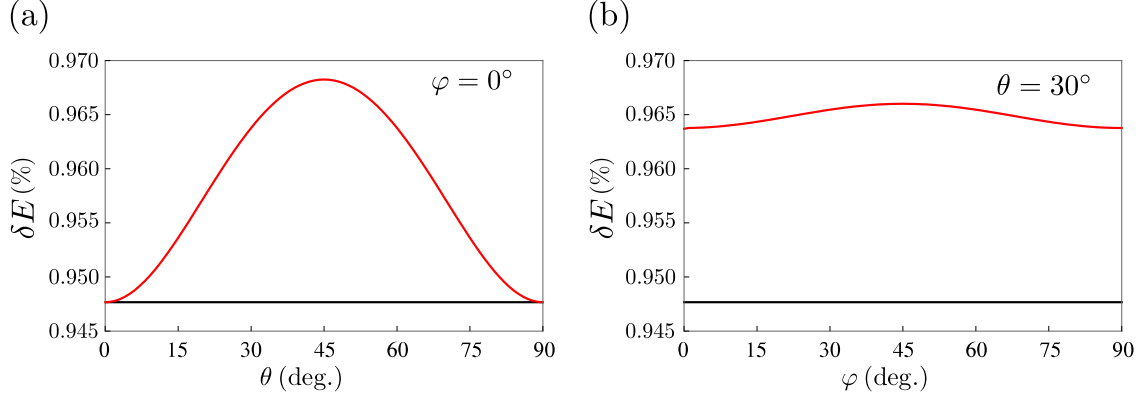


**Figure 2.4:** Relative total energy shift  $\delta E$  given by Equation (2.99) for  $N = 7 \times 10^4$  KRb molecules with electric dipoles of  $d = 0.25$  D trapped in spherical trap with  $\omega_i = 500 \times 2\pi$  Hz as a function of: (a) angle  $\theta$ , for fixed  $\varphi = 0^\circ$ ; (b) angle  $\varphi$  for fixed  $\theta = 30^\circ$ . The two curves, correspond to  $\delta E^{(3)}$  (red line, off-on-axis scenario), and  $\delta E^{(4)}$  (black line, off-off-axis scenario).

$\varphi = 14^\circ$  are shown in Figure 2.4(a). The two curves, from top to bottom, correspond to  $\delta E^{(3)}$ , and  $\delta E^{(4)}$ , respectively. As a cross-check, we note that the total energies  $E_{\text{tot}}^{(3)}$  and  $E_{\text{tot}}^{(4)}$  coincide for  $\theta = 0^\circ$ , which is expected, since the off-on-axis scenario is a special case of the off-off-axis one for  $\theta = 0^\circ$ . From this Figure we again see that there are no intersections between the curves, and that it always holds  $E_{\text{tot}}^{(3)} \geq E_{\text{tot}}^{(4)}$ . As a consequence, we conclude that the off-off-axis scenario, in which the FS, as well as, the gas cloud are deformed into an ellipsoid that follows the orientation of the dipoles, is favored among the considered cases as it has the minimal total energy. The same conclusion is obtained if we consider the  $\varphi$ -dependence of the relative total energy shift, depicted in Figure 2.4(b) for a fixed value of the angle  $\theta = 30^\circ$ .

The above conclusion is valid not only for the parameters used in Figure 2.4, but, in fact, we have numerically verified that the off-off-axis scenario for the ansatz (2.7) for the Wigner function in global equilibrium always yields a minimal energy given by expression (2.72) for arbitrary angles  $\theta$  and  $\varphi$ , trap frequencies, as well as number of fermions. Thus, we will use it throughout this Thesis as a realistic model for the description of a dipolar Fermi gas at zero temperature.

---

## Ground state properties

---

Degenerate Fermi gases in the normal phase are well described by the Fermi liquid theory, which was formulated by Landau in 1950s. Due to the Pauli exclusion principle, the ground state of  $N$  fermions consists of  $N$  lowest fully occupied momentum states, which is termed the Fermi sea. In the Fermi liquid picture, excitations can be matched to quasiparticles populating any states in the Fermi sea with the same spin, charge and momentum as the original particles, but with the mass and interaction that are dressed by the interaction with the whole gas. Weak excitations then correspond to quasiparticle states close to the Fermi surface, a surface in  $k$ -space that separates occupied states in the Fermi sea from non-occupied ones. For isotropically interacting fermions, which is the commonly encountered case, the Fermi surface is a sphere, while it can get modified in the case of more complex interactions. For instance, for dipolar Fermi gases it was predicted that the DDI leads in equilibrium to an anisotropic deformation of the Fermi surface from a sphere to an ellipsoid [90]. A recent time-of-flight expansion experiment has unambiguously detected such an ellipsoidal FS deformation in a fermionic erbium gas, which turns out to be of the order of a few percent [48]. It was shown that the FS deformation arises purely due to the dipolar interactions and the quantum statistics of the particles.

In the previous Chapter we have presented the generalized Hartree-Fock mean-field theory, while here we present our main results for the system's stability, the FS deformation, as well as for the gas cloud deformation. We discuss the DDI dependence of the variational parameters and their impact on the Hartree-Fock total energy for the considered system. We also study in detail the ground-state properties for an arbitrary orientation of the dipoles, as well as for different parameters of the system,

e.g., trap frequencies, number of particles, and dipolar species.

The stability of normal and quantum degenerate dipolar Fermi gases was previously considered in cylindrically symmetric harmonic traps [91–94, 118, 119], as well as in homogeneous systems [139]. Here, we study the ground state stability of ultracold dipolar Fermi gases in triaxial harmonic traps and reveal a universal behavior of the critical DDI strength using a variational phase-space approach based on the Wigner function [49, 50, 125, 126]. In particular, we investigate the stability of a polarized  $^{40}\text{K}^{87}\text{Rb}$  gas in an experimentally realistic parameter regime and calculate critical values of the electric dipole moment and the corresponding deformation of the FS. Furthermore, we obtain stability diagrams for an arbitrary orientation of the dipoles and for an angular dependence of the FS deformation. We consider the system to be at zero temperature, which is justified if we consider that  $T/T_F \approx 0.3$  in the experiments [109], and that the thermal corrections to the total energy are proportional to  $(T/T_F)^2$  [142].

The approach presented here is very general and can be applied to both fermionic atoms and molecules with electric [98, 99, 143, 144] or magnetic [89] dipole moments arbitrary oriented, and any triaxial trap geometry. Our calculation provides a starting point to address more complex dipolar phenomena. Indeed, many physical properties depend on the shape of the FS and on its deformation, as the FS is directly connected to the density distribution in momentum space. For instance, our theory can serve as a solid basis for understanding and interpreting phenomena in future experiments with dipolar fermionic gases, where the investigated physics depends on the underlying structure of the FS, such as transport properties or fermionic pairing and superfluidity. Namely, the possibility of Cooper pairing in a polarized one-component Fermi gas of dipolar particles was already predicted a few years ago [41], but initial studies have neglected the deformation of the FS [42–45]. The first work to combine these initial theoretical approaches towards achieving dipolar fermionic superfluidity with ellipsoidal deformation of the FS in a form of the self-consistent Hartree-Fock-Bogoliubov theory of dipolar uniform Fermi gases is Reference [46]. The comprehensive mean-field approach presented in this Reference can be extended to the superfluid pairing in a harmonic confinement with the most general trap and the dipoles' geometry. Such investigation would address important questions on how the anisotropic order parameter of the emergent superfluidity and its critical temperature can be tuned by both the trap geometry and the dipoles' orientation.

Since the large DDI increases the critical temperature [43, 46], all our results pre-

sented here are relevant for the realization of the dipolar fermionic superfluidity.

### 3.1 Dimensionless form of static equations

As it was shown in Section 2.3.1 and summarized in Appendix C, if we eliminate the angles  $\theta', \varphi'$  and set  $\theta' = \theta, \varphi' = \varphi$  in all equations, the system is described by the 9 variational parameters  $(R_i'', K_i', \theta'', \varphi'', \mu)$ , which are obtained by solving the set of Equations (C.32)–(C.31). Our aim is to understand effects of the DDI on the system, so it is natural to express the TF radii  $R_i''$  and momenta  $K_i'$  in units of noninteracting quantities,  $R_i^0$  and  $K_F^0$ , illustrated in Figures 2.1(a) and 2.1(d), and given by Equations (1.21) and (1.22), respectively. In this way all equations are transformed into a dimensionless form, where the dimensionless radii and momenta are defined by  $\tilde{R}_i'' = R_i''/R_i^0$  and  $\tilde{K}_i' = K_i'/K_F^0$ , and the set of Equations (C.32)–(C.31) can be written as

$$1 - \tilde{R}_x'' \tilde{R}_y'' \tilde{R}_z'' \tilde{K}_x' \tilde{K}_y' \tilde{K}_z' = 0, \quad (3.1)$$

$$\tilde{K}_x' - \tilde{K}_y' = 0, \quad (3.2)$$

$$2\tilde{K}_x'^2 - \tilde{K}_y'^2 - \tilde{K}_z'^2 + \frac{3\varepsilon_{\text{dd}}c_{\text{d}}}{\tilde{R}_x'' \tilde{R}_y'' \tilde{R}_z''} \frac{\tilde{K}_z'}{\tilde{K}_z'} \partial_{\tilde{K}_x'} f \left( \frac{\tilde{K}_z'}{\tilde{K}_x'}, \frac{\tilde{K}_z'}{\tilde{K}_y'} \right) = 0, \quad (3.3)$$

$$\begin{aligned} & \sum_i \frac{\omega_i^2}{\omega_x^2} \mathbb{R}_{ix}'' \tilde{R}_x'' - \frac{1}{3} \sum_i \tilde{K}_i'^2 + \frac{\varepsilon_{\text{dd}}c_{\text{d}}}{\tilde{R}_x'' \tilde{R}_y'' \tilde{R}_z''} F_A \left( \frac{\tilde{R}_x'' \omega_z}{\tilde{R}_z'' \omega_x}, \frac{\tilde{R}_y'' \omega_z}{\tilde{R}_z'' \omega_y}, \theta, \varphi, \theta'', \varphi'' \right) \\ & + \frac{\varepsilon_{\text{dd}}c_{\text{d}}}{\tilde{R}_x'' \tilde{R}_y'' \tilde{R}_z''} \left[ -f \left( \frac{\tilde{K}_z'}{\tilde{K}_x'}, \frac{\tilde{K}_z'}{\tilde{K}_y'} \right) - \tilde{R}_x'' \partial_{\tilde{R}_x''} F_A \left( \frac{\tilde{R}_x'' \omega_z}{\tilde{R}_z'' \omega_x}, \frac{\tilde{R}_y'' \omega_z}{\tilde{R}_z'' \omega_y}, \theta, \varphi, \theta'', \varphi'' \right) \right] = 0, \quad (3.4) \end{aligned}$$

$$\begin{aligned} & \sum_i \frac{\omega_i^2}{\omega_y^2} \mathbb{R}_{iy}'' \tilde{R}_y'' - \frac{1}{3} \sum_i \tilde{K}_i'^2 + \frac{\varepsilon_{\text{dd}}c_{\text{d}}}{\tilde{R}_x'' \tilde{R}_y'' \tilde{R}_z''} F_A \left( \frac{\tilde{R}_x'' \omega_z}{\tilde{R}_z'' \omega_x}, \frac{\tilde{R}_y'' \omega_z}{\tilde{R}_z'' \omega_y}, \theta, \varphi, \theta'', \varphi'' \right) \\ & + \frac{\varepsilon_{\text{dd}}c_{\text{d}}}{\tilde{R}_x'' \tilde{R}_y'' \tilde{R}_z''} \left[ -f \left( \frac{\tilde{K}_z'}{\tilde{K}_x'}, \frac{\tilde{K}_z'}{\tilde{K}_y'} \right) - \tilde{R}_y'' \partial_{\tilde{R}_y''} F_A \left( \frac{\tilde{R}_x'' \omega_z}{\tilde{R}_z'' \omega_x}, \frac{\tilde{R}_y'' \omega_z}{\tilde{R}_z'' \omega_y}, \theta, \varphi, \theta'', \varphi'' \right) \right] = 0, \quad (3.5) \end{aligned}$$

$$\begin{aligned} & \sum_i \frac{\omega_i^2}{\omega_z^2} \mathbb{R}_{iz}'' \tilde{R}_z'' - \frac{1}{3} \sum_i \tilde{K}_i'^2 + \frac{\varepsilon_{\text{dd}}c_{\text{d}}}{\tilde{R}_x'' \tilde{R}_y'' \tilde{R}_z''} F_A \left( \frac{\tilde{R}_x'' \omega_z}{\tilde{R}_z'' \omega_x}, \frac{\tilde{R}_y'' \omega_z}{\tilde{R}_z'' \omega_y}, \theta, \varphi, \theta'', \varphi'' \right) \\ & + \frac{\varepsilon_{\text{dd}}c_{\text{d}}}{\tilde{R}_x'' \tilde{R}_y'' \tilde{R}_z''} \left[ -f \left( \frac{\tilde{K}_z'}{\tilde{K}_x'}, \frac{\tilde{K}_z'}{\tilde{K}_y'} \right) - \tilde{R}_z'' \partial_{\tilde{R}_z''} F_A \left( \frac{\tilde{R}_x'' \omega_z}{\tilde{R}_z'' \omega_x}, \frac{\tilde{R}_y'' \omega_z}{\tilde{R}_z'' \omega_y}, \theta, \varphi, \theta'', \varphi'' \right) \right] = 0, \quad (3.6) \end{aligned}$$

$$\sum_{i,j} \frac{\omega_i^2}{\omega_j^2} \mathbb{R}_{ij}'' \partial_{\theta''} \mathbb{R}_{ij}'' \tilde{R}_j'' - \frac{\varepsilon_{\text{dd}}c_{\text{d}}}{\tilde{R}_x'' \tilde{R}_y'' \tilde{R}_z''} \partial_{\theta''} F_A \left( \frac{\tilde{R}_x'' \omega_z}{\tilde{R}_z'' \omega_x}, \frac{\tilde{R}_y'' \omega_z}{\tilde{R}_z'' \omega_y}, \theta, \varphi, \theta'', \varphi'' \right) = 0, \quad (3.7)$$

$$\sum_{i,j} \frac{\omega_i^2}{\omega_j^2} \mathbb{R}_{ij}'' \partial_{\varphi''} \mathbb{R}_{ij}'' \tilde{R}_j'' - \frac{\varepsilon_{\text{dd}}c_{\text{d}}}{\tilde{R}_x'' \tilde{R}_y'' \tilde{R}_z''} \partial_{\varphi''} F_A \left( \frac{\tilde{R}_x'' \omega_z}{\tilde{R}_z'' \omega_x}, \frac{\tilde{R}_y'' \omega_z}{\tilde{R}_z'' \omega_y}, \theta, \varphi, \theta'', \varphi'' \right) = 0, \quad (3.8)$$

where  $c_d = \frac{2^{38}}{3^{23} \cdot 5 \cdot 7 \cdot \pi^2}$  is a number and

$$\varepsilon_{\text{dd}} = \frac{d^2}{4\pi\varepsilon_0} \sqrt{\frac{M^3}{\hbar^5}} (\omega_x \omega_y \omega_z N)^{1/6}, \quad (3.9)$$

represents the dimensionless relative DDI strength, which gives a rough estimate of the ratio between the mean dipolar interaction energy and the Fermi energy [11, 122]. We use this quantity to characterize the strength of the DDI when comparing its effects for different species.

The set of Equations (3.1)–(3.8) represents a remarkable result and reveals a universality governing the ground-state properties of dipolar Fermi gases. The universality is reflected in the species-independent form of those equations: for a given orientation of the dipoles, they only depend on three parameters, namely the two trap aspect ratios  $\omega_z/\omega_x$  and  $\omega_z/\omega_y$ , and the relative DDI strength  $\varepsilon_{\text{dd}}$ . Furthermore, this allows us to determine the universal stability diagram of the system, which is, for instance, crucial for the design of new experiments with polar molecules, in particular in the strong dipolar regime.

Before we analyze in detail the effects on the DDI on ground state properties, such as stability of the system, and the FS and the gas cloud deformation, we present one illustrative example. Namely, Figure 3.1 depicts the aspect ratios of corresponding TF radii and momenta of stable solutions in global equilibrium for the dipolar Fermi gases given in Table 3.1. These results are obtained for the dipoles oriented in the direction of the  $z$  axis, i.e., for angles  $\theta = \varphi = 0^\circ$ , see Figure 1.3(b). For the limiting case of a noninteracting Fermi gas we know that the aspect ratios in real space become  $R_x/R_z \rightarrow R_x^0/R_z^0 = \omega_z/\omega_x$  and  $R_y/R_z \rightarrow R_y^0/R_z^0 = \omega_z/\omega_y$ , while in momentum space the Fermi surface becomes the Fermi sphere and therefore we have  $K_x/K_z \rightarrow K_F^0/K_F^0 = 1$ .

**Table 3.1:** Dipole moments ( $m$  for species with a magnetic dipole and  $d$  for species with an electric dipole) and the corresponding relative interaction strengths of fermionic atoms and molecules to be used throughout the Thesis, calculated using the parameters of the Innsbruck experiments [48],  $N = 6.6 \times 10^4$ ,  $(\omega_x, \omega_y, \omega_z) = (579, 91, 611) \times 2\pi$  Hz.

gas	$^{53}\text{Cr}$ [85]	$^{167}\text{Er}$ [84]	$^{161}\text{Dy}$ [83]	$^{40}\text{K}^{87}\text{Rb}$ [98]	$^{167}\text{Er}^{168}\text{Er}$ [89]
$m/d$	$6 \mu_B$	$7 \mu_B$	$10 \mu_B$	0.2 D	$14 \mu_B$
$\varepsilon_{\text{dd}}$	0.02	0.15	0.30	0.97	1.76

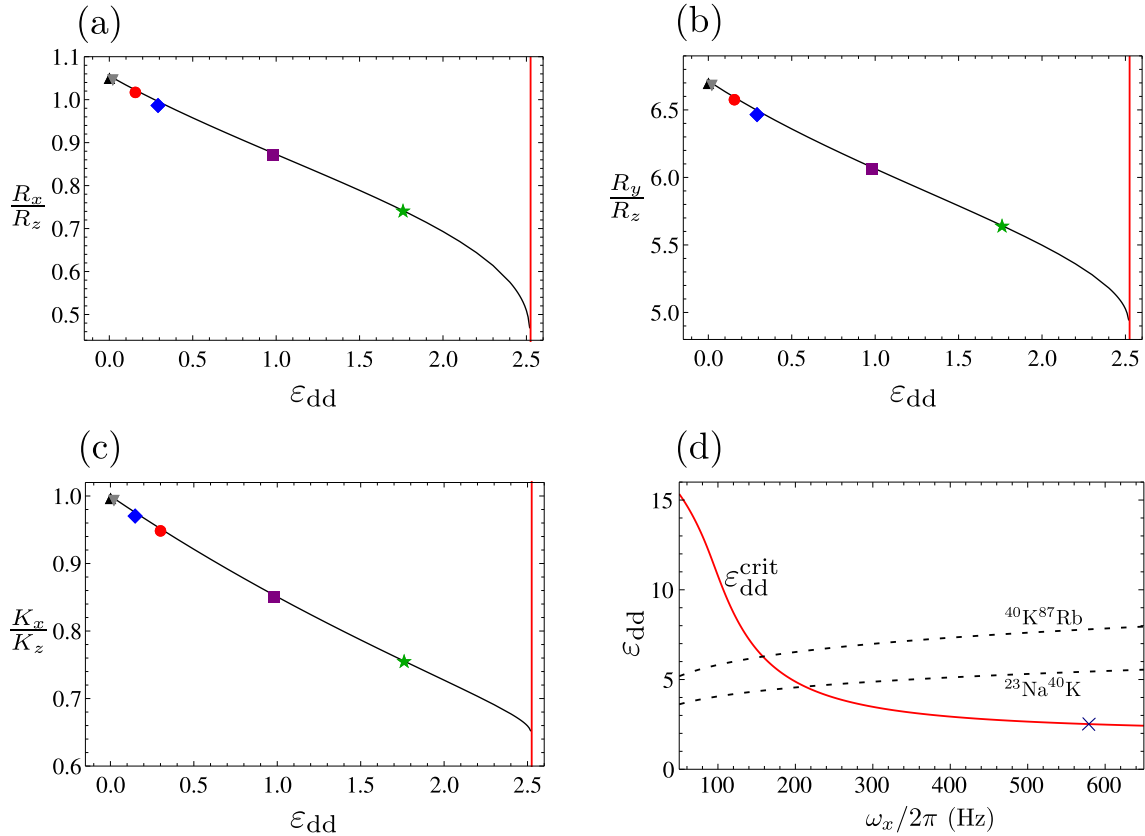


**Figure 3.1:** Aspect ratios in real and momentum space as functions of relative dipolar interaction strength  $\epsilon_{dd}$  for Fermi gases in global equilibrium for considered trap geometry with dipoles parallel to  $z$  axis: (a)  $R_x/R_z$ , (b)  $R_y/R_z$ , and (c)  $K_x/K_z$ . Black up-pointing triangles represent aspect ratios for the limiting case of a noninteracting Fermi gas: in real space  $R_x/R_z = \omega_z/\omega_x$  and  $R_y/R_z = \omega_z/\omega_y$ , while in momentum space  $K_x/K_z = 1$  (Fermi sphere). Other symbols represent aspect ratios for dipolar atoms and molecules from Table 3.1:  $^{53}\text{Cr}$  (gray down-pointing triangles),  $^{167}\text{Er}$  (red circles),  $^{161}\text{Dy}$  (blue diamonds),  $^{40}\text{K}^{87}\text{Rb}$  (purple squares),  $^{167}\text{Er}^{168}\text{Er}$  (green stars). Red vertical line corresponds to a critical value of the relative dipolar interaction strength  $\epsilon_{dd}^{\text{crit}} \approx 2.52$  for considered trap geometry; for  $\epsilon_{dd} > \epsilon_{dd}^{\text{crit}}$  no stable stationary solution exists for a system of Equations (3.1)–(3.8). (d) Critical value of relative dipolar interaction strength  $\epsilon_{dd}^{\text{crit}}$  (red solid line) as function of trap frequency  $\omega_x$  for fixed values  $(\omega_y, \omega_z) = (91, 611) \times 2\pi$  Hz and particle number  $N = 7 \times 10^4$ . Blue cross corresponds to experimental value of frequency  $\omega_x = 579 \times 2\pi$  Hz from the Innsbruck experiment [48], for which  $\epsilon_{dd}^{\text{crit}} \approx 2.52$ . Black dashed lines depict relative dipolar interaction strength  $\epsilon_{dd}$  for dipolar molecular species  $^{23}\text{Na}^{40}\text{K}$  and  $^{40}\text{K}^{87}\text{Rb}$  according to Equation (3.9), for the same parameters and for maximal values of their electric dipole moments given in Table 1.1.

Red vertical lines in Figures 3.1(a)–(c) represent a critical value of the relative interaction strength  $\epsilon_{dd}^{\text{crit}} \approx 2.52$  for the considered trap geometry. Namely, for  $\epsilon_{dd} > \epsilon_{dd}^{\text{crit}}$  stable stationary solutions for Equations (3.1)–(3.8) do not exist [92, 119] for the considered system parameters from the Innsbruck experiment [48]. Note that the value

of  $\varepsilon_{\text{dd}}^{\text{crit}}$  does not depend on the mass of the species and is universal for a given trap geometry and a number of fermions, as stressed above.

It turns out that electric dipolar molecules  $^{23}\text{Na}^{40}\text{K}$  and  $^{40}\text{K}^{87}\text{Rb}$  with the largest values of the relative DDI strength  $\varepsilon_{\text{dd}}$  are unstable for the considered system parameters if their maximal possible values of the permanent electric dipole moment (see Table 1.1) are used, since in both cases  $\varepsilon_{\text{dd}} > \varepsilon_{\text{dd}}^{\text{crit}}$ . However, by using an external electric field, their dipole moments can be tuned to smaller values, and therefore we will consider the case of  $^{40}\text{K}^{87}\text{Rb}$  with the value of electric dipole moment tuned down to  $d = 0.2\text{D}$  [86], for which one obtains  $\varepsilon_{\text{dd}} = 0.97 < \varepsilon_{\text{dd}}^{\text{crit}}$ . Table 3.1 gives the corresponding parameters of the five atomic and molecular dipolar species we consider in the rest of this Thesis.

In Figure 3.1 the aspect ratios in real and momentum space for the noninteracting case are shown as black up-pointing triangles, together with the corresponding aspect ratios for interacting Fermi gases listed in Table 3.1. For atomic gases of  $^{53}\text{Cr}$ ,  $^{167}\text{Er}$ , and  $^{161}\text{Dy}$  the DDI is not that strong, and their aspect ratios in momentum space deviate less than 5% from unity, see Figure 3.1(c). Actually, for  $^{53}\text{Cr}$  (gray down-pointing triangles) the aspect ratio in momentum space is just 1% smaller than 1, which would be quite challenging to observe in an experiment. Nevertheless, for  $^{167}\text{Er}$  (red circles) the aspect ratio in momentum space turns out to be about 3% less than 1 and has already been experimentally observed in Reference [48], which means that the 5% deformation for  $^{161}\text{Dy}$  (blue diamonds) should clearly be observable. For the considered parameters for  $^{40}\text{K}^{87}\text{Rb}$  (purple squares) with  $\varepsilon_{\text{dd}} = 0.97$  we obtain even larger value of the FS deformation of about 15%. Furthermore, a molecule of  $^{168}\text{Er}^{167}\text{Er}$  (green stars) with  $\varepsilon_{\text{dd}} = 1.76$  would yield the the aspect ratio in momentum space of nearly 25% smaller than 1.

Note that the critical value  $\varepsilon_{\text{dd}}^{\text{crit}}$  strongly depends on the trap geometry, as can be seen in Figure 3.1(d), where we show its dependence on the frequency  $\omega_x$  for fixed values of the trap frequencies  $(\omega_y, \omega_z) = (91, 611) \times 2\pi\text{ Hz}$ , motivated by the Innsbruck experiment [48]. For the corresponding experimental value  $\omega_x = 579 \times 2\pi\text{ Hz}$  we obtain  $\varepsilon_{\text{dd}}^{\text{crit}} \approx 2.52$  (blue cross), the same value that can be also deduced from Figure 3.1(a)-(c). In Figure 3.1(d) we also show relative DDI strength  $\varepsilon_{\text{dd}}$  for molecular species  $^{23}\text{Na}^{40}\text{K}$  and  $^{40}\text{K}^{87}\text{Rb}$  for maximal values of their electric dipole moments from Table 1.1. Note that the relative interaction strengths also depend on the trap geometry according to Equation (3.9). As already pointed out, for the cigar-shaped trap geometry of the Innsbruck experiment [48] both molecular species turn out to be

unstable. However, for the pancake-shaped trap with the sufficiently small value of the frequency  $\omega_x$ , i.e.,  $\omega_x < 210 \times 2\pi$  Hz for  $^{23}\text{Na}^{40}\text{K}$  and  $\omega_x < 155 \times 2\pi$  Hz for  $^{40}\text{K}^{87}\text{Rb}$ , both species can be made stable even if their maximal electric dipole moments are used.

## 3.2 Stability of the system

The energy of the system given by Equation (2.72) is not bounded from below, due to the fact that the DDI is partially attractive, meaning that the system cannot have a global minimum for any  $\varepsilon_{\text{dd}} > 0$ . However, for interactions weak enough, a local minimum might exist to which the system would return after a small perturbation. The regions of system parameters satisfying this property are called stable and the mathematical criterion used for this classification is given by positive eigenvalues of the Hessian matrix of the energy functional [92]. Such analysis allows us to determine the stability diagram of the system, shown in Figure 3.2(a) for the case when the dipoles are parallel to  $z$  axis ( $\theta = \varphi = 0^\circ$ ), in terms of the maximal DDI strength  $\varepsilon_{\text{dd}}^{\text{crit}}$  for which the ground state exists. We see that large aspect ratios significantly increase the critical DDI strength, for more than one order of magnitude, and thus stabilize the system in a much broader parameter range. This reflects the fact that a pancake-shaped gas cloud ( $\omega_x, \omega_y \ll \omega_z$ ) tends to allow for a larger  $\varepsilon_{\text{dd}}$  because it favors the repelling part of the interaction, in contrast to a cigar-shaped gas cloud ( $\omega_x, \omega_y \gg \omega_z$ ), when the attractive part of the interaction is dominant. We also note that  $\varepsilon_{\text{dd}}^{\text{crit}}$  turns out to be a symmetric function of its arguments  $\omega_z/\omega_x$  and  $\omega_z/\omega_y$ , which is a consequence of symmetry of anisotropy function  $F_A(x, y, 0, 0, 0, 0) = f(x, y) = f(y, x)$ .

If we consider the experimentally available species  $^{40}\text{K}^{87}\text{Rb}$ , the stability diagram from Figure 3.2(a) can be used to obtain a species-specific stability diagram for a particular value of one of the trap frequencies, as shown in Figures 3.2(b)-(d). Here we see how the critical value of the dipole moment  $d^{\text{crit}}$  depends on  $\omega_x$  and  $\omega_y$  for a fixed value of  $\omega_z$ . Taking into account that the permanent electric dipole moment of  $^{40}\text{K}^{87}\text{Rb}$  has the value  $d = 0.57$  D, denoted by black lines in Figures 3.2(b)-(d), we see that, for the trap frequencies which lie in the region below black lines, the system will be stable even for maximal values of electric dipole moments, while otherwise the system can be stabilized only by tuning the values of the electric dipoles below the calculated  $d^{\text{crit}}$ . For instance, we read off from Figure 3.2(b) that for  $\omega_z = 50 \times 2\pi$  Hz the instability can kick in already for frequencies  $\omega_x, \omega_y$  of that order or larger. In the

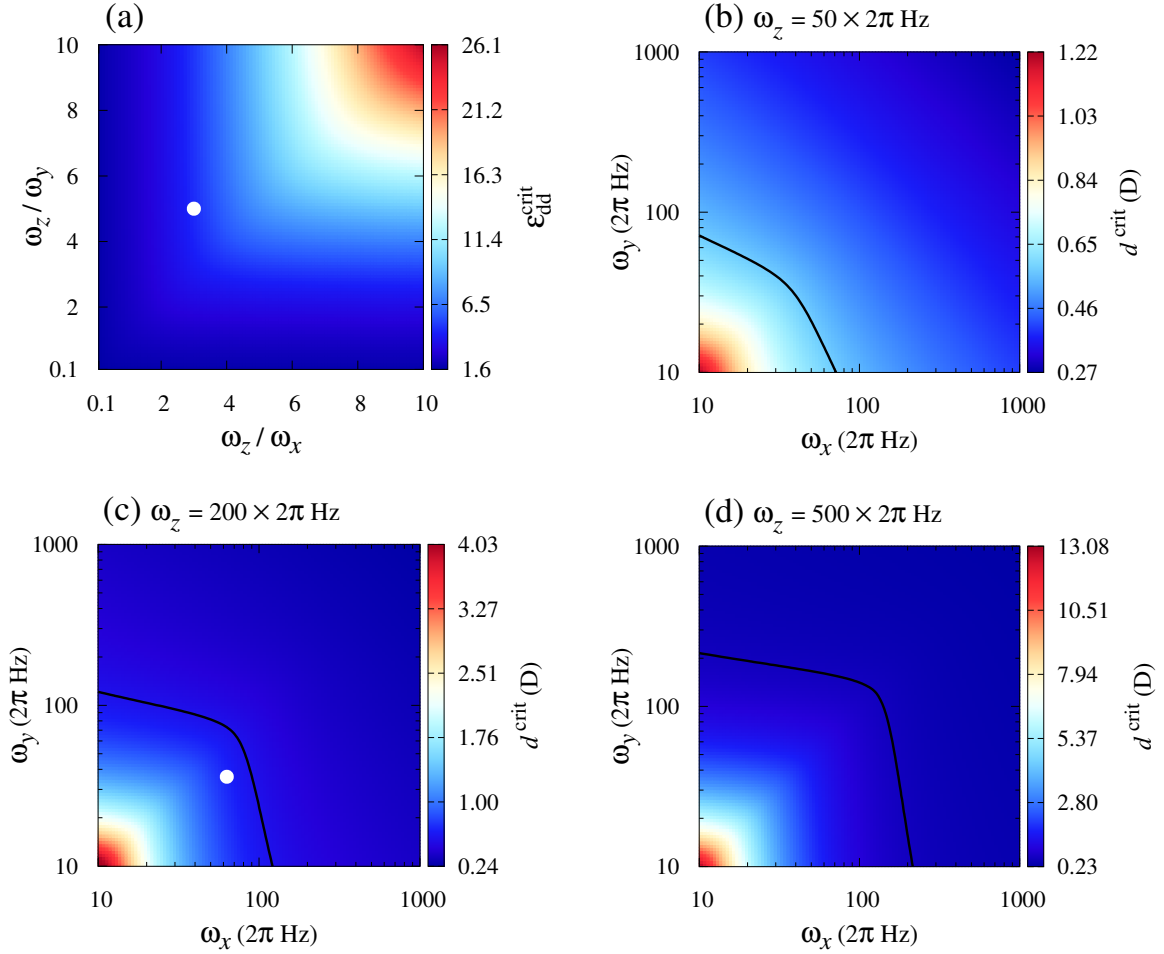


**Figure 3.2:** (a) A universal stability diagram for harmonically trapped ultracold dipolar Fermi gases at quantum degeneracy: critical value of the relative dipole-dipole interaction strength  $\epsilon_{\text{dd}}^{\text{crit}}$  as a function of the trap aspect ratios  $\omega_z/\omega_x$  and  $\omega_z/\omega_y$ , for the dipoles parallel to  $z$  axis. The system has a stable ground state for  $\epsilon_{\text{dd}} \leq \epsilon_{\text{dd}}^{\text{crit}}$ . (b), (c), (d) Critical value of the electric dipole moment  $d^{\text{crit}}$ , below which a stable ground state of  $N = 3 \times 10^4$  ultracold molecules of  $^{40}\text{K}^{87}\text{Rb}$  exists, as a function of the trap frequencies  $\omega_x$  and  $\omega_y$ , for: (b)  $\omega_z = 50 \times 2\pi$  Hz; (c)  $\omega_z = 200 \times 2\pi$  Hz; (d)  $\omega_z = 500 \times 2\pi$  Hz. The dipoles are oriented along  $z$  axis. The permanent dipole moment of  $^{40}\text{K}^{87}\text{Rb}$  molecules has a value of  $d = 0.57$  D, and can be fine-tuned by applying an external electric field. White dots on panels (a) and (c) correspond to the system parameters from the JILA experiment [109].

experiment of Reference [109] the frequencies used are  $(\omega_x, \omega_y, \omega_z) = (63, 36, 200) \times 2\pi$  Hz, and Figure 3.2(c) reveals that the system may easily become unstable for slightly larger frequencies if the dipoles would be polarized along  $z$  axis. In contrast to Figure 3.2(a), we now fix the frequencies to the values of the JILA experiment [109] and vary the direction of the dipoles. The angular-dependent stability diagram is shown in Figure 3.3(a), from which we can see that the critical DDI strength strongly depends on dipoles' orientation, defined by the polar angles  $\theta$  and  $\varphi$ . Furthermore,

in Figure 3.3(b) we show the corresponding stability diagram for the critical value of the dipole moment  $d^{\text{crit}}$  for  $^{40}\text{K}^{87}\text{Rb}$ , where black lines again correspond to the value of the permanent electric dipole moment. The angular dependence of  $d^{\text{crit}}$  suggests that the system's stability can be easily fine-tuned by changing the orientation of the dipoles, i.e., by rotating the external electric field. We note here that, due to the symmetry of the FS and gas cloud ellipsoids, to obtain angular dependence it is enough to investigate only the range  $\theta \in [0, 90^\circ]$  and  $\varphi \in [0, 90^\circ]$ . However, for completeness we will always present results for angular dependencies in a full interval range  $\theta \in [0, 180^\circ]$  and  $\varphi \in [0, 360^\circ]$ .

The orientation of the dipoles with respect to the harmonic trap affects not only the shape of the molecular cloud in real space, but also its orientation, as it is considered in the off-off-axis scenario. In order to illustrate this effect, in Figures 3.3(c) and 3.3(d) we present the results analog to the ones shown in Figures 3.3(a) and 3.3(b), but for the off-on-axis scenario, where we assume that the axes of the molecular cloud coincide with the axes of the trap ( $\theta' = \varphi' = 0$ ). These angular distributions are markedly different for both  $\varepsilon_{\text{dd}}^{\text{crit}}$  and  $d^{\text{crit}}$ , although the extreme, minimal and maximal, values are the same. As a consequence, the stability region is actually reduced when the off-off-axis scenario is applied, instead of the simplified off-on-axis scenario, which can be easily seen by comparing the areas between black lines in Figures 3.3(b) and 3.3(d). This is of particular importance for experiments with strong dipolar fermions, where the off-off-axis scenario is the only one that corresponds to the actual physics of the system.

### 3.3 Fermi surface deformation

Since we have shown analytically that the FS is deformed by the DDI into an ellipsoid, we study here this striking effect in more detail. Having in mind that the FS follows the orientation of the dipoles, which is proven by deriving Equation (2.86), and has a cylindrical symmetry in a plane perpendicular to the dipoles' orientation, see Figure 2.1(c) and Equation (2.87), we define the FS deformation as the difference between the momentum-space aspect ratio for the dipolar and for the noninteracting Fermi gas according to

$$\Delta = \frac{K'_z}{K'_x} - 1. \quad (3.10)$$

This quantity measures the degree of deformation, which emerges purely due to the DDI. We investigate how the deformation  $\Delta$  depends on and can be tuned by the

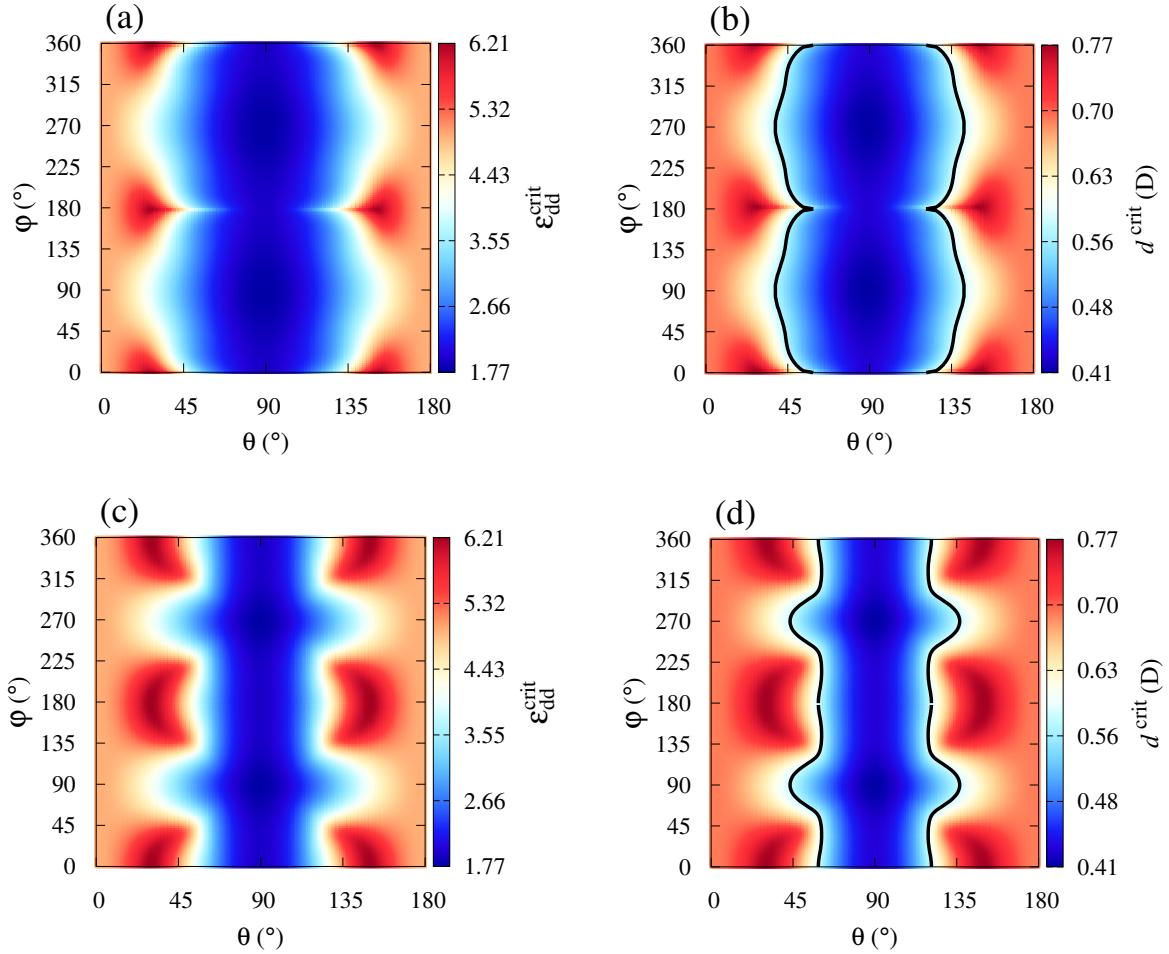


**Figure 3.3:** Angular stability diagram for harmonically trapped ultracold dipolar Fermi gases at quantum degeneracy: (a) and (c) critical value of the relative dipole-dipole interaction strength  $\varepsilon_{\text{dd}}^{\text{crit}}$  and (b) and (d) critical value of the electric dipole moment  $d^{\text{crit}}$  of  $^{40}\text{K}^{87}\text{Rb}$  as a function of the orientation of the dipoles, defined by the polar angles  $\theta$  and  $\varphi$ . Black lines correspond to the permanent electric dipole moment  $d = 0.57 \text{ D}$  of  $^{40}\text{K}^{87}\text{Rb}$ . Panels (a) and (b) correspond to off-off-axis scenario, while panels (c) and (d) correspond to off-on-axis-scenario. The system parameters correspond to the JILA experiment [109]:  $N = 3 \times 10^4$  molecules, trap frequencies  $(\omega_x, \omega_y, \omega_z) = (63, 36, 200) \times 2\pi \text{ Hz}$ .

the DDI strength, trap geometry, the orientation of the dipoles, and the number of particles.

We first calculate the FS deformation of  $^{167}\text{Er}$  for the parameters of the Innsbruck experiment [48], yielding the relative interaction strength  $\varepsilon_{\text{dd}} = 0.15$ . In Figure 3.4(a) we present the angular dependence of  $\Delta$  on  $\theta$  and  $\varphi$ , whose values turn out to be around 2.6%, consistent with earlier experimental results [48]. We observe that there is a maximum deformation of the FS at  $\theta = \varphi = 90^\circ$ , which corresponds to the direction of the smallest trapping frequency  $\omega_y$  ( $y$  axis). This can be understood heuristically, if one recalls that the DDI is attractive for dipoles oriented head-to-tail.

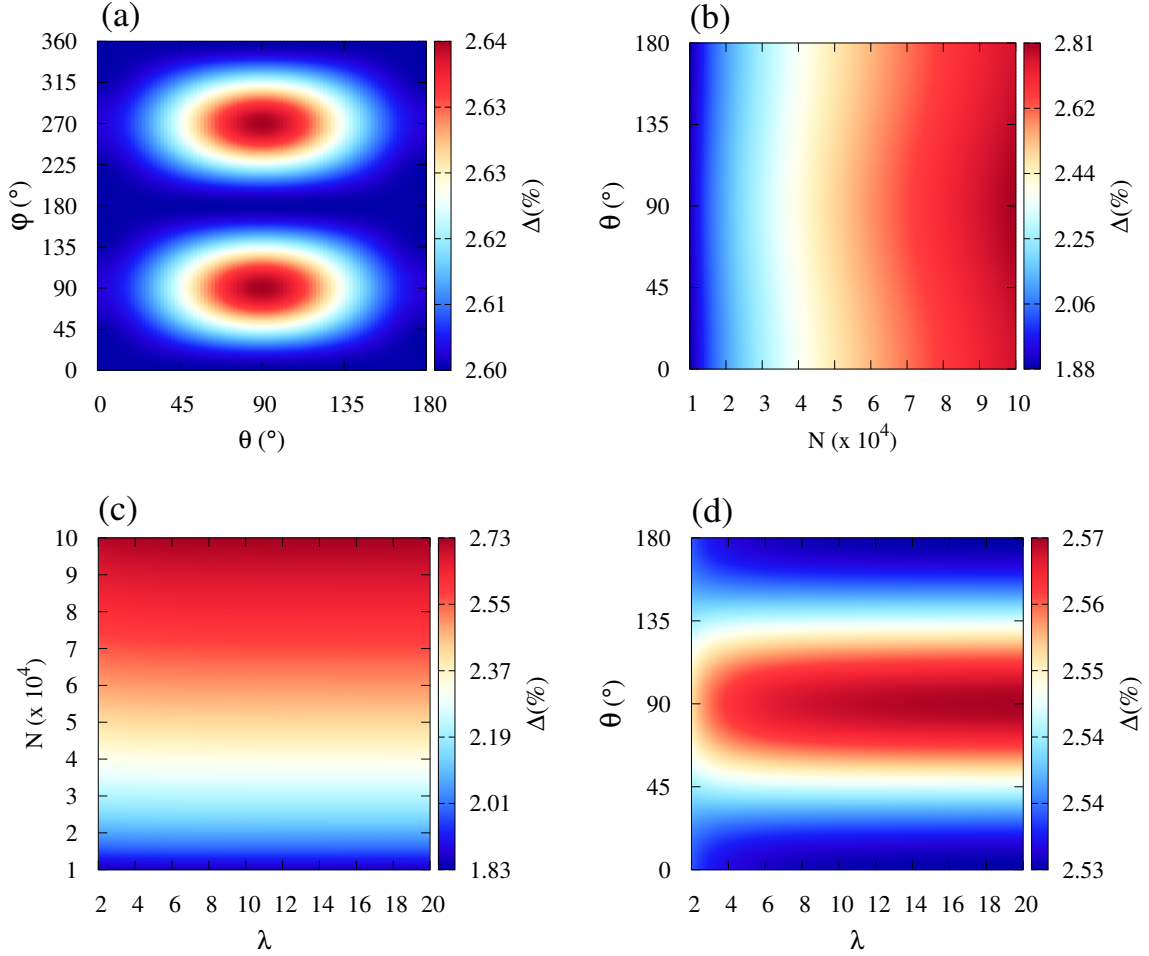


**Figure 3.4:** FS deformation  $\Delta$  for  $^{167}\text{Er}$  atoms with magnetic dipole moment  $m = 7\mu_B$  as a function of: (a) dipoles' orientation angles  $\theta$  and  $\varphi$ , for parameters of Reference [48]; (b) particle number  $N$  and angle  $\theta$ , for  $\varphi = 90^\circ$  and trap frequencies of Reference [48]; (c) particle number  $N$  and trap anisotropy  $\lambda$ , for  $\theta = \varphi = 90^\circ$ ; (d) angle  $\theta$  and trap anisotropy  $\lambda$ , for  $\varphi = 90^\circ$  and  $N = 6.6 \times 10^4$ . Trap anisotropy  $\lambda$  in (c) and (d) was varied by changing the frequencies  $\omega_x = \omega_z$  and  $\omega_y$ , while keeping the mean frequency  $\bar{\omega} = 300 \times 2\pi$  Hz constant.

Thus, a weaker trapping frequency favours the stretching of the gas in that direction so that, in turn, this cigar-shaped configuration enhances the relative contribution of the DDI to the total energy.

Another aspect relevant for experiments is the influence of the particle number  $N$  and the trap geometry on the deformation of the FS. Tuning these parameters and the direction of the dipoles might lead to an enhancement of the DDI effects, and therefore to a stronger deformation of the FS. This is investigated in Figures 3.4(b)-3.4(d), where the FS deformation is given as a function of parameters  $N$ ,  $\theta$  and the trap anisotropy  $\lambda = \sqrt{\omega_x \omega_z} / \omega_y$  for a fixed value of the angle  $\varphi = 90^\circ$ . Figures 3.4(c) and 3.4(d) explore the FS deformation as a function of the trap anisotropy  $\lambda$ , which

was varied by changing the frequencies  $\omega_x = \omega_z$  and  $\omega_y$ , while keeping the mean frequency  $\bar{\omega} = 300 \times 2\pi$  Hz constant. From all these figures we conclude that the increase in the particle number yields a dominant increase in  $\Delta$  compared to all other parameters. We note that, in fact,  $\Delta$  also depends on  $\bar{\omega}$ , which we do not show here, since it can be directly connected to the particle number dependence. Indeed, the FS deformation depends on  $\varepsilon_{\text{dd}}$  [48], yielding a dependence of  $\Delta$  on  $N^{1/6}\bar{\omega}^{1/2}$ . As the trap frequencies can be more easily tuned than the particle number,  $\bar{\omega}$  can be considered as a predominant control knob in the experiment. However, a precise control of the angles and the anisotropy, which is experimentally easy to realize, may help to achieve an even larger increase in the deformation of the FS. We also note that the  $\lambda$  dependence is the weakest one, and therefore the formalism for calculating the angular dependence presented here is important for a systematic study of the influence of the relevant parameters.

Furthermore, we study the role of the DDI strength and explore whether qualitative changes of the system's behavior emerge by increasing the value of the dipole moment. To this aim, we compare the erbium case with a molecular Fermi gas of  $^{40}\text{K}^{87}\text{Rb}$ , assuming that the same gas characteristics can be achieved in the same trap with this species. The latter possesses an electric dipole moment of strength  $d = 0.57\text{D}$ , yielding a much larger relative interaction strength  $\varepsilon_{\text{dd}} = 7.76$  for the same parameters. Since the critical value of  $\varepsilon_{\text{dd}}$ , for which the system is stable, amounts to  $\varepsilon_{\text{dd}}^{\text{crit}} = 2.5$  [125], the molecular  $^{40}\text{K}^{87}\text{Rb}$  gas in such a geometry and with the maximal strength of the DDI would in fact not be stable and would collapse under the attractive action of the DDI. For the sake of simplicity and comparison between the systems, we consider a molecular sample of similar geometry and particles number but in which the electric dipole moment has been tuned to  $d = 0.25\text{D}$  by means of an external field [86]. This leads to the relative DDI strength  $\varepsilon_{\text{dd}} = 1.51 < \varepsilon_{\text{dd}}^{\text{crit}}$ , which is exactly 10 times larger than corresponding  $\varepsilon_{\text{dd}}$  for atomic Er gas.

As we see, the FS deformation  $\Delta$  has a much stronger angular dependence in Figure 3.5(a) than in Figure 3.4(a) for the erbium case. Indeed, we have the competition between two different anisotropic effects: the trapping frequencies and very strong DDI. Therefore, the system turns out to have a strong dependence on the various parameters involved, and it is not possible to draw general conclusions on the behavior of the FS deformation. Only a detailed numerical study based on the formalism developed here can provide a precise landscape of the FS deformation behavior for a concrete experimental setup. In contrast to Figure 3.4(b), we see in Figure 3.5(b) that

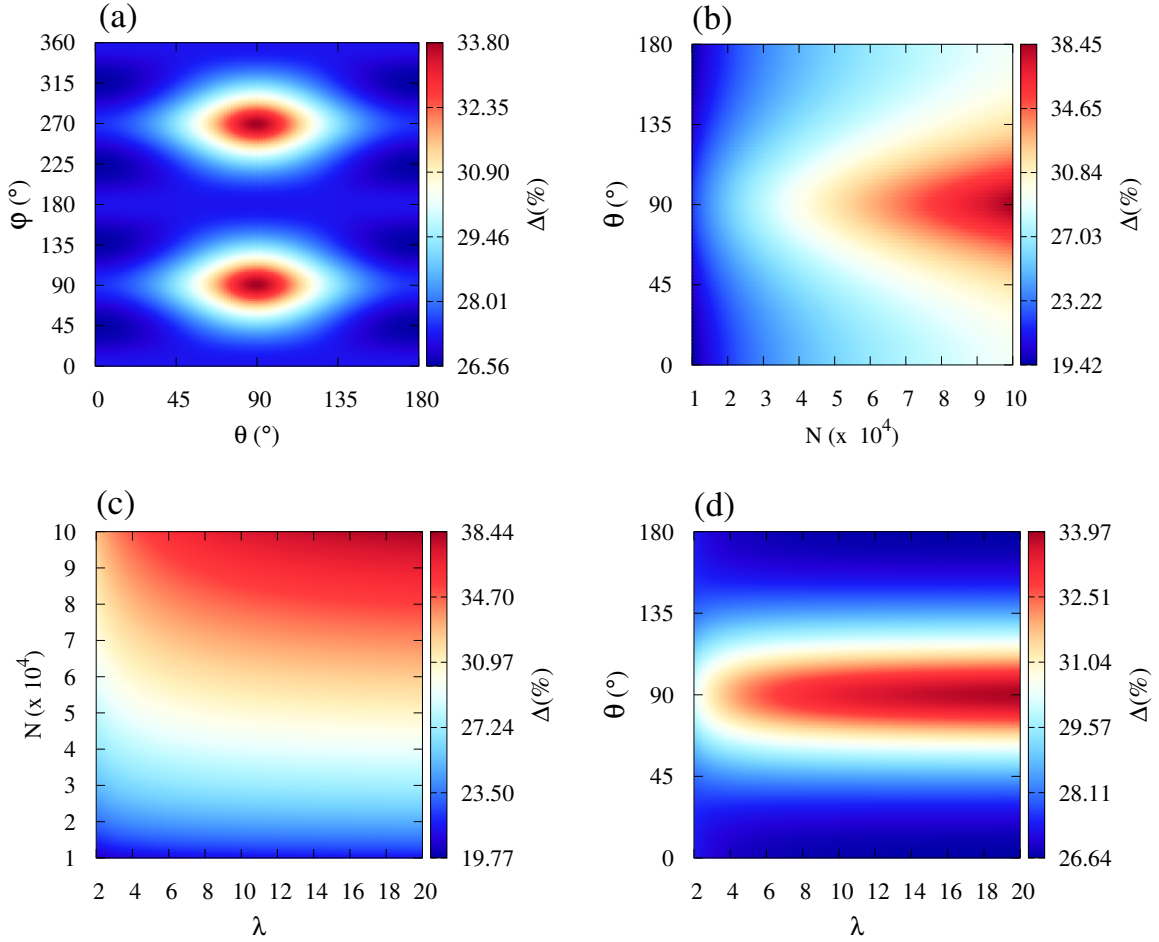


**Figure 3.5:** FS deformation  $\Delta$  for  $^{40}\text{K}^{87}\text{Rb}$  molecules with electric dipole moment  $m = 0.25$  D as a function of: (a) dipoles' orientation angles  $\theta$  and  $\varphi$ , for parameters of Reference [48]; (b) particle number  $N$  and angle  $\theta$ , for  $\varphi = 90^\circ$  and trap frequencies of Reference [48]; (c) particle number  $N$  and trap anisotropy  $\lambda$ , for  $\theta = \varphi = 90^\circ$ ; (d) angle  $\theta$  and trap anisotropy  $\lambda$ , for  $\varphi = 90^\circ$  and  $N = 6.6 \times 10^4$ . Trap anisotropy  $\lambda$  in (c) and (d) was varied by changing the frequencies  $\omega_x = \omega_z$  and  $\omega_y$ , while keeping the mean frequency  $\bar{\omega} = 300 \times 2\pi$  Hz constant.

the increase in the particle number yields an increase in  $\Delta$ , however a precise control of the angle  $\theta$ , which is experimentally much easier to realize, may yield an even larger increase in the deformation of the FS. This is particularly important for the currently available fermionic dipolar heteronuclear molecules, since the Pauli exclusion principle poses serious challenges on the cooling of the sample by suppressing collisions, hence severely limiting the particle number  $N$ . From Figures 3.5(c) and 3.5(d) we conclude that the  $\lambda$  dependence is practically flat in both cases, contrary to the particle number  $N$  and angle  $\theta$ , which have much larger impact on the FS deformation and can be effectively used as tuning parameters.

Although the shapes of both angular dependencies in Figures 3.4(a) and 3.5(a) are

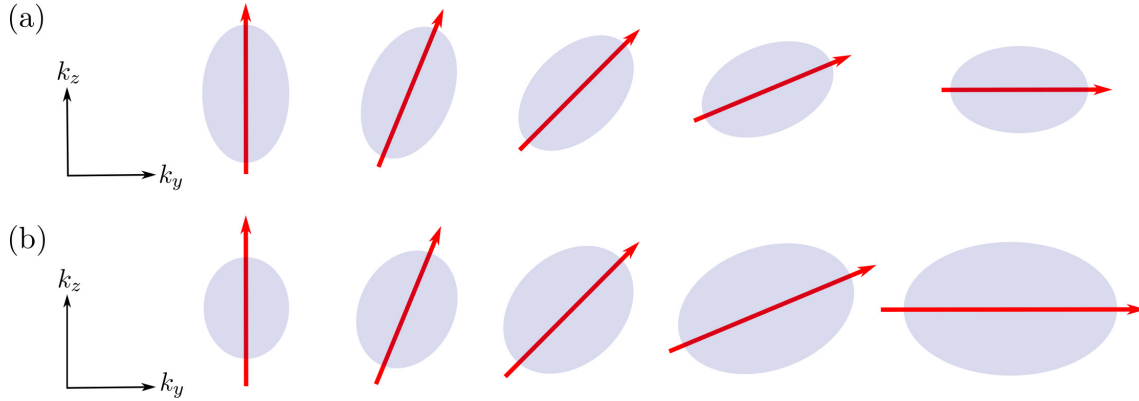


**Figure 3.6:** Illustration of the angular dependence of the FS deformation in momentum space for system in an anisotropic trap elongated along the horizontal  $y$  axis : (a) for weak DDI, when the FS ellipsoid just rotates like a rigid object; (b) for strong DDI, when the FS ellipsoid stretches in all directions and its deformation strongly depends on the dipoles' orientation.

quite similar, the main difference is that the deformation of the FS for polar molecules is an order of magnitude larger than for erbium and has a value of around 30%. However, we also observe that the variation in the values of  $\Delta$  for different angles  $\theta$  and  $\varphi$  is around 0.03% in the case of an atomic erbium gas, while for the molecules it amounts to around 5%, i.e., the variations of  $\Delta$  are two orders of magnitude larger for the molecular case. The reason for this increase in both the maximal FS deformation and its angular variation is the same, namely the increase in the relative DDI strength  $\varepsilon_{\text{dd}}$ , which is one order of magnitude larger for the considered molecules compared to  $^{167}\text{Er}$ . While the FS deformation is proportional to  $\varepsilon_{\text{dd}}$ , as expected [125] and as evidenced by our results above, our findings suggest that its maximal angular variation is proportional to  $\varepsilon_{\text{dd}}^2$ .

The calculated angular dependence of the FS deformation on the DDI strength has the following important physical consequence. For erbium atoms, where  $\varepsilon_{\text{dd}}$  is small, the angular variation of the FS deformation is even smaller, since it is proportional to  $\varepsilon_{\text{dd}}^2$ , and it would be difficult to observe in experiments. Therefore, one could say that the FS behaves as a rigid ellipsoid, which just rotates following the orientation of the dipoles, without changing its shape [48], as illustrated in Figure 3.6(a). This also implies that the atomic cloud shape in real space is practically disentangled from the FS, and is mainly determined by the trap shape. On the other hand, when  $\varepsilon_{\text{dd}}$  is large enough, as in the case of  $^{40}\text{K}^{87}\text{Rb}$ , the FS not only rotates, but also significantly changes its shape, since the angular variation can be as high as 5%, which is experimentally observable. This is schematically shown in Figure 3.6(b), where the FS

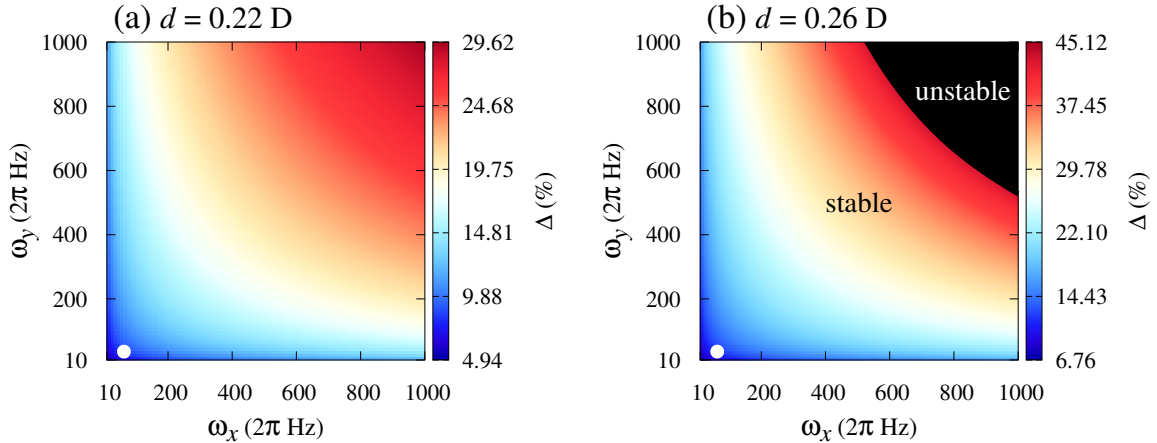


**Figure 3.7:** The FS deformation  $\Delta$  as a function of the trap frequencies  $\omega_x$  and  $\omega_y$ , for a system of  $N = 3 \times 10^4$  ultracold molecules of  $^{40}\text{K}^{87}\text{Rb}$ , with  $\omega_z = 200 \times 2\pi$  Hz. The dipoles are oriented along  $z$  axis and have electric dipole moments: (a)  $d = 0.22$  D and (b)  $d = 0.26$  D. White dots correspond to the parameters of the JILA experiment [109].

behaves as a soft ellipsoid, whose axes are stretched as it rotates. Although we know that the phase-space volume is preserved, according to the particle number conservation (2.17), Figure 3.6(b) illustrates that the FS, i.e., the momentum-space volume increases ( $K'_i$  increase), while in real space the volume of the cloud shape decreases ( $R''_i$  decrease). From this we see that the real-space atomic cloud shape is indeed coupled to the FS, and this effect can become measurable in future dipolar fermion experiments, with sufficiently large values of  $\varepsilon_{\text{dd}}$ . Since the  $^{40}\text{K}^{87}\text{Rb}$  molecules are promising candidates in this context, we will continue with investigation of the FS deformation in such systems.

Let us assume that the electric dipole moments of  $^{40}\text{K}^{87}\text{Rb}$  molecules are aligned along  $z$  axis and that their value is tuned down to  $d = 0.22$  D, such that it is below the critical value of  $d^{\text{crit}} = 0.24$  D determined in Figure 3.2(c). For fixed  $\omega_z = 200 \times 2\pi$  Hz and realistic values of the trapping frequencies  $\omega_x$  and  $\omega_y$  we obtain that  $\Delta$  varies between 5% and 30%, as shown in Figure 3.7(a). We also note that  $\Delta$  is a symmetric function of arguments  $\omega_x$  and  $\omega_y$ , for the same reasons  $\varepsilon_{\text{dd}}^{\text{crit}}$  is a symmetric function in Figure 3.2(a).

Furthermore, the theory presented here makes it possible to calculate the stability properties for experimentally relevant dipolar Fermi systems, where even relatively small changes in the dipolar moment strength can significantly affect the system's stability. This is demonstrated in Figure 3.7(b), where for a slightly larger value of  $d = 0.26$  D we read off that the FS deformation becomes significantly larger than in Figure 3.7(a). Namely, in this case the FS deformation goes up to 45%, and, even

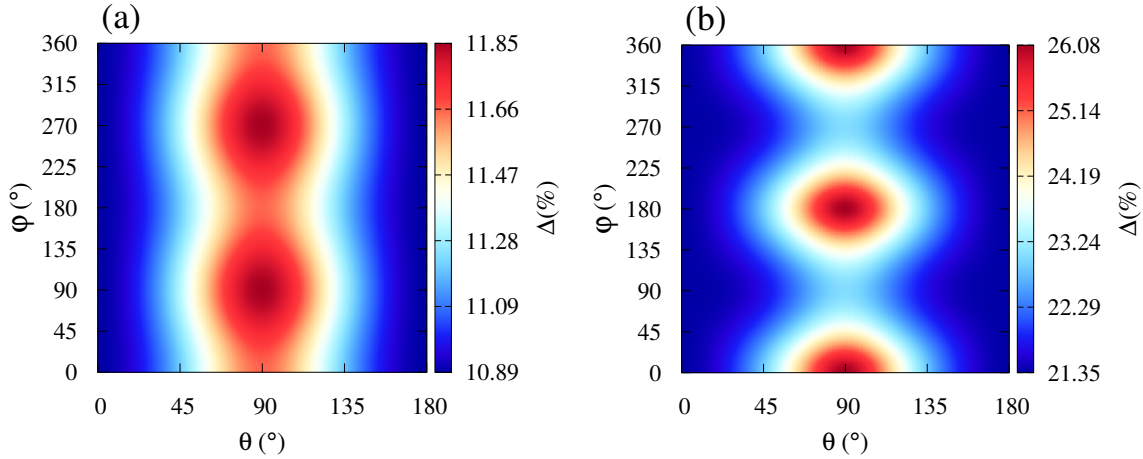


**Figure 3.8:** Angular dependence of FS deformation  $\Delta$  for ultracold Fermi gas of  $N = 3 \times 10^4$  molecules of  $^{40}\text{K}^{87}\text{Rb}$  with fixed value of the electric dipole moment  $d = 0.25$  D and the trap frequencies: (a)  $(\omega_x, \omega_y, \omega_z) = (63, 36, 200) \times 2\pi$  Hz, and (b)  $(\omega_x, \omega_y, \omega_z) = (50, 500, 900) \times 2\pi$  Hz.

more significantly, an unstable region appears for higher frequencies, which does not support a stable ground state of the system.

Next, we discuss the angular dependence of the FS deformation shown in Figures 3.8(a) and 3.8(b) for two different trap configurations, which illustrate that the trap geometry also strongly affects the system's behavior. Namely, the FS deformation and its angular distribution can be tuned by changing the trap frequencies. Not only the range of the FS deformation values can be increased or decreased this way, but also its minima and maxima and their position can be freely modified. In contrast to atomic magnetic species, where the angular dependence of the FS deformation is of the order of few per mill [49] and is, thus, quite weak, the strong DDI in the samples of polar molecules leads to a much stronger angular dependence [50], as shown in Figures 3.8(a) and 3.8(b). For stronger DDI we expect not only an increased critical temperature of Cooper pairing, but also a higher degree of tunability as the deformation of the FS depends on the dipoles' orientation relative to the trap geometry.

One of the prominent tuning parameters in the realm of quantum gases is dimensionality of the system. Namely, by tuning the frequencies of the trap potential one can achieve a very thin pancake-shaped gas cloud, which is considered as a quasi-2D system, or analogously a cigar-shaped gas cloud which is considered as a quasi-1D. We will focus now on a polarized quantum degenerate Fermi gas of  $^{40}\text{K}^{87}\text{Rb}$  with  $N = 3 \times 10^4$  molecules with electric dipole moment value of  $d = 0.35$  D in the strong 2D confinement, which is of special interest if one wants to study the phase transition in the regime of strong interactions across the 2D BEC-BCS crossover. We

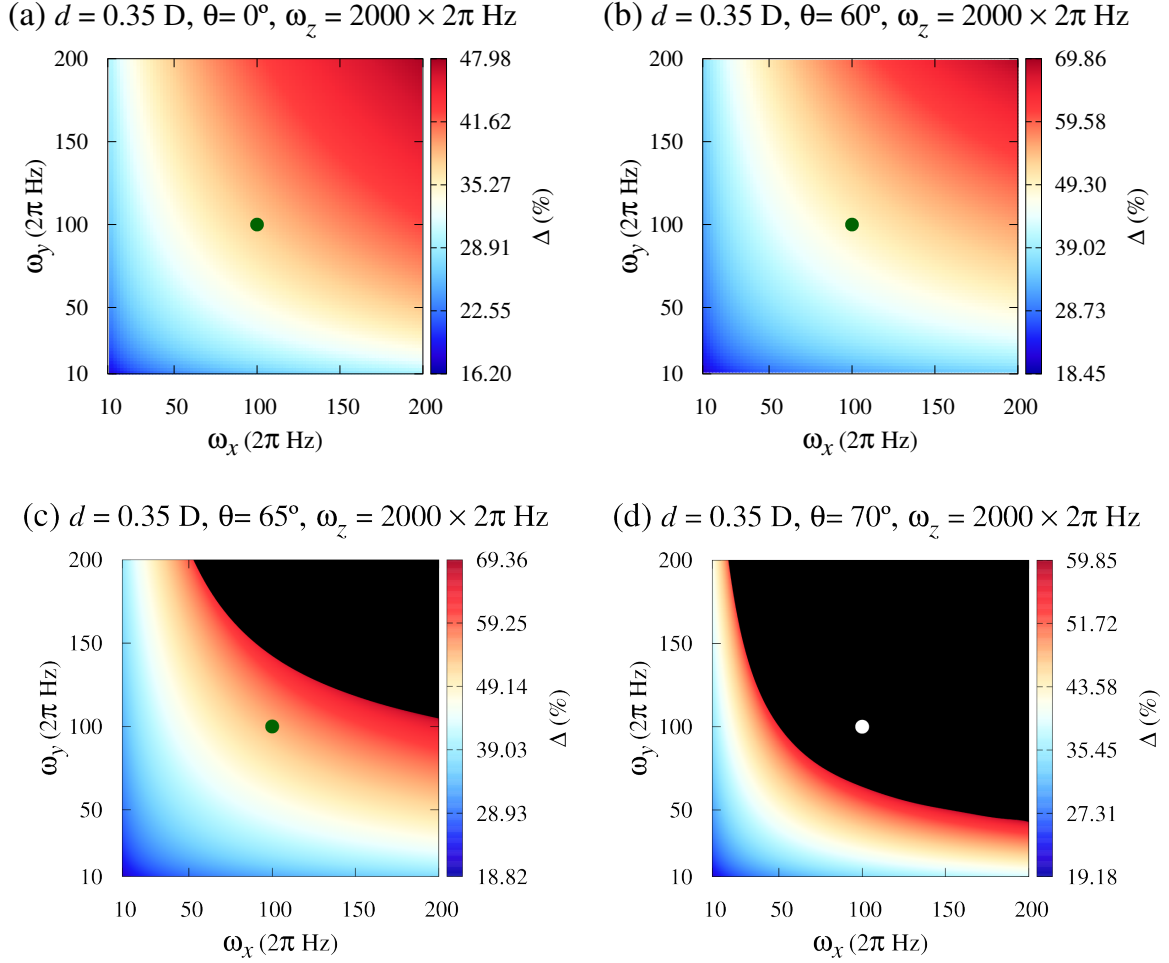


**Figure 3.9:** FS deformation  $\Delta$  as a function of  $\omega_x$  and  $\omega_y$  for a  $^{40}\text{K}^{87}\text{Rb}$  gas with  $N = 3 \times 10^4$  molecules with electric dipole moment  $d = 0.35$  D. Each panel corresponds to a different orientation of the dipoles, defined by the angles  $\theta, \varphi$ : (a)  $\theta = \varphi = 0^\circ$ ; (b)  $\theta = 60^\circ, \varphi = 0^\circ$ ; (c)  $\theta = 65^\circ, \varphi = 0^\circ$ ; (d)  $\theta = 70^\circ, \varphi = 0^\circ$ . Green/white dots correspond to the target trap parameters  $(\omega_x, \omega_y, \omega_z) = (100, 100, 2000) \times 2\pi$  Hz.

show that, depending on the electric dipole moment value  $d$  and the orientation of the dipoles  $(\theta, \varphi)$ , the system can either have a stable ground state or exhibit an instability in an experimentally interesting region around the target trap parameters  $(\omega_x, \omega_y, \omega_z) = (100, 100, 2000) \times 2\pi$  Hz.

The trap aspect ratios for the target configuration are  $\omega_z/\omega_x = \omega_z/\omega_y = 20$ . Performing the numerical calculations for those parameters, similarly as it was done to calculate results presented in Figure 3.2(a), we obtain the critical interaction strength  $\varepsilon_{\text{dd}}^{\text{crit}} = 123.4$  for the dipoles oriented along  $\theta = \varphi = 0^\circ$ . This  $\varepsilon_{\text{dd}}^{\text{crit}}$  yields the critical dipole moment of  $d^{\text{crit}} = 2.51$  D, which is much larger than the actually considered value of the electric dipole moment  $d = 0.35$  D, and even much larger than the permanent dipole moment of  $^{40}\text{K}^{87}\text{Rb}$  given in Table 1.1. Therefore, as we see from

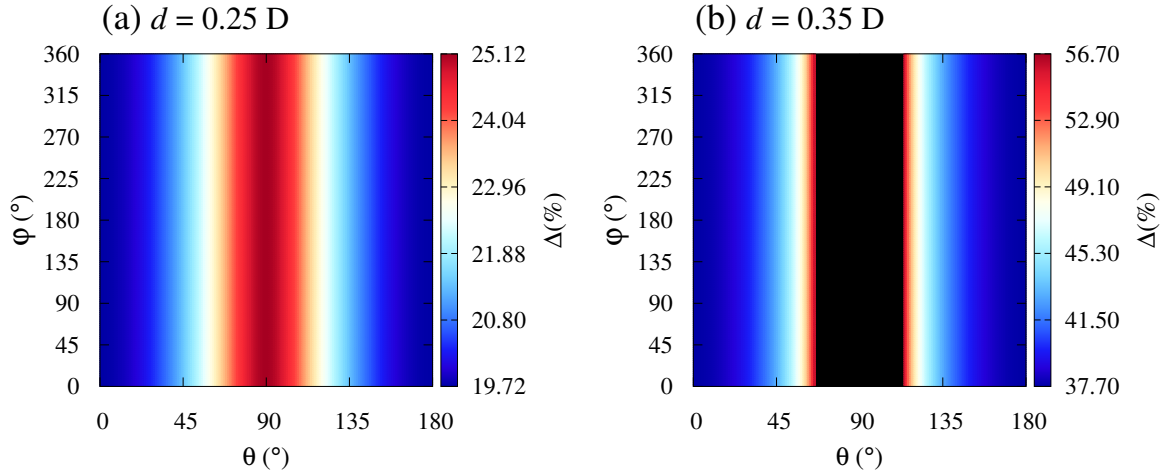


**Figure 3.10:** Angular dependence of FS deformation  $\Delta$  for the target trap parameters  $(\omega_x, \omega_y, \omega_z) = (100, 100, 2000) \times 2\pi$  Hz, of  $^{40}\text{K}^{87}\text{Rb}$  gas with  $N = 3 \times 10^4$  molecules with a fixed value of electric dipole moment: (a)  $d = 0.25$  D; (b)  $d = 0.35$  D. Since  $\omega_x = \omega_y$ , there is no  $\varphi$  dependence.

Figure 3.9(a), the system has a stable ground state in the region around the target trap configuration, with the FS deformation ranging from 16% to 48%. For the dipoles oriented in the direction  $\theta = 60^\circ$ ,  $\varphi = 0^\circ$ , shown in Figure 3.9(b), we obtain a much smaller value  $\varepsilon_{\text{dd}}^{\text{crit}} = 3.18$  for the target trap parameters, but still  $d^{\text{crit}} = 0.40$  D is larger than the value of  $d$  used. In this case the FS deformation becomes significantly larger than in Figure 3.9(a), namely up to 70%. Tilting the dipoles further to  $\theta = 65^\circ$ ,  $\varphi = 0^\circ$ , we numerically calculate  $\varepsilon_{\text{dd}}^{\text{crit}} = 2.585$  for the target configuration, which leads to critical electric dipole moment of  $d^{\text{crit}} = 0.36$  D. Since it still holds  $d < d^{\text{crit}}$ , the target trap configuration is stable, but we see in Figure 3.9(c) that the instability region appears in its vicinity. The FS deformation range stays practically the same as in the previous case, presented in Figure 3.9(b), but achieved for smaller frequencies. Finally, for  $\theta = 70^\circ$ ,  $\varphi = 0^\circ$  we numerically obtain  $\varepsilon_{\text{dd}}^{\text{crit}} = 2.20$  for the target configuration, which corresponds to  $d^{\text{crit}} = 0.336$  D  $< d$ . This explains larger unstable region in Figure 3.9(d) in comparison to Figure 3.9(c), which now includes the target configuration. However, the FS deformation still remains large and ranges from 19% to 60%.

The angular dependence of the FS deformation for the target trap configuration and for two values of the dipole moment is presented in Figure 3.10. For a smaller value  $d = 0.25$  D the system is always stable, as can be seen in Figure 3.10(a), while for  $d = 0.35$  D the system becomes unstable for  $60^\circ < \theta < 120^\circ$ , as can be read off in Figure 3.10(b). This can be expected if we take into account results from Figure 3.9. Here we note that, due to the symmetry of the target trap configuration ( $\omega_x = \omega_y$ ),

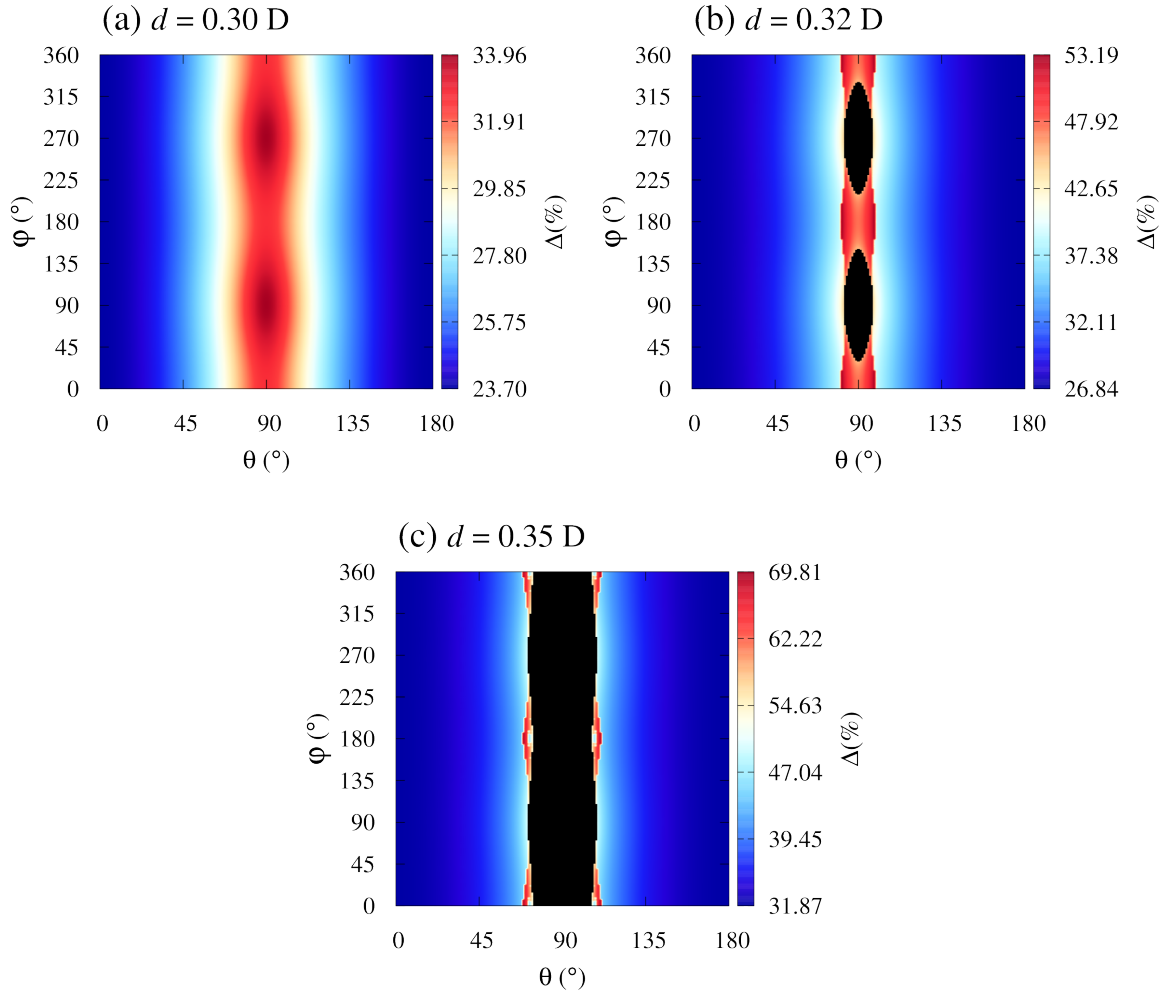


**Figure 3.11:** Angular dependence of  $\Delta$  for a fixed value of  $d$  and trap parameters  $(\omega_x, \omega_y, \omega_z) = 2\pi \times (100, 36, 2000)$  Hz, with  $N = 3 \times 10^4$  molecules of  $^{40}\text{K}^{87}\text{Rb}$  for: (a)  $d = 0.25$  D; (b)  $d = 0.32$  D; (c)  $d = 0.35$  D. Now the  $\varphi$  dependence is clearly visible. Depending on the dipole moment value  $d$ , the system can either have a stable ground state or exhibit an instability.

there is no  $\varphi$  dependence in both panels of Figure 3.10.

However, if we consider a trap configuration with a slightly broken cylindrical symmetry, such as  $(\omega_x, \omega_y, \omega_z) = (100, 36, 2000) \times 2\pi$  Hz, a  $\varphi$ -dependence will appear, as can be seen in Figure 3.11. There we observe that, depending on the dipole moment value, we can have a stable system for all orientations of the dipoles as in Figure 3.11(a), a system with isolated instability regions as in Figure 3.11(b), or a system with a single instability region, Figure 3.11(c), similar to the one from Figure 3.10(b).

All results presented in this Section, as well as the formalism used here, allow for a systematic study of the influence of different parameters on the FS deformation and strengthen the importance of tuning techniques, such as the one recently developed for polar molecules [145], based on a sophisticated electrode geometry system.

Furthermore, the generalized Hartee-Fock mean-field theory presented here provides the basis for understanding and interpreting phenomena in which the investigated physics depends on the underlying structure of the FS, such as fermionic pairing and superfluidity.

### 3.4 Gas cloud deformation

The presence of the DDI in both bosonic [146] and fermionic [118] quantum gases has been predicted and evidenced in experiments by detailed TOF expansion measurements [147] to induce magnetostriction in real space, i.e., a stretching of the gas cloud along the direction of the dipoles, see Figure 2.1(d)-(f). Here we investigate the dependence of this effect on the orientation of the dipoles for the fermionic case. To this end, we first define the real-space aspect ratios

$$A_{ij} = \frac{R_i''}{R_j''}, \quad (3.11)$$

of the corresponding TF radii, as well as their noninteracting counterparts

$$A_{ij}^0 = \frac{R_i^0}{R_j^0} = \frac{\omega_j}{\omega_i}. \quad (3.12)$$

The gas cloud deformation can now be studied in terms of the relative cloud deformations

$$\delta_{zx} = \frac{A_{zx}}{A_{zx}^0} - 1, \quad (3.13)$$

$$\delta_{zy} = \frac{A_{zy}}{A_{zy}^0} - 1. \quad (3.14)$$

Here the anisotropies due to the harmonic trap are already taken into account and eliminated from the consideration, such that only effects of the DDI contribute to the nontrivial value of  $\delta_{zx}$  and  $\delta_{zy}$ . This is in close analogy to the definition of the relative total energy shift of the system in Equation (2.99), or the FS deformation in Equation (3.10). The situation would be identical if we consider a spherically symmetric trap configuration, since in this case, as mention before, Equations (2.93) and (2.94) can be solved analytically, independently of other equations, yielding

$$\theta'' = \theta \quad \text{and} \quad \varphi'' = \varphi. \quad (3.15)$$

This means that the gas cloud is stretched into an ellipsoid along the orientation of dipoles, just as the FS is. Additionally, from Equations (2.96) and (2.97) it follows that

$$R_x'' = R_y'', \quad (3.16)$$

which means that the gas cloud ellipsoid has a cylindrical symmetry in a plane perpendicular to the dipoles' orientation, and therefore  $\delta_{zx}$  and  $\delta_{zy}$  become equal. This leads to

$$\delta_{zx} = \delta_{zy} \equiv \delta = \frac{R_z''}{R_x''} - 1. \quad (3.17)$$

Therefore, we start investigation of the DDI effects on the gas cloud shape with the spherically symmetric trap, indicated as Case 1 in Table 3.2. From Figure 3.12(a) we see that all TF radii are equal in the noninteracting case ( $\varepsilon_{\text{dd}} = 0$ ), as expected. If we increase  $\varepsilon_{\text{dd}}$  TF radius along dipoles' orientation increases, while the other two TF radii decrease. It is interesting that in this case the relative cloud deformation  $\delta$  and FS deformation  $\Delta$  increase linearly and are almost identical up to the  $\varepsilon_{\text{dd}} \approx 1.3$ , when  $\delta$  starts to increase faster, as indicated in Figure 3.12(b).

In the following we consider a dipolar Fermi gas with the dipoles along  $z$  axis confined in a pancake-shaped, as well as in a cigar-shaped traps, as listed in Table 3.2. Namely, Case 2 corresponds to a pancake in  $xy$  plane, Case 3 to a pancake in  $xz$  plane, while Case 4 represents a cigar along  $z$  axis, and Case 5 a cigar along  $x$  axis. In all cases the dipoles are oriented along  $z$  axis, and therefore the coordinate systems  $S$ ,  $S'$  and  $S''$  coincide, see Figure 2.1.

In the inset of Figure 3.12(b) we show the FS deformation  $\Delta$  as a function of the relative DDI strength  $\varepsilon_{\text{dd}}$  for all considered cases. We observe that for the relatively weak DDI, i.e.,  $\varepsilon_{\text{dd}} < 1$ , for any trap configuration,  $\Delta$  linearly increases with  $\varepsilon_{\text{dd}}$ . Furthermore, it is clear that a linear part of this dependence extends further as the critical value of the relative DDI strength  $\varepsilon_{\text{dd}}^{\text{crit}}$  is larger, see Table 3.2.

Figures 3.12(c) and 3.12(d) show TF radii as functions of the relative DDI strength  $\varepsilon_{\text{dd}}$ , for the pancake-shaped trap configurations, Case 2 with the solid lines, and Case 3 with the dashed lines. As a cross-check, we note that in the noninteracting case all the corresponding TF radii are equal, since the gas cloud is fully determined by the trap frequencies. Namely, by a simple cyclic permutation of the TF radii indices  $x \rightarrow z \rightarrow y \rightarrow x$  one can switch from Case 2 to Case 3. The dipoles in Case 2 have the side-by-side configuration, such that they repel each other. As  $\varepsilon_{\text{dd}}$  increase this results

**Table 3.2:** Trap configurations with corresponding critical value of the relative dipole-dipole interaction strength  $\varepsilon_{\text{dd}}^{\text{crit}}$ , obtained as in Figure 3.2(a), for ultracold Fermi gas with dipoles oriented along  $z$  axis.

Case	Trap shape	Trap frequencies	$\varepsilon_{\text{dd}}^{\text{crit}}$
1	spherical	$\omega_x = \omega_y = \omega_z$	2.10
2	pancake	$10 \omega_x = 10 \omega_y = \omega_z$	10.10
3	pancake	$10 \omega_x = \omega_y = 10 \omega_z$	1.73
4	cigar	$\omega_x = \omega_y = 10 \omega_z$	1.65
5	cigar	$10 \omega_x = \omega_y = \omega_z$	2.48

in the increase of all the TF radii. Contrary to this, the dipoles in Case 3 have the head-to-tail configuration and attract each other more as  $\varepsilon_{\text{dd}}$  increases, thus leading to the decrease of all the TF radii. While in Case 2 all TF radii increase with the same rate as  $\varepsilon_{\text{dd}}$  increases, in Case 3 the radii  $R_x$  and  $R_y$  decrease with the same rate, while  $R_z$  decreases slower. This can be explained by the symmetry of the system. Namely, in Case 2 the cylindrical symmetry of the pancake-shaped trap is preserved ( $R_x = R_y$ ), while in Case 3 this symmetry is broken by the DDI, such that always  $R_x \leq R_z$ .

A similar analysis can be used for the cigar-shaped trap configurations, Cases 4 and 5 in Table 3.2. In Figures 3.12(e) and 3.12(f) we show the TF radii as functions of the relative DDI strength  $\varepsilon_{\text{dd}}$  for these trap configurations, Case 4 with the solid lines, and Case 5 with the dashed lines. Again, as a cross-check, we note that in the noninteracting case all the corresponding TF radii are the same, which can be verified by using a simple cyclic permutation of the TF radii indices  $x \rightarrow y \rightarrow z \rightarrow x$  to switch from Case 4 to Case 5. Due to the "head to tail" configuration of the dipoles in Case 4, all the TF radii decrease with increasing  $\varepsilon_{\text{dd}}$ , since the attraction between the dipoles dominates. In Case 5, it turns out that behavior of the TF radii cannot be explained by such simple arguments. Namely, the TF radius  $R_y$  ( $R_z$ ) monotonously decreases (increases) with increasing  $\varepsilon_{\text{dd}}$ , while  $R_x$  is a non-monotonic function of  $\varepsilon_{\text{dd}}$ . Concerning the symmetry reasoning, in Case 4 the cylindrical symmetry of the cigar-shaped trap is preserved ( $R_x = R_y$ ), while in Case 5 this symmetry is again broken by the DDI and  $R_y \leq R_z$ .

In what follows, we present angular dependence of the relative cloud deformations  $\delta_{zx}$  and  $\delta_{zy}$  for the atomic, as well as for the molecular Fermi gas. First, in Figure 3.13 we present the angular dependence for the erbium case with the same parameters as

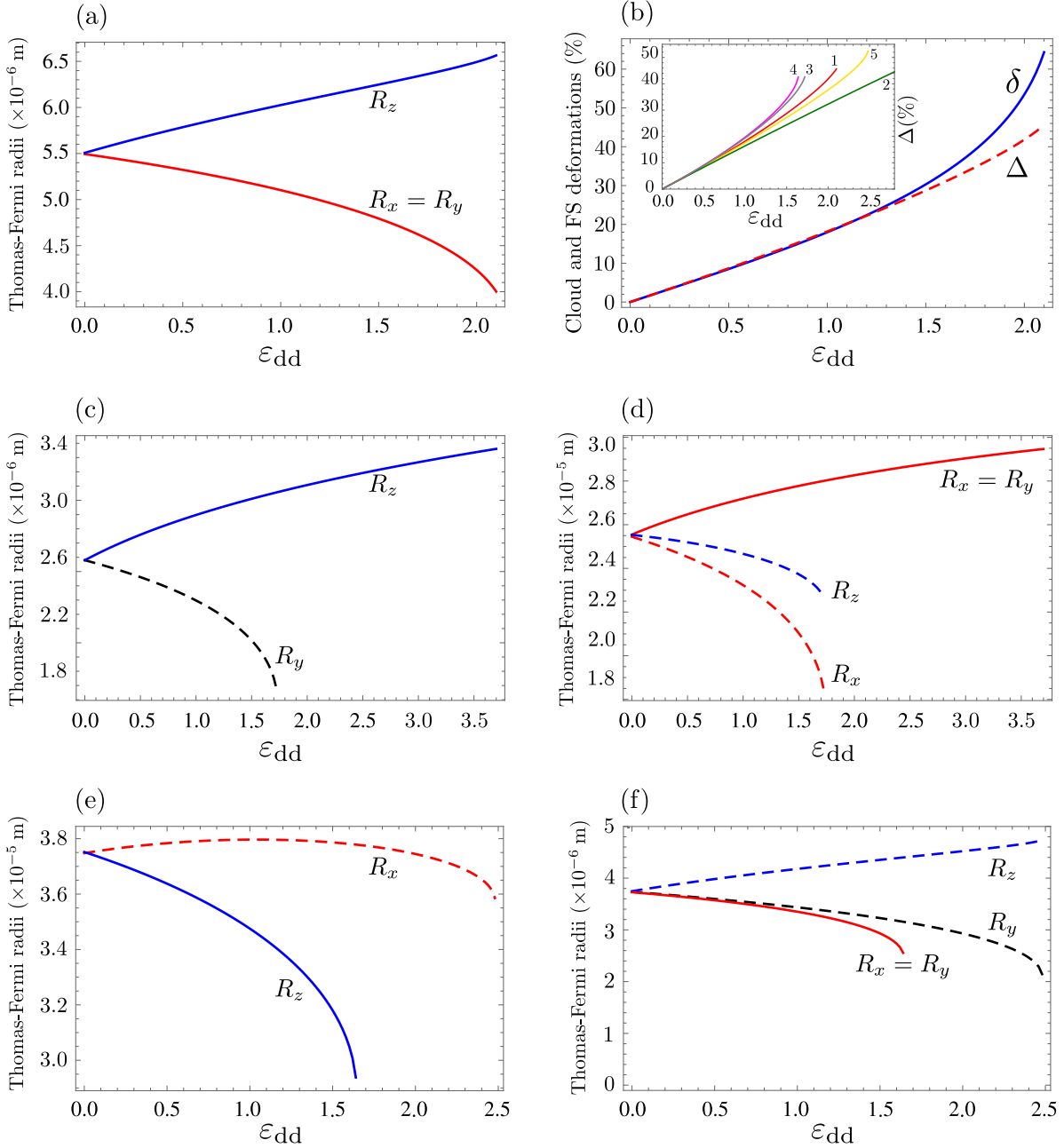


**Figure 3.12:** TF radii as functions of relative dipolar interaction strength  $\varepsilon_{dd}$  for Fermi gases in global equilibrium for considered trap geometries from Table 3.2, with dipoles parallel to  $z$  axis: (a) Case 1, (c)-(d) Case 2 solid line, Case 3 dashed lines, and (e)-(f) Case 4 solid line, Case 5 dashed lines. (b) Gas cloud  $\delta$  and FS deformation  $\Delta$  as functions of  $\varepsilon_{dd}$  for Case 1. Inset gives to the FS deformation  $\Delta$  for all 5 considered cases.

in Figure 3.4(a). We see that both deformations for a fixed angle  $\theta = 90^\circ$  possess a minimum for  $\varphi = (0^\circ, 180^\circ, 360^\circ)$ . Also, along the  $\varphi$ -direction the FS deformation monotonously decreases up to  $\theta = 90^\circ$ , after which it monotonously increases. If we compare this to the behavior in momentum space, see Figure 3.4(b), we see that the

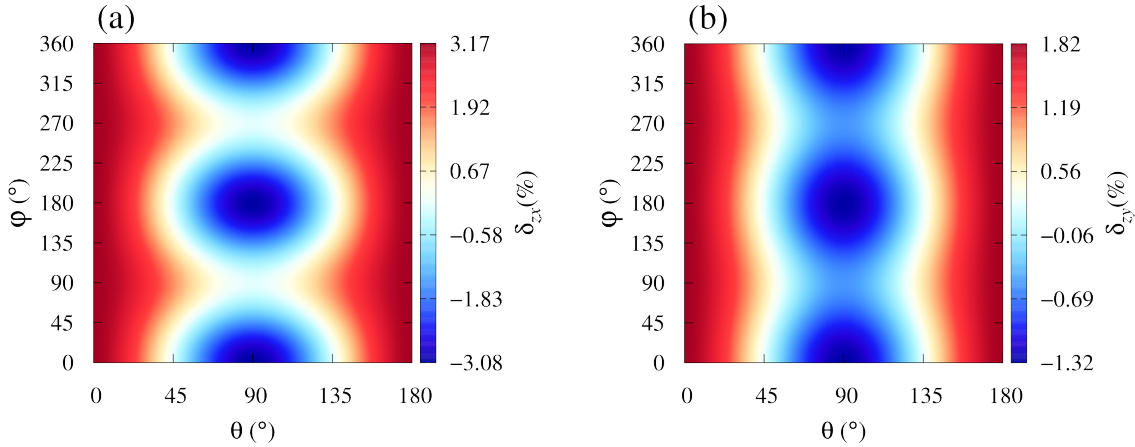


**Figure 3.13:** Angular dependence of relative cloud deformations for  $^{167}\text{Er}$ , with parameters as in Figure 3.4(a): (a)  $\delta_{zx}$ ; (b)  $\delta_{zy}$ .

order of magnitude for both types of deformation is the same, around few percent. However, along the  $\varphi$ -direction we have qualitatively different behavior: when  $\Delta$  increases,  $\delta_{zx}$  and  $\delta_{zy}$  decrease, and vice versa. The same applies for the behavior along the  $\theta$ -direction, with the main difference that the relative cloud deformations possess three minimal values along  $\theta = 90^\circ$  direction, while the FS deformation has only two maxima.

Similarly, Figure 3.14 presents the angular dependence of  $\delta_{zx}$  and  $\delta_{zy}$  for the molecular  $^{40}\text{K}^{87}\text{Rb}$  Fermi gas for the same parameters as in Figure 3.8. In general, the positions of minima in all plots occur for  $\theta = 90^\circ$ , and along the  $\varphi$ -direction the FS deformation monotonously decreases up to  $\theta = 90^\circ$ , after which it monotonously increases. By comparing this to the behavior in momentum space, see Figure 3.8, we can conclude that the behavior of the corresponding deformations in real and momentum space are quite different. This can be most clearly seen from Figure 3.8(a) and Figure 3.14(b), while by comparing other plots one can conclude that relative positions of minima (maxima) of the gas cloud (FS) deformations can be shifted along  $\varphi$ -direction for  $90^\circ$ . Additionally, while  $\Delta$  is always a positive quantity, we see that  $\delta_{zx}$  and  $\delta_{zy}$  can change the sign. In particular, in some plots their range is symmetric around zero, which means that there are orientations of the dipoles for which the gas cloud deformations vanish.

A related effect has been previously found, showing that the Bose gas momentum becomes distorted in the opposite sense to that of the Fermi gas [123]. There, the effect can be traced back to the differences in the quantum statistics nature of bosons and fermions. Here, however, the different behavior is due to the anisotropic nature of the DDI and its interplay with the arbitrary orientation of the dipoles and the trap

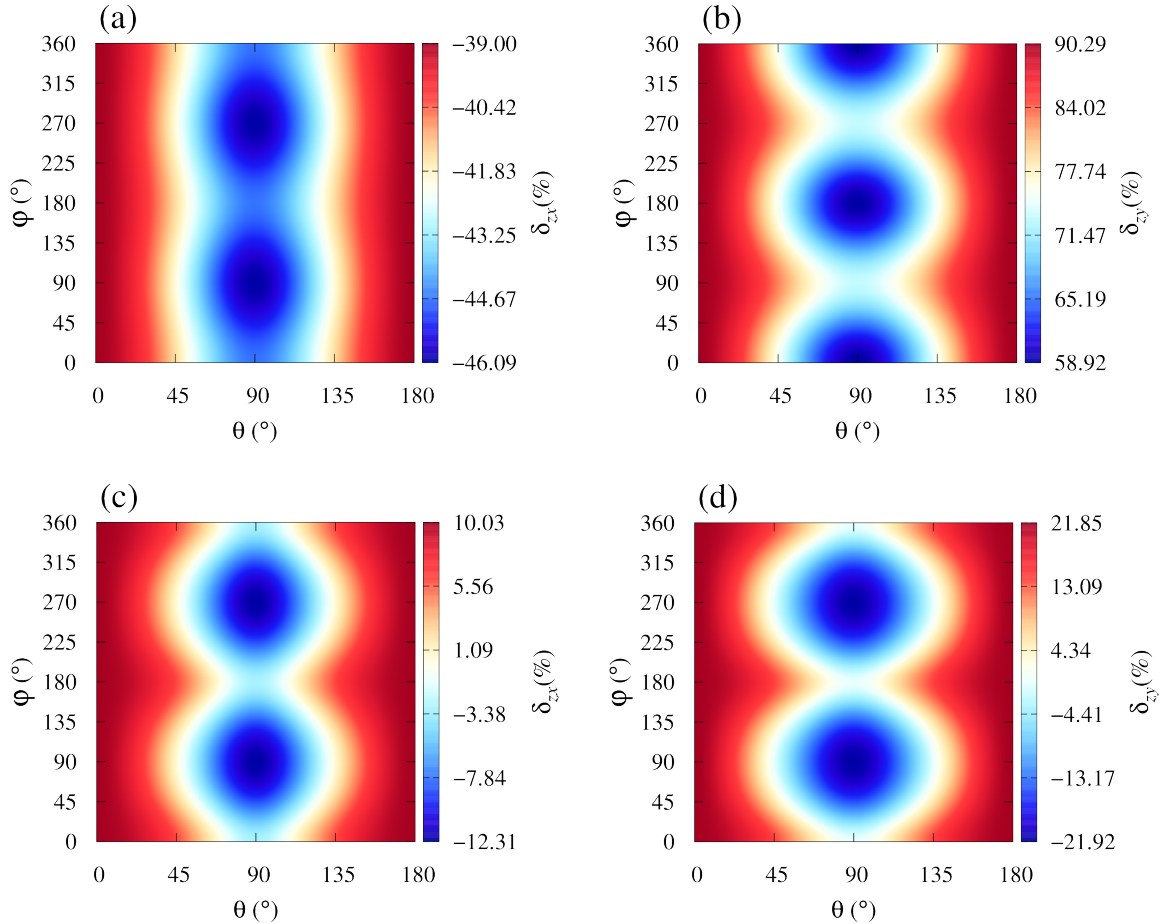


**Figure 3.14:** Angular dependence of relative cloud deformations for  $^{40}\text{K}^{87}\text{Rb}$ : (a)  $\delta_{zx}$  and (b)  $\delta_{zy}$  for parameters as in Figure 3.8(a); (c)  $\delta_{zx}$  and (d)  $\delta_{zy}$  for parameters as in Figure 3.8(b).

geometry.

### 3.5 Beyond Hartre-Fock mean-field theory

The variational approach for the Wigner function  $\nu^0(\mathbf{r}, \mathbf{k})$  used in Chapter 2 relies on the Hartree-Fock mean-field approximation. Here we estimate beyond-mean-field effects in the calculation of the FS shape and the stability of the system for strong DDI. We follow Reference [130], which derives beyond-mean-field corrections to both the FS deformation and inverse compressibility of the system. Note that this reference considers a homogeneous system, and that the estimates based on these results might not be fully applicable to a trapped system. However, the corresponding results for a trapped system are not available, and therefore Reference [130] is used as a baseline to estimate beyond-mean-field corrections in our case.

The FS deformation up to first order in the interaction strength within the theory

presented in Reference [130] is found to be

$$\Delta_h^{(1)} = \frac{k_F(0^\circ)}{k_F(90^\circ)} - 1 = \frac{1 + \frac{1}{6}P_2(1)u}{1 + \frac{1}{6}P_2(0)u} - 1, \quad (3.18)$$

while the second order of result [130, 131] reads

$$\Delta_h^{(2)} = \frac{k_F(0^\circ)}{k_F(90^\circ)} - 1 = \frac{1 + \frac{1}{6}P_2(1)u - \left[\frac{1}{180} - 0.031P_2(1) - 0.016P_4(1)\right]u^2}{1 + \frac{1}{6}P_2(0)u - \left[\frac{1}{180} - 0.031P_2(0) - 0.016P_4(0)\right]u^2}. \quad (3.19)$$

Here  $P_i$  is the Legendre polynomial of degree  $i$  and  $u$  is a dimensionless parameter given by [130]

$$u = \frac{n C_{\text{dd}}}{E_F}, \quad (3.20)$$

where  $n$  is the particle density of homogeneous system. In order to properly compare this with our case, we replace the noninteracting homogeneous Fermi energy with the Fermi energy of a noninteracting harmonically trapped Fermi gas, given by Equation (1.20). Also, the homogeneous density is identified here with the average density of the trapped system, calculated as  $N/V$ , where

$$V = \frac{4\pi}{3} R_x'' R_y'' R_z'', \quad (3.21)$$

is a volume of the TF ellipsoid in real space for specific parameters in the experimental setup. Using this, together with the definition of the relative interaction strength  $\varepsilon_{\text{dd}}$  given by Equation (3.9), we get

$$u = \frac{3^{\frac{1}{6}} \varepsilon_{\text{dd}}}{2^{\frac{7}{3}} \tilde{R}_x \tilde{R}_y \tilde{R}_z}, \quad (3.22)$$

where  $\tilde{R}_i = R_i''/R_i^0$  are earlier introduced dimensionless TF radii. We are now able to estimate beyond-mean-field corrections to the FS deformation, which we define as follows

$$\delta\Delta_h^{(2)} = \frac{\Delta_h^{(2)}}{\Delta_h^{(1)}} - 1. \quad (3.23)$$

This correction is illustrated in Figure 3.15(a) for the experimental system parameters [109] with  $d = 0.25$  D, which are used to obtain Figure 3.8(a). It turns out that corrections are just a fraction of one percent. In Figure 3.15(b) we show how the beyond-mean-field correction depends on the dipole moment, for fixed values of the tilt angles  $\theta = \varphi \in \{0^\circ, 30^\circ, 45^\circ, 60^\circ, 90^\circ\}$ . We see that  $\delta\Delta_h^{(2)}$  amounts to a few

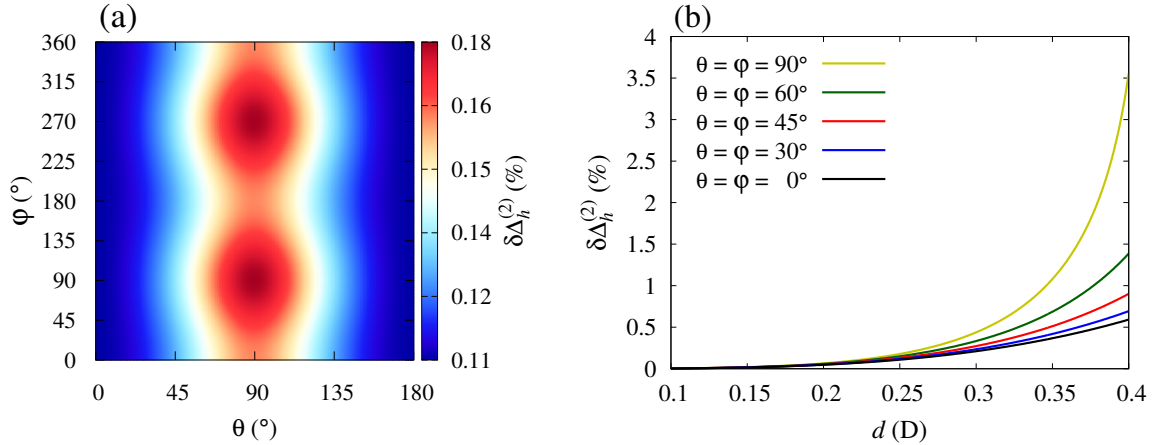


**Figure 3.15:** Beyond-mean-field corrections to the FS deformation for the trap parameters  $(\omega_x, \omega_y, \omega_z) = (63, 36, 200) \times 2\pi$  Hz of Reference [109], with  $N = 3 \times 10^4$  molecules  $^{40}\text{K}^{87}\text{Rb}$ : (a) angular dependence for  $d = 0.25$  D, which is used to obtain Figure 3.8(a); (b) the corresponding dependence on the dipole moment  $d$  for fixed values of tilt angles  $\theta$  and  $\varphi$ .

percent even for the largest values of  $d$  that can be achieved in current experiments with  $^{40}\text{K}^{87}\text{Rb}$  [109].

However, the situation is more complex when we consider the bulk modulus, i.e., the inverse compressibility  $\kappa$  of the system, which is used to estimate the stability border according to the Pomeranchuk criterion [111, 148], and whose beyond-mean-field correction is [130]

$$\delta\kappa^{(2)} = \frac{\kappa^{(2)}}{\kappa^{(1)}} - 1 \approx 0.42 u^2. \quad (3.24)$$

For instance, for system parameters used to obtain Figure 3.8(a), the corresponding correction is of the order of one percent, as can be seen in Figure 3.16(a), where we plot its angular dependence. These corrections are calculated for the dipole moment value  $d = 0.25$  D. In Figure 3.16(b) we see how the beyond-mean-field correction for the inverse compressibility depends on the strength of the dipole moment, for fixed values of the tilt angles  $\theta = \varphi \in \{0^\circ, 30^\circ, 45^\circ, 60^\circ, 90^\circ\}$ . In contrast to the FS deformation correction, the inverse compressibility correction can be much higher for larger values of  $d$ , and it strongly depends on the orientation of the dipoles. If we use a 10% threshold for the inverse compressibility correction, we see that dipole moment value can be as high as 0.35 D in the worst-case scenario, when the dipoles lie within the pancake plane, while for other values of the angles one can use even larger values of  $d$ . Taking into account that this coincides with the maximal achievable dipole moment in the current experiment with  $^{40}\text{K}^{87}\text{Rb}$  [109], for such trap configuration our mean-field theory is applicable with reasonable accuracy, as shown in Figure 3.16. However, for

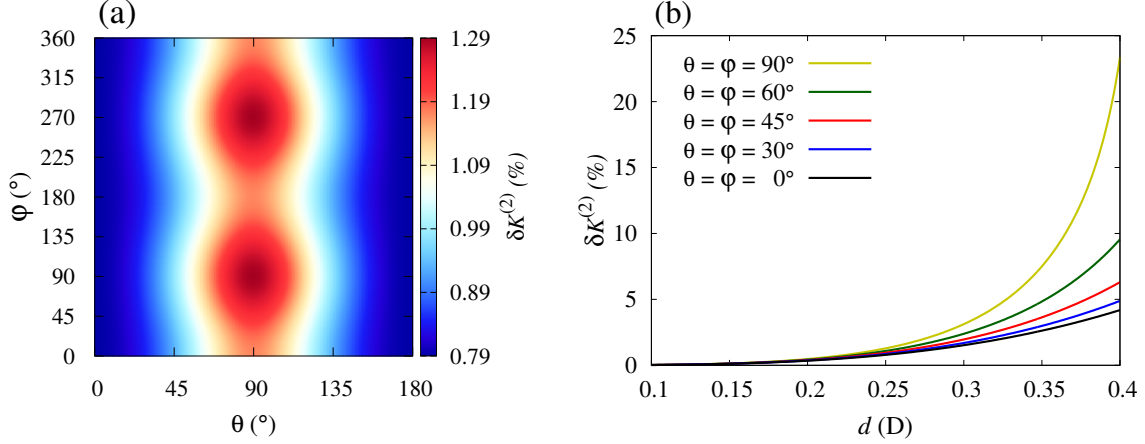


**Figure 3.16:** Beyond-mean-field corrections to the system’s inverse compressibility for the trap parameters  $(\omega_x, \omega_y, \omega_z) = (63, 36, 200) \times 2\pi$  Hz of Reference [109], with  $N = 3 \cdot 10^4$  molecules of  $^{40}\text{K}^{87}\text{Rb}$ : (a) angular dependence for  $d = 0.25$  D, which is used to obtain Figure 3.8(a); (b) the corresponding dependence on the dipole moment  $d$  for fixed values of tilt angles  $\theta$  and  $\varphi$ .

other trap configurations the mean-field theory could break down for smaller values of  $d$ , as the inverse compressibility  $\kappa$  of the system can have a strong angular dependency. One can use a similar calculation as the one presented here to make an appropriate estimate for any given trap configuration.

In summary, we conclude that the second-order terms in the DDI in the theory beyond Hartree-Fock [130, 131] yield a small correction even for polar molecules with strong DDI, although the geometry may have an impact. Furthermore, this beyond-mean-field correction turns out to destabilize the system [130, 131], so our results on the stability represent proper upper boundaries. This is in stark contrast to bosonic systems, where the quantum fluctuations are known to stabilize the system and lead, for instance, to the formation of quantum droplets in Bose-Einstein condensates of dysprosium and erbium as demonstrated recently in Stuttgart and in Innsbruck [57–60, 71, 78, 80–82]. In the outlook we mention that possible fermionic analogues of the already observed bosonic quantum droplets may exist. Although the leading beyond-mean-field correction seems to destabilize fermionic system, further studies might reveal an alternative stabilization mechanism.

---

## Dynamics of dipolar Fermi gases

---

The deformation of the Fermi sphere was recently experimentally observed in a dipolar gas of  $^{167}\text{Er}$  [48]. This measurement was based on the analysis of the momentum-state populations at equilibrium. A complementary and even richer approach to studying dipolar quantum gases considers their dynamical properties and investigates the excitation spectrum. Both of these approaches give access to FS properties and reveal deviation from the Fermi liquid picture due to strong dipolar features.

In this Chapter we present the theory which enables to describe the dynamics of dipolar Fermi gases at zero temperature in all regimes: from collisionless, over the collisional, to the hydrodynamic regime. First, we briefly present the derivation of the quantum kinetic equation, or Boltzmann equation, which we use to model the dynamics of the system.

In order to describe the time evolution of the system, we start with von Neumann equation. Instead of using density matrix approach, we introduce a time-dependent quasidistribution function which leads, due to a gradient expansion, to a semiclassical description of the system. Namely, using the perturbation theory in the first order we get mean-field description by the Hartree and Fock terms, while the second order term accounts for two-particle interactions via the binary collision integral.

Afterwards we solve the derived Boltzmann equation within the relaxation-time approximation in the vicinity of local equilibrium state by using a suitable rescaling of the equilibrium distribution. The resulting ordinary differential equations for the respective scaling parameters are then solved numerically for experimentally realistic setups and relaxation times that correspond to the collisionless, collisional, and hy-

hydrodynamic regime. The equations for the collisional regime are first solved in the approximation of a fixed relaxation time, and then this we extend by developing new approach, where the relaxation time is determined self-consistently. The presented analytical and numerical results are relevant for a studies of the dynamics of dipolar Fermi gases, and in particular for a detailed quantitative understanding of ongoing experiments.

## 4.1 Boltzmann quantum kinetic equation

The dynamics of a trapped ultracold dipolar degenerate Fermi gas can be described in terms of the quantum kinetic equation, also known as the Boltzmann equation, which was previously prominently used in the realm of nuclear [149] and plasma [150, 151] physics. It was already used to study the TOF dynamics of ultracold fermions with the contact [152, 153] and dipolar interaction [90, 93, 125], as well as their collective modes [126, 154, 155]. In this Section we present just a brief overview of the Boltzmann equation derivation at zero temperature.

Let us consider a harmonically trapped ultracold Fermi gas, where the particles can interact via a two-body interaction, in our case the DDI. If the system is described by a time-dependent pure state  $|\psi(t)\rangle$ , then its time evolution is given by

$$i\hbar\frac{\partial}{\partial t}|\psi(t)\rangle = \hat{H}|\psi(t)\rangle, \quad (4.1)$$

where  $\hat{H}$  represents the Hamilton operator of the system. It can be decomposed according to

$$\hat{H} = \hat{H}_0 + \hat{H}_{\text{int}}, \quad (4.2)$$

and written in terms of the creation and annihilation operators  $\hat{\psi}^\dagger(\mathbf{r})$  and  $\hat{\psi}(\mathbf{r})$ , which satisfy the anticommutation relations

$$\begin{aligned} \{\hat{\psi}(\mathbf{r}), \hat{\psi}(\mathbf{r}')\} &= 0, \\ \{\hat{\psi}^\dagger(\mathbf{r}), \hat{\psi}^\dagger(\mathbf{r}')\} &= 0, \\ \{\hat{\psi}(\mathbf{r}), \hat{\psi}^\dagger(\mathbf{r}')\} &= \delta(\mathbf{r} - \mathbf{r}'). \end{aligned} \quad (4.3)$$

where the blue curly brackets denote the anticommutator

$$\{\hat{A}, \hat{B}\} = \hat{A}\hat{B} + \hat{B}\hat{A}. \quad (4.4)$$

The one-particle Hamilton operator  $\hat{H}_0$  contains the kinetic energy and the trapping potential  $V_{\text{trap}}(\mathbf{r})$  in the form

$$\hat{H}_0 = \int d^3r \hat{\psi}^\dagger(\mathbf{r}) \left[ -\frac{\hbar^2 \nabla^2}{2M} + V_{\text{trap}}(\mathbf{r}) \right] \hat{\psi}(\mathbf{r}), \quad (4.5)$$

while the interaction part of the Hamilton  $\hat{H}_{\text{int}}$  describes two-body interactions via the DDI potential  $V_{\text{dd}}(\mathbf{r} - \mathbf{r}')$  according to

$$\hat{H}_{\text{int}} = \frac{1}{2} \int d^3r d^3r' \hat{\psi}^\dagger(\mathbf{r}) \hat{\psi}^\dagger(\mathbf{r}') V_{\text{dd}}(\mathbf{r} - \mathbf{r}') \hat{\psi}(\mathbf{r}') \hat{\psi}(\mathbf{r}). \quad (4.6)$$

As described in Chapter 2, we use here the Wigner function approach, which relies on the time-dependent quasidistribution, defined as a Fourier transform of the correlation function  $G^{(2)}(\mathbf{x}; \mathbf{x}'; t)$  with respect to the relative coordinate  $\mathbf{s} = \mathbf{x} - \mathbf{x}'$ ,

$$\nu(\mathbf{r}, \mathbf{k}, t) = \int d^3s e^{i\mathbf{k}\cdot\mathbf{s}} G^{(2)}\left(\mathbf{r} + \frac{\mathbf{s}}{2}; \mathbf{r} - \frac{\mathbf{s}}{2}; t\right). \quad (4.7)$$

The correlation function is defined as the ensemble average

$$G^{(2)}(\mathbf{x}; \mathbf{x}'; t) = \langle \hat{\psi}^\dagger(\mathbf{x}) \hat{\psi}(\mathbf{x}') \rangle_t \quad (4.8)$$

which is calculated as the trace over the field operators' product with respect to the underlying density matrix  $\hat{\rho}(t)$

$$\langle \hat{\psi}^\dagger(\mathbf{x}) \hat{\psi}(\mathbf{x}') \rangle_t = \text{Tr} [\hat{\rho}(t) \hat{\psi}^\dagger(\mathbf{x}) \hat{\psi}(\mathbf{x}')]. \quad (4.9)$$

Note that this approach enables also the study of systems in mixed states, not only those that are in pure states. Here the density matrix  $\hat{\rho}(t)$  contains the whole time evolution of the system in the Schrödinger picture, which is governed by the von Neumann equation

$$i\hbar \frac{\partial \hat{\rho}}{\partial t}(t) = [\hat{H}, \hat{\rho}(t)], \quad (4.10)$$

where the blue square brackets denote the commutator

$$[\hat{A}, \hat{B}] = \hat{A}\hat{B} - \hat{B}\hat{A}. \quad (4.11)$$

The resulting time evolution of the Wigner function can be computed with the help of Equations (4.7)–(4.10) by using the cyclic permutation of the operators under the

trace and the explicit form of the Hamiltonian given by Equations (4.2), (4.5), and (4.6), yielding

$$\begin{aligned}
i\hbar \frac{\partial \nu(\mathbf{r}, \mathbf{k}, t)}{\partial t} &= \iint d^3 s d^3 r' e^{i\mathbf{k}\cdot\mathbf{s}} \\
&\times \text{Tr} \left\{ \hat{\rho}(t) \left[ \hat{\psi}^\dagger \left( \mathbf{r} + \frac{\mathbf{s}}{2} \right) \hat{\psi} \left( \mathbf{r} - \frac{\mathbf{s}}{2} \right), \hat{\psi}^\dagger(\mathbf{r}') \left[ -\frac{\hbar^2 \nabla_{\mathbf{r}'}^2}{2m} + V_{\text{trap}}(\mathbf{r}') \right] \hat{\psi}(\mathbf{r}') \right] \right\} \\
&+ \frac{1}{2} \iiint d^3 s d^3 r' d^3 r'' e^{i\mathbf{k}\cdot\mathbf{s}} \\
&\times \text{Tr} \left\{ \hat{\rho}(t) V_{\text{dd}}(\mathbf{r}' - \mathbf{r}'') \left[ \hat{\psi}^\dagger \left( \mathbf{r} + \frac{\mathbf{s}}{2} \right) \hat{\psi} \left( \mathbf{r} - \frac{\mathbf{s}}{2} \right), \hat{\psi}^\dagger(\mathbf{r}') \hat{\psi}^\dagger(\mathbf{r}'') \hat{\psi}(\mathbf{r}'') \hat{\psi}(\mathbf{r}') \right] \right\}.
\end{aligned} \tag{4.12}$$

Namely, both the kinetic term  $I_{\text{kin}}$  and trapping term  $I_{\text{trap}}$  contain anticommutators involving four field operators, which leads to ensemble averages of two field operators. Together with Equations (4.7) and (4.8) this leads to the expressions containing the gradient of the Wigner function,

$$I_{\text{kin}} = -i\hbar^2 \frac{\mathbf{k}}{M} \cdot \nabla_{\mathbf{r}} \nu(\mathbf{r}, \mathbf{k}, t), \tag{4.13}$$

$$I_{\text{trap}} = i\nabla_{\mathbf{r}} V_{\text{trap}}(\mathbf{r}) \cdot \nabla_{\mathbf{k}} \nu(\mathbf{r}, \mathbf{k}, t). \tag{4.14}$$

In the above equation for the trapping term we use gradient expansions, which assume that the Wigner function  $\nu(\mathbf{r}, \mathbf{k}, t)$  is slowly varying in its spatial argument. In this way the part of the quantum-mechanical information about the system is lost, which yields a semiclassical Wigner function [156]. We also use this assumption in all further calculations.

Using this and calculating the commutator of six operators in the interaction term Equation (4.12) simplifies to

$$\begin{aligned}
\frac{\partial \nu(\mathbf{r}, \mathbf{k}, t)}{\partial t} + \frac{\hbar \mathbf{k}}{M} \cdot \nabla_{\mathbf{r}} \nu(\mathbf{r}, \mathbf{k}, t) - \frac{1}{\hbar} \nabla_{\mathbf{r}} V_{\text{trap}}(\mathbf{r}) \cdot \nabla_{\mathbf{k}} \nu(\mathbf{r}, \mathbf{k}, t) &= \frac{1}{i\hbar} \int d^3 s \int d^3 x e^{i\mathbf{k}\cdot\mathbf{s}} \\
&\times \left[ V_{\text{dd}} \left( \mathbf{x} - \mathbf{r} + \frac{\mathbf{s}}{2} \right) - V_{\text{dd}} \left( \mathbf{x} - \mathbf{r} - \frac{\mathbf{s}}{2} \right) \right] \text{Tr} \left[ \hat{\rho}(t) \hat{\psi}^\dagger \left( \mathbf{r} + \frac{\mathbf{s}}{2} \right) \hat{\psi}^\dagger(\mathbf{x}) \hat{\psi}(\mathbf{x}) \hat{\psi} \left( \mathbf{r} - \frac{\mathbf{s}}{2} \right) \right].
\end{aligned} \tag{4.15}$$

The right-hand side of the above equation shows the main problem to derive a closed-form equation that determines the time evolution of the Wigner function. Namely, its time derivative, i.e., the time derivative of the average of two field operators, leads to an average of four-field operators. In the next step, the time derivative of four-field operator average would lead to a six-field operator average, and so on. With such a

hierarchical structure it is not possible to get a closed set of equations without further approximations. Thus, we have to cut hierarchy and approximate this term with the help of the perturbation theory in the interaction. However, this can only be done in the case of weak interparticle interactions, thereby limiting the validity of the resulting quantum kinetic equation. If we apply the perturbation theory to the first order in the interaction potential, we get the self-consistent Hartree-Fock dynamic mean-field theory, where the direct and exchange interaction terms read

$$I_{\text{dd}}^{\text{D}} = \nabla_{\mathbf{r}} \left[ \int d^3x V_{\text{dd}}(\mathbf{r} - \mathbf{x}) n(\mathbf{x}, t) \right] \cdot \nabla_{\mathbf{k}} \nu(\mathbf{r}, \mathbf{k}, t), \quad (4.16)$$

$$\begin{aligned} I_{\text{dd}}^{\text{E}} = & \nabla_{\mathbf{k}} \left[ \int \frac{d^3k'}{(2\pi)^3} \nu(\mathbf{r}, \mathbf{k}', t) \tilde{V}_{\text{dd}}(\mathbf{k} - \mathbf{k}') \right] \cdot \nabla_{\mathbf{r}} \nu(\mathbf{r}, \mathbf{k}, t) \\ & - \nabla_{\mathbf{r}} \left[ \int \frac{d^3k'}{(2\pi)^3} \nu(\mathbf{r}, \mathbf{k}', t) \tilde{V}_{\text{dd}}(\mathbf{k} - \mathbf{k}') \right] \cdot \nabla_{\mathbf{k}} \nu(\mathbf{r}, \mathbf{k}, t). \end{aligned} \quad (4.17)$$

The the second order perturbation theory in the interaction potential yields well known collision integral  $I_{\text{coll}}[\nu](\mathbf{r}, \mathbf{k}, t)$ , which describes collisions between two particles, and has the following form [157, p. 54]

$$\begin{aligned} I_{\text{coll}}[\nu] = & \int \frac{d^3k_2}{(2\pi)^3} \int \frac{d^3k_3}{(2\pi)^3} \int \frac{d^3k_4}{(2\pi)^3} \frac{1}{2} \left[ \tilde{V}_{\text{dd}}(\mathbf{k} - \mathbf{k}_3) - \tilde{V}_{\text{dd}}(\mathbf{k} - \mathbf{k}_4) \right]^2 \\ & \times 2\pi \delta(E_{\mathbf{k}} + E_{\mathbf{k}_2} - E_{\mathbf{k}_3} - E_{\mathbf{k}_4}) (2\pi)^3 \delta(\mathbf{k} + \mathbf{k}_2 - \mathbf{k}_3 - \mathbf{k}_4) \\ & \times [(1 - \nu)(1 - \nu_2)\nu_3\nu_4 - \nu\nu_2(1 - \nu_3)(1 - \nu_4)], \end{aligned} \quad (4.18)$$

where  $\nu = \nu(\mathbf{r}, \mathbf{k}, t)$ ,  $\nu_i = \nu(\mathbf{r}, \mathbf{k}_i, t)$ , and

$$E_{\mathbf{k}} = \frac{\hbar^2 \mathbf{k}^2}{2M} + V_{\text{trap}}(\mathbf{r}). \quad (4.19)$$

Delta functions in the above expression ensure the momentum and energy conservation during the collision process. However, the energy conservation delta function shows precisely the limit of this form of the collision integral. Although the total energy of the system should be conserved, here just the kinetic and trapping energy sum is conserved. Thus, the interaction energy is neglected, which can only be justified if we assume weak two-body interactions. Note that the minus sign between the potentials  $\tilde{V}_{\text{dd}}$  in Equation (4.18) reflects the fact that we consider fermions and, therefore, we have to deal with anticommutators. In contrast to this, in the case of a bosonic gas, when one has to deal with commutators, there would appear a plus sign instead of the minus sign.

Finally, if we combine the intermediate result (4.15) with Equations (4.16)-(4.18), we obtain the quantum kinetic equation in the following form

$$\begin{aligned} \frac{\partial \nu(\mathbf{r}, \mathbf{k}, t)}{\partial t} + \frac{\hbar \mathbf{k}}{M} \nabla_{\mathbf{r}} \nu(\mathbf{r}, \mathbf{k}, t) + \frac{1}{\hbar} \nabla_{\mathbf{k}} V(\mathbf{r}, \mathbf{k}, t) \nabla_{\mathbf{r}} \nu(\mathbf{r}, \mathbf{k}, t) \\ - \frac{1}{\hbar} \nabla_{\mathbf{r}} V(\mathbf{r}, \mathbf{k}, t) \nabla_{\mathbf{k}} \nu(\mathbf{r}, \mathbf{k}, t) = I_{\text{coll}}[\nu](\mathbf{r}, \mathbf{k}, t), \end{aligned} \quad (4.20)$$

where the mean-field potential  $V(\mathbf{r}, \mathbf{k}, t)$  is written in a condensed form, such that it includes the external trap potential, as well as the respective mean-field terms,

$$\begin{aligned} V(\mathbf{r}, \mathbf{k}, t) &= V_{\text{trap}}(\mathbf{r}) + V_{\text{mf}}(\mathbf{r}, \mathbf{k}, t) \\ &= V_{\text{trap}}(\mathbf{r}) + \int d^3 r' V_{\text{dd}}(\mathbf{r} - \mathbf{r}') n(\mathbf{r}', t) - \int \frac{d^3 k'}{(2\pi)^3} \tilde{V}_{\text{dd}}(\mathbf{k} - \mathbf{k}') \nu(\mathbf{r}, \mathbf{k}', t). \end{aligned} \quad (4.21)$$

The first term in the mean-field potential represents the direct Hartree term, containing the interaction potential  $V_{\text{dd}}$  and the spatial density  $n(\mathbf{r}, t)$  given by Equation (2.3), and is thus calculated purely in real space. The second term corresponds to the Fock exchange term and contains the Fourier transform of the interaction potential  $\tilde{V}_{\text{dd}}$ . The Fock term is calculated purely in momentum space.

## 4.2 Scaling ansatz

The time evolution of the Wigner function  $\nu(\mathbf{r}, \mathbf{k}, t)$  can be approximately calculated by solving the derived Boltzmann equation, as suggested in Reference [126]. Numerically this is tremendously difficult task due to substantial memory requirements, due to the fact that the Wigner function is defined in 6D phase space. Also analytically this equation cannot be solved, and we have to resort to certain approximations in order to obtain the solution. Therefore, we will assume that the functional form of the Wigner distribution always corresponds to that of the system in local equilibrium, and that the dynamics can be modeled by introducing only the appropriate scaling of the coordinates and momenta in this functional form. Since, Equation (4.20) is a nonlinear integro-partial differential equation, by a such rescaling, we get ordinary differential equations for the scaling parameters, which can then be solved numerically. In this way, we combine an analytic approximation with a numerical approach in order to be able to solve the underlying quantum kinetic equation.

Another problem is how to deal with the complexities of the collision integral. In

recent years, approximative approaches were developed such that, instead of using full expression for the collision integral, which would require a detailed modeling of scattering processes between atoms or molecules, one simply uses the relaxation-time approximation [12, 158] in the form

$$I_{\text{coll}}[\nu](\mathbf{r}, \mathbf{k}, t) = -\frac{\nu(\mathbf{r}, \mathbf{k}, t) - \nu^{\text{le}}(\mathbf{r}, \mathbf{k})}{\tau}. \quad (4.22)$$

Here  $\tau$  denotes the relaxation time, which is related to the average time between collisions, and  $\nu^{\text{le}}$  stands for the distribution function corresponding to local equilibrium. The physical idea is that the particles interact via collisions and exchange energy and momentum, which eventually leads to a relaxation of the system into a local equilibrium state in which the collisions will no longer change the distribution function. In contrast to that, the local velocity field or the density can still be spatially dependent. The local thermodynamical equilibrium of a dipolar Fermi gas is defined by  $I_{\text{coll}}[\nu^{\text{le}}] = 0$ . If the time-dependent distribution function  $\nu(\mathbf{r}, \mathbf{k}, t)$  is close to the global equilibrium  $\nu^0(\mathbf{r}, \mathbf{k})$ , it can be approximately expressed by a suitable rescaling of the equilibrium distribution [158]:

$$\nu(\mathbf{r}, \mathbf{k}, t) \rightarrow \Gamma(t)\nu^0(\mathcal{R}(\mathbf{r}, t), \mathcal{K}(\mathbf{r}, \mathbf{k}, t)), \quad (4.23)$$

with the rescaled variables defined by

$$\mathcal{R}_i(\mathbf{r}, t) = \frac{r_i}{b_i(t)}, \quad (4.24)$$

and

$$\mathcal{K}_i(\mathbf{r}, \mathbf{k}, t) = \frac{1}{\sqrt{\Theta_i(t)}} \left[ k_i - \frac{M\dot{b}_i(t)r_i}{\hbar b_i(t)} \right], \quad (4.25)$$

where  $b_i(t)$  and  $\Theta_i(t)$  are time-dependent dimensionless scaling parameters. The normalization factor  $\Gamma(t)$  is given by [158]

$$\Gamma(t)^{-1} = \bar{b}(t)^3 \bar{\Theta}(t)^{\frac{3}{2}}. \quad (4.26)$$

The second term in the brackets of Equation (4.25) is proportional to the local velocity. Namely, taking the time derivative of Equation (4.24) we get

$$\dot{\mathcal{R}}_i(\mathbf{r}, t) \sim k_i - \frac{M\dot{b}_i(t)r_i}{\hbar b_i(t)}, \quad (4.27)$$

with  $k_i = M\dot{r}_i/\hbar$  [122, 159]. Subtracting the drift velocity  $\dot{b}_i(t)r_i/b_i(t)$  in the ansatz (4.25) it is ensured that the momentum  $\mathcal{K}(\mathbf{r}, \mathbf{k}, t)$  is not affected by the time dependence of the ansatz for  $\mathcal{R}(\mathbf{r}, t)$ . The time dependence of the Wigner function is governed by the scaling parameters  $b_i(t)$  and  $\Theta_i(t)$ , which can be connected with the time-dependent deformations of the spatial and momentum variables, respectively. Inserting the ansatz (4.24)-(4.26) into Equation (4.21) yields

$$V_{b\Theta}(\mathcal{R}, \mathcal{K}) = V_{\text{trap}}(b, \mathcal{R}) + V_{\text{mf}, b\Theta}(\mathcal{R}, \mathcal{K}) = V_{\text{trap}}(b_x \mathcal{R}_x, b_y \mathcal{R}_y, b_z \mathcal{R}_z) + \int d^3 \mathcal{R}' n^0(\mathcal{R}') V_{\text{dd}}(b, \mathcal{R} - \mathcal{R}') - \frac{1}{\bar{b}^3} \int \frac{d^3 \mathcal{K}'}{(2\pi)^3} \nu^0(\mathcal{R}, \mathcal{K}') \tilde{V}_{\text{dd}}(\Theta, \mathcal{K} - \mathcal{K}'), \quad (4.28)$$

where  $n^0(\mathbf{r})$  denotes the spatial density in local equilibrium, the rescaled DDI potential is

$$V_{\text{dd}}(b, \mathcal{R} - \mathcal{R}') = V_{\text{dd}} \left[ b_x (\mathcal{R}_x - \mathcal{R}'_x), b_y (\mathcal{R}_y - \mathcal{R}'_y), b_z (\mathcal{R}_z - \mathcal{R}'_z) \right], \quad (4.29)$$

and the rescaled Fourier-transformed DDI potential is given by

$$\tilde{V}_{\text{dd}}(\Theta, \mathcal{K} - \mathcal{K}') = \tilde{V}_{\text{dd}} \left[ \Theta_x^{\frac{1}{2}} (\mathcal{K}_x - \mathcal{K}'_x), \Theta_y^{\frac{1}{2}} (\mathcal{K}_y - \mathcal{K}'_y), \Theta_z^{\frac{1}{2}} (\mathcal{K}_z - \mathcal{K}'_z) \right]. \quad (4.30)$$

It is important to note here that the Fourier transformation and rescaling do not commute, so the correct order of performing these two operations is very important.

Substituting the scaling ansatz (4.24)-(4.26) into all terms of Equation (4.20) leads to

$$\begin{aligned} \frac{\partial \nu(\mathbf{r}, \mathbf{k}, t)}{\partial t} &= \dot{\Gamma} \nu^0(\mathcal{R}, \mathcal{K}) + \Gamma \frac{\partial \nu^0(\mathcal{R}, \mathcal{K})}{\partial t} \\ &= -\Gamma \sum_i \left( \frac{1}{2} \frac{\dot{\Theta}_i}{\Theta_i} + \frac{\dot{b}_i}{b_i} \right) + \Gamma \sum_i \left( \frac{\partial \nu^0(\mathcal{R}, \mathcal{K})}{\partial \mathcal{R}_i} \frac{\partial \mathcal{R}_i}{\partial t} + \frac{\partial \nu^0(\mathcal{R}, \mathcal{K})}{\partial \mathcal{K}_i} \frac{\partial \mathcal{K}_i}{\partial t} \right), \end{aligned} \quad (4.31)$$

$$\begin{aligned} \frac{\hbar \mathbf{k}}{M} \nabla_{\mathbf{r}} \nu(\mathbf{r}, \mathbf{k}, t) &= \frac{\hbar}{M} \sum_i k_i \frac{\partial \nu(\mathbf{r}, \mathbf{k}, t)}{r_i} \\ &= \frac{\Gamma \hbar}{M} \sum_i \left( \Theta_i^{\frac{1}{2}} \mathcal{K}_i + \frac{M \dot{b}_i \mathcal{R}_i}{\hbar} \right) \left( \frac{\partial \nu^0(\mathcal{R}, \mathcal{K})}{\partial \mathcal{R}_i} \frac{\partial \mathcal{R}_i}{\partial r_i} + \frac{\partial \nu^0(\mathcal{R}, \mathcal{K})}{\partial \mathcal{K}_i} \frac{\partial \mathcal{K}_i}{\partial r_i} \right), \end{aligned} \quad (4.32)$$

$$\begin{aligned} \frac{1}{\hbar} \nabla_{\mathbf{k}} V(\mathbf{r}, \mathbf{k}, t) \nabla_{\mathbf{r}} \nu(\mathbf{r}, \mathbf{k}, t) - \frac{1}{\hbar} \nabla_{\mathbf{r}} V(\mathbf{r}, \mathbf{k}, t) \nabla_{\mathbf{k}} \nu(\mathbf{r}, \mathbf{k}, t) \\ = \frac{\Gamma}{\hbar} \sum_i \left( \frac{\partial V_{b\Theta}(\mathcal{R}, \mathcal{K})}{\partial \mathcal{K}_i} \frac{\partial \nu^0(\mathcal{R}, \mathcal{K})}{\partial \mathcal{R}_i} - \frac{\partial V_{b\Theta}(\mathcal{R}, \mathcal{K})}{\partial \mathcal{R}_i} \frac{\partial \nu^0(\mathcal{R}, \mathcal{K})}{\partial \mathcal{K}_i} \right) \frac{\partial \mathcal{R}_i}{\partial r_i} \frac{\partial \mathcal{K}_i}{\partial k_i}, \end{aligned} \quad (4.33)$$

$$I_{\text{coll}}[\nu] = -\frac{\Gamma \nu^0(\mathcal{R}, \mathcal{K}) - \Gamma^{\text{le}} \nu^{\text{le}}(\mathcal{R}, \mathcal{K})}{\tau}, \quad (4.34)$$

which, together with

$$\frac{\partial \mathcal{R}_i}{\partial t} = -\frac{\dot{b}_i \mathcal{R}_i}{b_i}, \quad (4.35)$$

$$\frac{\partial \mathcal{K}_i}{\partial t} = -\frac{\dot{\Theta}_i \mathcal{K}_i}{2\Theta_i} - \frac{M\ddot{b}_i \mathcal{R}_i}{\hbar\Theta_i^{\frac{1}{2}}} + \frac{M\dot{b}_i^2 \mathcal{R}_i}{\hbar b_i \Theta_i^{\frac{1}{2}}}, \quad (4.36)$$

$$\frac{\partial \mathcal{R}_i}{\partial r_i} = \frac{1}{b_i}, \quad (4.37)$$

$$\frac{\partial \mathcal{R}_i}{\partial k_i} = 0, \quad (4.38)$$

$$\frac{\partial \mathcal{K}_i}{\partial r_i} = \frac{M\dot{b}_i}{\hbar\Theta_i^{\frac{1}{2}} b_i}, \quad (4.39)$$

$$\frac{\partial \mathcal{K}_i}{\partial k_i} = \frac{1}{\Theta_i^{\frac{1}{2}}}, \quad (4.40)$$

yields the rescaled Boltzmann equation in the following form

$$\begin{aligned} \dot{\Gamma}\nu^0 + \Gamma \sum_i \frac{\partial \nu^0}{\partial \mathcal{R}_i} \frac{\hbar \mathcal{K}_i \Theta_i^{\frac{1}{2}}}{M b_i} - \Gamma \sum_i \frac{\partial \nu^0}{\partial \mathcal{K}_i} \left[ \mathcal{K}_i \left( \frac{1}{2} \frac{\dot{\Theta}_i}{\Theta_i} + \frac{\dot{b}_i}{b_i} \right) + \frac{\mathcal{R}_i M \ddot{b}_i}{\hbar \Theta_i^{\frac{1}{2}}} + \frac{1}{\hbar b_i \Theta_i^{\frac{1}{2}}} \frac{\partial V_{\text{trap}}}{\partial \mathcal{R}_i} \right] \\ - \frac{\Gamma}{\hbar} \sum_i \frac{1}{b_i \Theta_i^{\frac{1}{2}}} \left[ \frac{\partial \nu^0}{\partial \mathcal{K}_i} \frac{\partial V_{\text{mf}, b\Theta}}{\partial \mathcal{R}_i} - \frac{\partial \nu^0}{\partial \mathcal{R}_i} \frac{\partial V_{\text{mf}, b\Theta}}{\partial \mathcal{K}_i} \right] = I_{\text{coll}}[\nu]. \end{aligned} \quad (4.41)$$

Multiplying Equation (4.41) by  $\mathcal{K}_i^2$  and integrating over the phase-space variables leads to a differential equation for the scaling parameters  $\Theta_i(t)$ ,

$$\frac{\dot{\Theta}_i}{\Theta_i} + 2\frac{\dot{b}_i}{b_i} = \frac{1}{\Gamma N \langle \mathcal{K}_i^2 \rangle^0} \iint \frac{d^3 \mathcal{R} d^3 \mathcal{K}}{(2\pi)^3} \mathcal{K}_i^2 I_{\text{coll}}[\nu], \quad (4.42)$$

where  $\langle \mathcal{K}_i^2 \rangle^0$  denotes the phase-space average of variable  $\mathcal{K}_i^2$  with respect to the equilibrium distribution function  $\nu^0$ , calculated in Appendix D.1. Note that a lot of terms vanish due to the fact that integral of odd function on a symmetric interval is zero. To assess this, we also use the fact that  $\nu^0(\mathcal{R}, \mathcal{K})$  is even function in both coordinates and momenta, and that the same applies to the DDI potential and its Fourier transform. With this, inserting the relaxation-time approximation (4.34) into the right-hand side of Equation (4.42) leads to

$$\frac{\dot{\Theta}_i}{\Theta_i} + 2\frac{\dot{b}_i}{b_i} = -\frac{1}{\tau} (\Theta_i - \Theta_i^{\text{le}}). \quad (4.43)$$

Similarly, multiplying Equation (4.41) instead by  $\mathcal{R}_i \mathcal{K}_i$  and integrating again over the phase-space leads to an integro-differential equation for the scaling parameters  $b_i(t)$ ,

$$\begin{aligned}
& -\Gamma \frac{\hbar \Theta_i^{\frac{1}{2}}}{M b_i} N \langle \mathcal{K}_i^2 \rangle^0 + \frac{\Gamma M \ddot{b}_i}{\hbar \Theta_i^{\frac{1}{2}}} N \langle \mathcal{R}_i^2 \rangle^0 + \frac{\Gamma}{\hbar b_i \Theta_i^{\frac{1}{2}}} \int \frac{d^3 \mathcal{R} d^3 \mathcal{K}}{(2\pi)^3} \mathcal{R}_i \frac{\partial V_{\text{trap}}}{\partial \mathcal{R}_i} \nu^0 \\
& - \frac{\Gamma}{\hbar} \iint \frac{d^3 \mathcal{R} d^3 \mathcal{K}}{(2\pi)^3} \mathcal{R}_i \mathcal{K}_i \sum_j \frac{1}{b_j \Theta_j^{\frac{1}{2}}} \left( \frac{\partial \nu^0}{\partial \mathcal{K}_j} \frac{\partial V_{\text{mf}, b\Theta}}{\partial \mathcal{R}_j} - \frac{\partial \nu^0}{\partial \mathcal{R}_j} \frac{\partial V_{\text{mf}, b\Theta}}{\partial \mathcal{K}_j} \right) = 0. \quad (4.44)
\end{aligned}$$

Here  $\langle \mathcal{R}_i^2 \rangle^0$  denotes the phase-space average of variable  $\mathcal{R}_i^2$  with respect to the equilibrium distribution function  $\nu^0$ , calculated also in Appendix D.1. Since  $\mathcal{R}_i \mathcal{K}_i$  is a conserved quantity of the collision integral, the right-hand side of Equation (4.44) is zero, as argued in Section 3.2 of Reference [160].

The trapping term can be evaluated as follows

$$\begin{aligned}
& \iint \frac{d^3 \mathcal{R} d^3 \mathcal{K}}{(2\pi)^3} \mathcal{R}_i \frac{\partial V_{\text{trap}}(b, \mathcal{R})}{\partial \mathcal{R}_i} \nu^0(\mathcal{R}, \mathcal{K}) \\
& = \iint \frac{d^3 \mathcal{R} d^3 \mathcal{K}}{(2\pi)^3} M \omega_i^2 b_i^2 \mathcal{R}_i^2 \nu^0(\mathcal{R}, \mathcal{K}) = M \omega_i^2 b_i^2 N \langle \mathcal{R}_i^2 \rangle^0. \quad (4.45)
\end{aligned}$$

Using the Fourier transformation to rewrite both mean-field terms in a more compact form, Equations (4.44) for the scaling parameters  $b_i(t)$  can be further simplified to

$$\ddot{b}_i + \omega_i^2 b_i - \frac{\hbar^2 \Theta_i \sum_j \mathbb{R}_{ij}^{\prime 2} K_j^{\prime 2}}{M^2 b_i \sum_j \mathbb{R}_{ij}^{\prime \prime 2} R_j^{\prime \prime 2}} + 8 \frac{B_i^{\text{D}}(b) + B_i^{\text{E}}(b, \Theta)}{M N b_i \sum_j \mathbb{R}_{ij}^{\prime \prime 2} R_j^{\prime \prime 2}} = 0, \quad (4.46)$$

where  $B_i^{\text{D}}(b)$  and  $B_i^{\text{E}}(b, \Theta)$  are the integrals corresponding to the Hartree direct (D) and Fock exchange (E) term, given by

$$B_i^{\text{D}}(b) = \frac{1}{2} \int \frac{d^3 \mathcal{K}}{(2\pi)^3} \tilde{W}_i(b, \mathcal{K}) \tilde{n}^0(\mathcal{K}) \tilde{n}^0(-\mathcal{K}), \quad (4.47)$$

$$B_i^{\text{E}}(b, \Theta) = -\frac{1}{2b^3} \iiint \frac{d^3 \mathcal{R} d^3 \mathcal{K} d^3 \mathcal{K}'}{(2\pi)^6} \nu^0(\mathcal{R}, \mathcal{K}) \nu^0(\mathcal{R}, \mathcal{K}') \tilde{W}_i(\Theta, \mathcal{K} - \mathcal{K}'). \quad (4.48)$$

Here  $\tilde{n}^0(\mathcal{K})$  represents the Fourier transform of the density, while quantities  $\tilde{W}_i(b, \mathcal{K})$  and  $\tilde{W}_i(\Theta, \mathcal{K} - \mathcal{K}')$  are defined as follows

$$\begin{aligned}
\tilde{W}_i(b, \mathcal{K}) & = \int d^3 \mathcal{R} e^{-i\mathcal{K} \cdot \mathcal{R}} \mathcal{R}_i \frac{\partial V_{\text{dd}}(b_x \mathcal{R}_x, b_y \mathcal{R}_y, b_z \mathcal{R}_z)}{\partial \mathcal{R}_i} \\
& = -\frac{1}{b^3} \frac{\partial}{\partial \mathcal{K}_i} \left[ \mathcal{K}_i \tilde{V}_{\text{dd}} \left( \frac{\mathcal{K}_x}{b_x}, \frac{\mathcal{K}_y}{b_y}, \frac{\mathcal{K}_z}{b_z} \right) \right]. \quad (4.49)
\end{aligned}$$

$$\begin{aligned}
\tilde{W}_i(\Theta, \mathcal{K} - \mathcal{K}') & = \left( \int d^3 \mathcal{R} e^{-i\mathcal{R} \cdot \mathcal{Q}} \mathcal{R}_i \frac{\partial V_{\text{dd}}}{\partial \mathcal{R}_i} \right) \Big|_{\mathcal{Q}_i = \Theta_i^{\frac{1}{2}} (\mathcal{K}_i - \mathcal{K}'_i)} \\
& = -\frac{\partial}{\partial \mathcal{K}_i} \left[ \mathcal{K}_i \tilde{V}_{\text{dd}} \left( \Theta_x^{\frac{1}{2}} (\mathcal{K}_x - \mathcal{K}'_x), \Theta_y^{\frac{1}{2}} (\mathcal{K}_y - \mathcal{K}'_y), \Theta_z^{\frac{1}{2}} (\mathcal{K}_z - \mathcal{K}'_z) \right) \right]. \quad (4.50)
\end{aligned}$$

Note that in the definitions of  $\tilde{W}_i(b, \boldsymbol{\mathcal{K}})$  and  $\tilde{W}_i(\Theta, \boldsymbol{\mathcal{K}} - \boldsymbol{\mathcal{K}}')$  the order of performing a Fourier transformation and rescaling is opposite. This is important since these two operations do not commute, as mentioned before.

### 4.2.1 Hartree and Fock kinetic integrals

In this Section we study the Hartree direct kinetic integral  $B_i^{\text{D}}(b)$ , and the Fock exchange kinetic integral  $B_i^{\text{E}}(b, \Theta)$ . Since both of them are similar to the energy integrals calculated in Sections 2.2.3 and 2.2.4, some of the previous results can be reused. For instance, the Fourier transform of the density  $\tilde{n}^0(\boldsymbol{\mathcal{K}})$  is calculated in Section 2.2.3, and the explicit result is given by Equation (2.48), which has a symmetry

$$\tilde{n}^0(\boldsymbol{\mathcal{K}}) = \tilde{n}^0(-\boldsymbol{\mathcal{K}}). \quad (4.51)$$

Together with the particle number conservation, given by Equation (2.17), this leads to the simplified expression for the Hartree integral (4.47),

$$\begin{aligned} B_i^{\text{D}}(b) = & -\frac{1}{2} \frac{48^2 N^2 C_{\text{dd}}}{3\bar{b}^3} \int \frac{d^3 \mathcal{K}}{(2\pi)^3} \frac{\partial}{\partial \mathcal{K}_i} \left\{ \mathcal{K}_i \left[ \frac{3 \left( \sum_n \mathbb{R}_{zn}^T \frac{\mathcal{K}_n}{b_n} \right)^2}{\frac{\mathcal{K}_x^2}{b_x^2} + \frac{\mathcal{K}_y^2}{b_y^2} + \frac{\mathcal{K}_z^2}{b_z^2}} - 1 \right] \right\} \\ & \times \frac{J_3^2 \left[ \left( c_x''^2 R_x''^2 + c_y''^2 R_y''^2 + c_z''^2 R_z''^2 \right)^{\frac{1}{2}} \right]}{\left( c_x''^2 R_x''^2 + c_y''^2 R_y''^2 + c_z''^2 R_z''^2 \right)^3}, \end{aligned} \quad (4.52)$$

with  $\mathbf{c}'' = \mathbb{R}''^T \boldsymbol{\mathcal{K}}$ . Using substitution of variables  $\boldsymbol{\mathcal{K}} = \mathbb{R}'' \mathbf{q}$  and the chain rule, the derivative  $\partial/\partial \mathcal{K}_i$  transforms to

$$\frac{\partial}{\partial \mathcal{K}_i} = \sum_j \frac{\partial q_j}{\partial \mathcal{K}_i} \frac{\partial}{\partial q_j} = \sum_j \mathbb{R}_{ji}''^T \frac{\partial}{\partial q_j}, \quad (4.53)$$

which leads to

$$\begin{aligned} B_i^{\text{D}}(b) = & -\frac{48 N^2 C_{\text{dd}}}{\pi^3 \bar{b}^3} \int d^3 q \left( \sum_j \mathbb{R}_{ji}''^T \frac{\partial}{\partial q_j} \right) \left\{ \left( \sum_l \mathbb{R}_{il}'' q_l \right) \left[ \frac{3 \left( \sum_{n,m} \mathbb{R}_{zn}^T \mathbb{R}_{nm}'' \frac{q_m}{b_n} \right)^2}{\sum_{n,r,s} \mathbb{R}_{nr}'' \mathbb{R}_{ns}'' \frac{q_r q_s}{b_n^2}} - 1 \right] \right\} \\ & \times \frac{J_3^2 \left[ \left( q_x^2 R_x''^2 + q_y^2 R_y''^2 + q_z^2 R_z''^2 \right)^{\frac{1}{2}} \right]}{\left( q_x^2 R_x''^2 + q_y^2 R_y''^2 + q_z^2 R_z''^2 \right)^3}. \end{aligned} \quad (4.54)$$

Now, performing a substitution  $u_i = q_i R''_i$ , we obtain

$$B_i^D(b) = -\frac{48N^2 C_{dd}}{\pi^3 \bar{R}''^3 \bar{b}^3} \int d^3 u \frac{J_3^2(u)}{u^6} \left( 1 + \sum_{j,l} \mathbb{R}''_{ji}{}^T \mathbb{R}''_{il} \frac{u_l}{R''_l} \frac{\partial}{\partial \frac{u_j}{R''_j}} \right) \left[ \frac{3 \left( \sum_{n,m} \mathbb{R}''_{zn}{}^T \mathbb{R}''_{nm} \frac{u_m}{R''_m b_n} \right)^2}{\sum_{n,r,s} \mathbb{R}''_{nr} \mathbb{R}''_{ns} \frac{u_r u_s}{R''_r R''_s b_n^2}} - 1 \right]. \quad (4.55)$$

Switching to spherical coordinates,  $u_i = \mathbb{R}_{iz}(\vartheta, \phi)u$ , and using the identity given by Equation (2.52), after integration over  $u$  the last expression simplifies to

$$B_i^D(b) = -\frac{6N^2 c_0}{\bar{R}''^3 \bar{b}^3} \frac{1}{4\pi} \int \sin \vartheta d\vartheta d\phi \left[ 1 + \sum_{j,l} \mathbb{R}''_{ji}{}^T \mathbb{R}''_{il} \frac{\mathbb{R}_{lz}(\vartheta, \phi)}{R''_l} \frac{\partial}{\partial \frac{\mathbb{R}_{jz}(\vartheta, \phi)}{R''_j}} \right] \times \left\{ \frac{3 \left[ \sum_{n,m} \mathbb{R}''_{zn}{}^T \mathbb{R}''_{nm} \frac{\mathbb{R}_{mz}(\vartheta, \phi)}{R''_m b_n} \right]^2}{\sum_{n,r,s} \mathbb{R}''_{nr} \mathbb{R}''_{ns} \frac{\mathbb{R}_{rz}(\vartheta, \phi) \mathbb{R}_{sz}(\vartheta, \phi)}{R''_r R''_s b_n^2}} - 1 \right\}. \quad (4.56)$$

Unfortunately, the above expression cannot be further simplified analytically.

Therefore, we switch now to the Fock integral (4.48), which can be treated in a similar way. Namely, using the Fourier transformation, the Fock integral can be rewritten in the following form

$$B_i^E(b, \Theta) = -\frac{1}{2\bar{b}^3} \iiint \frac{d^3 \mathcal{K}'' d^3 \mathcal{K}' d^3 \mathcal{R}'}{(2\pi)^6} \tilde{W}_i(\Theta, \mathcal{K}'') \tilde{\nu}^0(\mathcal{K}', \mathcal{R}') \tilde{\nu}^0(-\mathcal{K}', -\mathcal{R}') e^{i\mathcal{R}' \cdot \mathcal{K}'}, \quad (4.57)$$

where  $\tilde{\nu}^0(\mathcal{K}', \mathcal{K})$  denotes the Fourier transform of  $\nu^0(\mathcal{R}, \mathcal{K})$  with respect to the first variable and  $\tilde{\nu}^0(\mathcal{R}, \mathcal{R}')$  the Fourier transform with respect to the second variable, as defined earlier in Section 2.2.4. The calculation of the  $\mathcal{R}'$  and  $\mathcal{K}'$  in Equation (4.57) is already done in Section 2.2.4, and the explicit result is given by Equation (2.66).

Putting all this together leads to

$$B_i^E(b, \Theta) = \frac{NC_{dd}}{1536\pi^4 \bar{b}^3} \int d^3 \mathcal{K} \frac{\partial}{\partial \mathcal{K}_i} \left\{ \mathcal{K}_i \left[ \frac{3 \left( \sum_n \mathbb{R}''_{zn}{}^T \Theta_n^{\frac{1}{2}} \mathcal{K}_n \right)^2}{\Theta_x \mathcal{K}_x^2 + \Theta_y \mathcal{K}_y^2 + \Theta_z \mathcal{K}_z^2} - 1 \right] \right\} \times \int_0^{\frac{\pi}{2}} \frac{dt}{\sin^6 t} \left( 4 \sin^2 t - \sum_j \frac{\kappa_j^2}{K_j^{\prime 2}} \right)^3 \text{H} \left( 2 \sin t - \sqrt{\sum_j \frac{\kappa_j^2}{K_j^{\prime 2}}} \right). \quad (4.58)$$

where  $\kappa = \mathbb{R}^T \mathcal{K}$ . By substituting variables according to  $\mathcal{K} = \mathbb{R} \mathbf{q}$  and using Equation (4.53) together with the particle number conservation Equation (2.17), we get

$$\begin{aligned}
B_i^E(b, \Theta) &= \frac{NC_{\text{dd}}}{1536\pi^4\bar{b}^3} \int d^3q \left( 1 + \sum_{j,l} \mathbb{R}_{ji}^T \mathbb{R}_{il} q_l \frac{\partial}{\partial q_j} \right) \left[ \frac{3 \left( \sum_{n,m} \mathbb{R}_{zn}^T \mathbb{R}_{nm} \Theta_n^{\frac{1}{2}} q_m \right)^2}{\sum_{n,r,s} \mathbb{R}_{nr} \mathbb{R}_{ns} \Theta_n q_r q_s} - 1 \right] \\
&\times \int_0^{\frac{\pi}{2}} \frac{dt}{\sin^6 t} \left( 4 \sin^2 t - \sum_j \frac{q_j^2}{K_j'^2} \right)^3 \text{H} \left( 2 \sin t - \sqrt{\sum_j \frac{q_j^2}{K_j'^2}} \right). \quad (4.59)
\end{aligned}$$

Using a new substitution  $q_i = u_i K_i'$ , we obtain

$$\begin{aligned}
B_i^E(b, \Theta) &= \frac{NC_{\text{dd}} \bar{K}'^3}{1536\pi^4\bar{b}^3} \int d^3u \left( 1 + \sum_{j,l} \mathbb{R}_{ji}^T \mathbb{R}_{il} K_l' u_l \frac{\partial}{\partial (K_j' u_j)} \right) \\
&\times \left[ \frac{3 \left( \sum_{n,m} \mathbb{R}_{zn}^T \mathbb{R}_{nm} \Theta_n^{\frac{1}{2}} K_m' u_m \right)^2}{\sum_{n,r,s} \mathbb{R}_{nr} \mathbb{R}_{ns} \Theta_n K_r' K_s' u_r u_s} - 1 \right] \int_0^{\frac{\pi}{2}} \frac{dt}{\sin^6 t} (4 \sin^2 t - u^2)^3 \text{H} (2 \sin t - u). \quad (4.60)
\end{aligned}$$

After again switching to spherical coordinates,  $u_i = \mathbb{R}_{iz}(\vartheta, \phi)u$ , the evaluation of the integral over variables  $u$  and  $t$  yields

$$\begin{aligned}
B_i^E(b, \Theta) &= \frac{6N^2 c_0}{R^{\nu^3} \bar{b}^3} \frac{1}{4\pi} \int \sin \vartheta d\vartheta d\phi \left[ 1 + \sum_{j,l} \mathbb{R}_{ji}^T \mathbb{R}_{il} K_l' \mathbb{R}_{lz}(\vartheta, \phi) \frac{\partial}{\partial (K_j' \mathbb{R}_{jz}(\vartheta, \phi))} \right] \\
&\times \left\{ \frac{3 \left[ \sum_{n,m} \mathbb{R}_{zn}^T \mathbb{R}_{nm} \Theta_n^{\frac{1}{2}} K_m' \mathbb{R}_{mz}(\vartheta, \phi) \right]^2}{\sum_{n,r,s} \mathbb{R}_{nr} \mathbb{R}_{ns} \Theta_n K_r' K_s' \mathbb{R}_{rz}(\vartheta, \phi) \mathbb{R}_{sz}(\vartheta, \phi)} - 1 \right\}. \quad (4.61)
\end{aligned}$$

Expressions for  $B_i^D(b)$  and  $B_i^E(b, \Theta)$  given by Equations (4.56) and (4.61), respectively, cannot be further simplified analytically. Thus, Equation (4.46) for the scaling parameters  $b_i(t)$  has to be solved numerically in the most general case. The expressions for the integrals  $B_i^D(b)$  and  $B_i^E(b, \Theta)$  derived here are prerequisites for such a numerical calculation. However, before one embarks in this direction, which we plan to do in the future, but not within the scope of this Thesis, there are special cases for which the above integrals can be calculated analytically. In the following Section we consider three such special cases.

## 4.2.2 Special cases

Although the Hartree direct kinetic integral  $B_i^D(b)$ , and the Fock exchange kinetic integral  $B_i^E(b, \Theta)$  cannot be solved analytically for the general orientation of dipoles, it is still possible to evaluate them in some special cases. For instance, when the dipoles

are oriented along one of the trap axes, both integrals can be expressed in terms of the well-known dipolar anisotropy function, see Appendix B.1.

Let us assume that the dipoles are oriented along  $z$  axis. Note that in this case  $\theta = \theta' = \theta'' = 0$  and  $\varphi = \varphi' = \varphi'' = 0$ , from which follows that  $\mathbb{R} = \mathbb{R}' = \mathbb{R}'' = \mathbb{I}_3$ , and thus  $K'_i = K_i$  and  $R''_i = R_i$ . Having this in mind the Hartree direct kinetic integral  $B_i^D(b)$  given by Equation (4.56) reduces to

$$\begin{aligned}
B_i^D(b) &= -\frac{6N^2c_0}{R^3b^3} \frac{1}{4\pi} \int \sin \vartheta d\vartheta d\phi \left[ 1 + \mathbb{R}_{iz}(\vartheta, \phi) \frac{\partial}{\partial \mathbb{R}_{iz}(\vartheta, \phi)} \right] \left[ \frac{3 \frac{\mathbb{R}_{zz}^2(\vartheta, \phi)}{R_z^2 b_z^2}}{\sum_n \frac{\mathbb{R}_{nz}^2(\vartheta, \phi)}{R_n^2 b_n^2}} - 1 \right] \\
&= -\frac{6N^2c_0}{R^3b^3} \left[ 1 - b_i R_i \frac{\partial}{\partial b_i R_i} \right] \frac{1}{4\pi} \int \sin \vartheta d\vartheta d\phi \\
&\quad \times \left( 3 \frac{\cos^2 \vartheta}{\frac{b_x^2 R_x^2}{b_x^2 R_x^2} \cos^2 \phi \sin^2 \vartheta + \frac{b_y^2 R_y^2}{b_y^2 R_y^2} \sin^2 \phi \sin^2 \vartheta + \cos^2 \vartheta} - 1 \right) \\
&= \frac{6N^2c_0}{R^3b^3} \left[ f \left( \frac{b_x R_x}{b_z R_z}, \frac{b_y R_y}{b_z R_z} \right) - b_i R_i \frac{\partial}{\partial b_i R_i} f \left( \frac{b_x R_x}{b_z R_z}, \frac{b_y R_y}{b_z R_z} \right) \right]. \tag{4.62}
\end{aligned}$$

Here we have used the anisotropy function definition given by Equation (B.1), as well as the identity

$$a \frac{\partial}{\partial a} f \left( \frac{x}{a} \right) = -x \frac{\partial}{\partial x} f \left( \frac{x}{a} \right). \tag{4.63}$$

The Fock exchange kinetic integral  $B_i^E(b, \Theta)$  can be evaluated in a similar way

$$\begin{aligned}
B_i^E(b, \Theta) &= \frac{6N^2c_0}{R^3b^3} \frac{1}{4\pi} \int \sin \vartheta d\vartheta d\phi \left[ 1 + \mathbb{R}_{iz}(\vartheta, \phi) \frac{\partial}{\partial \mathbb{R}_{iz}(\vartheta, \phi)} \right] \left[ \frac{3\Theta_z K_z^2 \mathbb{R}_{zz}^2(\vartheta, \phi)}{\sum_n \Theta_n K_n^2 \mathbb{R}_{nz}^2(\vartheta, \phi)} - 1 \right] \\
&= \frac{6N^2c_0}{R^3b^3} \left[ 1 + \Theta_i^{\frac{1}{2}} K_i \frac{\partial}{\partial \Theta_i^{\frac{1}{2}} K_i} \right] \frac{1}{4\pi} \int \sin \vartheta d\vartheta d\phi \\
&\quad \times \left( 3 \frac{\cos^2 \vartheta}{\frac{\Theta_x K_x^2}{\Theta_z K_z^2} \cos^2 \phi \sin^2 \vartheta + \frac{\Theta_y K_y^2}{\Theta_z K_z^2} \sin^2 \phi \sin^2 \vartheta + \cos^2 \vartheta} - 1 \right) \\
&= \frac{6N^2c_0}{R^3b^3} \left[ f \left( \frac{\Theta_z^{\frac{1}{2}} K_z}{\Theta_x^{\frac{1}{2}} K_x}, \frac{\Theta_z^{\frac{1}{2}} K_z}{\Theta_y^{\frac{1}{2}} K_y} \right) + \Theta_i^{\frac{1}{2}} K_i \frac{\partial}{\partial \Theta_i^{\frac{1}{2}} K_i} f \left( \frac{\Theta_z^{\frac{1}{2}} K_z}{\Theta_x^{\frac{1}{2}} K_x}, \frac{\Theta_z^{\frac{1}{2}} K_z}{\Theta_y^{\frac{1}{2}} K_y} \right) \right], \tag{4.64}
\end{aligned}$$

where we have again used the definition of the anisotropy function and another identity,

$$a \frac{\partial}{\partial a} f(ax) = x \frac{\partial}{\partial x} f(ax). \tag{4.65}$$

Inserting Equations (4.64) and (4.62) into Equation (4.46), together with Equation (4.43), yields a system of coupled ordinary differential equations of motion for the respective

scaling parameters [125, 126],

$$\begin{aligned} \ddot{b}_i + \omega_i^2 b_i - \frac{\hbar^2 K_i^2 \Theta_i}{M^2 b_i R_i^2} + \frac{48Nc_0}{Mb_i R_i^2 \bar{b}^3 \bar{R}^3} \left[ f \left( \frac{b_x R_x}{b_z R_z}, \frac{b_y R_y}{b_z R_z} \right) - b_i R_i \frac{\partial}{\partial b_i R_i} f \left( \frac{b_x R_x}{b_z R_z}, \frac{b_y R_y}{b_z R_z} \right) \right] \\ - \frac{48Nc_0}{Mb_i R_i^2 \bar{b}^3 \bar{R}^3} \left[ f \left( \frac{\Theta_z^{\frac{1}{2}} K_z}{\Theta_x^{\frac{1}{2}} K_x}, \frac{\Theta_z^{\frac{1}{2}} K_z}{\Theta_y^{\frac{1}{2}} K_y} \right) + \Theta_i^{\frac{1}{2}} K_i \frac{\partial}{\partial \Theta_i^{\frac{1}{2}} K_i} f \left( \frac{\Theta_z^{\frac{1}{2}} K_z}{\Theta_x^{\frac{1}{2}} K_x}, \frac{\Theta_z^{\frac{1}{2}} K_z}{\Theta_y^{\frac{1}{2}} K_y} \right) \right] = 0, \quad (4.66) \\ \dot{\Theta}_i + 2 \frac{\dot{b}_i}{b_i} \Theta_i + \frac{1}{\tau} (\Theta_i - \Theta_i^{\text{le}}) = 0. \quad (4.67) \end{aligned}$$

Note that in the global equilibrium the three Equations (4.66), with the initial conditions  $b_i(0) = \Theta_i(0) = 1$  and  $\dot{b}_i(0) = \dot{\Theta}_i(0) = 0$  at  $t = 0$ , reduce to Equations (2.96)–(2.98), as expected. Also, we remark that these initial conditions correspond to  $\nu(\mathbf{r}, \mathbf{k}, t = 0) \equiv \nu^0(\mathcal{R}, \mathcal{K})$ .

Another special case worth considering is when the dipoles are oriented along the  $x$  axis, i.e.,  $\theta = 90^\circ$  and  $\varphi = 0^\circ$ . In order to obtain the corresponding equations for the scaling parameters, we perform the analogous calculation as in the previous case. However, we can also take advantage of the system's symmetry and just use simple cyclic permutation of the indices  $x \rightarrow y \rightarrow z \rightarrow x$  in Equation (4.66). This immediately leads to the set of equations for this special case,

$$\begin{aligned} \ddot{b}_i + \omega_i^2 b_i - \frac{\hbar^2 K_i^2 \Theta_i}{M^2 b_i R_i^2} + \frac{48Nc_0}{Mb_i R_i^2 \bar{b}^3 \bar{R}^3} \left[ f \left( \frac{b_y R_y}{b_x R_x}, \frac{b_z R_z}{b_x R_x} \right) - b_i R_i \frac{\partial}{\partial b_i R_i} f \left( \frac{b_y R_y}{b_x R_x}, \frac{b_z R_z}{b_x R_x} \right) \right] \\ - \frac{48Nc_0}{Mb_i R_i^2 \bar{b}^3 \bar{R}^3} \left[ f \left( \frac{\Theta_x^{\frac{1}{2}} K_x}{\Theta_y^{\frac{1}{2}} K_y}, \frac{\Theta_x^{\frac{1}{2}} K_x}{\Theta_z^{\frac{1}{2}} K_z} \right) + \Theta_i^{\frac{1}{2}} K_i \frac{\partial}{\partial \Theta_i^{\frac{1}{2}} K_i} f \left( \frac{\Theta_x^{\frac{1}{2}} K_x}{\Theta_y^{\frac{1}{2}} K_y}, \frac{\Theta_x^{\frac{1}{2}} K_x}{\Theta_z^{\frac{1}{2}} K_z} \right) \right] = 0, \quad (4.68) \\ \dot{\Theta}_i + 2 \frac{\dot{b}_i}{b_i} \Theta_i + \frac{1}{\tau} (\Theta_i - \Theta_i^{\text{le}}) = 0. \quad (4.69) \end{aligned}$$

Now, we can easily write down equations for the third special case, when the dipoles are oriented along  $y$  axis. Using a cyclic permutation of the indices  $x \rightarrow z \rightarrow y \rightarrow x$  in Equation (4.66) or  $x \rightarrow y \rightarrow z \rightarrow x$  in Equation (4.68) the corresponding set of equations for this special case reads

$$\begin{aligned} \ddot{b}_i + \omega_i^2 b_i - \frac{\hbar^2 K_i^2 \Theta_i}{M^2 b_i R_i^2} + \frac{48Nc_0}{Mb_i R_i^2 \bar{b}^3 \bar{R}^3} \left[ f \left( \frac{b_z R_z}{b_y R_y}, \frac{b_x R_x}{b_y R_y} \right) - b_i R_i \frac{\partial}{\partial b_i R_i} f \left( \frac{b_z R_z}{b_y R_y}, \frac{b_x R_x}{b_y R_y} \right) \right] \\ - \frac{48Nc_0}{Mb_i R_i^2 \bar{b}^3 \bar{R}^3} \left[ f \left( \frac{\Theta_y^{\frac{1}{2}} K_y}{\Theta_z^{\frac{1}{2}} K_z}, \frac{\Theta_y^{\frac{1}{2}} K_y}{\Theta_x^{\frac{1}{2}} K_x} \right) + \Theta_i^{\frac{1}{2}} K_i \frac{\partial}{\partial \Theta_i^{\frac{1}{2}} K_i} f \left( \frac{\Theta_y^{\frac{1}{2}} K_y}{\Theta_z^{\frac{1}{2}} K_z}, \frac{\Theta_y^{\frac{1}{2}} K_y}{\Theta_x^{\frac{1}{2}} K_x} \right) \right] = 0, \quad (4.70) \\ \dot{\Theta}_i + 2 \frac{\dot{b}_i}{b_i} \Theta_i + \frac{1}{\tau} (\Theta_i - \Theta_i^{\text{le}}) = 0. \quad (4.71) \end{aligned}$$

The resulting ordinary differential equations for the respective scaling parameters for all three special cases can be solved numerically for experimentally realistic parameters and relaxation times in order to describe the dynamics of dipolar Fermi gases. The studies of collective oscillations and TOF dynamics of dipolar Fermi gases have so far focused on either the collisionless regime [93, 95, 122], where collisions can be neglected, or on the hydrodynamic regime [91, 92], where collisions occur so often that local equilibrium can be assumed. The recent paper of Wächtler *et al.* [126] even studied the behavior of collective oscillations when the system undergoes a crossover from one regime to the other.

Motivated by the experimental observation of the ellipsoidal FS deformation in the TOF experiment [48], we continue here the analytical analysis and investigate in detail the expansion dynamics for the collisional regime, which represents the transition zone between the limiting collisionless and hydrodynamic regimes. We also extend previous approaches based on the relaxation-time approximation by introducing a self-consistently determined relaxation time, and study how this quantitatively affects the TOF dynamics.

### 4.3 Time-of-flight dynamics

The most ubiquitous method to study the physics of trapped ultracold gases is their absorption imaging after the release of the atomic or molecular cloud from the trap. Turning off the trap potential allows the ultracold gas cloud to expand for tens of milliseconds, which is called time of flight, and then the gas is illuminated by a laser beam with the frequency resonant to one of the allowed atomic or molecular transitions. The absorption of light by the atoms or molecules casts a shadow, which is then imaged by charge-coupled device (CCD) camera, and an absorption image is obtained. Note that expansion is essential here, since it ensures that the atomic or molecular sample is large enough so that it can be imaged by a camera. This technique, known as the time-of-flight (TOF) imaging, is one of the most important probes of ultracold quantum systems. The TOF expansion experiments serve as a key diagnostic tool to study many of their properties. For example, they can provide information about the various physical parameters of the system, such as the density distribution of atoms or molecules, its number, frequencies of the collective modes, temperature, pressure, chemical potential, entropy, system size, etc.

From the size of the expanded cloud and the known time of flight one can directly

obtain, for instance, the Fermi energy of a noninteracting degenerate Fermi gas. In the case of free ballistic expansion, which is usually applied to theoretically model the TOF, the ellipsoidal FS deformation due to the DDI is taken into account before expansion, while all interactions between the atoms during the TOF are neglected. In contrast to that, a nonballistic expansion model takes into account interactions for calculating both the global equilibrium before expansion and the subsequent expansion dynamics. Here we show how the quantitative information about the ellipsoidal FS deformation, in the parameter regime relevant for the current experiments, can be determined by solving the kinetic Boltzmann equation for the TOF expansion of a dipolar Fermi gas.

In this Section we focus on systems in triaxial trap geometries, where the dipoles are oriented either along the  $z$  direction ( $\theta = \varphi = 0^\circ$ ) or along the  $x$  direction ( $\theta = 90^\circ, \varphi = 0^\circ$ ). This reflects the situation in ongoing experiments and also corresponds to the special cases for which the equations can be derived analytically and solved numerically. Bearing in mind that the trap potential is turned off during the TOF, Equations (4.66) or (4.68) can be used to describe the TOF dynamics of such systems geometry if we just remove the terms  $\omega_i^2 b_i$ , which stem from the harmonic trap potential. The resulting TOF equations are then solved numerically for relaxation times that correspond to the collisionless, the collisional, and the hydrodynamic regime.

Within this formalism, the average size of the Fermi gas cloud in real space in the  $i$ -th direction is described in terms of the root mean squares  $\sqrt{\langle r_i^2(t) \rangle}$  (see Appendix D.2 for more details). For the considered system configuration it is given by

$$\langle r_i^2(t) \rangle = \frac{1}{N} \int \frac{d^3 k}{(2\pi)^3} \int d^3 r r_i^2 \nu(\mathbf{r}, \mathbf{k}, t) = \frac{1}{8} R_i^2 b_i^2(t). \quad (4.72)$$

The deformation of the cloud shape is described in terms of the time-dependent cloud aspect ratio  $A_R(t)$ , which is defined by the ratio of the root mean square of the transversal and longitudinal cloud radii, i.e., the average sizes of the cloud in the vertical  $\sqrt{\langle r_v^2(t) \rangle}$  and horizontal  $\sqrt{\langle r_h^2(t) \rangle}$  direction with respect to the imaging plane. Since the imaging axis in the Innsbruck experiment [48] has an angle of  $\alpha = 28^\circ$  with respect to the  $y$  axis, according to Equation (D.14) from Appendix D.2 this leads to

$$A_R(t) = \sqrt{\frac{\langle r_z^2(t) \rangle}{\langle r_x^2(t) \rangle \cos^2 \alpha + \langle r_y^2(t) \rangle \sin^2 \alpha}} = \frac{R_z b_z(t)}{\sqrt{R_x^2 b_x^2(t) \cos^2 \alpha + R_y^2 b_y^2(t) \sin^2 \alpha}}. \quad (4.73)$$

This aspect ratio in real space represents a directly measurable quantity in the TOF

dynamics experiments. In order to describe the DDI influence on the FS we also use the corresponding aspect ratio in momentum space. In analogy to  $A_R(t)$ , the average sizes of the Fermi gas cloud in momentum space read (see Appendix D for more details)

$$\langle k_i^2(t) \rangle = \frac{1}{N} \int d^3r \int \frac{d^3k}{(2\pi)^3} k_i^2 \nu(\mathbf{r}, \mathbf{k}, t) = \frac{1}{8} \left( K_i^2 \Theta_i(t) + \frac{M^2 R_i^2 \dot{b}_i^2(t)}{\hbar^2} \right). \quad (4.74)$$

The corresponding aspect ratio in momentum space, according to Equation (D.23) from Appendix D.3, is given by

$$\begin{aligned} A_K(t) &= \sqrt{\frac{\langle k_z^2(t) \rangle}{\langle k_x^2(t) \rangle \cos^2 \alpha + \langle k_y^2(t) \rangle \sin^2 \alpha}} \\ &= \sqrt{\frac{\hbar^2 K_z^2 \Theta_z(t) + M^2 R_z^2 \dot{b}_z^2(t)}{\left[ \hbar^2 K_x^2 \Theta_x(t) + M^2 R_x^2 \dot{b}_x^2(t) \right] \cos^2 \alpha + \left[ \hbar^2 K_y^2 \Theta_y(t) + M^2 R_y^2 \dot{b}_y^2(t) \right] \sin^2 \alpha}}. \end{aligned} \quad (4.75)$$

The relaxation time  $\tau$  in Equation (4.67) determines the regime of the dipolar Fermi gas with respect to the collisions frequency. Therefore, by solving the appropriate equations for varying values of  $\tau$ , we are able to describe the dynamic properties of the Fermi gas all the way from the collisionless ( $\bar{\omega}\tau \gg 1$ ) to the hydrodynamic ( $\bar{\omega}\tau \ll 1$ ) regime, which represent two limiting regimes. In Section 4.3.1 we study the collisionless regime, in Section 4.3.2 the hydrodynamic regime, while in Sections 4.3.3 and 4.3.4 we investigate the system's behavior in the intermediate, collisional regime. At first, we treat the relaxation time as a phenomenological parameter, and later on we improve the relaxation-time approximation in the collisional regime even further by determining the relaxation time in a self-consistent way, without free fitting parameters.

### 4.3.1 Collisionless regime

The value of the relaxation time  $\tau$  determines the regime of the Fermi gas during the expansion. In the low-density or collisionless regime, which is determined by the condition  $\bar{\omega}\tau \gg 1$ , the relaxation time  $\tau$  can be taken to be infinite. In the limit  $\tau \rightarrow \infty$  the differential Equations (4.67) for the scaling parameters  $\Theta_i$  decouple and the dynamic behavior in each direction is independent from the others. Due to this, Equations (4.67) can be solved analytically. With the respective initial conditions  $b_i(0) = \Theta_i(0) = 1$  and  $\dot{b}_i(0) = \dot{\Theta}_i(0) = 0$  we obtain

$$\Theta_i(t) = b_i(t)^{-2}. \quad (4.76)$$

Inserting this solution to Equations (4.66) for the scaling parameters  $b_i(t)$  yields the equations of motion in the collisionless regime [93, 122, 125]. We numerically solve them for a general system geometry, where the trap frequencies in the three spatial directions are different and correspond to the values of the Innsbruck experiment [48].

Graphs in the left-hand side column of Figure 4.1 show aspect ratios  $\sqrt{\langle r_x^2 \rangle / \langle r_z^2 \rangle}$ ,  $\sqrt{\langle r_y^2 \rangle / \langle r_z^2 \rangle}$ , as well the cloud aspect ratio  $A_R$  in real space during the TOF expansion in the collisionless regime. The black dotted line in the middle corresponds to the case of a noninteracting Fermi gas, when the differential equations for the scaling parameters  $b_i(t)$  can be solved analytically, yielding

$$b_i^{\text{ni}}(t) = \sqrt{1 + \left( \frac{\hbar K_{\text{F}}^0}{M R_i^0} \right)^2 t^2}, \quad (4.77)$$

with  $R_i^0$  and  $K_{\text{F}}^0$  denoting the global equilibrium radius and momentum in the  $i$ -th direction, given by Equations (1.21) and (1.22), respectively. Furthermore, in the long TOF limit all aspect ratios for a noninteracting Fermi gas in real space satisfy

$$\lim_{t \rightarrow \infty} \sqrt{\frac{\langle r_i^2(t) \rangle^{\text{ni}}}{\langle r_j^2(t) \rangle^{\text{ni}}}} = \lim_{t \rightarrow \infty} \sqrt{\frac{M^2 R_i^{02} + \hbar^2 K_{\text{F}}^{02} t^2}{M^2 R_j^{02} + \hbar^2 K_{\text{F}}^{02} t^2}} = 1. \quad (4.78)$$

This shows that the cloud of noninteracting fermions becomes spherical after a long enough expansion, reflecting its isotropic momentum distribution even in the triaxial harmonic trap. As the DDI is absent here, the orientation of the magnetic or the electric field, i.e., orientation of the dipole moments of atoms or molecules, has no influence on the FS deformation [158]. Graphs in the right-hand side column of Figure 4.1 show the corresponding time-dependence of the aspect ratios in momentum space. As expected, the black dotted line is constant and equal to one, as for the noninteracting fermions the FS is not deformed. Namely, as the expectation value of the momentum root mean square reads

$$\langle k_i^2(t) \rangle^{\text{ni}} = K_{\text{F}}^{02}, \quad (4.79)$$

this further leads to the conclusion that the FS in noninteracting case remains of the same size during the TOF.

Furthermore, Figure 4.1 also depicts the time dependence of the aspect ratios when the DDI is taken into account. The dashed lines correspond to the ballistic expansion, when the DDI is assumed to affect the initial ground state, but not later during the expansion. Mathematically, this means that the ballistic expansion is also determined

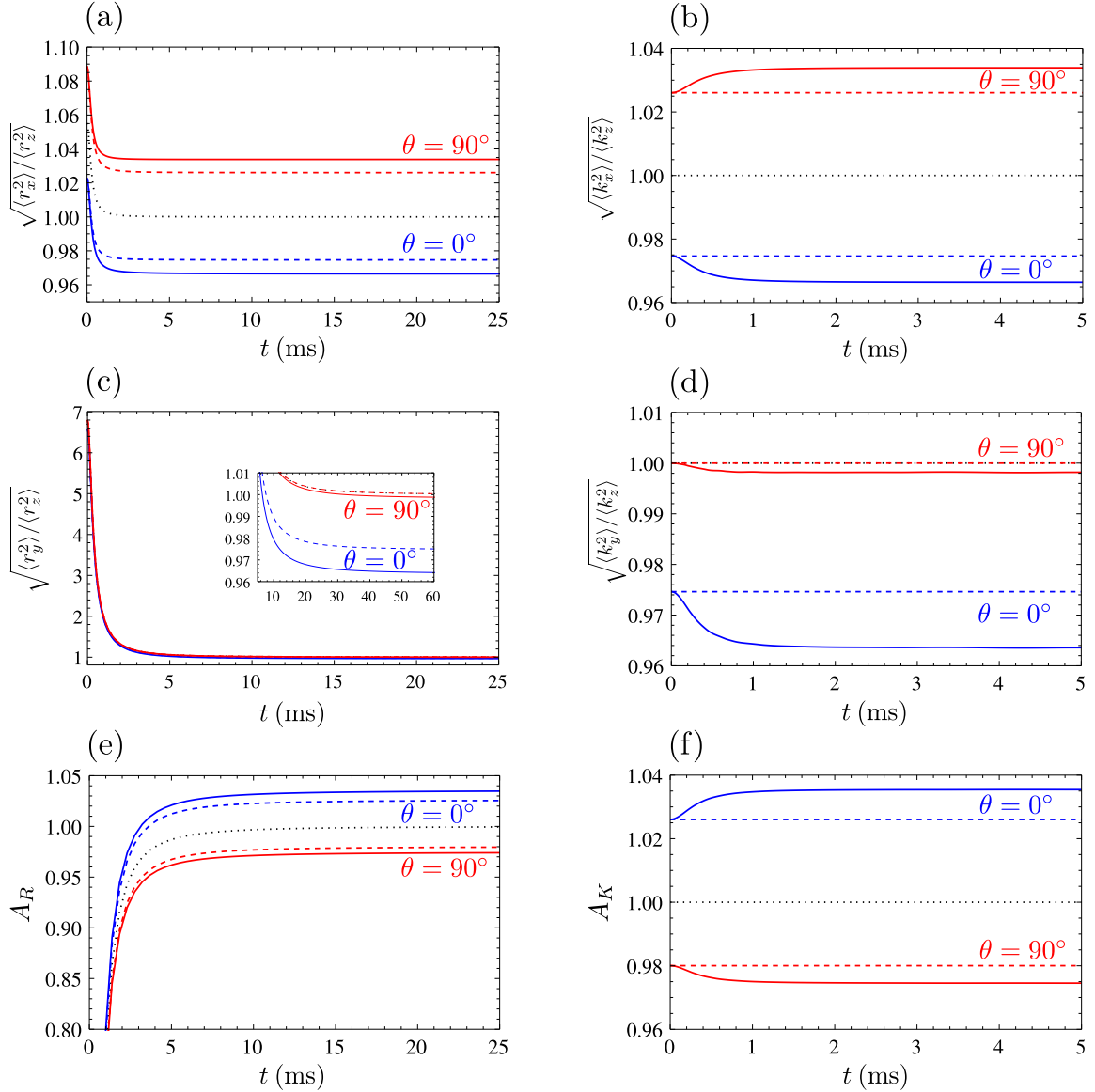


**Figure 4.1:** Aspect ratios in real and momentum space in the collisionless regime during TOF expansion of ultracold gas of  $^{167}\text{Er}$ : (a)  $\sqrt{\langle r_x^2 \rangle / \langle r_z^2 \rangle}$ , (b)  $\sqrt{\langle r_y^2 \rangle / \langle r_z^2 \rangle}$ , (c)  $A_R$ , (d)  $\sqrt{\langle k_x^2 \rangle / \langle k_z^2 \rangle}$ , (e)  $\sqrt{\langle k_y^2 \rangle / \langle k_z^2 \rangle}$ , (f)  $A_K$ . Black dotted lines represent aspect ratios for noninteracting case, dashed lines represent ballistic expansion, and solid lines represent nonballistic expansion. As indicated in the graphs (a)-(d), two lower blue solid and dashed lines correspond to  $\theta = 0^\circ$ , and two upper red solid and dashed lines correspond to  $\theta = 90^\circ$ , while in graphs (e) and (f) the position of lines is reversed: two upper blue solid and dashed lines are for  $\theta = 0^\circ$ , and two lower red solid and dashed lines are for  $\theta = 90^\circ$ .

by Equation (4.77), but now with the parameters  $R_i$  and  $K_i$  instead of  $R_i^0$  and  $K_F^0$ , respectively

$$b_i^{\text{bal}}(t) = \sqrt{1 + \left( \frac{\hbar K_i}{M R_i} \right)^2 t^2}. \quad (4.80)$$

The solid lines in Figure 4.1 represent results for the nonballistic expansion, when we take the DDI into account for calculating both the initial ground state and the subsequent expansion. To obtain these results, one has to solve numerically the coupled differential Equations (4.66) together with Equation (4.76). In Figures 4.1(a) to 4.1(d), top red solid and dashed lines correspond to the orientation of the dipoles in the  $x$  direction, and bottom blue solid and dashed lines correspond to the dipoles' orientation in the  $z$  direction. In Figures 4.1(e) and 4.1(f) the position of lines turns out to be reversed: top blue lines give results for the dipoles in the  $z$  direction, and bottom red lines for the dipoles in the  $x$  direction.

From the graphs in the right-hand column of Figure 4.1 we read off that the aspect ratios in momentum space are constant if ballistic expansion approximation is used (all dashed lines). This is not surprising, since here the DDI is neglected during the expansion. This can also be shown mathematically, since, similarly to Equation (4.79), it follows that  $\langle k_i^2(t) \rangle^{\text{bal}} = K_i^2$ , and thus the momentum-space aspect ratios leads to

$$\sqrt{\frac{\langle k_i^2(t) \rangle^{\text{bal}}}{\langle k_j^2(t) \rangle^{\text{bal}}}} = \frac{K_i}{K_j}. \quad (4.81)$$

So, the momentum-space aspect ratios for the ballistic expansion are clearly time-independent and are therefore determined by the initial ground state distribution.

From Figure 4.1 we see that the cloud aspect ratios in real space reach their corresponding plateaus after several tens of milliseconds. The asymptotic value of  $A_R$  for  $\theta = 0^\circ$  for ballistic expansion is 1.025, whereas for nonballistic expansion it is 1.035, thus resulting in a 1% difference due to the DDI. For  $\theta = 90^\circ$  the asymptotic value of  $A_R$  for ballistic expansion is 0.98, while for nonballistic expansion it is 0.97, representing again a 1% difference. We also note that for  $\theta = 0^\circ$  the usual inversion of the cloud shape occurs, while for  $\theta = 90^\circ$  this is not the case. All these results are in excellent quantitative agreement with the experimental values reported in Reference [48].

Aspect ratios in momentum space behave similarly, and again a difference of around 0.5 – 1% between their asymptotic values in a ballistic and nonballistic expansion are observed. But one important difference is that here they are reached much faster, already after several milliseconds. A more detailed analysis reveals that the two terms in Equation (4.74) compete with each other during the TOF expansion, but the second term becomes dominant quite fast. Although the corresponding term in Equation (4.72) has the same asymptotic behavior, the initial value of  $A_K$  is much closer to its asymptotic value than in the case of  $A_R$  and, as a consequence, all aspect ratios

in momentum space converge faster.

Note that the aspect ratio in momentum space at the initial time  $t = 0$  coincides with the asymptotic aspect ratio in real space for ballistic expansion,

$$A_K^{\text{bal}}(0) = \lim_{t \rightarrow \infty} A_R^{\text{bal}}(t). \quad (4.82)$$

To prove this, we start by calculating the ballistic expansion aspect ratio in momentum space at  $t = 0$ . It can be obtained from Equation (4.75) by using the initial conditions for the scaling parameters, yielding

$$A_K^{\text{bal}}(0) = \frac{K_z}{\sqrt{K_x^2 \cos^2 \alpha + K_y^2 \sin^2 \alpha}}. \quad (4.83)$$

On the other hand, long-time limit of the ballistic expansion aspect ratio in real space can be obtained if we insert Equation (4.80) into Equation (4.73),

$$\begin{aligned} \lim_{t \rightarrow \infty} A_R^{\text{bal}}(t) &= \lim_{t \rightarrow \infty} \sqrt{\frac{M^2 R_z^2 + \hbar^2 K_z^2 t^2}{(M^2 R_x^2 + \hbar^2 K_x^2 t^2) \cos^2 \alpha + (M^2 R_y^2 + \hbar^2 K_y^2 t^2) \sin^2 \alpha}} \\ &= \frac{K_z}{\sqrt{K_x^2 \cos^2 \alpha + K_y^2 \sin^2 \alpha}}, \end{aligned} \quad (4.84)$$

and is the same as the above obtained expression for  $A_K^{\text{bal}}(0)$  in Equation (4.83). This fact is systematically used in a variety of TOF experiments, and in particular it was used in Reference [48] in order to observe the ellipsoidal deformation of the FS, as real-space aspect ratios can be readily measured during the TOF expansion. However, this is only correct within the ballistic approximation, as for the truly nonballistic expansion, when interactions during the expansion cannot be neglected, such a relationship is no longer valid.

However, from Figure 4.2 we read off that both for ballistic (dashed lines) and nonballistic (solid lines) expansion another relationship seems to hold. Namely, the aspect ratios in momentum space and the corresponding aspect ratios in real space turn out to have the same asymptotic values

$$\lim_{t \rightarrow \infty} A_K(t) = \lim_{t \rightarrow \infty} A_R(t). \quad (4.85)$$

The above is true for both considered orientations of dipoles. A similar conclusion was reached in Reference [90] for a dipolar Fermi gas that was initially in a cylindrically symmetric harmonic trap, but we see here that this is true even for a fully anisotropic

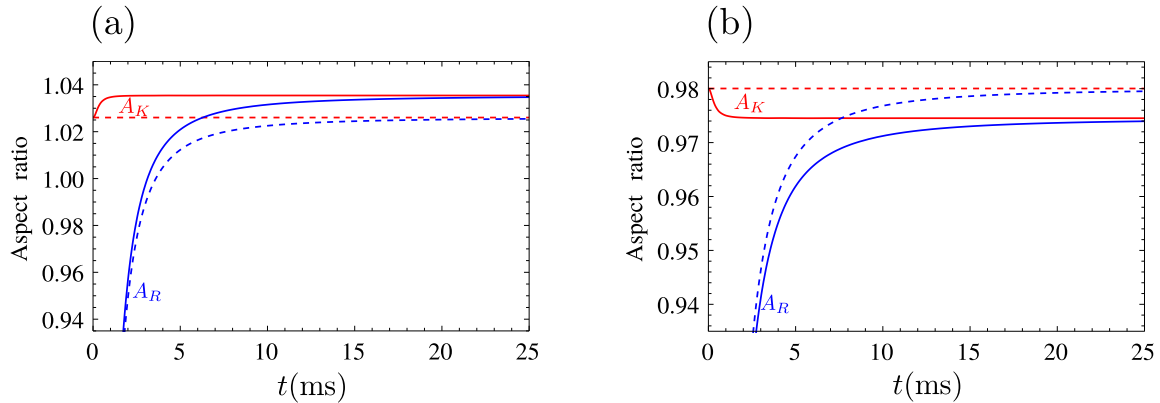


**Figure 4.2:** Aspect ratios in real and momentum space in the collisionless regime converge to the same asymptotic values during TOF expansion of ultracold gas of  $^{167}\text{Er}$ : (a)  $\theta = 0^\circ$ , (b)  $\theta = 90^\circ$ . Solid (dashed) lines represent aspect ratios for nonballistic (ballistic) expansion of  $^{167}\text{Er}$ . The initially lower branch of blue lines corresponds to real space aspect ratios  $A_R$ , while the initially upper branch of red lines corresponds to momentum space aspect ratios  $A_K$ .

harmonic trapping potential. Note that this finding cannot be directly used to determine the aspect ratio in momentum space at  $t = 0$  and the corresponding initial deformation of the FS, as for the ballistic expansion according to Equation (4.82). But this observation still allows to theoretically extract information on the momentum space distribution from experimental data. However, this requires that the corresponding equations are propagated backwards in time, so that the initial distribution in momentum space is calculated starting from the experimentally measured distribution in real space. Here the numerical challenge is that this backward propagation has to be calculated for an infinitely long expansion time.

### 4.3.2 Hydrodynamic regime

In contrast to the previously considered collisionless regime, where collisions are completely neglected, we now turn to the hydrodynamic regime, where the system is supposed to have such a high density and, therefore, such a high collision rate, that it is always in local equilibrium. Although realistic systems, even if initially in the hydrodynamic regime, eventually become collisionless during the expansion, we follow References [91, 92] and consider this theoretical limiting case for the sake of completeness. It turns out that this limit is also necessary as a prerequisite for considering the more complex collisional case.

In the hydrodynamic regime, the scaling parameters  $\Theta_i^{\text{hd}}$  always coincide with the local equilibrium values, i.e., we have  $\Theta_i^{\text{hd}} = \Theta_i^{\text{le}}$ . However, since the limit  $\tau \rightarrow 0$  holds,

the last term in the left-hand side of Equations (4.67) is undetermined. Therefore, instead of Equations (4.67), the hydrodynamic regime is defined via the following condition [158]

$$\Gamma^{\text{hd}}(t)^{-1} = \prod_i b_i^{\text{hd}}(t) \sqrt{\Theta_i^{\text{hd}}(t)} = 1. \quad (4.86)$$

Using this condition, minimizing the Hartree-Fock energy (2.75) in the local equilibrium leads to [91, 92]

$$\Theta_x^{\text{hd}} = \Theta_y^{\text{hd}}, \quad (4.87)$$

$$\frac{\hbar^2 \Theta_z^{\text{hd}} K_z^2}{2M} - \frac{\hbar^2 \Theta_x^{\text{hd}} K_x^2}{2M} = \frac{72Nc_0}{\prod_j b_j^{\text{hd}} R_j} \left[ 1 + \frac{\left( 2\Theta_x^{\text{hd}} K_x^2 + \Theta_z^{\text{hd}} K_z^2 \right) f_s \left( \frac{\sqrt{\Theta_z^{\text{hd}} K_z}}{\sqrt{\Theta_x^{\text{hd}} K_x}} \right)}{2 \left( \Theta_z^{\text{hd}} K_z^2 - \Theta_x^{\text{hd}} K_x^2 \right)} \right]. \quad (4.88)$$

Equations (4.66), with the identifications  $b_i(t) = b_i^{\text{hd}}(t)$  and  $\Theta_i(t) = \Theta_i^{\text{hd}}(t)$ , together with Equations (4.87) and (4.88), and the normalization condition (4.86) represent a closed set of six equations for the six scaling parameters in the hydrodynamic regime. We solve these equations numerically during the nonballistic TOF expansion. For comparison, we have also solved the corresponding equations for the ballistic expansion, although the hydrodynamic regime implies that the DDI cannot be neglected at any point.

Figure 4.3 shows the corresponding aspect ratios in real and momentum space for  $^{167}\text{Er}$ . As expected, we see that there is a significant difference between the ballistic and nonballistic expansion, in contrast to the collisionless regime in Figure 4.1. From graphs in the left column of Figure 4.3 we observe that the real-space aspect ratios for  $\theta = 0^\circ$  behave, in general, similarly to those in the collisionless regime, including the cloud shape inversion, although the asymptotic values differ more from their initial values for nonballistic expansion. On the other hand, for  $\theta = 90^\circ$  we see qualitatively different behavior in Figure 4.3(a), where the aspect ratio  $\sqrt{\langle r_x^2 \rangle} / \langle r_z^2 \rangle$  increases, while in Figure 4.1(a) it decreases. In Figure 4.3(c) for  $\theta = 90^\circ$  we read off that the aspect ratio  $A_R$  even behaves nonmonotonously, with a local maximum at around 1 ms, while in the collisionless regime it only increases monotonously until it reaches its asymptotic value. However, again the inversion of the cloud shape is not present for  $\theta = 90^\circ$ , unlike for  $\theta = 0^\circ$ . We also note that the positions of ballistic expansion curves are reversed in all graphs compared to the collisionless regime, including those for momentum-space aspect ratios.

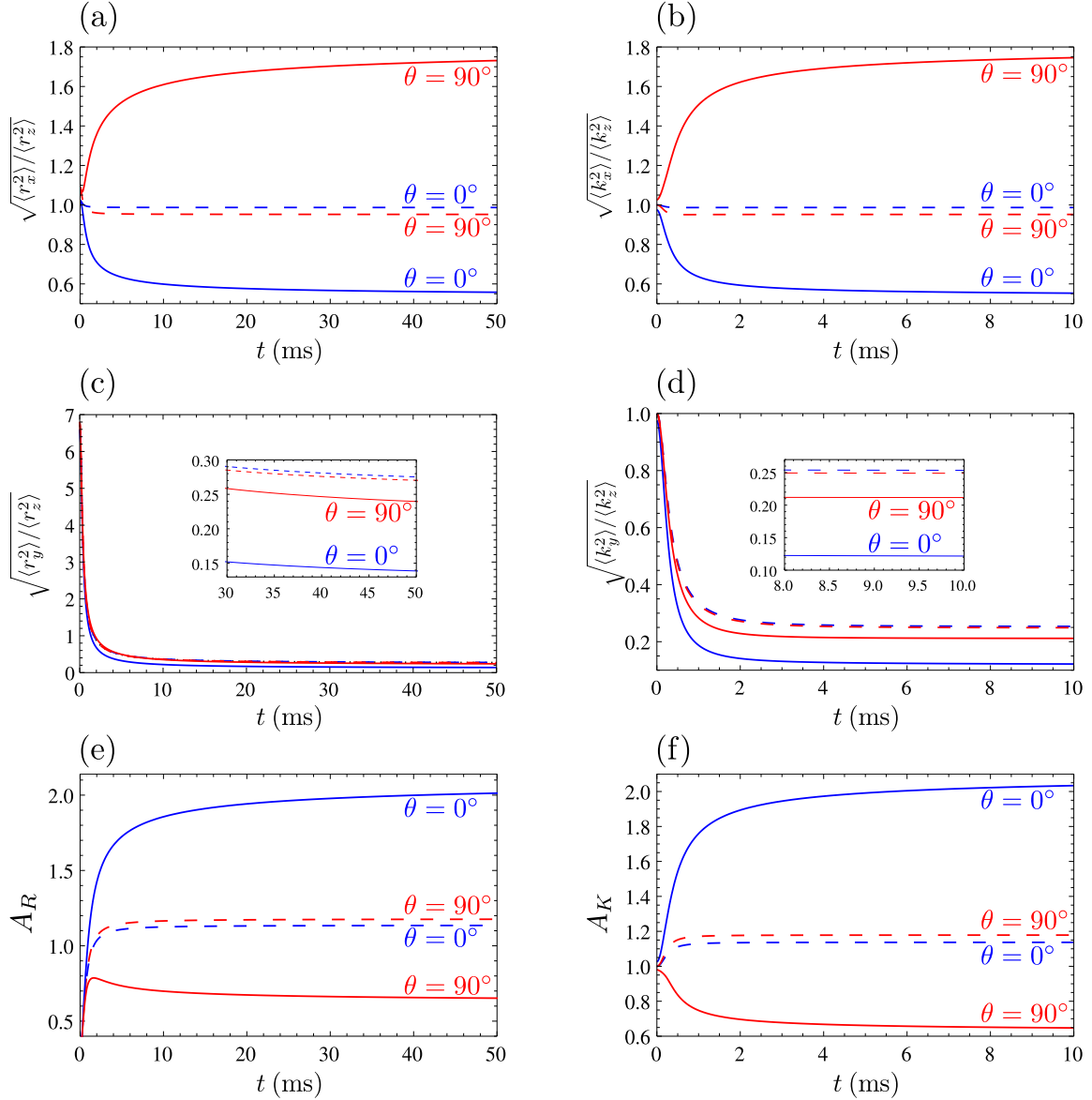


**Figure 4.3:** Aspect ratios in real and momentum space in the hydrodynamic regime during TOF expansion of ultracold gas of  $^{167}\text{Er}$ : (a)  $\sqrt{\langle r_x^2 \rangle / \langle r_z^2 \rangle}$ , (b)  $\sqrt{\langle r_y^2 \rangle / \langle r_z^2 \rangle}$ , (c)  $A_R$ , (d)  $\sqrt{\langle k_x^2 \rangle / \langle k_z^2 \rangle}$ , (e)  $\sqrt{\langle k_y^2 \rangle / \langle k_z^2 \rangle}$ , (f)  $A_K$ . Dashed lines represent ballistic expansion and solid lines represent nonballistic expansion. As indicated in graphs (a)-(d), the lower blue solid and the upper blue dashed line correspond to  $\theta = 0^\circ$ , while the upper red solid and the lower red dashed line correspond to  $\theta = 90^\circ$ . In graphs (e) and (f) the position of lines is reversed: the upper blue solid and the lower blue dashed line are for  $\theta = 0^\circ$ ; the lower red solid and the upper red dashed line are for  $\theta = 90^\circ$ .

The behavior of momentum-space aspect ratios in the right column of Figure 4.3 is generally the same as in Figure 4.1 for the collisionless regime, just with larger differences between initial and asymptotic values, for both cases  $\theta = 0^\circ$  and  $\theta = 90^\circ$ .

The final cloud aspect ratio in real space for nonballistic expansion is twice as large as the corresponding collisionless value for  $\theta = 0^\circ$ , while for  $\theta = 90^\circ$  the asymptotic

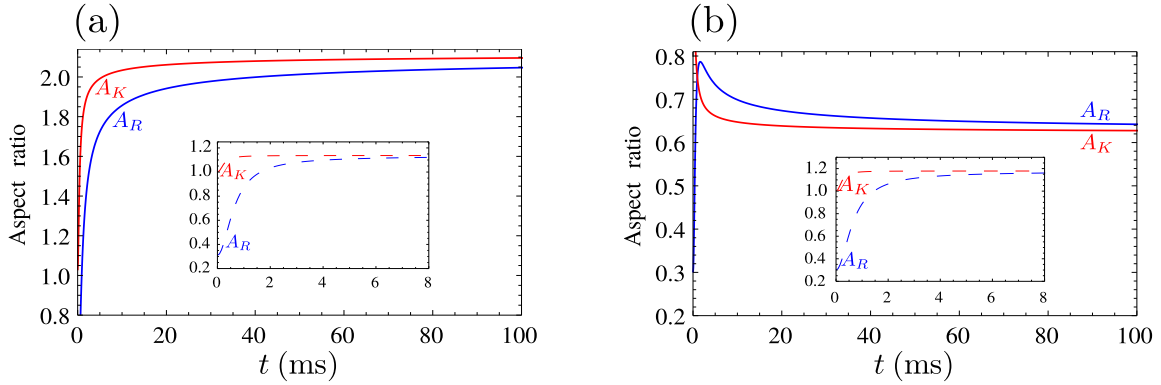


**Figure 4.4:** Aspect ratios in real and momentum space in the hydrodynamic regime converge to the same asymptotic values during TOF expansion of ultracold gas of  $^{167}\text{Er}$ : (a)  $\theta = 0^\circ$ , (b)  $\theta = 90^\circ$ . Solid lines give aspect ratios for nonballistic expansion, while dashed lines in the insets show the corresponding ballistic results. Blue lower lines in (a) and blue upper lines in (b) correspond to  $A_R$ , while red upper lines in (a) and red lower lines in (b) correspond to  $A_K$ .

value of the aspect ratio is around 0.65, which amounts to a decrease of around 35% compared to the collisionless value. For ballistic expansion, which we know to be unrealistic in the hydrodynamic regime, both the corresponding increase and decrease amounts to around 12%. Similar numbers are also obtained for the momentum-space aspect ratio  $A_K$ , as can be seen from the graphs on the right-hand side in Figure 4.3. Since the corresponding values in the collisionless regime are all close to one, the above percentages also apply here, and directly represent the results for the ellipsoidal deformation of the FS in the hydrodynamic regime.

The same conclusion can be also obtained from Figure 4.4, where we compare aspect ratios in real and momentum space. Furthermore, these graphs confirm that the asymptotic values of the aspect ratios  $A_R$  and  $A_K$  also coincide in the hydrodynamic regime for both cases  $\theta = 0^\circ$  and  $\theta = 90^\circ$ , as stated by Equation (4.85) for the collisionless regime. If we compare the convergence of aspect ratios to their asymptotic values in Figures 4.2 and 4.4, we see that in the hydrodynamic regime typical times to reach the plateau are similar in real and in momentum-space, and have the value of several tens of milliseconds. This coincides with the corresponding convergence times for real-space aspect ratios in the collisionless regime, where also a significant difference between the initial and the asymptotic value of aspect ratios occurs. Only in the case of momentum space aspect ratios in the collisionless regime, where the deformation of the FS is small during the whole expansion, the asymptotic values can be reached faster, namely in just a few milliseconds.

However, as already emphasized, even if initially in the hydrodynamic regime,

the dipolar Fermi gas becomes more and more dilute during the TOF expansion, and the hydrodynamic regime continuously goes over into the collisional regime, and, finally, into the collisionless regime. Therefore, we model the collisional regime in the remainder of this section, since it is relevant for experiments where the density of the Fermi gas is high enough so that we can assume it is initially in the collisional or in the hydrodynamic regime.

### 4.3.3 Collisional regime with constant relaxation time

Here we start considering the collisional regime and assume that the relaxation-time approximation given by Equation (4.22) can be applied. Furthermore, we presume that the relaxation time  $\tau$  remains constant during the TOF. The latter assumption is only valid for short times of flight, before the density of the gas decreases significantly. We will improve upon this approximation later, when the relaxation time will be determined self-consistently.

However, provided that the relaxation time is constant, the TOF dynamics can be obtained by directly solving Equations (4.66) and (4.67) for a given value of  $\tau$ . Note that the values of the scaling parameters  $\Theta_i^{\text{le}}$  in local equilibrium are obtained according to Section 4.3.2, i.e., they represent the solutions of the equations for the hydrodynamic regime  $\Theta_i^{\text{hd}}$ .

The physical meaning of Equations (4.67) is that dissipation occurs when the system is outside of a local equilibrium as long as there are collisions, i.e., as long as the relaxation time  $\tau$  remains finite. Effects of collisions are therefore described through Equations (4.67), whereas Equations (4.66) for the scaling parameters  $b_i$  do not directly contain such terms. However, effects of collisions enter indirectly into Equations (4.66) through the scaling parameters  $\Theta_i$ .

Here we numerically solve the coupled system of Equations (4.66) and (4.67) during the nonballistic expansion for a fixed value of the relaxation time  $\tau$ . Varying the value of the relaxation time we are able to describe all regimes, from the collisionless, obtained in the limit  $\tau \rightarrow \infty$ , to the hydrodynamic, obtained in the limit  $\tau \rightarrow 0$ . In particular, although the approximation of a fixed relaxation time is not realistic for longer expansion times, it allows us to understand and describe in more detail different collisional regimes, for finite values of  $\tau$ , when the system undergoes a crossover from one limiting regime to the other.

Figure 4.5 shows the obtained aspect ratios for  $^{167}\text{Er}$  in real and momentum space for the two limiting cases considered previously, the collisionless and the hydrodynamic

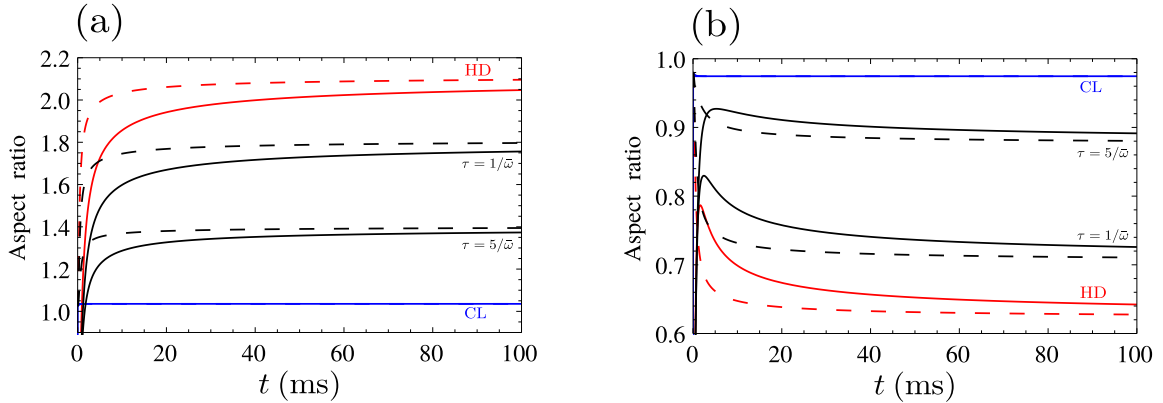


**Figure 4.5:** Aspect ratios in real (solid lines) and momentum space (dashed lines) in the collisional regime during TOF expansion of ultracold gas of  $^{167}\text{Er}$ : (a)  $\theta = 0^\circ$ , (b)  $\theta = 90^\circ$ . The pairs of curves in (a) from top to bottom and in (b) from bottom to top correspond to: hydrodynamic regime (HD, red), collisional regime (black) for fixed relaxation times  $\tau = 1/\bar{\omega}$  and  $\tau = 5/\bar{\omega}$ , and collisionless regime (CL, blue).

regime, as well as for the collisional regime with the fixed relaxation times  $\tau = 1/\bar{\omega}$  and  $\tau = 5/\bar{\omega}$ . Depending on the respective geometry, asymptotic values of aspect ratios either decrease with increasing relaxation time, see Figures 4.5(a) for  $\theta = 0^\circ$ , or vice versa, see Figure 4.5(b) for  $\theta = 90^\circ$ . We also read off from these figures that the corresponding asymptotic values of aspect ratios in real and momentum space in the collisional regime are again equal according to the relation given by Equation (4.85).

Motivated by the experiment reported in Reference [48], in Figure 4.6 we plot the aspect ratio in real space  $A_R$  obtained after  $t = 10$  ms TOF as a function of a fixed relaxation time  $\tau$  for two different orientations of the dipoles for the respective ultracold Fermi gases given in Table 3.1. If the dipoles are oriented along the  $z$  axis, i.e., Figure 4.6(a), the corresponding aspect ratios for any fixed value of the relaxation time  $\tau$  increase monotonously with the relative dipolar interaction strength  $\varepsilon_{\text{dd}}$ , while for the dipoles along the  $x$  axis, i.e., Figure 4.6(b), the situation is just opposite, as expected. Note that the corresponding curves for the noninteracting case  $\varepsilon_{\text{dd}} = 0$  would be quite close to those for  $^{53}\text{Cr}$ , as can already be expected according to Figure 3.1.

Plots like those in Figure 4.6 represent powerful diagnostic tools for estimating the relaxation time  $\tau$  from experimentally measured values of aspect ratios  $A_R$  for sufficiently short TOF, when the fixed relaxation-time approximation is still applicable. Furthermore, these graphs can be used for estimating the time scale  $t$  to approach the asymptotic values of the aspect ratios from experimentally available TOF expansion data. Provided that it turns out for a TOF  $t$  that the corresponding relaxation time  $\tau$  satisfies the condition  $\bar{\omega}\tau \gg 1$ , one has already reached the collisionless regime. This

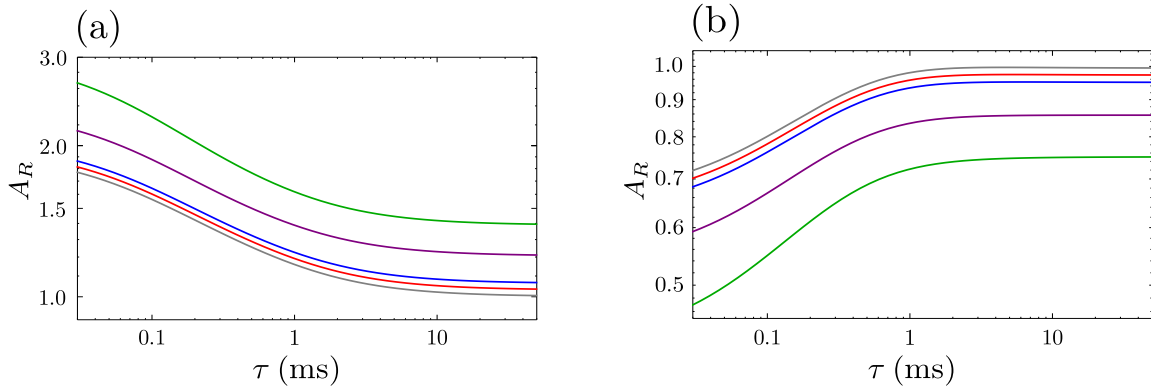


**Figure 4.6:** Aspect ratios in real space after  $t = 10$  ms TOF as function of fixed relaxation time  $\tau$  for different ultracold Fermi gases: (a)  $\theta = 0^\circ$ , (b)  $\theta = 90^\circ$ . The curves in (a) from bottom to top and in (b) from top to bottom correspond to:  $^{53}\text{Cr}$  (gray),  $^{167}\text{Er}$  (red),  $^{161}\text{Dy}$  (blue),  $^{40}\text{K}^{87}\text{Rb}$  (purple), and  $^{167}\text{Er}^{168}\text{Er}$  (green).

means that for longer times  $t$  no further change of the aspect ratio is expected as one is already quite close to its asymptotic value.

#### 4.3.4 Collisional regime with self-consistent relaxation time

Whereas we assumed before that the relaxation time is constant, now we model the TOF expansion of ultracold dipolar Fermi gases more realistically and take into account that the relaxation time changes and is also time dependent. Namely, during TOF the gas rapidly expands, the distance between atoms grows, and as a consequence the relaxation time increases, thus eventually leading the system into the collisionless regime, even if initially it was in the hydrodynamic or in the collisional regime.

In order to quantify this physical notion, one would have to calculate the collision integral on the right-hand side of Equation (4.20), which requires a detailed modeling of scattering processes in the system, i.e., the elastic collisions of fermionic atoms or molecules that arise purely from universal dipolar scattering. The standard approach for the case of a system close to local equilibrium is to use the relaxation-time approximation [12, 158], which is given by Equation (4.22). In Reference [161] it was derived that the characteristic relaxation time for a classical gas can be expressed as follows

$$\tau = \frac{\alpha_{\text{coll}}}{\bar{n}\sigma_{\text{el}}v}, \quad (4.89)$$

where the parameter  $\alpha_{\text{coll}}$  denotes a geometry-dependent average number of collisions which is necessary to rethermalize the system after a collision,  $\bar{n}$  represents the mean number density,  $\sigma_{\text{el}}$  is the total elastic cross section, and  $v$  is the mean relative velocity.

In Reference [87] it was heuristically argued and experimentally confirmed that for quantum degenerate dipolar fermionic systems at low temperatures and parameter regimes considered here, the relaxation time can be modeled by a modified expression

$$\tau_{\text{SC}} = \frac{\alpha_{\text{coll}}}{\eta \bar{n} \sigma_{\text{el}} v}, \quad (4.90)$$

which allows us to calculate it self-consistently, hence the subscript SC. In the above equation,  $\eta$  stands for a Pauli suppression factor, which represents the reduction of the rethermalization rate in a degenerate Fermi gas due to Pauli blocking, and amounts to  $\eta = 1$  for non-degenerate gases. The Pauli suppression factor depends on the degeneration level of fermions and is usually expressed as a function of the dimensionless temperature  $T/T_{\text{F}}$ .

In the considered case, the mean number density is given by

$$\bar{n} = \frac{N}{V(t)}, \quad (4.91)$$

where the volume  $V(t)$  of the Fermi gas cloud increases during the TOF expansion according to

$$V(t) = \frac{4\pi}{3} \prod_i R_i b_i(t). \quad (4.92)$$

The total elastic cross section  $\sigma_{\text{el}}$  is universally related to the dipole moment of fermions [86] according to

$$\sigma_{\text{el}} = \frac{32\pi}{15} a_{\text{dd}}^2, \quad (4.93)$$

where

$$a_{\text{dd}} = \frac{C_{\text{dd}} M}{8\pi \hbar^2}, \quad (4.94)$$

represents a characteristic dipole length. The mean relative velocity  $v$  is given by

$$v = \sqrt{\frac{16k_{\text{B}}T}{\pi M}}. \quad (4.95)$$

For the parameters of the experiment [48] with atomic  $^{167}\text{Er}$  used throughout this paper, the universal dipolar scattering theory [87] predicts the total elastic cross section value  $\sigma_{\text{el}} = 1.8 \times 10^{-12} \text{ cm}^2$ , which agrees with the value measured in Reference [89]. The temperature of the system was set to  $T/T_{\text{F}} = 0.18$ , with  $T_{\text{F}} = 1.1 \mu\text{K}$ , which yields the Pauli suppression factor  $\eta = 0.3$  [87], as well as the mean relative velocity  $v$  according to Equation (4.95). To completely fix all parameters which are necessary

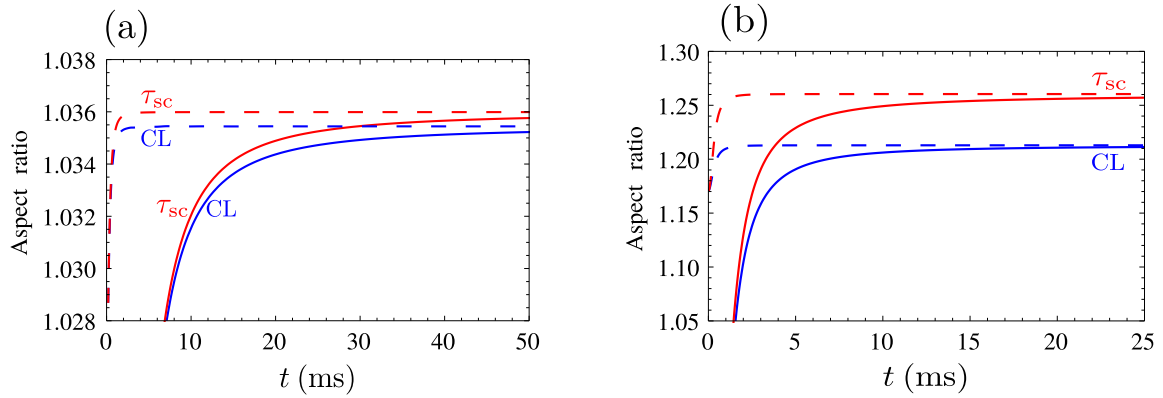


**Figure 4.7:** Aspect ratios in real (solid lines) and momentum space (dashed lines) in the collisional regime during TOF expansion for  $\theta = 0^\circ$ : (a)  $^{167}\text{Er}$ , (b)  $^{40}\text{K}^{87}\text{Rb}$ . Red upper solid and dashed line correspond to expansion dynamics with self-consistently determined relaxation time  $\tau_{\text{sc}}$ . For comparison, blue lower solid and dashed line give the corresponding aspect ratios for the collisionless regime (CL).

for a self-consistent determination of the relaxation time with Equation (4.90), we still need to take the appropriate value of the number of collisions  $\alpha_{\text{coll}}$  for the given geometry, i.e., for the given angle  $\theta$  from Reference [87].

Figure 4.7(a) shows the corresponding aspect ratios in real and momentum space for  $^{167}\text{Er}$  during the TOF expansion for  $\theta = 0^\circ$ , for which the average number of collisions to rethermalize is  $\alpha_{\text{coll}} = 3.2$  [87]. The red upper solid and dashed line in Figure 4.7(a) are obtained by numerically solving Equations (4.66) and (4.67), with the relaxation time determined self-consistently through Equation (4.90). In the same plot, we also see for the sake of comparison the results for the collisionless regime in terms of the blue lower solid and dashed line. The difference between the corresponding lines is less than 0.1%, which is certainly within the experimental error bars, and confirms that the system is indeed very close to the collisionless regime, as it was assumed in Reference [48].

However, systems with a stronger DDI can easily reach the collisional regime, where a finite value for the relaxation time has to be taken into account. In order to demonstrate this, we analyze the TOF expansion of a  $^{40}\text{K}^{87}\text{Rb}$  dipolar Fermi gas [98], whose relative dipolar interaction strength is  $\varepsilon_{\text{dd}} = 0.97$ , compared to  $\varepsilon_{\text{dd}} = 0.15$  for  $^{167}\text{Er}$  (see Table 3.1). Polar molecules have generically stronger electric dipole moments in comparison with the magnetic dipole moments of atoms, which is expected to yield a sensible difference in the respective aspect ratios.

In Figure 4.7(b) we show the TOF expansion dynamics for  $^{40}\text{K}^{87}\text{Rb}$  for the same number of fermions and trap frequencies as in Reference [48]. The temperature of

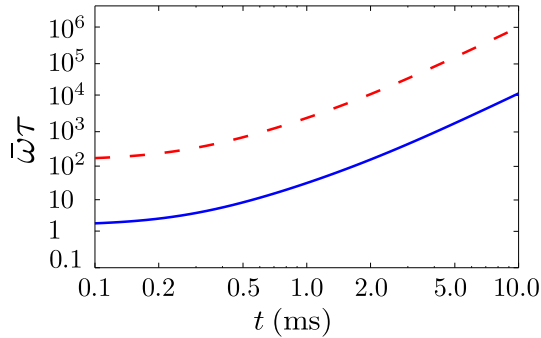


**Figure 4.8:** Self-consistently determined relaxation time given by Equation (4.90) as function of TOF  $t$  for ultracold Fermi gas of  $^{167}\text{Er}$  (red dashed line) and  $^{40}\text{K}^{87}\text{Rb}$  (blue solid line) for  $\theta = 0^\circ$ . The collisionless regime is achieved for  $\bar{\omega}\tau_{\text{SC}} \gg 1$ .

the system is assumed to be  $T = 350 \text{ nK} = 0.3 T_{\text{F}}$ , as in Reference [98], which yields the Pauli suppression factor  $\eta = 0.5$  [87]. The total elastic cross section according to Equation (4.93) in this case is  $\sigma_{\text{el}} = 9.6 \times 10^{-11} \text{ cm}^2$ , in agreement with the results of Reference [86]. The average number of collisions to rethermalize is again taken to be  $\alpha_{\text{coll}} = 3.2$  for  $\theta = 0^\circ$  [87]. The difference between the aspect ratios calculated using the self-consistently determined relaxation time and those calculated assuming that the system is in the collisionless regime are here around 10%, which could be clearly observed in future experiments. Furthermore, for polar molecules with a stronger DDI the differences are expected to be even more pronounced. Thus, in experiments with such systems, the relaxation time must be taken into account, for instance through the self-consistent approach presented here. We also note that the asymptotic values of aspect ratios in real and momentum space turn out to be again the same, as was already the case in both limiting regimes, the collisionless and the hydrodynamic.

Figure 4.8 shows the resulting time dependence of the self-consistently determined relaxation time during the TOF expansion for both analyzed species, i.e.,  $^{167}\text{Er}$  (red dashed line) and  $^{40}\text{K}^{87}\text{Rb}$  (blue solid line). As we can see, for an atomic gas of  $^{167}\text{Er}$  the relaxation time satisfies the condition  $\bar{\omega}\tau_{\text{SC}} \gg 1$  right from the beginning, which further justifies the previous conclusion that the system is always in the collisionless regime [48]. For a molecular gas of  $^{40}\text{K}^{87}\text{Rb}$ , however, this condition is satisfied only after 1-2 ms, so initially the system is in the collisional regime. Furthermore, we recognize that the relaxation time increases quite fast, namely faster than exponential, as we can see from the log-log plot of Figure 4.8. Thus, the approximation of Section 4.3.3 with a fixed relaxation time would clearly not be suitable, and a self-consistent approach as presented here is indispensable.

In order to summarize our results for the aspect ratios during the TOF expansion in

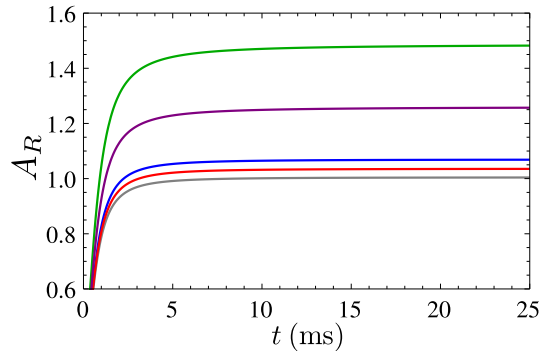


**Figure 4.9:** Aspect ratios in real space during TOF expansion in the collisional regime with self-consistently determined relaxation time for different ultracold Fermi gases for  $\theta = 0^\circ$ . The curves from bottom to top correspond to:  $^{53}\text{Cr}$  (gray),  $^{167}\text{Er}$  (red),  $^{161}\text{Dy}$  (blue),  $^{40}\text{K}^{87}\text{Rb}$  (purple), and  $^{167}\text{Er}^{168}\text{Er}$  (green).

the collisional regime with self-consistently determined relaxation time, in Figure 4.9 we combine our results for the time dependence of aspect ratios in real space  $A_R$  for  $\theta = 0^\circ$  for  $^{167}\text{Er}$  from Figure 4.7(a) and  $^{40}\text{K}^{87}\text{Rb}$  from Figure 4.7(b) with the results for three other considered dipolar fermionic species  $^{53}\text{Cr}$ ,  $^{161}\text{Dy}$ , and  $^{167}\text{Er}^{168}\text{Er}$  (see Table 3.1). We see that increasing the relative DDI strength leads to increasing aspect ratios after a long TOF. While for  $^{53}\text{Cr}$ ,  $^{167}\text{Er}$ , and  $^{161}\text{Dy}$  the asymptotic values of  $A_R$  are just few percent larger than 1, for  $^{40}\text{K}^{87}\text{Rb}$  we obtain a value of about 1.26, and for  $^{167}\text{Er}^{168}\text{Er}$  about 1.48.

Effects of the DDI and their interplay with the geometry quite strongly influence the dynamics of the system. As we already pointed out, this is of particular importance for interpreting the TOF imaging data, which are commonly used for experimental measurements of the properties of ultracold Fermi gases. It was previously shown that, even for magnetic atomic species such as erbium, the DDI effects could be experimentally observed in the TOF dynamics, and that a nonballistic expansion has to be used in order to properly describe the system's behavior [49, 50, 125]. For polar molecules with a strong DDI we expect that nonballistic effects are more pronounced, as can be read off from Figure 4.10. Even more significant are large variations of nonballistic effects, which can be as small as 8% or as large as 60% for quite similar configurations, as is illustrated for the two examples in Figure 4.10(a). Although the trap geometry plays a role here, Figure 4.10(b) reveals that the ballistic behavior is roughly the same, as is expected based on the system parameters, while the DDI strength gives a major contribution. Furthermore, the inset in Figure 4.10(a) shows that even the qualitative behavior of the system can be incorrectly predicted (monotonous vs. nonmonotonous behavior) when nonballistic effects are neglected. This demonstrates that the DDI has

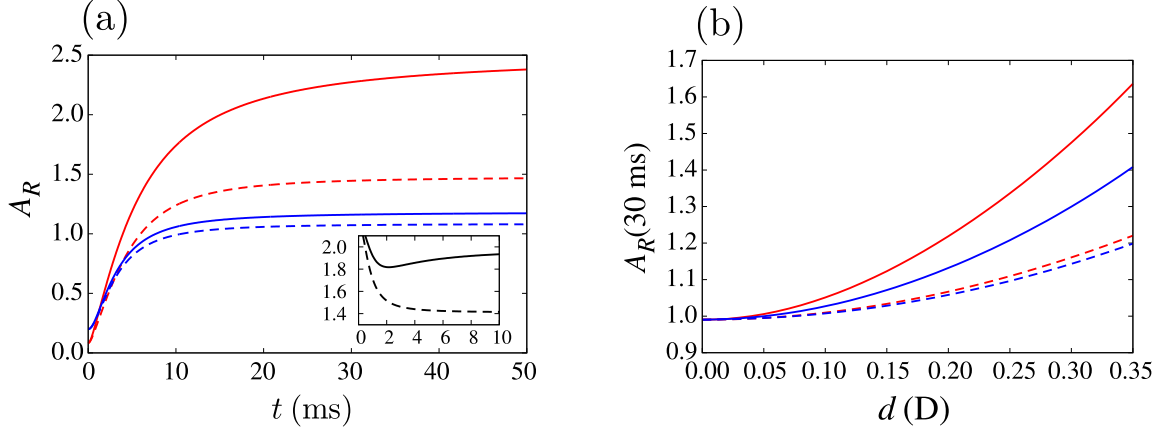


**Figure 4.10:** (a) Real-space aspect ratio  $A_R$  of the  $^{40}\text{K}^{87}\text{Rb}$  molecular cloud as a function of time  $t$  during the TOF expansion from the ground state, after the trap is switched off. Top (red) solid and dashed lines are obtained for  $d = 0.5$  D and frequencies  $(63, 36, 500) \times 2\pi$  Hz, bottom (blue) solid and dashed lines for  $d = 0.22$  D and  $(63, 36, 200) \times 2\pi$  Hz, and inset for  $d = 0.35$  D and  $(250, 150, 100) \times 2\pi$  Hz. (b)  $A_R(30 \text{ ms})$  after the TOF expansion for  $t = 30$  ms as a function of  $d$ . Trap frequencies corresponding to all line types are the same as in (a). In both plots solid lines correspond to a nonballistic expansion, where the DDI is taken into account, while the dashed lines represent calculated results for a free (ballistic) expansion,  $N = 3 \times 10^4$ ,  $\theta = 0^\circ$ .  $A_R$  is calculated using the imaging angle  $22.5^\circ$  of Reference [109], in the geometry of Reference [49].

to be taken into account even during the TOF expansion, and that the interpretation of experimental data is hugely affected by the model used. The generalized theory presented in this Chapter enables an accurate modeling of the dynamics of strongly interacting dipolar Fermi systems.

For future work, it would be of interest to go beyond References [87, 161] and derive more accurate results for the relaxation time from first principles. This would amount to linearizing the Boltzmann equation and treating the linearization with the rescaling technique introduced in Reference [158]. Furthermore, the approach developed here, based on the relaxation-time approximation for the Boltzmann equation, can also be applied to other fields of physics. The examples include nuclear physics, such as a study of viscosity of the quark-gluon plasma [162, 163] and ultra-relativistic heavy-ion collisions [164], as well as plasma physics [165], where, e.g., transient regimes of degenerate electrons can be studied using the relaxation-time approximation [166].

---

## Comparison with experiment

---

Having developed a general theoretical framework presented in Chapters 2 and 4, and having numerically studied the ground state properties of dipolar Fermi gases with arbitrary oriented dipoles in Chapter 3, we now compare those results with experimental data obtained in Innsbruck, with a degenerate Fermi gases of erbium [84]. As we have already emphasized, the FS deformation was first observed with this setup and reported in Reference [48], but additional measurements are performed using different trapping configurations to test our newly developed theoretical understanding about the influence of the dipoles' orientation on the FS deformation [49]. In these experiments the FS deformation is probed by the TOF expansion measurements. Starting from a degenerate Fermi gas confined into an elongated harmonic trap with  $N \sim 6 - 7 \times 10^4$  erbium atoms and at the temperature  $T/T_F \sim 0.2$ , the cloud geometry and dipole's orientation are slowly set to the desired configuration. After that the cloud equilibrate for several hundreds of milliseconds and then the trapping potential is suddenly removed to initiate yhe TOF expansion. Finally, after a free expansion of duration  $t$ , the standard absorption imaging along a fixed direction is performed, as illustrated in Figure 2.2.

Before we compare theory and experiment, let us note again that our theoretical results are only valid for at zero temperature. For finite temperatures the isotropic thermal fluctuations have already been shown to work against any directional dependence stemming from either the harmonic confinement or the DDI, thus they diminish the FS deformation. The thermal corrections to the total energy are known to be proportional to  $(T/T_F)^2$  at low  $T$  [142]. The corresponding effect on the FS deformation was also previously theoretically [123] and experimentally [48] investigated, showing

similar scalings. However, for the low temperatures of experiments in Reference [49], this would yield only a few percent correction to the zero-temperature results, which lies within the experimental error bars. Therefore, we neglect the thermal corrections here. Generally speaking, the value of  $(T/T_F)^2$  can be used to estimate the relevance of the finite-temperature effects for  $T/T_F < 0.5$ , while  $(T/T_F)^{-\frac{5}{2}}$  should be considered for larger temperatures [123].

## 5.1 Aspect ratios and FS deformation

The TOF images are taken in the plane perpendicular to the imaging axis and the deformation of the atomic cloud can be investigated in terms of the time-dependent cloud aspect ratio  $A_R(t)$ , which is given by Equation (4.73). Since this quantity is directly measurable in the experiment, we use it to extract the value of the FS deformation, which is connected to the aspect ratio in momentum space in the global equilibrium. Using Equation (D.3), and having in mind that  $\nu(\mathbf{r}, \mathbf{k}, t = 0) \equiv \nu^0(\mathcal{R}, \mathcal{K})$ ,  $\mathcal{R}(t = 0) = \mathbf{r}$ , and  $\mathcal{K}(t = 0) = \mathbf{k}$ , we get that the average size of the FS in a global equilibrium in the  $i$ -th direction is described by

$$\langle k_i^2(t = 0) \rangle = \langle \mathcal{K}_i^2 \rangle^0 = \frac{1}{8} \sum_j \mathbb{R}_{ij}^{\prime 2} K_j^{\prime 2}. \quad (5.1)$$

This result, together with Equations (D.21) and (2.86), yields the following expression for the aspect ratio in momentum space in global equilibrium in terms of the Fermi momenta  $K'_i$ ,

$$\begin{aligned} A_K &= \sqrt{\frac{\sum_j \mathbb{R}_{zj}^{\prime 2} K_j^{\prime 2}}{\sum_j \mathbb{R}_{xj}^{\prime 2} K_j^{\prime 2} \cos^2 \alpha + \sum_j \mathbb{R}_{yj}^{\prime 2} K_j^{\prime 2} \sin^2 \alpha}} \\ &= \sqrt{\frac{K_x^{\prime 2} \sin^2 \theta + K_z^{\prime 2} \cos^2 \theta}{K_x^{\prime 2} + (K_z^{\prime 2} - K_x^{\prime 2}) \sin^2 \theta (\cos^2 \varphi \cos^2 \alpha + \sin^2 \varphi \sin^2 \alpha)}}. \end{aligned} \quad (5.2)$$

Please note that only for  $\theta = 0^\circ$ , when the dipoles are parallel to the  $z$  axis, the above momentum-space aspect ratio coincides with the ratio between the Fermi momenta,

$$A_K = \frac{K'_z}{K'_x} = 1 + \Delta, \quad (5.3)$$

where  $\Delta$  denotes the deformation of the FS previously introduced in Equation (3.10).

In general, however, the relation between  $A_K$  and  $\Delta$  is nonlinear and can be obtained from Equation (5.2), as follows

$$\Delta = \sqrt{\frac{A_K^2[1 - \sin^2 \theta(\cos^2 \varphi \cos^2 \alpha + \sin^2 \varphi \sin^2 \alpha)] - \sin^2 \theta}{\cos^2 \theta - A_K^2 \sin^2 \theta(\cos^2 \varphi \cos^2 \alpha + \sin^2 \varphi \sin^2 \alpha)}} - 1. \quad (5.4)$$

## 5.2 Ballistic expansion

In order to extract the value of the FS deformation from the experimental data using the above equation, we still need to calculate the momentum-space aspect ratio  $A_K$ . This is done by using the fact that the long-time expansion is mainly dominated by the velocity distribution right after the release from the trap. Here we rely on the ballistic approximation, which assumes that the TOF images, that show the shape of the atomic cloud in real space, purely reflect the momentum distribution in the global equilibrium. Namely, in Chapter 4 we have shown that ballistic expansion relation given by Equation (4.82) is valid in the collisionless regime for the case when the dipoles are oriented along one of the trap axis. Now we have to prove that this is also valid for the general orientation of the dipoles, as it is varied in the experiment. Since the experiment is done in the collisionless regime, Equation (4.76) is still applicable, while equations for the scaling parameters  $b_i$  can be obtain from Equation (4.46). Actually, the terms  $B_i^D(b)$  and  $B_i^E(b, \Theta)$  in Equation (4.46) represent contributions of the DDI, which is neglected during the ballistic expansion, so removing these terms and term corresponding to the trapping potential we obtain

$$\ddot{b}_i(t) - \frac{\hbar^2 \sum_j \mathbb{R}_{ij}^2 K_j'^2}{M^2 R_i^2} \frac{1}{b_i^3(t)} = 0. \quad (5.5)$$

Here we have used Equation (4.76), as well as the fact that the trap is elongated, such that we can assume  $\mathbb{R}'' = \mathbb{I}$ . This cooresponds to using the off-on-axis scenario (see Section 2.1), which is justified for weak DDI in the erbium case and elongated traps.

Differential Equations (5.5) can be solved analytically, and we obtain for the scaling parameters  $b_i$  the following expression,

$$b_i(t) = \sqrt{1 + \frac{\hbar^2 \sum_j \mathbb{R}_{ij}^2 K_j'^2}{M^2 R_i^2} t^2}. \quad (5.6)$$

Together with Equation (D.14) from Appendix D.2, this enables to calculate the bal-

listic expansion aspect ratio in real space, with the asymptotic value

$$\begin{aligned} \lim_{t \rightarrow \infty} A_R^{\text{bal}}(t) &= \lim_{t \rightarrow \infty} \sqrt{\frac{M^2 R_z^2 + \hbar^2 \sum_j \mathbb{R}_{zj}^{\prime 2} K_j^{\prime 2} t^2}{(M^2 R_x^2 + \hbar^2 \sum_j \mathbb{R}_{xj}^{\prime 2} K_j^{\prime 2} t^2) \cos^2 \alpha + (M^2 R_y^2 + \hbar^2 \sum_j \mathbb{R}_{yj}^{\prime 2} K_j^{\prime 2} t^2) \sin^2 \alpha}} \\ &= \sqrt{\frac{\sum_j \mathbb{R}_{zj}^{\prime 2} K_j^{\prime 2}}{\sum_j \mathbb{R}_{xj}^{\prime 2} K_j^{\prime 2} \cos^2 \alpha + \sum_j \mathbb{R}_{yj}^{\prime 2} K_j^{\prime 2} \sin^2 \alpha}}, \end{aligned} \quad (5.7)$$

which coincides with Equation (5.2) and proves that Equation (4.82) is valid not only for the special case when the dipoles are oriented along one of the trap axes, but also in general case, for arbitrary orientation of the dipoles.

We note that this is true just in the case of ballistic expansion, when the effects of the DDI can safely be neglected during the TOF. However, since the DDI is long-range, ideally it should be taken into account, rendering the TOF results always nonballistic. A general theory that would allow such a treatment is not yet available and is beyond the scope of this Thesis. Nevertheless, if the DDI is weak enough, as in the case of erbium atomic gases, the difference between the ballistic (free) and nonballistic expansion is small, as already shown in Reference [125]. Thus, Equation (4.82) can approximately be used in our case and the value of  $A_K$  in global equilibrium can be extracted from the long-time limit of  $A_R$ , which is available from the experimental data. We highlight that in some limiting cases it is still possible to take into account a nonballistic expansion by using the previously developed dynamical theory [125]. This is expected to yield a more precise value of the aspect ratio, as show in the next section.

With those cautionary remarks in mind, we can complete the description of the algorithm for analyzing experimentally obtained data. Now it only remains to calculate the FS deformation from the extracted aspect ratio using Equation (5.4), which enables its comparison with our numerical results.

### 5.3 Experimental and theoretical results

Here we consider three different datasets corresponding to the experimental parameters listed in Table 5.1, where we also give the mean frequency of the trap  $\bar{\omega}$  and the trap anisotropy  $\lambda = \sqrt{\omega_x \omega_z} / \omega_y$  for each case. While Cases 1 and 2 represent cigar-shaped traps, Case 2 is selected so that it has the same value of  $\omega_y$  as Case 1, but a smaller anisotropy  $\lambda$ . On the other hand, Case 3 is chosen so that its mean frequency  $\bar{\omega}$  is

**Table 5.1:** Number of atoms  $N$ , trap frequencies  $\omega_i$ , mean frequencies  $\bar{\omega}$  and anisotropies  $\lambda$  for three sets of experimental parameters used throughout this Chapter. Case 1 corresponds to Reference [48], while Case 2 and Case 3 correspond to Reference [49].

$^{167}\text{Er}$	$N (\times 10^4)$	$\omega_x$ (Hz)	$\omega_y$ (Hz)	$\omega_z$ (Hz)	$\bar{\omega}$ (Hz)	$\lambda$
Case 1	6.6	$579 \times 2\pi$	$91 \times 2\pi$	$611 \times 2\pi$	$318 \times 2\pi$	6.54
Case 2	6.3	$428 \times 2\pi$	$91 \times 2\pi$	$459 \times 2\pi$	$261 \times 2\pi$	4.87
Case 3	6.1	$408 \times 2\pi$	$212 \times 2\pi$	$349 \times 2\pi$	$311 \times 2\pi$	1.78

approximately the same as for Case 1, but its anisotropy  $\lambda$  is much reduced. For each dataset, we probe the FS deformation for various angles  $\theta$  and a fixed angle  $\varphi = 14^\circ$ . The measurement for each experimental configuration was repeated a large number of times, typically twenty, so that the mean value can be reliably estimated and the statistical error is reduced below 0.2%.

Figure 5.1 shows a direct comparison between our theoretical and experimental results without any free parameters. The experiments measured the mean value of the aspect ratio  $A_R$  in free expansion using the TOF  $t = 12$  ms, which is taken to be sufficiently long so that the ballistic approximation given by Equation (4.82) can be used, and yet not too long so that the cloud does not get too dilute and a reliable fit of the density distribution from the absorption images is possible. In Figure 5.1(a) we show the  $\theta$  dependence of the measured quantity  $A_R(12 \text{ ms})$  for the parameters of Case 1 (red circles), Case 2 (blue squares) and Case 3 (black triangles), as well as the corresponding theoretical curves (solid red, dashed blue and dotted black line, respectively) for  $A_K$  at global equilibrium, calculated according to Equation (5.2). We see that the agreement is generally very good, and that the experimental data are closely matched by the shape predicted by our theory. At the same time, this figure also presents an a posteriori justification for using the ballistic approximation in those three cases.

The discrepancies observed in Figure 5.1(a) can be accredited to the effects of the DDI, which are neglected during the TOF by using the ballistic approximation. Even better agreement between the experiment and the theory can be expected if a nonballistic expansion would be taken into account. Although a theory for this is not yet available for an arbitrary orientation of the dipoles, Reference [125] allows us to perform a nonballistic expansion calculation for the special case  $\theta = 0^\circ$  in the

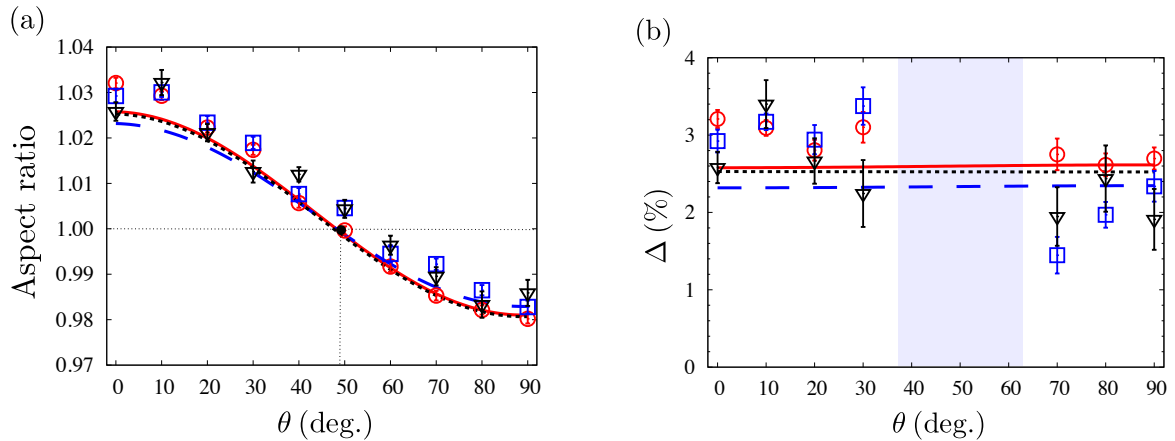


**Figure 5.1:** Comparison of our results for  $\theta$  dependence of: (a) theoretical value of aspect ratio  $A_K$  and its experimental estimate  $A_R^{\text{exp}}(t = 12 \text{ ms})$  according to Equation (4.82); (b) theoretical value of the FS deformation  $\Delta$  and its experimental estimate (see main text). Red solid lines and circles correspond to Case 1, blue dashed lines and squares correspond to Case 2, and black dotted lines and triangles correspond to Case 3. Vertical bars for experimental results correspond to statistical errors. Angle  $\varphi = 14^\circ$  was kept constant during the experiment. Intersection point of three curves in panel (a) corresponds to  $(\theta^*, A_K^*) = (49.16^\circ, 1)$ , while shaded area in panel (b) is excluded due to a pole in Equation (5.8); see main text for further details.

collisionless regime. The comparison of the results is given in Table 5.2, where we see that accounting for the DDI during the TOF yields theoretical values of the TOF real-space aspect ratio equal to the experimental ones, within the error bars of the order of 0.1%. Table 5.2 also shows that nonballistic effects amount to 0.7% for Case 1, which has the largest anisotropy, and becomes smaller as the trap is closer to a spherical shape, i.e., as the trap anisotropy approaches the value of 1. Therefore, we conclude that the agreement of experimental data and our theoretical results in Figure 5.1(a)

**Table 5.2:** Comparison of theoretical values of aspect ratios in momentum space  $A_K$  in global equilibrium and TOF aspect ratios in real space: theoretical value of  $A_R^{\text{nbal}}$  and experimental value of  $A_R^{\text{exp}}$ , with corresponding statistical errors  $\Delta A_R^{\text{exp}}$ . Real-space aspect ratios correspond to TOF of  $t = 12 \text{ ms}$  and  $\theta = 0^\circ$ . Last two columns give trap mean frequency  $\bar{\omega}$  and anisotropy  $\lambda$  for each case.

$^{167}\text{Er}$	$A_K$	$A_R^{\text{nbal}}$	$A_R^{\text{exp}}$	$\Delta A_R^{\text{exp}}$	$\bar{\omega}$ (Hz)	$\lambda$
Case 1	1.0258	1.0324	1.0321	0.0012	$318 \times 2\pi$	6.54
Case 2	1.0232	1.0282	1.0292	0.0015	$261 \times 2\pi$	4.87
Case 3	1.0253	1.0270	1.0258	0.0020	$311 \times 2\pi$	1.78

can be further improved by using numerical solution of Equations (4.56) and (4.61), together with Equation (4.46), which represents theory for nonballistic expansion in case of the most general experiment geometry.

Figure 5.1(b) shows a comparison of our theoretical and experimental results for the deformation  $\Delta$  of the FS for the three considered cases, where the experimental values are calculated according to Equation (5.4), assuming ballistic expansion relation and using the real-space aspect ratios shown in Figure 5.1(a). Although the statistical error bars  $\Delta A_R^{\text{exp}}$  for the experimentally measured values of the real-space aspect ratios are small and almost constant, the corresponding errors for the FS deformation, calculated as

$$\Delta A_R^{\text{exp}} \left| \frac{\partial \Delta}{\partial A_K} \right|_{A_K = A_R^{\text{exp}}}, \quad (5.8)$$

show a strong angular dependence, due to the presence of a pole in the function  $\partial \Delta / \partial A_K$ . For the parameters of Figure 5.1, the pole emerges at around  $\theta = 50^\circ$ . Therefore, the error bars appear significantly larger in the neighboring region, which justifies to drop the data points around  $\theta = 50^\circ$  (shaded area in the graph).

As can be seen in Figure 5.1(b), for all three cases the deformation of the FS is almost constant for all angles  $\theta$ . Therefore, we have compared theoretical and experimental values for the FS deformation  $\Delta$  averaged over the angle  $\theta$ . In Table 5.3 we give the mean values for all measurements and compare them to our theory results, with the corresponding errors. As can be seen the agreement between the theory and experiment is very good. We conclude that, from the experimental point of view, in this case it would be enough just to measure the aspect ratio for one value of  $\theta$ , e.g.,  $\theta = 0^\circ$  in order to determine the deformation of the FS. However, this is only true for a weak enough DDI. Nevertheless, even if this is the case, the measurement of

**Table 5.3:** Comparison of theoretical and experimental values for the FS deformation  $\Delta$  averaged over  $\theta$ : theoretical value of  $\Delta^{\text{th}}(\%)$  and experimental value of  $\Delta^{\text{exp}}(\%)$  with corresponding errors  $\Delta(\Delta^{\text{th}})(\%)$  and  $\Delta(\Delta^{\text{exp}})(\%)$ .

$^{167}\text{Er}$	$\Delta^{\text{th}}(\%)$	$\Delta(\Delta^{\text{th}})(\%)$	$\Delta^{\text{exp}}(\%)$	$\Delta(\Delta^{\text{exp}})(\%)$
Case 1	2.59	0.02	2.9	0.3
Case 2	2.33	0.02	2.6	0.5
Case 3	2.52	0.01	2.5	0.6

the angular dependence of  $A_R$  is an indispensable tool for a full verification of the developed theory, as demonstrated in Figures 5.1(a) and 5.1(b).

We now briefly comment on the beyond-Hartree-Fock corrections, which we calculate for the FS deformation according to Section 3.5. The results are presented in Table 5.4, where we see that these corrections are extremely small differences and definitely cannot be resolved experimentally.

**Table 5.4:** Beyond-mean-field corrections to the FS deformation  $\delta\Delta_h^2(\%)$  for  $\theta = 0^\circ$  for all three considered cases from Table 5.1. First two columns give relative DDI strength  $\varepsilon_{\text{dd}}$  and parameter  $u$ , given by Equations (3.9) and (3.20), respectively.

$^{167}\text{Er}$	$\varepsilon_{\text{dd}}$	$u$	$\delta\Delta_h^2(\%)$
Case 1	0.153	0.0359	0.007
Case 2	0.138	0.0323	0.006
Case 3	0.149	0.0355	0.007

## 5.4 Universal consequences of geometry

As already observed in Figure 5.1(a), the  $A_K$  curves for all three considered cases intersect at a special point  $(\theta^*, A_K^* = 1)$ . Figure 5.2 reveals that this is not just a coincidence. It shows the  $\theta$ -dependence of the momentum-space aspect ratio  $A_K$  for several trapped geometries for erbium atomic gases, ranging from a cigar-shaped trap,

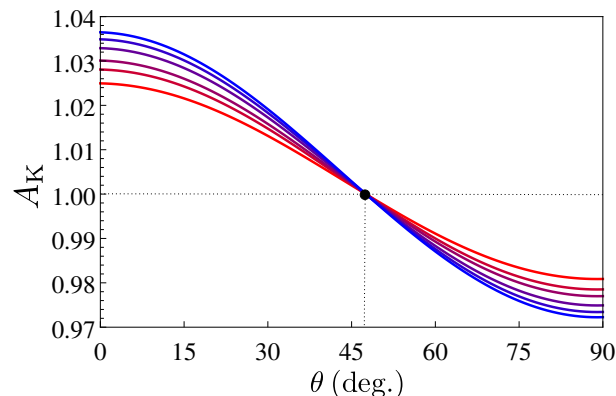


**Figure 5.2:** Aspect ratio in momentum space  $A_K$  as a function of  $\theta$  for  $^{167}\text{Er}$  for  $\varphi = 0^\circ$ ,  $\alpha = 28^\circ$ ,  $N = 7 \times 10^4$  and  $\omega_x = \omega_z = 500 \times 2\pi$  Hz. Different curves correspond to varying  $\omega_y = n \times 100 \times 2\pi$  Hz,  $n \in \{1, 2, 3, 5, 7, 9\}$ , bottom to top on the left-hand side of the intersection, respectively. Intersection point is at  $(\theta^*, A_K^*) = (48.56^\circ, 1)$ .

through a spherical, to a pancake-shaped trap. The azimuthal angle is kept constant at the value  $\varphi = 0^\circ$ , as well as the trapping frequencies  $\omega_x = \omega_z = 500 \times 2\pi$  Hz, while the frequency  $\omega_y = n \times 100 \times 2\pi$  Hz is varied by changing the value  $n \in \{1, 2, 3, 5, 7, 9\}$ , which corresponds to the trap anisotropy  $\lambda = 5/n$ . The number of particles was fixed at  $N = 7 \times 10^4$ . We observe again that all curves intersect for  $A_K^* = 1$ , which suggests that this is a general rule. Indeed, if we take into account that  $K'_z \geq K'_x > 0$ , for  $A_K^* = 1$  we can show from Equation (5.2) that the following relation holds, which connects the intersection angles  $\theta^*$  and  $\varphi^*$ ,

$$\sin^2 \theta^* = \frac{1}{1 + \cos^2 \varphi^* \cos^2 \alpha + \sin^2 \varphi^* \sin^2 \alpha}. \quad (5.9)$$

This result is universal, i.e., it is independent of other system parameters as the trap geometry, the number of particles, and the DDI strength. In other words, this intersection point is purely a consequence of the geometry, and for any orientation of the dipoles there exists an imaging angle such that the aspect ratio is given by  $A_K = 1$ , while the FS deformation  $\Delta$  can be nontrivial and even can have a significant value. We note that for larger  $\varepsilon_{\text{dd}}$  values additional parameter-specific intersection points may appear for some geometries, but the intersection point for  $A_K = 1$  is universal and always present.

To further illustrate this, in Figure 5.3 we plot a diagram in the  $(\theta^*, \varphi^*)$ -plane for  $\alpha = 28^\circ$ , where the regions with  $A_K > 1$  and  $A_K < 1$  are delineated by a solid line defined by Equation (5.9). The two black dots correspond to intersection points from Figure 5.2 for  $\varphi = 0^\circ$  and from Figure 5.1(a) for  $\varphi = 14^\circ$ , respectively.

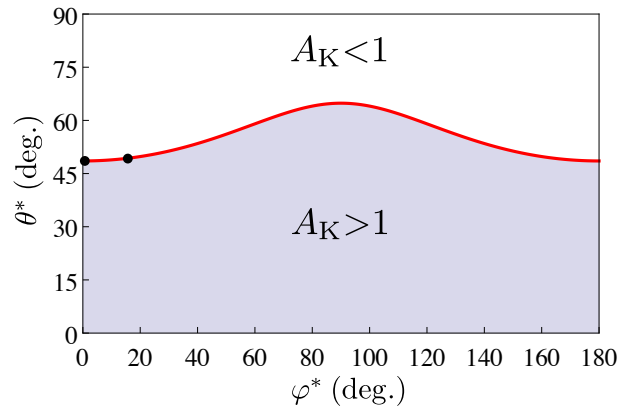


**Figure 5.3:** Relation between intersection angles  $\theta^*$  and  $\varphi^*$  for  $\alpha = 28^\circ$ , determined by Equation (5.9): red solid line corresponds to  $A_K^* = 1$ , region below to  $A_K > 1$ , and region above to  $A_K < 1$ . Black dots correspond to intersection points identified in Figures 5.2 and 5.1(a) for  $\varphi = 0^\circ$  and  $14^\circ$ , respectively.

---

## Conclusions

---

This Thesis contributes to understanding of the behavior and properties of dipolar Fermi gases in two different directions. First, it presents a generalization of the Hartree-Fock mean-field theory based on a variational approach for the Wigner distribution function, which is precisely tailored to describe the ground state of polarized, harmonically trapped dipolar Fermi gases at zero temperature, with an arbitrary orientation of the dipoles. Until now, there was no theory capable of describing such a system in a general harmonic trap geometry with respect to the dipoles' orientation.

To explore the ground-state properties of the system, we have used the newly developed approach and studied the stability of strongly dipolar Fermi gases. We have shown that it has universal features, i.e., that it can be expressed in terms of species-independent parameters such as the trap aspect ratios and the orientation of the dipoles. We have further investigated the stability of polarized  $^{40}\text{K}^{87}\text{Rb}$  molecules, as this is currently the most relevant experimental system, and demonstrated significant effects due to presence of the DDI. This opens up a new avenue of research of dipolar fermions and enables addressing the stability problem in general geometry, which is of critical importance for the design of new experiments with polar molecules.

The new ansatz for the Wigner function that we have used takes into account effects of the DDI on both the shape of the gas cloud in real space and the shape of the FS in momentum space. By means of the developed Hartree-Fock mean-field theory with this new ansatz, we have proven that, due to the DDI, the ground-state FS is deformed from a sphere to an ellipsoid such that its main axis coincides with the orientation of the dipoles. We have then studied effects of the dipoles' orientation, the particle number, the trap anisotropy and the DDI strength on the deformation of the

FS. We have found that the FS deformation is maximal when the dipoles point along the axis with the smallest trapping frequency and demonstrated this for two systems with different DDI strengths, values of which are achievable with atomic  $^{167}\text{Er}$  in one case and with  $^{40}\text{K}^{87}\text{Rb}$  molecules in the other case. Furthermore, for both species we have observed that the angular dependence of the FS deformation is larger than the corresponding dependence on the trap anisotropy, and that both are less pronounced than the corresponding effect when the number of particles is varied. However, for a fixed trap geometry and number of particles, the angular dependence of the FS deformation is quite strong for the polar molecules with a strong DDI compared to the atomic species with a weak DDI. This has an important consequence, namely, that in the case of polar molecules the FS does not only follow the dipoles' orientation, but its shape gets modified as well, which is a qualitatively different behavior compared to atomic magnetic species, where the FS just rigidly follows the dipoles' orientation.

The gas cloud orientation obtained within the presented theory strongly depends on both the DDI strength and the anisotropy of the trap. In the special case of a spherical trap the cloud is elongated along the dipoles' direction, as the FS, but in a general case the cloud orientation can only be determined numerically. This demonstrates that the theory developed here is important for an accurate qualitative and quantitative description of dipolar Fermi systems with moderate to strong DDI.

The theory for the ground-state properties of trapped Fermi gases of tilted dipoles presented in this Thesis is also important for the study of the interplay between the FS deformation and superfluid pairing, in particular to address the open question of how the anisotropic order parameter of the emergent superfluidity and its critical temperature are tunable by both the trap geometry and the dipoles' orientation. The presented theory paves the way towards new methods for quantum engineering of properties of dipolar Fermi gases that depend on the FS shape, such as the emergence of superfluidity.

Second contribution of this Thesis is in extending of the existing theoretical models for the dynamics of dipolar fermions, and in providing a unified framework for modeling of all experimentally relevant regimes: collisionless, collisional, and hydrodynamic, which was lacking before. In order to describe dynamics of dipolar Fermi gases during the TOF expansion, we have used the quantum kinetic Boltzmann formalism within the relaxation-time approximation for the collision integral. We have performed a systematic study of the TOF dynamics of dipolar Fermi systems from the collisionless to the hydrodynamic regime at zero temperature. We have studied the aspect ratios

---

of the fermionic cloud in real and momentum space. The obtained theoretical results for the TOF expansion aspect ratios in the collisionless regime are compared with measurements on degenerate gases of atomic  $^{167}\text{Er}$  in different trap geometries. In order to do so, we have first established a relationship between the FS deformation and the momentum-space aspect ratio for a general system geometry, which is experimentally accessible by measuring the real-space aspect ratio during the TOF, if we assume ballistic expansion. Using this, we have found a very good agreement between the theory and experiment, without any free fitting parameters.

In the collisional regime we have introduced an approach for self-consistently determining the relaxation time, which allows a detailed modeling of the global equilibrium and the TOF expansion in cases when the collision integral cannot be neglected. We have also shown that a strong DDI could place the system into the collisional regime, which requires to use a self-consistent determination of the relaxation time presented in this Thesis. Furthermore, we have found that in the collisional regime the TOF dynamics can be accurately studied only if the nonballistic expansion is used, and the DDI is properly taken into account, not only to calculate the ground state, but also during the whole TOF. Therefore, the presented analytical and numerical results are relevant for a detailed quantitative understanding of ongoing and future experiments. In particular, the obtained results are relevant for systems with strong DDI, which turn out to affect significantly the aspect ratios during the TOF expansion.



## Fourier transform of dipolar interaction potential

In this Appendix, we calculate the Fourier transform of the DDI potential between two polarized fermions, which is given by Equation (1.30) and reads

$$V_{\text{dd}}(\mathbf{r}) = \frac{C_{\text{dd}}}{4\pi} \frac{\mathbf{r}^2 - 3(\mathbf{e} \cdot \mathbf{r})^2}{|\mathbf{r}|^5}. \quad (\text{A.1})$$

In contrast to majority of literature, where this kind of calculation is presented for the dipoles oriented along  $z$  axis, we consider the most general orientation of the dipoles defined by the vector  $\mathbf{e} = (\cos \alpha, \cos \beta, \cos \gamma)$ , where  $\alpha, \beta$  and  $\gamma$  denote the angles between the dipole's orientation and  $x, y$  and  $z$  axis, respectively, as illustrated in Figure A.1(a). In the spherical coordinates, the DDI potential has the following form,

$$V_{\text{dd}}(\mathbf{r}) = -\frac{C_{\text{dd}}}{4\pi} \frac{1}{r^3} [3(\sin \vartheta \cos \phi \cos \alpha + \sin \vartheta \sin \phi \cos \beta + \cos \vartheta \cos \gamma)^2 - 1]. \quad (\text{A.2})$$

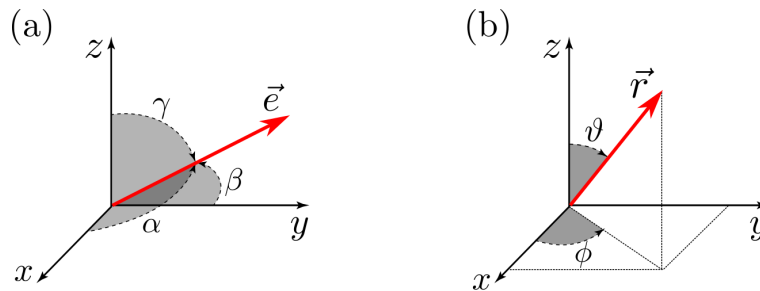


**Figure A.1:** (a) Schematic illustration of the dipoles' orientation and angles  $\alpha, \beta, \gamma$ . (b) Spherical coordinates  $r, \vartheta$ , and  $\phi$ .

The Fourier transform of the last expression reads

$$\begin{aligned} V_{\text{dd}}(\mathbf{k}) &= -\frac{C_{\text{dd}}}{4\pi} \int d^3r \frac{e^{-i\mathbf{k}\cdot\mathbf{r}}}{r^3} [3(\sin\vartheta \cos\phi \cos\alpha + \sin\vartheta \sin\phi \cos\beta + \cos\vartheta \cos\gamma)^2 - 1] \\ &= -\frac{C_{\text{dd}}}{4\pi} \int_0^\infty \frac{dr}{r} \int_0^\pi d\vartheta \sin\vartheta [\cos(rk_z \cos\vartheta) - i \sin(rk_z \cos\vartheta)] I_\phi(\vartheta, r), \end{aligned} \quad (\text{A.3})$$

where  $I_\phi(\vartheta, r)$  is the following  $\phi$ -integral

$$I_\phi(\vartheta, r) = \int_0^{2\pi} d\phi e^{-irK \sin\vartheta \sin(\phi+\phi_0)} A(\vartheta, \phi). \quad (\text{A.4})$$

The quantities  $K$  and  $\phi_0$ , used in the above expressions, are defined by

$$k_x = K \sin\phi_0 \quad (\text{A.5})$$

$$k_y = K \cos\phi_0 \quad (\text{A.6})$$

$$A(\vartheta, \phi) = 3(\sin\vartheta \cos\phi \cos\alpha + \sin\vartheta \sin\phi \cos\beta + \cos\vartheta \cos\gamma)^2 - 1. \quad (\text{A.7})$$

Using the identities

$$e^{ix \sin\varphi} = \sum_{n=-\infty}^{\infty} J_n(x) e^{in\varphi}, \quad (\text{A.8})$$

$$J_n(x) = J_{-n}(x) = (-1)^n J_n(x), \quad (\text{A.9})$$

where  $J_n(x)$  is a Bessel function of the first kind, the integral  $I_\phi(\vartheta, r)$  can be calculated as

$$\begin{aligned} I_\phi(\vartheta, r) &= \int_{\phi_0}^{2\pi+\phi_0} d\varphi e^{-irK \sin\vartheta \sin\varphi} A(\vartheta, \varphi - \phi_0) \\ &= \int_{\phi_0}^{2\pi+\phi_0} d\varphi \sum_{n=-\infty}^{\infty} (-1)^n J_n(rK \sin\vartheta) e^{in\varphi} A(\vartheta, \varphi - \phi_0) \\ &= 2\pi J_0(rK \sin\vartheta) \left[ 3 \cos^2\gamma \cos^2\vartheta - 1 + \frac{3}{2} (\cos^2\alpha + \cos^2\beta) \sin^2\vartheta \right] \\ &\quad - 12\pi i J_1(rK \sin\vartheta) \cos\gamma \cos\vartheta \sin\vartheta (\cos\alpha \sin\phi_0 + \cos\beta \cos\phi_0) \\ &\quad + 3\pi J_2(rK \sin\vartheta) \sin^2\vartheta \left[ (\cos^2\alpha - \cos^2\beta) \cos 2\phi_0 - 2 \cos\alpha \cos\beta \sin 2\phi_0 \right]. \end{aligned} \quad (\text{A.10})$$

Here we have also used the following identities,

$$\int_{\phi_0}^{2\pi+\phi_0} d\varphi e^{\pm in\varphi} \cos m(\varphi - \phi_0) = \delta_{n,m} \pi e^{\pm in\phi_0}, \quad n, m \in \mathbb{N}, \quad (\text{A.11})$$

$$\int_{\phi_0}^{2\pi+\phi_0} d\varphi e^{\pm in\varphi} \sin m(\varphi - \phi_0) = \pm \delta_{n,m} i \pi e^{\pm in\phi_0}, \quad n, m \in \mathbb{N}. \quad (\text{A.12})$$

The next step is evaluation of the  $\vartheta$ -integral in Equation (A.3), which yields

$$\begin{aligned}
I_\vartheta(r) &= \int_0^\pi d\vartheta \sin \vartheta [\cos(rk_z \cos \vartheta) - i \sin(rk_z \cos \vartheta)] I_\phi(\vartheta, r) \\
&= 4\pi \int_0^{\pi/2} d\vartheta \cos(rk_z \cos \vartheta) J_0(rK \sin \vartheta) \left( \sin \vartheta - \frac{3}{2} \sin^3 \vartheta \right) (3 \cos^2 \gamma - 1) \\
&\quad - 24\pi \int_0^{\pi/2} d\vartheta \sin(rk_z \cos \vartheta) J_1(rK \sin \vartheta) \cos \vartheta \sin^2 \vartheta \cos \gamma (\cos \alpha \sin \phi_0 + \cos \beta \cos \phi_0) \\
&\quad + 6\pi \int_0^{\pi/2} d\vartheta \cos(rk_z \cos \vartheta) J_2(rK \sin \vartheta) \sin^3 \vartheta \\
&\quad \times \left[ (\cos^2 \alpha - \cos^2 \beta) \cos 2\phi_0 - 2 \cos \alpha \cos \beta \sin 2\phi_0 \right]. \tag{A.13}
\end{aligned}$$

In the next step we use the following identities [140, (6.688.2)],

$$\begin{aligned}
&\int_0^{\pi/2} dx \cos(\beta \cos x) J_\nu(\alpha \sin x) \sin^{\nu+1} x \\
&= \sqrt{\frac{\pi}{2}} \alpha^\nu (\alpha^2 + \beta^2)^{-\frac{1}{2}\nu - \frac{1}{4}} J_{\nu+\frac{1}{2}} \left[ (\alpha^2 + \beta^2)^{\frac{1}{2}} \right], \quad \text{for } \text{Re } \nu > -1, \tag{A.14}
\end{aligned}$$

$$\begin{aligned}
&\int_0^{\pi/2} dx \sin(\beta \cos x) J_\nu(\alpha \sin x) \sin^{\nu+1} x \cos x \\
&= \sqrt{\frac{\pi}{2}} \alpha^\nu \beta (\alpha^2 + \beta^2)^{-\frac{1}{2}\nu - \frac{3}{4}} J_{\nu+\frac{3}{2}} \left[ (\alpha^2 + \beta^2)^{\frac{1}{2}} \right], \quad \text{for } \text{Re } \nu > -1, \tag{A.15}
\end{aligned}$$

where the identity (A.15) is obtained by differentiating (A.14) with respect to  $\beta$  and using the identity

$$\frac{d}{dx} J_s(x) = \frac{s}{x} J_s(x) - J_{s+1}(x). \tag{A.16}$$

In addition, the term which contains  $J_0(rK \sin \vartheta) \sin^3 \vartheta$  in Equation (A.13) is transformed using the identity

$$\frac{2}{x} J_1(x) = J_2(x) + J_0(x). \tag{A.17}$$

Finally, the  $\vartheta$ -integral can be solved to obtain

$$\begin{aligned}
I_\vartheta(r) &= (3 \cos^2 \gamma - 1) \left[ 4\pi \sqrt{\frac{\pi}{2}} \frac{J_{1/2}(rk)}{(rk)^{1/2}} - 12\pi \sqrt{\frac{\pi}{2}} \frac{J_{3/2}(rk)}{(rk)^{3/2}} + 6\pi \sqrt{\frac{\pi}{2}} \frac{(rK)^2 J_{5/2}(rk)}{(rk)^{5/2}} \right] \\
&\quad - 24\pi (\cos \gamma \cos \alpha \sin \phi_0 + \cos \gamma \cos \beta \cos \phi_0) k_z K \sqrt{\frac{\pi}{2}} \frac{r^2 J_{5/2}(rk)}{(rk)^{5/2}} \\
&\quad + 6\pi [(\cos^2 \alpha - \cos^2 \beta) \cos 2\phi_0 - 2 \cos \alpha \cos \beta \sin 2\phi_0] K^2 \sqrt{\frac{\pi}{2}} \frac{r^2 J_{5/2}(rk)}{(rk)^{5/2}}. \tag{A.18}
\end{aligned}$$

Now, the expression for  $V_{\text{dd}}(\mathbf{k})$  becomes

$$\begin{aligned}
V_{\text{dd}}(\mathbf{k}) &= -\frac{C_{\text{dd}}}{4\pi} \int_0^\infty \frac{dr}{r} I_\vartheta(r) \\
&= C_{\text{dd}} \int_0^\infty \frac{dr}{r} \left\{ \sqrt{\frac{\pi}{2}} \left( \frac{J_{1/2}(rk)}{(rk)^{1/2}} - \frac{3J_{3/2}(rk)}{(rk)^{3/2}} \right) (1 - 3\cos^2 \gamma) \right. \\
&\quad + \sqrt{\frac{\pi}{2}} \frac{r^2 J_{5/2}(rk)}{(rk)^{5/2}} \left[ \frac{3}{2} (1 - 3\cos^2 \gamma) (k_x^2 + k_y^2) - \frac{3}{2} (\cos^2 \alpha - \cos^2 \beta) (k_y^2 - k_x^2) \right. \\
&\quad \left. \left. + 6k_z k_x \cos \gamma \cos \alpha + 6k_z k_y \cos \gamma \cos \beta + 6k_x k_y \cos \alpha \cos \beta \right] \right\}. \tag{A.19}
\end{aligned}$$

The Bessel functions  $J_{1/2}(x)$  and  $J_{3/2}(x)$  are elementary functions

$$J_{1/2}(x) = \sqrt{\frac{2}{\pi x}} \sin x, \tag{A.20}$$

$$J_{3/2}(x) = \sqrt{\frac{2}{\pi}} \frac{\sin x - x \cos x}{x^{3/2}}, \tag{A.21}$$

and therefore the  $r$ -integral which contains  $J_{1/2}(rk)$  and  $J_{3/2}(rk)$  can be calculated with the help of partial integrations,

$$\begin{aligned}
&\int_0^\infty \frac{dr}{r} \sqrt{\frac{\pi}{2}} \left( \frac{J_{1/2}(rk)}{(rk)^{1/2}} - \frac{3J_{3/2}(rk)}{(rk)^{3/2}} \right) \\
&= \lim_{a \rightarrow 0} \int_a^\infty \frac{dr}{r} \left[ 3 \frac{\cos(rk)}{(rk)^2} - 3 \frac{\sin(rk)}{(rk)^3} + \frac{\sin(rk)}{rk} \right] \\
&= \lim_{a \rightarrow 0} \left[ \frac{\cos(ak)}{(ak)^2} - \frac{\sin(ak)}{(ak)^3} \right] = -\frac{1}{3}. \tag{A.22}
\end{aligned}$$

The remainig  $r$ -integral can be evaluated using the identity [140, (6.561.14)]

$$\int_0^\infty dx x^\mu J_\nu(\alpha x) = 2^\mu \alpha^{-\mu-1} \frac{\Gamma\left(\frac{1}{2} + \frac{1}{2}\nu + \frac{1}{2}\mu\right)}{\Gamma\left(\frac{1}{2} + \frac{1}{2}\nu - \frac{1}{2}\mu\right)} \tag{A.23}$$

for  $-\text{Re } \nu - 1 < \text{Re } \mu < \frac{1}{2}$ ,

which yields

$$\int_0^\infty \frac{dr}{r} \sqrt{\frac{\pi}{2}} \frac{r^2 J_{5/2}(rk)}{(rk)^{5/2}} = \frac{1}{3k^2}. \tag{A.24}$$

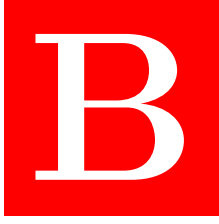
---

Combining Equations (A.19), (A.22) and (A.24) we get

$$\begin{aligned}
V_{\text{dd}}(\mathbf{k}) &= \frac{C_{\text{dd}}}{3k^2} \left[ (1 - 3 \cos^2 \gamma) \left( \frac{1}{2}k_x^2 + \frac{1}{2}k_y^2 - k_z^2 \right) + (\cos^2 \alpha - \cos^2 \beta)(k_y^2 - k_x^2) \right. \\
&\quad \left. + 6k_x k_y \cos \alpha \cos \beta + 6k_x k_z \cos \alpha \cos \gamma + 6k_y k_z \cos \beta \cos \gamma \right] \\
&= \frac{C_{\text{dd}}}{3k^2} \left[ 3(k_x \cos \alpha + k_y \cos \beta + k_z \cos \gamma)^2 - k_x^2 - k_y^2 - k_z^2 \right] \tag{A.25}
\end{aligned}$$

This expression can be further simplified, and we finally obtain

$$V_{\text{dd}}(\mathbf{k}) = \frac{C_{\text{dd}}}{3} \left[ 3 \frac{(\mathbf{e} \cdot \mathbf{k})^2}{k^2} - 1 \right]. \tag{A.26}$$




---

## Generalized anisotropy function

---

In theoretical descriptions of ultracold quantum gases, whether fermionic or bosonic, the anisotropic character of the DDI is reflected through the appearance of an anisotropic special function, which determines the dipolar energy of the system. Here we define and summarize the properties of all forms of anisotropy functions that appear in different scenarios in Chapter 2.

### B.1 Anisotropy function

Here we recall the definition of the standard anisotropy function [141]

$$\begin{aligned}
 f(x, y) &= -\frac{1}{4\pi} \int_0^{2\pi} d\phi \int_0^\pi d\vartheta \sin\vartheta \left[ \frac{3x^2y^2\cos^2\vartheta}{(y^2\cos^2\phi + x^2\sin^2\phi)\sin^2\vartheta + x^2y^2\cos^2\vartheta} - 1 \right] \\
 &= 1 + 3xy \frac{E(\vartheta_x, \kappa) - F(\vartheta_x, \kappa)}{(1-y^2)\sqrt{1-x^2}}, \tag{B.1}
 \end{aligned}$$

where  $\vartheta_x = \vartheta(x) = \arccos x$  and  $\kappa^2 = (1-y^2)/(1-x^2)$ . Furthermore,  $F(\varphi, k)$  is the elliptic integral of the first kind and  $E(\varphi, k)$  is the elliptic integral of the second kind, which are defined as follows

$$\begin{aligned}
 F(\vartheta_x, \kappa) &= \int_0^{\sin\vartheta_x} du \frac{1}{\sqrt{(1-u^2)(1-\kappa^2u^2)}}, \\
 E(\vartheta_x, \kappa) &= \int_0^{\sin\vartheta_x} du \frac{\sqrt{1-k^2u^2}}{\sqrt{1-u^2}}. \tag{B.2}
 \end{aligned}$$

One of the most important properties of the anisotropy function is its symmetry,

$$f(x, y) = f(y, x), \quad (\text{B.3})$$

as well as the sum rule,

$$f(x, y) + f\left(\frac{y}{x}, \frac{1}{x}\right) + f\left(\frac{1}{y}, \frac{x}{y}\right) = 0. \quad (\text{B.4})$$

The physical origin of the symmetry (B.3) is related to the cylindrical symmetry of the system in momentum space, after its spherical symmetry is broken due to the preferential direction of the dipoles. On the other hand, the sum rule can be connected to the fact that the average of the polarization over all directions gives zero contribution to the dipolar energy [141].

In the special case, when the arguments of the anisotropy function are equal, it reduces to a symmetric anisotropy function [29, 30, 146, 167]

$$f_s(x) = f(x, x) = \frac{3x^2}{1-x^2} \left(1 - \frac{\operatorname{arctanh}\sqrt{1-x^2}}{\sqrt{1-x^2}}\right) + 1. \quad (\text{B.5})$$

## B.2 Anisotropy function for off-on-axis scenario

When we consider the off-on-axis scenario, it is expected that the geometry of the FS has impact on dipolar energy. In order to define the corresponding anisotropy function, we first introduce some auxiliary functions,

$$\begin{aligned} 4\pi f_{Ax}(x, y) &= \int_0^{2\pi} d\phi \int_0^\pi d\vartheta \frac{y^2 \sin^3 \vartheta \cos^2 \phi}{y^2 \cos^2 \phi \sin^2 \vartheta + x^2 \sin^2 \phi \sin^2 \vartheta + x^2 y^2 \cos^2 \vartheta} \\ &= 4\pi \frac{y^2}{y^2 - x^2} \left[1 - \frac{x E(\vartheta_x, \kappa)}{y \sqrt{1-x^2}}\right], \end{aligned} \quad (\text{B.6})$$

$$\begin{aligned} 4\pi f_{Ay}(x, y) &= \int_0^{2\pi} d\phi \int_0^\pi d\vartheta \frac{x^2 \sin^3 \vartheta \sin^2 \phi}{y^2 \cos^2 \phi \sin^2 \vartheta + x^2 \sin^2 \phi \sin^2 \vartheta + x^2 y^2 \cos^2 \vartheta} \\ &= 4\pi \frac{x^2}{x^2 - y^2} \left[1 - \frac{y E(\vartheta_y, \frac{1}{\kappa})}{x \sqrt{1-y^2}}\right], \end{aligned} \quad (\text{B.7})$$

$$\begin{aligned} 4\pi f_{Az}(x, y) &= \int_0^{2\pi} d\phi \int_0^\pi d\vartheta \frac{x^2 y^2 \cos^2 \vartheta \sin \vartheta}{y^2 \cos^2 \phi \sin^2 \vartheta + x^2 \sin^2 \phi \sin^2 \vartheta + x^2 y^2 \cos^2 \vartheta} \\ &= -4\pi xy \frac{E(\vartheta_x, \kappa) - F(\vartheta_x, \kappa)}{(1-y^2)\sqrt{1-x^2}}. \end{aligned} \quad (\text{B.8})$$

Using these definitions and Equations (B.3) and (B.4), the following identities can be obtained

$$f(x, y) = 1 - 3f_{Az}(x, y), \quad (\text{B.9})$$

$$f_{Ax}(x, y) = f_{Az}\left(\frac{y}{x}, \frac{1}{x}\right), \quad (\text{B.10})$$

$$f_{Ay}(x, y) = f_{Az}\left(\frac{x}{y}, \frac{1}{y}\right), \quad (\text{B.11})$$

$$\sum_{i=x,y,z} f_{Ai}(x, y) = 1. \quad (\text{B.12})$$

The generalized anisotropy function  $f_A(x, y, \theta, \varphi)$ , which includes the momentum-space dependence on the general orientation of the dipoles reads

$$\begin{aligned} f_A(x, y, \theta, \varphi) &= 1 - 3 \sum_i \mathbb{R}_{iz}^2 f_{Ai}(x, y) \\ &= \sin^2 \theta \cos^2 \varphi f\left(\frac{y}{x}, \frac{1}{x}\right) + \sin^2 \theta \sin^2 \varphi f\left(\frac{x}{y}, \frac{1}{y}\right) + \cos^2 \theta f(x, y), \end{aligned} \quad (\text{B.13})$$

where  $\mathbb{R}_{ij}$  are matrix elements of the rotation matrix  $\mathbb{R} = \mathbb{R}(\theta, \varphi)$ , defined by Equation (2.14). Note that in the special case  $\theta = \varphi = 0^\circ$  the generalized function  $f_A$  satisfies

$$f_A(x, y, 0^\circ, 0^\circ) = f(x, y). \quad (\text{B.14})$$

### B.3 Anisotropy function for off-off-axis scenario

In the case of the off-off-axis scenario, the features of the DDI are embodied into the generalized anisotropy function  $F_A(x, y, \theta, \varphi, \tilde{\theta}, \tilde{\phi})$ , which includes both the momentum- and real-space dependence on the general orientation of the dipoles. This function is defined as follows

$$\begin{aligned} F_A(x, y, \theta, \varphi, \tilde{\theta}, \tilde{\phi}) &= \left( \sum_i \mathbb{R}_{iz} \tilde{\mathbb{R}}_{ix} \right)^2 f\left(\frac{y}{x}, \frac{1}{x}\right) \\ &+ \left( \sum_i \mathbb{R}_{iz} \tilde{\mathbb{R}}_{iy} \right)^2 f\left(\frac{x}{y}, \frac{1}{y}\right) \\ &+ \left( \sum_i \mathbb{R}_{iz} \tilde{\mathbb{R}}_{iz} \right)^2 f(x, y). \end{aligned} \quad (\text{B.15})$$

---

Here  $\mathbb{R}_{ij}$  and  $\tilde{\mathbb{R}}_{ij}$  are matrix elements of the rotation matrix  $\mathbb{R} = \mathbb{R}(\theta, \varphi)$  and  $\tilde{\mathbb{R}} = \mathbb{R}(\tilde{\theta}, \tilde{\varphi})$ , respectively. Note that in the three relevant limiting cases the function  $F_A$  satisfies

$$F_A(x, y, 0^\circ, 0^\circ, 0^\circ, 0^\circ) = f(x, y), \quad (\text{B.16})$$

$$F_A(x, y, \alpha, \beta, \alpha, \beta) = f(x, y), \quad (\text{B.17})$$

$$F_A(x, y, \theta, \varphi, 0^\circ, 0^\circ) = f_A(x, y, \theta, \varphi). \quad (\text{B.18})$$

Due to these identities and the fact that  $f(x, y)$  is a symmetric function, the obtained distributions of  $\varepsilon_{\text{dd}}^{\text{crit}}$  and  $d^{\text{crit}}$  in Figure 3.2, as well as the distributions of  $\Delta$  in Figure 3.7 are symmetric with respect to their arguments for  $\theta = \varphi = 0^\circ$ . Note that the definition (B.15) of the generalized anisotropy function  $F_A$  enables symmetric treatment of both the Hartree and the Fock term in the expression for the total energy given by Equation (2.72).



## Equations for variational parameters

Here we present the respective equations for the variational parameters of the Wigner function ansätze for all four considered scenarios in Section 2.1. The derivation procedure of the following equations is presented in Sections 2.3.1 and 2.3.2 for the most general off-off-axis scenario, but the same can be applied to any of the considered scenarios. The resulting sets of equations are given in what follows.

### C.1 Spherical scenario

The total energy of the system  $E_{\text{tot}}^{(1)}$  in the spherical scenario is given by Equation (2.76). The five variational parameters  $(K_F, R_i, \mu)$  are determined by minimizing the grand-canonical potential  $\Omega^{(1)} = E_{\text{tot}}^{(1)} - \mu N^{(1)}$ , where  $N^{(1)}$  is defined by Equation (2.10). The minimization leads to the following set of equations:

$$\mu - \frac{\hbar^2 K_F^2}{8M} = 0, \quad (\text{C.1})$$

$$\omega_x^2 R_x^2 + \frac{48Nc_0}{M\bar{R}^3} \left[ f_A \left( \frac{R_x}{R_z}, \frac{R_y}{R_z}, \theta, \varphi \right) - R_x \partial_{R_x} f_A \left( \frac{R_x}{R_z}, \frac{R_y}{R_z}, \theta, \varphi \right) \right] - \frac{8\mu}{M} = 0, \quad (\text{C.2})$$

$$\omega_y^2 R_y^2 + \frac{48Nc_0}{M\bar{R}^3} \left[ f_A \left( \frac{R_x}{R_z}, \frac{R_y}{R_z}, \theta, \varphi \right) - R_y \partial_{R_y} f_A \left( \frac{R_x}{R_z}, \frac{R_y}{R_z}, \theta, \varphi \right) \right] - \frac{8\mu}{M} = 0, \quad (\text{C.3})$$

$$\omega_z^2 R_z^2 + \frac{48Nc_0}{M\bar{R}^3} \left[ f_A \left( \frac{R_x}{R_z}, \frac{R_y}{R_z}, \theta, \varphi \right) - R_z \partial_{R_z} f_A \left( \frac{R_x}{R_z}, \frac{R_y}{R_z}, \theta, \varphi \right) \right] - \frac{8\mu}{M} = 0, \quad (\text{C.4})$$

$$N - \frac{1}{48} \bar{R}^3 K_F^3 = 0. \quad (\text{C.5})$$

Note that Equation (C.5) represents the particle-number conservation constraint given by Equation (2.10).

## C.2 On-on-axis scenario

The total energy of the system  $E_{\text{tot}}^{(2)}$  in this case is given by Equation (2.75). The seven variational parameters ( $K_i$ ,  $R_i$ ,  $\mu$ ) are determined by minimizing the grand-canonical potential  $\Omega^{(2)} = E_{\text{tot}}^{(2)} - \mu N^{(2)}$ , where  $N^{(2)}$  is defined by Equation (2.12). The minimization yields the following set of equations

$$\frac{\hbar^2 K_x^2}{2M} + \frac{24Nc_0}{\bar{R}^3} K_x \partial_{K_x} f_A \left( \frac{K_z}{K_x}, \frac{K_z}{K_y}, \theta, \varphi \right) - 4\mu = 0, \quad (\text{C.6})$$

$$\frac{\hbar^2 K_y^2}{2M} + \frac{24Nc_0}{\bar{R}^3} K_y \partial_{K_y} f_A \left( \frac{K_z}{K_x}, \frac{K_z}{K_y}, \theta, \varphi \right) - 4\mu = 0, \quad (\text{C.7})$$

$$\frac{\hbar^2 K_z^2}{2M} + \frac{24Nc_0}{\bar{R}^3} K_z \partial_{K_z} f_A \left( \frac{K_z}{K_x}, \frac{K_z}{K_y}, \theta, \varphi \right) - 4\mu = 0, \quad (\text{C.8})$$

$$\begin{aligned} \omega_x^2 R_x^2 + \frac{48Nc_0}{M\bar{R}^3} \left[ f_A \left( \frac{R_x}{R_z}, \frac{R_y}{R_z}, \theta, \varphi \right) - R_x \partial_{R_x} f_A \left( \frac{R_x}{R_z}, \frac{R_y}{R_z}, \theta, \varphi \right) \right] \\ - \frac{48Nc_0}{M\bar{R}^3} f_A \left( \frac{K_z}{K_x}, \frac{K_z}{K_y}, \theta, \varphi \right) - \frac{8\mu}{M} = 0, \end{aligned} \quad (\text{C.9})$$

$$\begin{aligned} \omega_y^2 R_y^2 + \frac{48Nc_0}{M\bar{R}^3} \left[ f_A \left( \frac{R_x}{R_z}, \frac{R_y}{R_z}, \theta, \varphi \right) - R_y \partial_{R_y} f_A \left( \frac{R_x}{R_z}, \frac{R_y}{R_z}, \theta, \varphi \right) \right] \\ - \frac{48Nc_0}{M\bar{R}^3} f_A \left( \frac{K_z}{K_x}, \frac{K_z}{K_y}, \theta, \varphi \right) - \frac{8\mu}{M} = 0, \end{aligned} \quad (\text{C.10})$$

$$\begin{aligned} \omega_z^2 R_z^2 + \frac{48Nc_0}{M\bar{R}^3} \left[ f_A \left( \frac{R_x}{R_z}, \frac{R_y}{R_z}, \theta, \varphi \right) - R_z \partial_{R_z} f_A \left( \frac{R_x}{R_z}, \frac{R_y}{R_z}, \theta, \varphi \right) \right] \\ - \frac{48Nc_0}{M\bar{R}^3} f_A \left( \frac{K_z}{K_x}, \frac{K_z}{K_y}, \theta, \varphi \right) - \frac{8\mu}{M} = 0, \end{aligned} \quad (\text{C.11})$$

$$N - \frac{1}{48} \bar{R}^3 \bar{K}^3 = 0. \quad (\text{C.12})$$

Similarly as in the spherical scenario, Equation (C.12) coincides with the particle-number conservation Equation (2.12).

## C.3 Off-on-axis scenario

The total energy  $E_{\text{tot}}^{(3)}$  of the system in the off-on-axis scenario is given by Equation (2.73). The nine variational parameters ( $K'_i$ ,  $R_i$ ,  $\theta'$ ,  $\varphi'$ ,  $\mu$ ) are determined by minimizing the grand-canonical potential  $\Omega^{(3)} = E_{\text{tot}}^{(3)} - \mu N^{(3)}$ , where  $N^{(3)}$  is defined by Equation (2.15). The minimization of  $\Omega^{(3)}$  with respect to  $\theta'$  and  $\varphi'$  directly yields

$$\theta' = \theta \quad , \quad \varphi' = \varphi. \quad (\text{C.13})$$

This simplifies the terms which come from the Fock exchange energy due to the identity (B.17). Taking this to account, the rest of the equations has the following form

$$\frac{\hbar^2 K_x'^2}{2M} + \frac{24Nc_0}{\bar{R}^3} K_x' \partial_{K_x'} f \left( \frac{K_z'}{K_x'}, \frac{K_z'}{K_y'} \right) - 4\mu = 0, \quad (\text{C.14})$$

$$\frac{\hbar^2 K_y'^2}{2M} + \frac{24Nc_0}{\bar{R}^3} K_y' \partial_{K_y'} f \left( \frac{K_z'}{K_x'}, \frac{K_z'}{K_y'} \right) - 4\mu = 0, \quad (\text{C.15})$$

$$\frac{\hbar^2 K_z'^2}{2M} + \frac{24Nc_0}{\bar{R}^3} K_z' \partial_{K_z'} f \left( \frac{K_z'}{K_x'}, \frac{K_z'}{K_y'} \right) - 4\mu = 0, \quad (\text{C.16})$$

$$\begin{aligned} \omega_x^2 R_x^2 + \frac{48Nc_0}{M\bar{R}^3} \left[ f_A \left( \frac{R_x}{R_z}, \frac{R_y}{R_z}, \theta, \varphi \right) - R_x \partial_{R_x} f_A \left( \frac{R_x}{R_z}, \frac{R_y}{R_z}, \theta, \varphi \right) \right] \\ - \frac{48Nc_0}{M\bar{R}^3} f \left( \frac{K_z'}{K_x'}, \frac{K_z'}{K_y'} \right) - \frac{8\mu}{M} = 0, \end{aligned} \quad (\text{C.17})$$

$$\begin{aligned} \omega_y^2 R_y^2 + \frac{48Nc_0}{M\bar{R}^3} \left[ f_A \left( \frac{R_x}{R_z}, \frac{R_y}{R_z}, \theta, \varphi \right) - R_y \partial_{R_y} f_A \left( \frac{R_x}{R_z}, \frac{R_y}{R_z}, \theta, \varphi \right) \right] \\ - \frac{48Nc_0}{M\bar{R}^3} f \left( \frac{K_z'}{K_x'}, \frac{K_z'}{K_y'} \right) - \frac{8\mu}{M} = 0, \end{aligned} \quad (\text{C.18})$$

$$\begin{aligned} \omega_z^2 R_z^2 + \frac{48Nc_0}{M\bar{R}^3} \left[ f_A \left( \frac{R_x}{R_z}, \frac{R_y}{R_z}, \theta, \varphi \right) - R_z \partial_{R_z} f_A \left( \frac{R_x}{R_z}, \frac{R_y}{R_z}, \theta, \varphi \right) \right] \\ - \frac{48Nc_0}{M\bar{R}^3} f \left( \frac{K_z'}{K_x'}, \frac{K_z'}{K_y'} \right) - \frac{8\mu}{M} = 0, \end{aligned} \quad (\text{C.19})$$

$$N - \frac{1}{48} \bar{R}^3 \bar{K}'^3 = 0. \quad (\text{C.20})$$

As before, Equation (C.20) coincides with the particle-number conservation equation (2.15). Due to the symmetry of the anisotropy function  $f(x, y) = f(y, x)$ , from Equations (C.14) and (C.16) that  $K_x' = K_y'$ , i.e., that the FS is cylindrically symmetric with respect to the dipoles' orientation. This is expected, since we have shown that the orientation of the dipoles in the rotated coordinate system coincides with the  $q_z$  axis and singles this particular direction out, leaving the perpendicular plane perfectly symmetric in momentum space. Additionally, in close analogy to the special case when the dipoles are aligned with one of the trapping axes [91, 92, 125, 126], the three equations (C.14)-(C.16) can be rewritten in the following form

$$K_x' - K_y' = 0, \quad (\text{C.21})$$

$$K_z'^2 - K_x'^2 - \frac{144MNc_0}{\hbar^2 \bar{R}^3} \left[ 1 + \frac{(2K_x'^2 + K_z'^2) f_s \left( \frac{K_z'}{K_x'} \right)}{2(K_z'^2 - K_x'^2)} \right] = 0, \quad (\text{C.22})$$

$$\mu - \frac{1}{12} \sum_j \frac{\hbar^2 K_j'^2}{2M} = 0. \quad (\text{C.23})$$

## C.4 Off-off-axis scenario

The total energy  $E_{\text{tot}}^{(4)}$  of the system in the off-off-axis scenario is given by Equation (2.72). The eleven variational parameters ( $K'_i, R''_i, \theta', \varphi', \theta'', \varphi'', \mu$ ) are determined by minimizing the grand-canonical potential  $\Omega^{(4)} = E_{\text{tot}}^{(4)} - \mu N^{(4)}$ , where  $N^{(4)}$  is defined by Equation (2.17). The minimization of  $\Omega^{(4)}$  with respect to parameters ( $K'_i, \theta', \varphi'$ ) is completely the same as in the previous case. This allows to eliminate the angles  $\theta'$  and  $\varphi'$  and to rewrite the equations for  $K'_i$  as (C.21)-(C.23). The minimization with respect to the other parameters leads to the complete set of equations

$$K'_x - K'_y = 0, \quad (\text{C.24})$$

$$K'_z - K'_x - \frac{144MNc_0}{\hbar^2 \bar{R}^3} \left[ 1 + \frac{(2K_x'^2 + K_z'^2) f_s \left( \frac{K'_z}{K'_x} \right)}{2(K_z'^2 - K_x'^2)} \right] = 0, \quad (\text{C.25})$$

$$\mu - \frac{1}{12} \sum_j \frac{\hbar^2 K_j'^2}{2M} = 0, \quad (\text{C.26})$$

$$\begin{aligned} \frac{N}{8} M \left[ (\omega_x^2 - \omega_z^2) \cos^2 \varphi'' + (\omega_y^2 - \omega_z^2) \sin^2 \varphi'' \right] (R_z'' - R_x'') \sin \theta'' \cos \theta'' \\ - \frac{6Nc_0}{\bar{R}''^3} F_{A,5} \left( \frac{R_x''}{R_z''}, \frac{R_y''}{R_z''}, \theta, \varphi, \theta'', \varphi'' \right) = 0, \end{aligned} \quad (\text{C.27})$$

$$\begin{aligned} \frac{N}{8} M (\omega_y^2 - \omega_x^2) \left[ (R_x'' - R_y'') \cos^2 \theta'' + (R_z'' - R_y'') \sin^2 \theta'' \right] \sin \varphi'' \cos \varphi'' \\ - \frac{6Nc_0}{\bar{R}''^3} F_{A,6} \left( \frac{R_x''}{R_z''}, \frac{R_y''}{R_z''}, \theta, \varphi, \theta'', \varphi'' \right) = 0, \end{aligned} \quad (\text{C.28})$$

$$\begin{aligned} \frac{N}{8} M \sum_j \omega_j^2 \mathbb{R}_{jx}'' R_x'' + \frac{6N^2 c_0}{\bar{R}''^3} \frac{1}{R_x''} \left[ F_A \left( \frac{R_x''}{R_z''}, \frac{R_y''}{R_z''}, \theta, \varphi, \theta'', \varphi'' \right) - f_s \left( \frac{K'_z}{K'_x} \right) \right] \\ - \frac{6N^2 c_0}{\bar{R}''^3} \frac{1}{R_z''} F_{A,1} \left( \frac{R_x''}{R_z''}, \frac{R_y''}{R_z''}, \theta, \varphi, \theta'', \varphi'' \right) - \frac{\mu}{48} R_y'' R_z'' \bar{K}'^3 = 0, \end{aligned} \quad (\text{C.29})$$

$$\begin{aligned} \frac{N}{8} M \sum_j \omega_j^2 \mathbb{R}_{jy}'' R_y'' + \frac{6N^2 c_0}{\bar{R}''^3} \frac{1}{R_y''} \left[ F_A \left( \frac{R_x''}{R_z''}, \frac{R_y''}{R_z''}, \theta, \varphi, \theta'', \varphi'' \right) - f_s \left( \frac{K'_z}{K'_x} \right) \right] \\ - \frac{6N^2 c_0}{\bar{R}''^3} \frac{1}{R_z''} F_{A,2} \left( \frac{R_x''}{R_z''}, \frac{R_y''}{R_z''}, \theta, \varphi, \theta'', \varphi'' \right) - \frac{\mu}{48} R_x'' R_z'' \bar{K}'^3 = 0, \end{aligned} \quad (\text{C.30})$$

$$\begin{aligned} \frac{N}{8} M \sum_j \omega_j^2 \mathbb{R}_{jz}'' R_z'' + \frac{6N^2 c_0}{\bar{R}''^3} \frac{1}{R_z''} \left[ F_A \left( \frac{R_x''}{R_z''}, \frac{R_y''}{R_z''}, \theta, \varphi, \theta'', \varphi'' \right) - f_s \left( \frac{K'_z}{K'_x} \right) \right] \\ + \frac{6N^2 c_0}{\bar{R}''^3} \frac{R_x''}{R_z''} F_{A,1} \left( \frac{R_x''}{R_z''}, \frac{R_y''}{R_z''}, \theta, \varphi, \theta'', \varphi'' \right) \\ + \frac{6N^2 c_0}{\bar{R}''^3} \frac{R_x''}{R_z''} F_{A,2} \left( \frac{R_x''}{R_z''}, \frac{R_y''}{R_z''}, \theta, \varphi, \theta'', \varphi'' \right) - \frac{\mu}{48} R_x'' R_z'' \bar{K}'^3 = 0, \end{aligned} \quad (\text{C.31})$$

$$N - \frac{1}{48} \bar{R}''^3 \bar{K}'^3 = 0. \quad (\text{C.32})$$




---

## Averages and aspect ratios in real and in momentum space

---

### D.1 Phase-space averages $\langle \mathcal{K}_i^2 \rangle^0$ and $\langle \mathcal{R}_i^2 \rangle^0$

The quantum-mechanical expectation values of the observable  $\mathcal{K}_i^2$  can be obtained as its phase-space average with respect to the equilibrium distribution function  $\nu^0$ , see Equation (2.5). This gives

$$\begin{aligned}
 \langle \mathcal{K}_i^2 \rangle^0 &= \frac{1}{N} \int \frac{d^3 \mathcal{K} d^3 \mathcal{R}}{(2\pi)^3} \mathcal{K}_i^2 \nu^0(\mathcal{R}(\mathbf{r}, t), \mathcal{K}(\mathbf{r}, \mathbf{k}, t)) \\
 &= \frac{1}{N} \int \frac{d^3 \mathcal{Q} d^3 \mathcal{X}}{(2\pi)^3} \left( \sum_j \mathbb{R}'_{ij} \mathcal{Q}_j \right)^2 \text{H} \left( 1 - \sum_i \frac{\mathcal{X}_i^2}{R_i'^2} - \sum_i \frac{\mathcal{Q}_i^2}{K_i'^2} \right) \\
 &= \frac{\bar{R}'^3}{6\pi^2 N} \int d^3 \mathcal{Q} \left( \sum_j \mathbb{R}''_{ij} \mathcal{Q}_j \right) \left( 1 - \sum_i \frac{\mathcal{Q}_i^2}{K_i'^2} \right)^{\frac{3}{2}} \text{H} \left( 1 - \sum_i \frac{\mathcal{Q}_i^2}{K_i'^2} \right), \quad (\text{D.1})
 \end{aligned}$$

where we switch coordinate systems from  $S$  to  $S'$  for momentum space and from  $S$  to  $S''$  for real space (see Figure 2.1). After that, we evaluate the real space integrals by rescaling variables according to  $\mathcal{X}_i = R_i'' u_i$  and switching to spherical coordinates. The remaining  $\mathcal{Q}$ -integral is simplified by eliminating all terms in the integrand which are odd functions in  $\mathcal{Q}_i$ , since their integrals vanish. Furthermore, using the substitution  $\mathcal{Q}_i = v_i K_i'$ , we get

$$\langle \mathcal{K}_i^2 \rangle^0 = \frac{8}{\pi^2} \int d^3 v \left( \sum_j \mathbb{R}''_{ij} K_j'^2 v_j^2 \right) \left( 1 - \sum_i v_i^2 \right)^{\frac{3}{2}} \text{H} \left( 1 - \sum_i v_i^2 \right). \quad (\text{D.2})$$

The  $\nu$ -integral is the same as the integral which appear in Equation (2.33), so we can use that result to obtain

$$\langle \mathcal{K}_i^2 \rangle^0 = \frac{1}{8} \sum_j \mathbb{R}_{ij}'^2 K_j'^2. \quad (\text{D.3})$$

Similarly, one can derive the quantum-mechanical expectation values of the system observable  $\mathcal{R}_i$  as follows

$$\begin{aligned} \langle \mathcal{R}_i^2 \rangle^0 &= \frac{1}{N} \int \frac{d^3 \mathcal{K} d^3 \mathcal{R}}{(2\pi)^3} \mathcal{R}_i^2 \nu^0(\mathcal{R}(\mathbf{r}, t), \mathcal{K}(\mathbf{r}, \mathbf{k}, t)) \\ &= \frac{1}{N} \int \frac{d^3 \mathcal{Q} d^3 \mathcal{X}}{(2\pi)^3} \left( \sum_j \mathbb{R}_{ij}'' \mathcal{X}_j \right)^2 \text{H} \left( 1 - \sum_i \frac{\mathcal{X}_i^2}{R_i''^2} - \sum_i \frac{\mathcal{Q}_i^2}{K_i'^2} \right) \\ &= \frac{\bar{K}^3}{6\pi^2 N} \int d^3 \mathcal{X} \left( \sum_j \mathbb{R}_{ij}''^2 \mathcal{X}_j^2 \right) \left( 1 - \sum_i \frac{\mathcal{X}_i^2}{R_i''^2} \right)^{\frac{3}{2}} \text{H} \left( 1 - \sum_i \frac{\mathcal{X}_i^2}{R_i''^2} \right), \end{aligned} \quad (\text{D.4})$$

which with a full analogy with previous calculation leads to a final result

$$\langle \mathcal{R}_i^2 \rangle^0 = \frac{1}{8} \sum_j \mathbb{R}_{ij}''^2 R_j'^2. \quad (\text{D.5})$$

## D.2 Aspect ratio in real space

To calculate aspect ratios in real space, we use the same geometry as in Reference [48], which is illustrated in Figure 2.2. The imaging plane is  $r'_x r_z$ , i.e., the imaging is performed along the  $r'_y$  axis, which is rotated counterclockwise for an angle  $\alpha$  in  $r_x r_y$  plane with respect to the  $r_y$  axis. The TOF absorption images correspond to density profiles of the system, so we first calculate the particle density  $n(\mathbf{r}, t)$  from the Wigner quasiprobability distribution function,

$$\begin{aligned} n(\mathbf{r}, t) &= \int \frac{d^3 k}{(2\pi)^3} \nu(\mathbf{r}, \mathbf{k}, t) = \int \frac{d^3 \mathcal{K}}{(2\pi)^3} \bar{\Theta}^{\frac{3}{2}}(t) \Gamma(t) \nu^0(\mathcal{R}(\mathbf{r}, t), \mathcal{K}(\mathbf{r}, \mathbf{k}, t)) \\ &= \int \frac{d^3 \mathcal{Q}}{(2\pi)^3} \frac{1}{\bar{b}^3(t)} \text{H} \left( 1 - \sum_i \frac{\mathcal{X}_i^2(\mathbf{r}, t)}{R_i''^2} - \sum_i \frac{\mathcal{Q}_i^2(\mathbf{r}, \mathbf{k}, t)}{K_i'^2} \right), \end{aligned} \quad (\text{D.6})$$

where  $\mathcal{X} = \mathbb{R}'' \mathcal{R}$  and  $\mathcal{Q} = \mathbb{R}' \mathcal{K}$ . Substituting  $\mathcal{Q}_i = u_i K_i'$  and switching to spherical coordinates yields

$$n(\mathbf{r}, t) = \frac{\bar{K}^3}{6\pi^2 \bar{b}^3(t)} \left( 1 - \sum_i \frac{\mathcal{X}_i^2(\mathbf{r}, t)}{R_i''^2} \right)^{\frac{3}{2}} \text{H} \left( 1 - \sum_i \frac{\mathcal{X}_i^2(\mathbf{r}, t)}{R_i''^2} \right). \quad (\text{D.7})$$

Since the expectation values of the coordinates vanish,

$$\langle r_i(t) \rangle = \frac{1}{N} \int d^3r r_i n(\mathbf{r}, t) = \frac{1}{N} \bar{b}^3(t) b_i(t) \sum_j \mathbb{R}_{ij}'' \int d^3\mathcal{X} \mathcal{X}_j n(\mathcal{X}(\mathbf{r}, t)) = 0, \quad (\text{D.8})$$

the width of an atomic or molecular cloud in the  $i$ -th direction in real space is described in terms of the root mean square  $\sqrt{\langle r_i^2(t) \rangle}$ . Using the expression (D.7) for the particle density, the corresponding expectation values are found to be

$$\begin{aligned} \langle r_i^2(t) \rangle &= \frac{1}{N} \int d^3r r_i^2 n(\mathbf{r}, t) \\ &= \frac{\bar{K}^3}{6\pi^2 N} \int d^3\mathcal{X} \left( b_i(t) \sum_j \mathbb{R}_{ij}'' \mathcal{X}_j \right)^2 \left( 1 - \sum_i \frac{\mathcal{X}_i^2}{R_i''^2} \right)^{\frac{3}{2}} \text{H} \left( 1 - \sum_i \frac{\mathcal{X}_i^2}{R_i''^2} \right), \end{aligned} \quad (\text{D.9})$$

which is equal to the as integral in Equation (D.4) and, therefore, reads

$$\langle r_i^2(t) \rangle = \frac{1}{8} \sum_j \mathbb{R}_{ij}''^2 R_j''^2 b_i^2(t). \quad (\text{D.10})$$

Since the imaging is performed in the  $r'_x r'_z$  plane, the aspect ratio in real space is defined by

$$A_R(t) = \sqrt{\frac{\langle r_z^2(t) \rangle}{\langle r_x^2(t) \rangle}}, \quad (\text{D.11})$$

and we also need to calculate the expectation value  $\langle r_x^2(t) \rangle$ , where  $\mathbf{r}' = \mathbb{R}(0^\circ, \alpha)\mathbf{r}$ . After a simple and straightforward calculation we get

$$\begin{aligned} \langle r_x^2(t) \rangle &= \frac{1}{N} \int d^3r r_x^2 n(\mathbf{r}, t) = \frac{1}{N} \int d^3r (r_x \cos \alpha + r_y \sin \alpha)^2 n(\mathbf{r}, t) \\ &= \langle r_x^2(t) \rangle \cos^2 \alpha + \langle r_y^2(t) \rangle \sin^2 \alpha = \frac{1}{8} \sum_j R_j''^2 \left[ \mathbb{R}_{xj}''^2 b_x^2(t) \cos^2 \alpha + \mathbb{R}_{yj}''^2 b_y^2(t) \sin^2 \alpha \right], \end{aligned} \quad (\text{D.12})$$

and finally the aspect ratio (D.11) found to be

$$A_R(t) = \sqrt{\frac{\sum_j \mathbb{R}_{zj}''^2 R_j''^2 b_z^2(t)}{\sum_j R_j''^2 \left[ \mathbb{R}_{xj}''^2 b_x^2(t) \cos^2 \alpha + \mathbb{R}_{yj}''^2 b_y^2(t) \sin^2 \alpha \right]}}. \quad (\text{D.13})$$

Note that in the special case when the dipoles are oriented along one of the trap axes, the aspect ratio in real space further simplifies

$$A_R(t) = \frac{R_z b_z(t)}{\sqrt{R_x^2 b_x^2(t) \cos^2 \alpha + R_y^2 b_y^2(t) \sin^2 \alpha}}. \quad (\text{D.14})$$

### D.3 Aspect ratio in momentum space

In order to quantify effects of the DDI on the Fermi surface, we use changes of the aspect ratio in momentum space, which is defined similarly as the aspect ratio in real space. However, in contrast to the aspect ratio in real space, the derivation of the expression for the aspect ratio in momentum space is much longer and more complex. Thus, we focus here on the special case when the dipoles' orientation is along the one of the trap axes, since we investigate dynamics of such systems in Section 4.3. First, we calculate the particle density in momentum space  $n(\mathbf{k}, t)$ , from the Wigner quasiprobability distribution function,

$$\begin{aligned} n(\mathbf{k}, t) &= \int d^3r \nu(\mathbf{r}, \mathbf{k}, t) = \int d^3r \Gamma(t) \nu^0(\mathcal{R}(\mathbf{r}, t), \mathcal{K}(\mathbf{r}, \mathbf{k}, t)) \\ &= \int d^3r \Gamma(t) \text{H} \left( 1 - \sum_i \frac{\mathcal{R}_i^2(\mathbf{r}, t)}{R_i^2} - \sum_i \frac{\mathcal{K}_i^2(\mathbf{r}, \mathbf{k}, t)}{K_i^2} \right), \end{aligned} \quad (\text{D.15})$$

where expressions for  $\mathcal{R}_i(\mathbf{r}, t)$  and  $\mathcal{K}_i(\mathbf{r}, \mathbf{k}, t)$  are given by Equations (4.24) and (4.25), respectively. After a change of spatial variables  $r_i$  according to

$$u_i = \frac{D_i(t)r_i}{R_i b_i(t)} - \frac{M R_i \dot{b}_i(t) k_i}{\hbar K_i^2 \Theta_i(t) D_i}, \quad (\text{D.16})$$

where  $D_i(t) = \sqrt{1 + \frac{M^2 R_i^2 \dot{b}_i^2(t)}{\hbar^2 K_i^2 \Theta_i(t)}}$ , we switch to spherical coordinates and obtain

$$n(\mathbf{k}, t) = \frac{4\pi}{3} \frac{\bar{R}^3}{\Theta^{\frac{3}{2}}(t) \bar{D}^3(t)} \left( 1 - \sum_i \frac{k_i^2}{K_i^2 \Theta_i(t) D_i^2(t)} \right)^{\frac{3}{2}} \text{H} \left( 1 - \sum_i \frac{k_i^2}{K_i^2 \Theta_i(t) D_i^2(t)} \right). \quad (\text{D.17})$$

The expectation value  $\langle k_i(t) \rangle$  in momentum space also vanishes

$$\langle k_i(t) \rangle = \frac{1}{N} \int \frac{d^3k}{(2\pi)^3} k_i n(\mathbf{k}, t) = 0, \quad (\text{D.18})$$

so the cloud widths in momentum space are instead defined by the root mean squares  $\sqrt{\langle k_i^2(t) \rangle}$ . The corresponding expectation values can be explicitly calculated and yield

$$\begin{aligned} \langle k_i^2(t) \rangle &= \frac{1}{N} \int \frac{d^3k}{(2\pi)^3} k_i^2 n(\mathbf{k}, t) = \frac{\bar{K}^3 \bar{\Theta}^{\frac{3}{2}}(t) \bar{D}^3(t)}{N} \int \frac{d^3v}{(2\pi)^3} K_i^2 \Theta_i(t) D_i^2(t) v_i^2 n(\mathbf{v}, t) \\ &= \frac{8}{\pi^2} K_i^2 \Theta_i(t) D_i^2(t) \int d^3v v_i^2 \left( 1 - \sum_i v_i^2 \right)^{\frac{3}{2}} \text{H} \left( 1 - \sum_i v_i^2 \right), \end{aligned} \quad (\text{D.19})$$

---

where we have used a substitution  $v_i = k_i/(K_i\Theta_i^{\frac{1}{2}}(t)D_i(t))$ . The  $v$ -integral is the same as the integral which appears in Equations (2.33) and (D.2), and therefore we obtain

$$\langle k_i^2(t) \rangle = \frac{1}{8} \left( K_i^2 \Theta_i(t) + \frac{M^2 R_i^2 \dot{b}_i^2(t)}{\hbar^2} \right). \quad (\text{D.20})$$

The aspect ratio in momentum space is defined as

$$A_K(t) = \sqrt{\frac{\langle k_z^2(t) \rangle}{\langle k_x^2(t) \rangle}}, \quad (\text{D.21})$$

where  $\mathbf{k}' = \mathbb{R}(0^\circ, \alpha)\mathbf{k}$ . After a simple and straightforward calculation we get

$$\begin{aligned} \langle k_x'^2(t) \rangle &= \frac{1}{N} \int d^3k k_x'^2 n(\mathbf{k}, t) = \frac{1}{N} \int d^3k (k_x \cos \alpha + k_y \sin \alpha)^2 n(\mathbf{k}, t) \\ &= \langle k_x^2(t) \rangle \cos^2 \alpha + \langle k_y^2(t) \rangle \sin^2 \alpha = \frac{1}{8} \left[ D_x^2 K_x^2 \Theta_x(t) \cos^2 \alpha + D_y^2 K_y^2 \Theta_y(t) \sin^2 \alpha \right], \end{aligned} \quad (\text{D.22})$$

and finally the momentum space aspect ratio (D.21) is found to be

$$A_K(t) = \sqrt{\frac{\hbar^2 K_z^2 \Theta_z(t) + M^2 R_z^2 \dot{b}_z^2(t)}{\left[ \hbar^2 K_x^2 \Theta_x(t) + M^2 R_x^2 \dot{b}_x^2(t) \right] \cos^2 \alpha + \left[ \hbar^2 K_y^2 \Theta_y(t) + M^2 R_y^2 \dot{b}_y^2(t) \right] \sin^2 \alpha}}. \quad (\text{D.23})$$

---

# Bibliography

---

- [1] R. P. Feynman, Simulating physics with computers, *International Journal of Theoretical Physics* **21**, 467–488 (1982).
- [2] F. C. Barenghi and G. N. Parker, A primer on quantum fluids, Springer International Publishing 1st edn (2016).
- [3] S. Giorgini, L. P. Pitaevskii, and S. Stringari, Theory of ultracold atomic Fermi gases, *Reviews of Modern Physics* **80**, 1215–1274 (2008).
- [4] L. Pitaevskii and S. Stringari, Bose-Einstein condensation and superfluidity, Oxford: Oxford University Press 1st edn (2016).
- [5] M. Inguscio, W. Ketterle, and C. Salomon, Ultra-cold Fermi gases: Varenna on Lake Como, Villa Monastero, 20-30 June 2006, IOS Press: Societa italiana di fisica (2007).
- [6] D. A. Butts and D. S. Rokhsar, Trapped Fermi gases, *Physical Review A* **55**, 4346–4350 (1997).
- [7] M. Marinescu and L. You, Controlling atom-atom interaction at ultralow temperatures by dc electric fields, *Physical Review Letters* **81**, 4596–4599 (1998).
- [8] S. Yi and L. You, Trapped atomic condensates with anisotropic interactions, *Physical Review A* **61**, 041604 (2000).
- [9] S. Yi and L. You, Trapped condensates of atoms with dipole interactions, *Physical Review A* **63**, 053607 (2001).
- [10] B. Deb and L. You, Low-energy atomic collision with dipole interactions, *Physical Review A* **64**, 022717 (2001).
- [11] B. Gadway and B. Yan, Strongly interacting ultracold polar molecules, *Journal of Physics B: Atomic, Molecular and Optical Physics* **49**, 152002 (2016).
- [12] C. J. Pethick and H. Smith, Bose-Einstein condensation in dilute gases, Cambridge: Cambridge University Press 2nd edn (2008).
- [13] I. Bloch, J. Dalibard, and W. Zwerger, Many-body physics with ultracold gases, *Reviews of Modern Physics* **80**, 885–964 (2008).

- 
- [14] M. A. Baranov, Theoretical progress in many-body physics with ultracold dipolar gases, *Physics Reports* **464**, 71–111 (2008).
- [15] T. Lahaye, C. Menotti, L. Santos, M. Lewenstein, and T. Pfau, The physics of dipolar bosonic quantum gases, *Reports on Progress in Physics* **72**, 126401 (2009).
- [16] D. Blume, Few-body physics with ultracold atomic and molecular systems in traps, *Reports on Progress in Physics* **75**, 046401 (2012).
- [17] P. Massignan, M. Zaccanti, and G. M. Bruun, Polarons, dressed molecules and itinerant ferromagnetism in ultracold Fermi gases, *Reports on Progress in Physics* **77**, 034401 (2014).
- [18] H. Ott, Single atom detection in ultracold quantum gases: a review of current progress, *Reports on Progress in Physics* **79**, 054401 (2016).
- [19] I. Bloch, Ultracold quantum gases in optical lattices, *Nature Physics* **1**, 23 (2005).
- [20] M. Lewenstein, A. Sanpera, V. Ahufinger, B. Damski, A. Sen(De), and U. Sen, Ultracold atomic gases in optical lattices: mimicking condensed matter physics and beyond, *Advances in Physics* **56**, 243–379 (2007).
- [21] I. Bloch, J. Dalibard, and S. Nascimbène, Quantum simulations with ultracold quantum gases, *Nature Physics* **8**, 267 (2012).
- [22] I. B. Mekhov and H. Ritsch, Quantum optics with ultracold quantum gases: towards the full quantum regime of the light-matter interaction, *Journal of Physics B: Atomic, Molecular and Optical Physics* **45**, 102001 (2012).
- [23] D.-W. Zhang, Z.-D. Wang, and S.-L. Zhu, Relativistic quantum effects of dirac particles simulated by ultracold atoms, *Front. Phys.* **7**, 31–53 (2012).
- [24] U.-J. Wiese, Ultracold quantum gases and lattice systems: quantum simulation of lattice gauge theories, *Annals of Physics* **525**, 777–796 (2013).
- [25] N. Goldman, G. Juzeliūnas, P. Öhberg, and I. B. Spielman, Light-induced gauge fields for ultracold atoms, *Reports on Progress in Physics* **77**, 126401 (2014).
- [26] E. Zohar, J. I. Cirac, and B. Reznik, Quantum simulations of lattice gauge theories using ultracold atoms in optical lattices, *Reports on Progress in Physics* **79**, 014401 (2016).

- 
- [27] C. Gross and I. Bloch, Quantum simulations with ultracold atoms in optical lattices, *Science* **357**, 995–1001 (2017).
- [28] L. Santos, G. V. Shlyapnikov, and M. Lewenstein, Roton-maxon spectrum and stability of trapped dipolar Bose-Einstein condensates, *Physical Review Letters* **90**, 250403 (2003).
- [29] K. Glaum, A. Pelster, H. Kleinert, and T. Pfau, Critical temperature of weakly interacting dipolar condensates, *Physical Review Letters* **98**, 080407 (2007).
- [30] K. Glaum and A. Pelster, Bose-Einstein condensation temperature of dipolar gas in anisotropic harmonic trap, *Physical Review A* **76**, 023604 (2007).
- [31] L. D. Carr and J. Ye, Focus on Cold and Ultracold Molecules, *New Journal of Physics* **11**, 055009 (2009).
- [32] C. Krumnow and A. Pelster, Dipolar Bose-Einstein condensates with weak disorder, *Physical Review A* **84**, 021608 (2011).
- [33] J. K. Block, N. T. Zinner, and G. M. Bruun, Density wave instabilities of tilted fermionic dipoles in a multilayer geometry, *New Journal of Physics* **14**, 105006 (2012).
- [34] B. Nikolić, A. Balaž, and A. Pelster, Dipolar Bose-Einstein condensates in weak anisotropic disorder, *Physical Review A* **88**, 013624 (2013).
- [35] H. Al-Jibbouri, I. Vidanović, A. Balaž, and A. Pelster, Geometric resonances in Bose-Einstein condensates with two- and three-body interactions, *Journal of Physics B: Atomic, Molecular and Optical Physics* **46**, 065303 (2013).
- [36] A. Balaž, R. Paun, A. I. Nicolin, S. Balasubramanian, and R. Ramaswamy, Faraday waves in collisionally inhomogeneous Bose-Einstein condensates, *Physical Review A* **89**, 023609 (2014).
- [37] M. Ghabour and A. Pelster, Bogoliubov theory of dipolar Bose gas in a weak random potential, *Physical Review A* **90**, 063636 (2014).
- [38] D. Jaksch, Optical lattices, ultracold atoms and quantum information processing, *Contemporary Physics* **45**, 367–381 (2004).
- [39] I. Bloch, Quantum coherence and entanglement with ultracold atoms in optical lattices, *Nature* **453**, 1016 (2008).
-

- 
- [40] M. Saffman, T. G. Walker, and K. Mølmer, Quantum information with Rydberg atoms, *Reviews of Modern Physics* **82**, 2313–2363 (2010).
- [41] L. You and M. Marinescu, Prospects for p-wave paired Bardeen-Cooper-Schrieffer states of fermionic atoms, *Physical Review A* **60**, 2324–2329 (1999).
- [42] M. A. Baranov, L. Dobrek, and M. Lewenstein, BCS pairing in a trapped dipolar Fermi gas, *New Journal of Physics* **6**, 198 (2004).
- [43] M. A. Baranov, M. S. Mar’enko, Val. S. Rychkov, and G. V. Shlyapnikov, Superfluid pairing in a polarized dipolar Fermi gas, *Physical Review A* **66**, 013606 (2002).
- [44] M. A. Baranov, L. Dobrek, and M. Lewenstein, Superfluidity of trapped dipolar Fermi gases, *Physical Review Letters* **92**, 250403 (2004).
- [45] T. Shi, J.-N. Zhang, C.-P. Sun, and S. Yi, Singlet and triplet bardeen-cooper-schrieffer pairs in a gas of two-species fermionic polar molecules, *Physical Review A* **82**, 033623 (2010).
- [46] C. Zhao, L. Jiang, X. Liu, W. M. Liu, X. Zou, and H. Pu, Hartree-Fock-Bogoliubov theory of dipolar Fermi gases, *Physical Review A* **81**, 063642 (2010).
- [47] A. Trautmann, P. Ilzhöfer, G. Durastante, C. Politi, M. Sohmen, M. J. Mark, and F. Ferlaino, Dipolar quantum mixtures of erbium and dysprosium atoms, *Physical Review Letters* **121**, 213601 (2018).
- [48] K. Aikawa, S. Baier, A. Frisch, M. Mark, C. Ravensbergen, and F. Ferlaino, Observation of Fermi surface deformation in a dipolar quantum gas, *Science* **345**, 1484–1487 (2014).
- [49] V. Veljić, A. R. P. Lima, L. Chomaz, S. Baier, M. J. Mark, F. Ferlaino, A. Pelster, and A. Balaž, Ground state of an ultracold Fermi gas of tilted dipoles in elongated traps, *New Journal of Physics* **20**, 093016 (2018).
- [50] V. Veljić, A. Pelster, and A. Balaž, Stability of quantum degenerate fermi gases of tilted polar molecules, *Physical Review Research* **1**, 012009(R) (2019).
- [51] B. C. Mulkerin, X.-J. Liu, and H. Hu, Leggett mode in a two-component Fermi gas with dipolar interactions, *Physical Review A* **99**, 023626 (2019).
- [52] A. Griesmaier, J. Werner, S. Hensler, J. Stuhler, and T. Pfau, Bose-Einstein condensation of chromium, *Physical Review Letters* **94**, 160401 (2005).

- 
- [53] J. Stuhler, A. Griesmaier, T. Koch, M. Fattori, T. Pfau, S. Giovanazzi, P. Pedri, and L. Santos, Observation of dipole-dipole interaction in a degenerate quantum gas, *Physical Review Letters* **95**, 150406 (2005).
- [54] M. A. Baranov, M. Dalmonte, G. Pupillo, and P. Zoller, Condensed matter theory of dipolar quantum gases, *Chemical Reviews* **112**, 5012–5061 (2012).
- [55] M. Lu, S. H. Youn, and B. L. Lev, Trapping ultracold dysprosium: A highly magnetic gas for dipolar physics, *Physical Review Letters* **104**, 063001 (2010).
- [56] K. Aikawa, A. Frisch, M. Mark, S. Baier, A. Rietzler, R. Grimm, and F. Ferlaino, Bose-Einstein condensation of erbium, *Physical Review Letters* **108**, 210401 (2012).
- [57] H. Kadau, M. Schmitt, M. Wenzel, C. Wink, T. Maier, I. Ferrier-Barbut, and T. Pfau, Observing the rosenweig instability of a quantum ferrofluid, *Nature* **530**, 194 (2016).
- [58] I. Ferrier-Barbut, H. Kadau, M. Schmitt, M. Wenzel, and T. Pfau, Observation of Quantum Droplets in a Strongly Dipolar Bose Gas, *Physical Review Letters* **116**, 215301 (2016).
- [59] L. Chomaz, S. Baier, D. Petter, M. J. Mark, F. Wächtler, L. Santos, and F. Ferlaino, Quantum-fluctuation-driven crossover from a dilute Bose-Einstein condensate to a macrodroplet in a dipolar quantum fluid, *Physical Review X* **6**, 041039 (2016).
- [60] M. Schmitt, M. Wenzel, F. Böttcher, I. Ferrier-Barbut, and T. Pfau, Self-bound droplets of a dilute magnetic quantum liquid, *Nature* **539**, 259 (2016).
- [61] L. Chomaz, R. M. W. van Bijnen, D. Petter, G. Faraoni, S. Baier, J. H. Becher, M. J. Mark, F. Wächtler, L. Santos, and F. Ferlaino, Observation of roton mode population in a dipolar quantum gas, *Nature Physics* **14**, 442–446 (2018).
- [62] P. Muruganandam and S. K. Adhikari, Fortran programs for the time-dependent Gross-Pitaevskii equation in a fully anisotropic trap, *Computer Physics Communications* **180**, 1888–1912 (2009).
- [63] D. Vudragović, I. Vidanović, A. Balaž, P. Muruganandam, and S. K. Adhikari, C programs for solving the time-dependent Gross-Pitaevskii equation in a fully anisotropic trap, *Computer Physics Communications* **183**, 2021 – 2025 (2012).

- 
- [64] R. K. Kumar, L. E. Young-S., D. Vudragović, A. Balaž, P. Muruganandam, and S.K. Adhikari, Fortran and c programs for the time-dependent dipolar Gross-Pitaevskii equation in an anisotropic trap, *Computer Physics Communications* **195**, 117 – 128 (2015).
- [65] V. Lončar, A. Balaž, A. Bogojević, S. Škrbić, P. Muruganandam, and S. K. Adhikari, CUDA programs for solving the time-dependent dipolar Gross-Pitaevskii equation in an anisotropic trap, *Computer Physics Communications* **200**, 406 – 410 (2016).
- [66] V. Lončar, L. E. Young-S., S. Škrbić, P. Muruganandam, S. K. Adhikari, and A. Balaž, OpenMP, OpenMP/MPI, and CUDA/MPI C programs for solving the time-dependent dipolar Gross-Pitaevskii equation, *Computer Physics Communications* **209**, 190 – 196 (2016).
- [67] A. K. Fedorov, I. L. Kurbakov, Y. E. Shchadilova, and Yu. E. Lozovik, Two-dimensional Bose gas of tilted dipoles: Roton instability and condensate depletion, *Physical Review A* **90**, 043616 (2014).
- [68] A. K. Fedorov, I. L. Kurbakov, and Yu. E. Lozovik, Roton-maxon spectrum and instability for weakly interacting dipolar excitons in a semiconductor layer, *Physical Review B* **90**, 165430 (2014).
- [69] C. Mishra and R. Nath, Dipolar condensates with tilted dipoles in a pancake-shaped confinement, *Physical Review A* **94**, 033633 (2016).
- [70] K.-T. Xi and H. Saito, Droplet formation in a Bose-Einstein condensate with strong dipole-dipole interaction, *Physical Review A* **93**, 011604 (2016).
- [71] F. Wächtler and L. Santos, Quantum filaments in dipolar Bose-Einstein condensates, *Physical Review A* **93**, 061603 (2016).
- [72] D. Baillie, R. M. Wilson, R. N. Bisset, and P. B. Blakie, Self-bound dipolar droplet: A localized matter wave in free space, *Physical Review A* **94**, 021602 (2016).
- [73] F. Wächtler and L. Santos, Ground-state properties and elementary excitations of quantum droplets in dipolar Bose-Einstein condensates, *Physical Review A* **94**, 043618 (2016).
- [74] P. B. Blakie, Properties of a dipolar condensate with three-body interactions, *Physical Review A* **93**, 033644 (2016).
-

- 
- [75] R. N. Bisset, R. M. Wilson, D. Baillie, and P. B. Blakie, Ground-state phase diagram of a dipolar condensate with quantum fluctuations, *Physical Review A* **94**, 033619 (2016).
- [76] D. Baillie, R. M. Wilson, and P. B. Blakie, Collective excitations of self-bound droplets of a dipolar quantum fluid, *Physical Review Letters* **119**, 255302 (2017).
- [77] V. Pastukhov, Beyond mean-field properties of binary dipolar Bose mixtures at low temperatures, *Physical Review A* **95**, 023614 (2017).
- [78] A. R. P. Lima and A. Pelster, Quantum fluctuations in dipolar bose gases, *Physical Review A* **84**, 041604(R) (2011).
- [79] A. R. P. Lima and A. Pelster, Beyond mean-field low-lying excitations of dipolar bose gases, *Physical Review A* **86**, 063609 (2012).
- [80] L. Tanzi, E. Lucioni, F. Famà, J. Catani, A. Fioretti, C. Gabbanini, R. N. Bisset, L. Santos, and G. Modugno, Observation of a Dipolar Quantum Gas with Metastable Supersolid Properties, *Physical Review Letters* **122**, 130405 (2019).
- [81] F. Böttcher, J.-N. Schmidt, M. Wenzel, J. Hertkorn, M. Guo, T. Langen, and T. Pfau, Transient supersolid properties in an array of dipolar quantum droplets, *Physical Review X* **9**, 011051 (2019).
- [82] L. Chomaz, D. Petter, P. Ilzhöfer, G. Natale, A. Trautmann, C. Politi, G. Durastante, R. M. W. van Bijnen, A. Patscheider, M. Sohmen, M. J. Mark, and F. Ferlaino, Long-lived and transient supersolid behaviors in dipolar quantum gases, *Physical Review X* **9**, 021012 (2019).
- [83] M. Lu, N. Q. Burdick, and B. L. Lev, Quantum Degenerate Dipolar Fermi Gas, *Physical Review Letters* **108**, 215301 (2012).
- [84] K. Aikawa, A. Frisch, M. Mark, S. Baier, R. Grimm, and F. Ferlaino, Reaching Fermi degeneracy via universal dipolar scattering, *Physical Review Letters* **112**, 010404 (2014).
- [85] B. Naylor, A. Reigue, E. Maréchal, O. Gorceix, B. Laburthe-Tolra, and L. Vernac, Chromium dipolar Fermi sea, *Physical Review A* **91**, 011603 (2015).
- [86] J. L. Bohn, M. Cavagnero, and C. Ticknor, Quasi-universal dipolar scattering in cold and ultracold gases, *New Journal of Physics* **11**, 055039 (2009).

- 
- [87] K. Aikawa, A. Frisch, M. Mark, S. Baier, R. Grimm, J. L. Bohn, D. S. Jin, G. M. Bruun, and F. Ferlaino, Anisotropic relaxation dynamics in a dipolar Fermi gas driven out of equilibrium, *Physical Review Letters* **113**, 263201 (2014).
- [88] N. Q. Burdick, K. Baumann, Y. Tang, M. Lu, and B. L. Lev, Fermionic suppression of dipolar relaxation, *Physical Review Letters* **114**, 023201 (2015).
- [89] A. Frisch, M. Mark, K. Aikawa, S. Baier, R. Grimm, A. Petrov, S. Kotochigova, G. Quémener, M. Lepers, O. Dulieu, and F. Ferlaino, Ultracold dipolar molecules composed of strongly magnetic atoms, *Physical Review Letters* **115**, 203201 (2015).
- [90] Miyakawa T., Sogo T., and Pu H., Phase-space deformation of a trapped dipolar Fermi gas, *Physical Review A* **77**, 061603 (2008).
- [91] A. R. P. Lima and A. Pelster, Collective motion of polarized dipolar Fermi gases in the hydrodynamic regime, *Physical Review A* **81**, 021606(R) (2010).
- [92] A. R. P. Lima and A. Pelster, Dipolar Fermi gases in anisotropic traps, *Physical Review A* **81**, 063629 (2010).
- [93] T. Sogo, L. He, T. Miyakawa, S. Yi, H. Lu, and H. Pu, Dynamical properties of dipolar Fermi gases, *New Journal of Physics* **11**, 055017 (2009).
- [94] Miyakawa T., Sogo T., and Pu H., Phase-space deformation of a trapped dipolar Fermi gas, *Physical Review A* **77**, 061603(R) (2008).
- [95] T. Sogo, L. He, T. Miyakawa, S. Yi, and H. L. Pu, Dynamical properties of dipolar Fermi gases, *New Journal of Physics* **12**, 079801–079801 (2010).
- [96] J.-N. Zhang and S. Yi, Thermodynamic properties of a dipolar Fermi gas, *Physical Review A* **81**, 033617 (2010).
- [97] K. Bergmann, N. V. Vitanov, and B. W. Shore, Perspective: Stimulated raman adiabatic passage: The status after 25 years, *The Journal of Chemical Physics* **142**, 170901 (2015).
- [98] K.-K. Ni, S. Ospelkaus, M. H. G. de Miranda, A. Pe’er, B. Neyenhuis, J. J. Zirbel, S. Kotochigova, P. S. Julienne, D. S. Jin, and J. Ye, A high phase-space-density gas of polar molecules, *Science* **322**, 231–235 (2008).
- [99] J. W. Park, S. A. Will, and M. W. Zwierlein, Ultracold dipolar gas of fermionic NaK molecules in their absolute ground state, *Physical Review Letters* **114**, 205302 (2015).
-

- 
- [100] J. W. Park, S. A. Will, and M. W. Zwierlein, Two-photon pathway to ultracold ground state molecules of  $^{23}\text{Na}^{40}\text{K}$ , *New Journal of Physics* **17**, 075016 (2015).
- [101] M. W. Gempel, T. Hartmann, T. A. Schulze, K. K. Voges, A. Zenesini, and S. Ospelkaus, Versatile electric fields for the manipulation of ultracold nak molecules, *New Journal of Physics* **18**, 045017 (2016).
- [102] F. Seesselberg, N. Buchheim, Z.-K. Lu, T. Schneider, X.-Y. Luo, E. Tiemann, I. Bloch, and C. Gohle, Modeling the adiabatic creation of ultracold polar  $^{23}\text{Na}^{40}\text{K}$  molecules, *Physical Review A* **97**, 013405 (2018).
- [103] T. M. Rvachov, H. Son, A. T. Sommer, S. Ebadi, J. J. Park, M. W. Zwierlein, W. Ketterle, and A. O. Jamison, Long-lived ultracold molecules with electric and magnetic dipole moments, *Physical Review Letters* **119**, 143001 (2017).
- [104] J. Deiglmayr, A. Grochola, M. Repp, K. Mörtlbauer, C. Glück, J. Lange, O. Dulieu, R. Wester, and M. Weidemüller, Formation of ultracold polar molecules in the rovibrational ground state, *Physical Review Letters* **101**, 133004 (2008).
- [105] J. Deiglmayr, A. Grochola, M. Repp, O. Dulieu, R. Wester, and M. Weidemüller, Permanent dipole moment of LiCs in the ground state, *Physical Review A* **82**, 032503 (2010).
- [106] T. Takekoshi, L. Reichsöllner, A. Schindewolf, J. M. Hutson, C. R. Le Sueur, O. Dulieu, F. Ferlaino, R. Grimm, and H.-C. Nägerl, Ultracold dense samples of dipolar rbcs molecules in the rovibrational and hyperfine ground state, *Physical Review Letters* **113**, 205301 (2014).
- [107] P. K. Molony, P. D. Gregory, Z. Ji, B. Lu, M. P. Köppinger, C. R. Le Sueur, C. L. Blackley, J. M. Hutson, and S. L. Cornish, Creation of ultracold  $^{87}\text{Rb}^{133}\text{Cs}$  molecules in the rovibrational ground state, *Physical Review Letters* **113**, 255301 (2014).
- [108] M. Guo, B. Zhu, B. Lu, X. Ye, F. Wang, R. Vexiau, N. Bouloufa-Maafa, G. Quémener, O. Dulieu, and D. Wang, Creation of an ultracold gas of ground-state dipolar  $^{23}\text{Na}^{87}\text{Rb}$  molecules, *Physical Review Letters* **116**, 205303 (2016).
- [109] Luigi D. M., Giacomo V., Kyle M., William G. T., Jacob P. C., and Jun Y., A degenerate Fermi gas of polar molecules, *Science* **363**, 853–856 (2019).
- [110] N. W. Ashcroft and D. N. Mermin, *Solid State Physics*, Holt, Rinehart and Winston New York (1976).
-

- 
- [111] E. Lifshitz and L. Pitaevskii, *Statistical physics, part 2*, New York (1980).
- [112] H. Kontani, *Transport Phenomena in Strongly Correlated Fermi Liquids*, Springer Berlin (2014).
- [113] M. Tinkham, *Introduction to Superconductivity*, McGraw Hill New York (1975).
- [114] K. H. Bennemann and J. B. Ketterson, *Superconductivity* volume 1: Conventional and Unconventional Superconductors, Vol. 2: Novel Superconductors, Springer Berlin (2008).
- [115] E. Fradkin, S. A. Kivelson, M. J. Lawler, J. P. Eisenstein, and A. P. Mackenzie, Nematic Fermi fluids in condensed matter physics, *Annual Review of Condensed Matter Physics* **1**, 153 (2010).
- [116] C.-K. Chan, C. Wu, W.-C. Lee, and S. Das Sarma, Anisotropic-Fermi-liquid theory of ultracold fermionic polar molecules: Landau parameters and collective modes, *Physical Review A* **81**, 023602 (2010).
- [117] L. M. Sieberer and M. A. Baranov, Collective modes, stability, and superfluid transition of a quasi-two-dimensional dipolar Fermi gas, *Physical Review A* **84**, 063633 (2011).
- [118] K. Góral, B.-G. Englert, and K. Rzażewski, Semiclassical theory of trapped fermionic dipoles, *Physical Review A* **63**, 033606 (2001).
- [119] D. Baillie, R. N. Bisset, and P. B. Blakie, Stability of a trapped dipolar quantum gas, *Physical Review A* **91**, 013613 (2015).
- [120] M. Wenzel, F. Böttcher, T. Langen, I. Ferrier-Barbut, and T. Pfau, Striped states in a many-body system of tilted dipoles, *Physical Review A* **96**, 053630 (2017).
- [121] A. K. Fedorov, S. I. Matveenko, V. I. Yudson, and G. V. Shlyapnikov, Novel p-wave superfluids of fermionic polar molecules, *Scientific Reports* **6**, 27448 (2016).
- [122] J.-N. Zhang, R.-Z. Qiu, L. He, and S. Yi, Dynamical properties of a trapped dipolar Fermi gas at finite temperature, *Physical Review A* **83**, 053628 (2011).
- [123] D. Baillie and P. B. Blakie, Magnetostriction and exchange effects in trapped dipolar Bose and Fermi gases, *Physical Review A* **86**, 023605 (2012).

- 
- [124] J.-N. Zhang and S. Yi, Fermi surface of a trapped dipolar Fermi gas, *Physical Review A* **80**, 053614 (2009).
- [125] V. Veljić, A. Balaž, and A. Pelster, Time-of-flight expansion of trapped dipolar Fermi gases: From the collisionless to the hydrodynamic regime, *Physical Review A* **95**, 053635 (2017).
- [126] F. Wächtler, A. R. P. Lima, and A. Pelster, Low-lying excitation modes of trapped dipolar Fermi gases: From the collisionless to the hydrodynamic regime, *Physical Review A* **96**, 043608 (2017).
- [127] E. G. C. P. van Loon, M. I. Katsnelson, L. Chomaz, and M. Leshko, Interaction-driven Lifshitz transition with dipolar fermions in optical lattices, *Physical Review B* **93**, 195145 (2016).
- [128] M. Abad, A. Recati, and S. Stringari, Quadrupole oscillation in a dipolar Fermi gas: Hydrodynamic versus collisionless regime, *Physical Review A* **85**, 033639 (2012).
- [129] B. Liu and L. Yin, Correlation energy of a homogeneous dipolar Fermi gas, *Physical Review A* **84**, 053603 (2011).
- [130] J. Krieg, P. Lange, L. Bartosch, and P. Kopietz, Second-order interaction corrections to the Fermi surface and the quasiparticle properties of dipolar fermions in three dimensions, *Physical Review A* **91**, 023612 (2015).
- [131] P. Lange, J. Krieg, and P. Kopietz, Physical dipoles and second-order perturbation theory for dipolar fermions in two dimensions, *Physical Review A* **93**, 033609 (2016).
- [132] W. P. Schleich, Quantum optics in phase space, Berlin: Wiley-VCH Verlag Berlin GmbH 1st edn (2005).
- [133] E. Wigner, On the quantum correction for thermodynamic equilibrium, *Physical Review* **40**, 749–759 (1932).
- [134] A. Bogojević, A. Balaž, and A. Belić, Asymptotic properties of path integral ideals, *Physical Review E* **72**, 036128 (2005).
- [135] A. Bogojević, I. Vidanović, A. Balaž, and A. Belić, Fast convergence of path integrals for many-body systems, *Physics Letters A* **372**, 3341 – 3349 (2008).

- 
- [136] I. Vidanović, A. Bogojević, A. Balaž, and A. Belić, Properties of quantum systems via diagonalization of transition amplitudes. II. Systematic improvements of short-time propagation, *Physical Review E* **80**, 066706 (2009).
- [137] A. Balaž, I. Vidanović, A. Bogojević, A. Belić, and A. Pelster, Fast converging path integrals for time-dependent potentials: I. Recursive calculation of short-time expansion of the propagator, *Journal of Statistical Mechanics: Theory and Experiment* **2011**, 03004 (2011).
- [138] A. Balaž, I. Vidanović, A. Bogojević, A. Belić, and A. Pelster, Fast converging path integrals for time-dependent potentials: II. Generalization to many-body systems and real-time formalism, *Journal of Statistical Mechanics: Theory and Experiment* **2011**, 03005 (2011).
- [139] S. Ronen and J. L. Bohn, Zero sound in dipolar Fermi gases, *Physical Review A* **81**, 033601 (2010).
- [140] I. S. Gradshteyn and I. M. Ryzhik, Table of integrals, series, and products (2007).
- [141] S. Giovanazzi, P. Pedri, L. Santos, A. Griesmaier, M. Fattori, T. Koch, J. Stuhler, and T. Pfau, Expansion dynamics of a dipolar Bose-Einstein condensate, *Physical Review A* **74**, 013621 (2006).
- [142] K. Howe, A. R.P. Lima, and A. Pelster, Rotating Fermi gases in an anharmonic trap, *The European Physical Journal D* **54**, 667–682 (2009).
- [143] N. V. Vitanov, A. A. Rangelov, B. W. Shore, and K. Bergmann, Stimulated raman adiabatic passage in physics, chemistry, and beyond, *Reviews of Modern Physics* **89**, 015006 (2017).
- [144] S. A. Moses, J. P. Covey, M. T. Miecnikowski, B. Yan, B. Gadway, J. Ye, and D. S. Jin, Creation of a low-entropy quantum gas of polar molecules in an optical lattice, *Science* **350**, 659–662 (2015).
- [145] M. W. Gempel, T. Hartmann, T. A. Schulze, K. K. Voges, A. Zenesini, and S. Ospelkaus, Versatile electric fields for the manipulation of ultracold NaK molecules, *New Journal of Physics* **18**, 045017 (2016).
- [146] S. Yi and L. You, Trapped condensates of atoms with dipole interactions, *Physical Review A* **63**, 053607 (2001).

- 
- [147] J. Stuhler, A. Griesmaier, T. Koch, M. Fattori, and T. Pfau, Magnetostriction in a degenerate quantum gas, *Journal of Magnetism and Magnetic Materials* **316**, 429 – 432 (2007).
- [148] I. Pomeranchuk, On the stability of a Fermi liquid, *Journal of Experimental and Theoretical Physics (U.S.S.R.)* **3**, 524 (1958).
- [149] V. Baran, M. Colonna, V. Greco, and M. Di Toro, Reaction dynamics with exotic nuclei, *Physics Reports* **410**, 335 – 466 (2005).
- [150] Z. Lj. Petrović, Z. M. Raspopović, S. Dujko, and T. Makabe, Kinetic phenomena in electron transport in radio-frequency fields, *Applied Surface Science* **192**, 1 – 25 (2002), Advance in Low Temperature RF Plasmas.
- [151] S. Dujko, U. Ebert, R. D. White, and Z. Lj. Petrović, Boltzmann equation analysis of electron transport in a N<sub>2</sub>-O<sub>2</sub> streamer discharge, *Japanese Journal of Applied Physics* **50**, 08JC01 (2011).
- [152] K. Dusling and T. Schäfer, Elliptic flow of the dilute Fermi gas: From kinetics to hydrodynamics, *Physical Review A* **84**, 013622 (2011).
- [153] P.-A. Pantel, D. Davesne, and M. Urban, Numerical solution of the Boltzmann equation for trapped Fermi gases with in-medium effects, *Physical Review A* **91**, 013627 (2015).
- [154] S. Chiacchiera, T. Lepers, D. Davesne, and M. Urban, Collective modes of trapped Fermi gases with in-medium interaction, *Physical Review A* **79**, 033613 (2009).
- [155] S. Chiacchiera, T. Lepers, D. Davesne, and M. Urban, Role of fourth-order phase-space moments in collective modes of trapped Fermi gases, *Physical Review A* **84**, 043634 (2011).
- [156] E. Timmermans, P. Tommasini, and K. Huang, Variational Thomas-Fermi theory of a nonuniform Bose condensate at zero temperature, *Physical Review A* **55**, 3645–3657 (1997).
- [157] L. P. Kadanoff and G. Baym, Quantum statistical mechanics, Cambridge: Cambridge University Press 1st edn (1962).
- [158] P. Pedri, D. Guéry-Odelin, and S. Stringari, Dynamics of a classical gas including dissipative and mean-field effects, *Physical Review A* **68**, 043608 (2003).

- 
- [159] Y. Castin and R. Dum, Bose-Einstein condensates in time dependent traps, *Physical Review Letters* **77**, 5315–5319 (1996).
- [160] F. Wächtler, Hartree-Fock Theory of Dipolar Fermi Gases, Diploma Thesis: University of Potsdam (2011).
- [161] J. L. Bohn and D. S. Jin, Differential scattering and rethermalization in ultracold dipolar gases, *Physical Review A* **89**, 022702 (2014).
- [162] M. Bluhm, B. Kämpfer, and K. Redlich, Viscosities of the quasidegluon plasma, *Journal of Physics: Conference Series* **270**, 012062 (2011).
- [163] W. Florkowski, R. Ryblewski, and M. Strickland, Chromoelectric oscillations in a dynamically evolving anisotropic background, *Physical Review D* **86**, 085023 (2012).
- [164] J. A. Bittencourt, Phenomenology of ultra-relativistic heavy-ion collisions, Singapore: World Scientific 1st edn (2010).
- [165] J. A. Bittencourt, Fundamentals of plasma physics, New York: Springer 3rd edn (2004).
- [166] K. F. Brennan, The physics of semiconductors with applications to optoelectronic devices, Cambridge: Cambridge University Press 1st edn (1999).
- [167] D. H. J. O’Dell, S. Giovanazzi, and C. Eberlein, Exact hydrodynamics of a trapped dipolar Bose-Einstein condensate, *Physical Review Letters* **92**, 250401 (2004).

---

# Biography of the author

---

Vladimir Veljić was born on December 30th, 1987 in Brus, Republic of Serbia. He completed his primary school education with honors at the Elementary school "Jovan Jovanović Zmaj" in Brus. He continued his education in the "May 9th" high school in Niš, specializing in physics, which he also completed with honors. He decided to pursue two university degrees in parallel, at the Faculty of Physics and the Faculty of Mechanical Engineering, University of Belgrade. He obtained his BSc degree at the Faculty of Mechanical Engineering in 2010 (GPA 9.97/10.0), and a year later at the Faculty of Physics, with a major in Theoretical and Experimental Physics, as the best student of the generation (GPA 9.90/10.0). He then pursued a Master's degree at both Faculties and graduated in 2012 at the Faculty of Physics (GPA 10.0/10.0), and at the Faculty of Mechanical Engineering (GPA 9.90/10.0).

During the BSc and MSc studies, he was an intern at CERN, in summer of 2011, and at the Clarendon Laboratory at Oxford University, in summer of 2012. He was awarded a scholarship by the Serbian Business Club "Privrednik" during the 2008/2009 academic year, and from the Fund for Young Talents of the Republic of Serbia in the period from 2009 to 2012.

Vladimir Veljić enrolled in the physics PhD program at the Faculty of Physics, University of Belgrade in 2013. Since then, he is employed at the Scientific Computing Laboratory, National Center of Excellence for the Study of Complex Systems of the Institute of Physics Belgrade. He participates in the national research project "Modeling and Numerical Simulations of Complex Many-body Systems" (ON171017) led by Dr. Antun Balaž, as well as in several bilateral projects with Germany (QDDB, IBEC, BEC-L) and with Austria (DUDFG). He attended several PhD schools and conferences in Germany, France, Japan, and the USA.

During the schools years 2012/13, 2015/16, and 2016/17 he actively participated in the work of the National Committee for High-School Physics Competitions, being the author of problems at all levels of competitions. Since 2017 he is the co-organizer of the Young Physicists' Tournament, a new form of high-school competitions in Serbia. He was one of the leaders of Serbia's team at the International Young Physicists' Tournament twice - in Singapore in 2017 and in China in 2018.

Vladimir Veljić has published three papers in leading international journals and presented his results at various international conferences.

# Изјава о ауторству

Име и презиме аутора - **Владимир Вељић**

Број индекса – **2013/8003**

## Изјављујем

да је докторска дисертација под насловом

**Quantum kinetic theory for ultracold dipolar Fermi gases**

**(Квантна кинетичка теорија за ултрахладне диполне Ферми гасове)**

- резултат сопственог истраживачког рада;
- да дисертација у целини ни у деловима није била предложена за стицање друге дипломе према студијским програмима других високошколских установа;
- да су резултати коректно наведени и
- да нисам кршио/ла ауторска права и користио/ла интелектуалну својину других лица.

**Потпис аутора**

У Београду, 24. 06. 2019. год.



## **Изјава о истоветности штампане и електронске верзије докторског рада**

Име и презиме аутора – **Владимир Вељић**

Број индекса – **2013/8003**

Студијски програм - **Физика кондензоване материје и статистичка физика**

Наслов рада - **Quantum kinetic theory for ultracold dipolar Fermi gases  
(Квантна кинетичка теорија за ултрахладне диполне Ферми гасове)**

Ментор - **др Антун Балаж**

Изјављујем да је штампана верзија мог докторског рада истоветна електронској верзији коју сам предао ради похрањења у **Дигиталном репозиторијуму Универзитета у Београду**.

Дозвољавам да се објаве моји лични подаци везани за добијање академског назива доктора наука, као што су име и презиме, година и место рођења и датум одбране рада.

Ови лични подаци могу се објавити на мрежним страницама дигиталне библиотеке, у електронском каталогу и у публикацијама Универзитета у Београду.

**Потпис аутора**

У Београду, 24. 06. 2019. год.



## Изјава о коришћењу

Овлашћујем Универзитетску библиотеку „Светозар Марковић“ да у Дигитални репозиторијум Универзитета у Београду унесе моју докторску дисертацију под насловом:

**Quantum kinetic theory for ultracold dipolar Fermi gases (Квантна кинетичка теорија за ултрахладне диполне Ферми гасове)**

која је моје ауторско дело.

Дисертацију са свим прилозима предао/ла сам у електронском формату погодном за трајно архивирање.

Моју докторску дисертацију похрањену у Дигиталном репозиторијуму Универзитета у Београду и доступну у отвореном приступу могу да користе сви који поштују одредбе садржане у одабраном типу лиценце Креативне заједнице (Creative Commons) за коју сам се одлучио/ла.

1. Ауторство (CC BY)
2. Ауторство – некомерцијално (CC BY-NC)
3. Ауторство – некомерцијално – без прерада (CC BY-NC-ND)
- 4. Ауторство – некомерцијално – делити под истим условима (CC BY-NC-SA)**
5. Ауторство – без прерада (CC BY-ND)
6. Ауторство – делити под истим условима (CC BY-SA)

(Молимо да заокружите само једну од шест понуђених лиценци.  
Кратак опис лиценци је саставни део ове изјаве).

**Потпис аутора**

У Београду, 24. 06. 2019. год.



1. **Ауторство.** Дозвољаваате умножавање, дистрибуцију и јавно саопштавање дела, и прераде, ако се наведе име аутора на начин одређен од стране аутора или даваоца лиценце, чак и у комерцијалне сврхе. Ово је најслободнија од свих лиценци.

2. **Ауторство – некомерцијално.** Дозвољаваате умножавање, дистрибуцију и јавно саопштавање дела, и прераде, ако се наведе име аутора на начин одређен од стране аутора или даваоца лиценце. Ова лиценца не дозвољава комерцијалну употребу дела.

3. **Ауторство – некомерцијално – без прерада.** Дозвољаваате умножавање, дистрибуцију и јавно саопштавање дела, без промена, преобликовања или употребе дела у свом делу, ако се наведе име аутора на начин одређен од стране аутора или даваоца лиценце. Ова лиценца не дозвољава комерцијалну употребу дела. У односу на све остале лиценце, овом лиценцом се ограничава највећи обим права коришћења дела.

4. **Ауторство – некомерцијално – делити под истим условима.** Дозвољаваате умножавање, дистрибуцију и јавно саопштавање дела, и прераде, ако се наведе име аутора на начин одређен од стране аутора или даваоца лиценце и ако се прерада дистрибуира под истом или сличном лиценцом. Ова лиценца не дозвољава комерцијалну употребу дела и прерада.

5. **Ауторство – без прерада.** Дозвољаваате умножавање, дистрибуцију и јавно саопштавање дела, без промена, преобликовања или употребе дела у свом делу, ако се наведе име аутора на начин одређен од стране аутора или даваоца лиценце. Ова лиценца дозвољава комерцијалну употребу дела.

6. **Ауторство – делити под истим условима.** Дозвољаваате умножавање, дистрибуцију и јавно саопштавање дела, и прераде, ако се наведе име аутора на начин одређен од стране аутора или даваоца лиценце и ако се прерада дистрибуира под истом или сличном лиценцом. Ова лиценца дозвољава комерцијалну употребу дела и прерада. Слична је софтверским лиценцама, односно лиценцама отвореног кода.